Discovering Galaxies In The Early Universe

Kristan Boyett
Wolfson College
University of Oxford

A thesis submitted for the degree of
Doctor of Philosophy

Trinity 2021

These 50 thousand words are dedicated to all those who struggle with Dyslexia.

I will be forever grateful to my parents and to the tutors who helped me build strategies to overcome my hurdles, and that I have always found support when needed.

Though it has taken years, I am slowly coming to reject my long-standing fear that I struggled because I was not bright enough. I submit my thesis as testament to that.

– – –

"He looks like a great dancer, until he moves"
Head coach, Oxford University Dance Sport, upon seeing my Waltz

"He's the Greatest Dancer." - Sister Sledge

Abstract

Star forming galaxies (SFGs) are expected to be the sources responsible for reionising the Universe, but detailed study of these within the Epoch of Reionisation (EoR, $z > 6$), will only become possible with the long-wavelength coverage and sensitivity of the James Webb Space Telescope (JWST). One approach to understanding these systems is to study lower-redshift galaxies which share similar properties and are potential analogues to galaxies in the reionisation era. In this Thesis I study star forming galaxies that exhibit large nebular emission line equivalent widths (EW), consistent with what has been inferred at high redshifts, using HST/WFC3 slitless spectroscopy to select galaxies at $z \sim 1 - 3$ directly on their emission line strength.

VLT/FORS2 spectroscopic follow-up on $z \sim 1$ emission line selected galaxies from the WFC3 WISPS survey confirms the slitless spectroscopic redshift of 95% of galaxies with emission line detections, and those galaxies with large rest-frame Hα EWs not only have high specific star formation rates but also high [OIII]/Hβ and [OIII]/[OII] ratios, suggesting lower metallicities or higher ionisation parameters than low-EW SFGs. I measure a strong EW evolution with redshift from WISPS, which I also confirm with a spectroscopic study of $z \sim 2$ SFGs from the 3D-HST survey where I determine the distribution of [OIII]λ5007 rest-frame EWs. The abundance of extreme emission line galaxies (EELGs) increases rapidly with redshift, and while abundance of these EELGs and their contribution to the ionising background at intermediate redshifts is minimal (only 3.6% of $z \sim 2$ SFGs have [OIII]λ5007 EWs above 750Å), EELGs may dominate the ionising output of the SFG population during the EoR.

I am a member of the JWST Advanced Deep Extra-galactic Survey (JADES), a joint NIRSpec and NIRCam instrument science team GTO programme whose main science goals are to trace galaxy evolution from $z \sim 1$ to within the EoR by measuring star formation rates, metallicities and stellar masses of a large sample of galaxies. As part of JADES, I re-analysed multi-band imaging in the GOODS fields to draw up a list of robust high redshift candidates and a prioritisation of these targets, in particular SFGs in the EoR, for NIRSpec spectroscopic follow-up. I confirm through simulations of JADES NIRSpec deep spectroscopy that our key science goals can be met with the achieved signal-to-noise from our observational strategy (in particular redshift confirmation, and metallicity measurements from line ratio diagnostics).

Statement of Originality

The work presented in this thesis was undertaken at the Department of Astrophysics at the University of Oxford between October 2017 and August 2021 under the supervision of Prof. Andrew Bunker. I hereby declare that no part of this thesis has been submitted in support of another degree, diploma, certificate or other qualification at the University of Oxford or elsewhere. Except where otherwise stated, or where reference is made to the work of others, the work in this thesis is entirely my own.

Chapter 2 forms the basis a paper that will be submitted to Monthly Notices of the Royal Astronomical Society for which I am the lead author, in collaboration with the WISPS team. This work was carried out with regular consolation with Prof. Bunker. The imaging data was originally reduced by members of the WISPS collaboration, particularly Dr. Andrew Battisti, and the SED fitting software BEAGLE used in the photometry fitting was carried out by Dr. Jacapo Chevallard and Imaan Wallace.

Chapter 3 forms the basis of another paper that will be presently submitted to Monthly Notices of the Royal Astronomical Society for which I am the lead author. This work was carried out with regular consolation with Prof. Dan Stark. The imaging data was originally observed and reduced by the 3D-HST Treasury Program (HST-GO-12177 and HST-GO-12328, which is operated by the Association of Universities for Research in Astronomy, Inc., under NASA contract NAS5-26555). The specific upper (B-V) limit for the selection was determined by Dr. Mengtao Tang.

Chapter 4 again makes use of the 3D-HST imaging and was carried out with regular consolation with Prof. Bunker. The SED fitting software BEAGLE used in the photometry fitting was run by Dr. Emma Curtis-Lake.

Chapter 5 uses the IPS simulations which were developed by Centre de Recherche Astrophysique de Lyon (CRAL) as part of a contract with Airbus Defence and Space (the prime contractor for NIRSpec). This work was carried out with regular consolation with Dr. Giovanna Giardino, Dr. Pierre Ferruit and Prof. Bunker.

Kristan Boyett

August 2021

Acknowledgements

I wish to acknowledge the tremendous academic support I have received during this degree which has shaped me into the astronomer I am today. Firstly, I wish to pay great thanks to my supervisor Prof. Andy Bunker for his unbelievable support and absolute dedication over these four years, especially during the last few months of writing up. Secondly, I extend deep gratitude to Prof. Dan Stark for his committed support, guidance and his patience, especially during all our late night and early morning international telecoms. Lastly, I would like to thank Dr. Giovanna Giardino and Dr. Pierre Ferruit for their support during my time working at ESTEC.

A degree is never truly completed alone and I would like to give special thanks to my friends and family who have helped me through this process. To Moa, thank you for your seemingly endless supply of motivational post-it notes and pick-me ups over the months of writing this thesis. To Eloise Brown and Nathan Adams, who have been alongside me as friends and flatmates over our degrees together, thank you for your continuous support. To David, thank you for our river swims and thesis chats. To all those in the Wolfson College Boat Club, thank you for making those early mornings worth waking up for, especially Jorn, Mary and Romy. To my dance partner Hannah, thank you for importantly reminding me that you don't have to be the best at something to enjoy it.

This DPhil would not have been half as fulfilling without the opportunities I had to travel and live in Tuscon, Arizona and Leiden, Netherlands, due to the wonderful and kind friends I made. To Kevin and Peter, thank you for all the days spent climbing on Mt Lemmon, and to Rachael, Charity, Katie, Raphael, and all their pets, thank you for making me feel welcome.

And finally, to my parents, Fay and Terry. Simply put, you have given me everything and everything I am is built from your ever-prescience at my side.

Contents

Chapter 1

Introduction

In this thesis, I study the emission line properties of star-forming galaxies at intermediate redshifts ($0.4 < z < 2.4$) and I study the target selection strategy for an upcoming extra-galactic survey using the Near Infrared Spectrograph (NIRSpec) on the James Webb Space Telescope (JWST) to explore star-forming emission line galaxies in the high redshift universe ($4 < z < 12+$). The forthcoming extra-galactic survey will provide a quality and quantity of data previously unobtainable for star-forming galaxies during the epoch of reionisation and will build upon my intermediate redshift work using similar observational and analysis techniques. In this introduction, I summarise the observational techniques and the inferred galaxy properties that have shaped our understanding of star-forming galaxies across cosmic time. I will discuss the current state of our understanding of the role star-forming galaxies play in the reionisation of the universe.

1.1 Observational astronomy

We have known for over 100 years that there exist galaxies outside of our own Milky Way (Hubble, 1926). We have seen in the 20^{th} century that our universe is expanding (Hubble, 1929) and contains not only the everyday (baryonic) matter we see around us but also dark matter (identified initially from rotation curves of galaxies, Rubin et al. 1978, and studies of clusters, Zwicky 1933). More recently, it has been discovered that the expansion of the Universe is currently accelerating, a discovery initially based on observations using supernovae type-Ia (SN-Ia) as standard candles (Riess et al., 1998; Perlmutter et al., 1999). This current acceleration is driven by dark energy which might correspond to a cosmological constant vacuum energy density (or could be something more complicated associated with a scalar field, such as quintessence, Caldwell et al. 1998). From various studies, including using supernovae

as lighthouses to mark cosmic distances, the large-scale structure of the Universe (from galaxy surveys) and observations of the Cosmic Microwave Background[1] (CMB), we today have reasonable constraints on the cosmological parameters that govern the expansion history of our Universe. In this thesis I will adopt a Λ-dominated, flat universe with dark energy and matter density parameters of $\Omega_\Lambda = 0.7$ and $\Omega_M = 0.3$, and a Hubble constant of $H_0 = 70$ km s^{-1} Mpc^{-1} from WMAP (Hinshaw et al., 2013).

The observed expansion of the Universe means that in the past it was more dense and hotter than today, and the current paradigm is the Hot Big Bang model, where the Universe formed $\sim$13.8 Gyrs ago and has expanded ever since. The expansion has meant that as light travels through the Universe it is being stretched, and the scale of the wavelength stretch of observed light tells us the redshift of the source ($1 + z = \lambda_{obs}/\lambda_{emit}$, where λ_{obs} and λ_{emit} are the observed and emitted wavelength). From the measured redshift, various cosmological distance measures to the source and the age of the Universe when the light was emitted can be determined, given the expansion history (dictated by the cosmology, see e.g., Hogg 1999).

It is believed that initial density fluctuations (perhaps Gaussian in nature and observed through temperature fluctuations in the CMB, Smoot et al. 1992) grow with time through gravitational collapse, seeding the formation of the first galaxies. Within galaxies, stars form, again through gravitational collapse and heating (the virial theorem) until the density and temperature are sufficient for nuclear processes to be triggered to achieve hydrostatic equilibrium. As stellar populations emerge, the pristine gas left over from the Big Bang (nearly completely comprised of hydrogen and helium, at $\sim 75\%$ and $\sim 25\%$ by mass) becomes chemically enriched with heavier elements, largely formed in stars and stellar deaths. Through the use of next generation observatories such as JWST, we may be able to find the "Population III" stars which are the first generation of metal-free stars to form at high redshift. The "Metallicity" (mass-fraction of elements heavier than He) is expected to evolve with time, with later generations of stars forming from an Interstellar Medium (ISM) which is "enriched" in heavier elements due to ejecta from stars and supernovae. Line ratios of different ionisation species of elements (from absorption and emission lines in stellar photospheres or the Interstellar Medium) give an indication of the abundances, and

[1] the CMB corresponds to the surface of last scattering at a redshift of $z \sim 1100$, where matter and radiation last interacted (on average) and the universe became optically thin following the formation of the atoms and capture of free electrons (which previously scattered photons)

also the ionisation state of the gas. Star formation is a complex process, depending on fragmentation and cooling of the gas (which in turn depends on the spectrum and the elements present), and stars are formed with a range of stellar masses. The Initial Mass Function (IMF) of stellar populations may not be constant, and it is expected that the Population III IMF is top-heavy (e.g., Abel et al., 2002; Bromm & Larson, 2004; Hirano et al., 2014), whereas many IMFs for later generations of stars favour many more low-mass stars than massive stars (Salpeter, 1955; Chabrier, 2003).

1.1.1 Development of extra-galactic observational astronomy

The driving force behind the expansion of our knowledge has come through larger telescopes (including observatories in space) and the technological development of sensitive detectors such as CCDs and Infrared (IR) Arrays. Unlike ground-based observatories, which are limited by atmospheric absorption across many wavelengths including parts of the infrared and the ultra-violet (UV), space-based observatories can access the full electromagnetic spectrum. Space telescopes can also achieve greater sensitivity as the "background" (light from non-astronomical sources which adds noise to the observations) is typically much lower because there is no emission or scattered light from the sky. The greater sensitivity and access to wavelengths further into the IR has allowed fainter galaxies to be detected out to greater distances, particularly with the Hubble Space Telescope (HST).

Another significant technological development in recent years has been multi-object spectroscopy, enabling the redshift determination and detailed study of large populations of objects. From the ground, a slit or fibre is needed to disperse the light from a galaxy of interest and avoid adding noise due to the sky background around it, which has led to many multi-object spectrographs (e.g. the SDSS survey, York et al. 2000, and the 2dF on AAT, Colless 1999, which are fibre-fed, and slitmasks such as on Keck/DEIMOS giving surveys such as DEEP2, Davis et al. 2003). From space, the low background means that light from an entire field of view can be dispersed and still achieve reasonable sensitivity, and this "slitless spectroscopy" approach has been used to build large samples of galaxy spectra with HST (e.g. WISPS, Atek et al. 2010, 3DHST, Brammer et al. 2012) and will be used in future on JWST, Euclid and Nancy Grace Roman Space Telescope. Another approach has been the use of integral field spectroscopy (IFS) where each spatial pixel generates a spectrum, and the

latest IFS instruments such as MUSE on VLT (Bacon et al., 2010) now cover sufficient area on the sky to do multi-object surveys (rather than just individual galaxies).

1.2 Observational properties of galaxies

Observational extra-galactic astronomy is the study of light from galaxies, and this is predominantly star light at UV to near-infrared wavelengths (although emission from an Active Galactic Nucleus can dominate the flux in rare cases); at longer wavelengths (the far-infrared) thermal re-emission from dust can dominate the emissivity. The total spectrum of all the stars in a galaxy will depend on the current stellar population, and dust obscuration and emission from the Interstellar Medium will modify the observed spectrum. Depending on the observations available, there can be degeneracies between the inferred properties (for example, a spectrum can be red either through having an old stellar population, or large dust obscuration which greatly affects short wavelengths) although many of these degeneracies may be broken with sufficiently good spectroscopy (of appropriate signal-to-noise ratio, spectral resolution and wavelength coverage), even in the case of the pernicious "age-metallicity degeneracy" (Worthey, 1994). Stars are formed with a range of masses, and the most massive stars have the shortest lifetimes of <10Myr on the "main sequence" (the core-hydrogen burning phase, where stars occupy a narrow track of surface temperatures and luminosities on the Hertzsprung-Russell diagram), and these luminous OB stars with masses $>\sim 10 M_\odot$ have extremely hot photospheres (>30,000K) whose black-body radiation makes these stars very bright at blue and UV wavelengths. A significant number of these photons are produced at wavelengths shorter than 912Å which are capable of photo-ionising atomic hydrogen (energies > 13.6eV). Conversely, low-mass stars live a long time, are cooler and redder, and do not produce significant ionising flux. Hence, if a stellar population forms instantaneously (a "single stellar population"), then as time goes on it will become redder with different spectral features becoming prominent as a function of time (e.g. early on recombination emission lines of hydrogen from OB stars; later on the Balmer break absorption strongest in A-stars of $\sim 2 M_\odot$ after the OB stars have died; and later still the metal and molecular absorption lines in the cooler photospheres of low-mass stars). We expect most galaxies to have a more complicated star formation history than a single stellar population, with multiple star formation episodes due to secular processes. However, the instantaneous star formation rate (SFR) is traced by the ionising photons produced

by the short-lived OB stars.

1.2.0.1 Measuring the star formation rate in galaxies

Since the instantaneous star formation rate is related to the production of ionising photons, observable properties that are sensitive to these ionising photons can be used to infer the SFR, and hydrogen recombination emission lines provide such a star formation rate tracer. The high-energy UV emission (< 912Å) photo-ionises the surrounding neutral hydrogen in the ISM, which re-emits photons as the electrons recombine and cascade back to the ground state. The transition from $n = 3 \rightarrow 2$ excitation states produces the rest-frame optical Hα emission line, and from measurements of the Hα line flux we can infer the ionizing-photon output from the stellar population, since from atomic physics about 60% of the ionising photons will result in Hα emission (Osterbrock, 1989). Stellar population models can be used to infer the number of massive stars producing the ionising flux, and from this the rate at which these short-lived stars must be forming can be derived. Given an assumed IMF, this can be converted to the total stellar mass formed per year (the star formation rate). The Lyα hydrogen recombination line ($n = 2 \rightarrow 1$ transition) was originally believed to be the strongest signature of star formation at high redshift (e.g., Partridge & Peebles, 1967), but early searches over many decades showed this line was either absent or much weaker than predicted by simple models (e.g., Thompson & Djorgovski, 1995; Thompson et al., 1995; Steidel et al., 1996b). The explanation for this is that the Lyα line is resonantly-scattered by neutral hydrogen, meaning that the photons have a very short mean-free-path as their frequency is tuned to excite hydrogen atoms in the ground state (which applies to most of the atoms in moderately cold atomic gas), unlike photons with slightly different frequencies which will not excite the n=1-2 transition and hence will travel further before interacting. These repeated scatters of Lyα photons will randomise the direction each time, and will produce longer escape paths than those for non-resonant photons (which have a much higher probability of travelling directly out of a gas cloud). The long escape path lengths of the resonant Lyman-alpha means that this line is often absorbed[2]. Hence Lyα is not as good a

[2]It has been argued that for certain geometries of multiphase media, where a dust cloud is embedded within an intercloud medium of negligible absorption, Lyα photons may actually suffer less attenuation than radiation which is not resonantly scattered because such photons spend most of their time in the intercloud medium Neufeld (1991). In any case it is clear that the effects of resonant scattering and dust make the Lyα line hard to interpret, and a poor tracer of the rest-UV ionising continuum which powers it.

SFR indicator as Hα, which in contrast is non-resonant and at longer wavelengths, so is less affected by dust absorption than Lyα (where the effect of dust absorption can led to SFRs being underestimated).

Measurements of the line flux ratios between multiple recombination lines places constraints the the level of dust extinction (with lines at shorter wavelengths experiencing greater reddening), and hence line luminosities can be corrected for absorption using an extinction law and the intrinsic line ratios set by atomic physics (e.g., the Balmer decrement, which has a Case B - density bounded recombination ratio between Hα and Hβ of 2.86, Osterbrock 1989, see discussion in Section 2.3.3.2). In addition to recombination lines, the sensitivity of other observable properties of young stellar populations means the we can also make use of less-direct indicators of the SFR, including: the non-ionising UV stellar continuum (which is predominately dominated by the blackbody radiation of young massive stars, subject to dust attenuation); the strength of rest-optical nebular emission lines from the ISM (such as [OII], Hβ and [OIII], which are sensitive to the SFR and ISM conditions); the far-infrared emission (which characterises the UV-light emitted by massive stars and reprocessed by dust); and the observed radio and x-ray emission (generated by non-thermal bremsstrahlung and synchrotron emission driven by supernovae and the population of high-mass x-ray binaries in young stellar populations, respectively). Applying calibrations to each of these measured properties allows them to be used as tracers of the underlying SFR (see e.g., Hopkins et al., 2003, for a relative comparison of these different SFR tracers).

Another potential source of ionising photons are active galactic nuclei (AGN) - the accretion disks around supermassive black holes (SMBHs) which probably lie at the centres of all galaxies can become super-heated through differential rotation, producing emission across the electromagnetic spectrum (including ionising photons and even X-ray emission). While all massive galaxies are thought to host a SMBH, the bright AGN phase (where emission from the accretion disk rivals or dominates the stellar light from the galaxy, for example in a quasi-stellar object, QSO) is short lived, set by the fuelling of the SMBH accretion disk. This conclusion stems from the low number density of QSOs compared to galaxies. AGN can be sub-divided in different categories based on their multi-wavelength broadband, emission line and radio properties, which may be partly driven by the relative orientation of a dusty torus obscuring our view of the central engine of the AGN for some sight lines (see e.g., Netzer (2015) for a recent review of the unifying theory). Unobscured views show a

bright central non-stellar point source and broad emission lines generated close to the nucleus due to the high dispersion velocity field in that region; these are classed as Type-I/QSOs. Alternatively, obscured views can hide these components with narrow line emission dominating (arising from gas a greater distance from the nucleus), and these are classed as Type-II AGN. The presence and strength of radio jets provides anther classification (radio-loud vs radio-quiet).

In this thesis, I focus on galaxies where the light is likely to be dominated by stars rather than an AGN. AGN have a harder ionizing spectrum (due to their hot accretion disks, which exceed the photospheric temperatures of the hottest OB stars), and this will produce different emission line ratios (with a larger fraction of atoms in highly-ionised states). Hence line ratios can be used to distinguish AGN from star forming galaxies, and I look further at such diagnostics (e.g. the BPT) in Section 2.3.5 X-ray and radio emission are also stronger in some AGN than SFGs.

1.2.0.2 The equivalent widths of emission lines in galaxies

In this thesis I pay particular attention to the equivalent width (EW) of the nebular emission lines in star forming galaxies, which gives the measure of a line's strength relative to the stellar continuum at the same wavelength (by definition the ratio of the flux of the emission line to the stellar continuum flux density per unit wavelength and I will detail my measurement of EW in Sections 2.3.7 and 3.3.1). Reliable measurements of EWs can be determined straight from spectroscopy if both the line emission and continuum flux density are significantly detected, however, for sources with a faint stellar continuum better constraints on the EW are achieved by estimating the stellar continuum from corresponding broadband photometry. Reasonable measurements can also be made using photometry alone by examining the flux-excess created between two neighbouring broadband filters due to contamination by an emission line with a given EW with an underlying set of assumptions on the spectral slope. The EW of nebular emission lines, such as Hα and [OIII]λ5007, are sensitive to changes in the stellar population over relatively short timescales. The stellar continuum in the rest-optical is dominated by older stellar populations and gives an indication of the star formation history (SFH) over much longer timescales ($\gg$ 100Myr), whilst the strength of the nebular emission lines is driven by the radiation field of massive short-lived OB stars, sensitive to timescales $<$ 10Myr (e.g., Sullivan et al., 2001). The EW therefore gives the measure of how the near-instantaneous SFR compares to the build

up of stellar mass over longer timescales, with larger EWs identifying upturns and bursts in SFR, as a young stellar population drives strong line emission but does not yet dominate the rest-optical stellar continuum. The young stellar populations that can drive large EWs make these galaxies of particular interest as they may also have larger specific star formation rates (sSFR, the rate of star formation per unit mass), higher ionisation parameters[3] (the ratio of ionising UV photon flux to the number density of neutral hydrogen) and lower gas-phase metallicities than SFGs with low EWs and potentially older stellar populations. The high ionisation parameter associated with a young stellar population and inferred for galaxies with large nebular emission line EWs (which can be inferred from the line ratios of different ionisation species of the same elements, such as the ratio between [OIII] and [OII]), has been seen to be a requirement, but not alone sufficient, for large escape fractions of ionising photons (f_{esc}, the fraction of HI ionising photons that reach the inter-galactic medium, e.g., Nakajima et al. 2013). The presence of bursty star formation, that may be inferred from large EWs, is seen through simulations (e.g., Trebitsch et al., 2017) as one path to generating large escape fractions, with supernovae feedback from the young stellar population creating sight lines for ionising photons to escape.

1.2.1 Galaxy evolution

By comparing samples of galaxies at different redshifts, astronomers are able to learn about the evolution of galaxies over cosmic time. Two important considerations affect the assembly of galaxies, the star formation in individual galaxies, and mergers of galaxies. The luminosity function is the distribution of galaxy comoving number density[4] with brightness in a particular rest-frame waveband, and at short wavelengths this luminosity is related to the star formation rate (since as explained in Section 1.2 the blue/UV light is dominated by short-lived massive OB stars) while at longer (near-IR) wavelengths it is more related to the stellar mass (since stars of all masses will contribute to the near-IR emission, which have a wide range of lifetimes). Evolution of the luminosity functions (which may also be affected by dust obscuration)

[3]The ionisation parameter of a galaxy follows the relative proportion of young to old stars, and hence is expected to trend with the sSFR, because the hydrogen ionising photons are produced by the short-lived massive stars (Kaasinen et al., 2018). Likewise, the relative proportion of young to old stars also sees an increase in the EW, with the Hβ EW commonly used to trace the age of the stellar population (Kewley et al., 2015; Groves et al., 2012).

[4]A comoving frame is one which accounts for the expansion of the Universe, (1+z) in each spatial direction, so a comoving volume conserves the baryonic mass within it.

provides constraints on the formation and evolution of galaxies (e.g., Bouwens et al., 2015a).

The redshift and wavelength range available for different SFR tracer methods has allowed the star formation rate density (SFRD) over cosmic time to be assembled, typically using nebular emission lines at lower redshifts and the non-ionising UV continuum at higher redshifts (where these various spectral features are redshifted into the optical at different redshifts e.g., Lilly et al. 1996; Madau et al. 1996). From studying the SFRD of different redshift samples, the peak of cosmic star formation rate density is determined to lie around $z \sim 2$ (e.g., Madau & Dickinson, 2014).

Many observable and inferred properties of galaxies also change with redshift. At local redshifts, spatially resolved images of the light from galaxies reveals that the luminous morphology is commonly seen to take the form of spirals and smooth ellipticals (e.g., the Hubble tuning fork diagram, Hubble 1926, 1936), whereas at higher redshifts the luminous profile becomes less structured and more clumpy (e.g., Abraham et al., 1996; Elmegreen et al., 2007), reflecting the growth and evolution of galaxy structure into what is seen today (e.g., Conselice 2014, note most existing spatially resolved studies of high-z galaxies observe the rest-frame UV which will trace the star-forming regions which may not reflect the older underlying stellar population). Inferred properties of the ISM including the metallicity, ionisation parameter and the related ionisation photon production efficiency (the measure of the number of ionising photons produced per unit UV luminosity for a galaxy, e.g., Chevallard et al. 2018; Tang et al. 2019) are also seen to evolve, as galaxies at higher redshifts are in earlier episodes of star formation and have younger stellar populations that dominate the galaxy.

1.2.2 Identifying high-redshift samples of galaxies

It is observationally very expensive to do spectroscopic follow-up on all galaxies identified in imaging, and many will be low-luminosity galaxies at modest redshifts, while for studies of galaxy evolution we are more interested in targeting galaxies at high redshift. We now consider how to find likely high-redshift candidates for spectroscopic follow-up on the basis of imaging surveys (in particular using the colours across different filters).

The Intergalactic Medium (IGM) along the line of sight between a distant galaxy and the observer can change the observed spectral energy distribution due to the interaction of the light and the IGM. The ionising UV emission of a galaxy at short wavelengths (< 912Å, the photoionisation edge of hydrogen) will be suppressed due to absorption by any intervening neutral atomic hydrogen providing a distinctive and almost total break in the flux at this "Lyman limit". Depending on the redshift of the object and the column density of intervening neutral hydrogen, the spectrum of a galaxy will feature another distinctive break shortward of Lyα (1216Å) in its rest-frame, as the flux below is suppressed by the Lyα forest absorption by neutral hydrogen in the intervening IGM. This effect (the Lyα break) is most apparent in high redshift galaxies ($z > 6$), where neutral hydrogen was abundant in the IGM unlike at lower redshifts when the IGM is mostly ionised and the Lyα forest is less optically thick. Detecting the wavelength of this spectral break can be used as a key method of identifying candidate galaxies at high-redshift.

The Lyman break can be clearly observed through spectroscopy and also through comparison of broadband photometry in adjacent filters. Figure 1.1 presents the characteristic Lyman break feature of a $z \sim 7$ galaxy showing the corresponding photometric drop out between the F814W "Z-band" and F105W "Y-band" filters on HST. The measured photometry either side of the spectral break shows a clear contrast and a very red colour as the shorter wavelength flux below the break is suppressed, with the particular filter in which the galaxy "drops-out" providing an estimate of the redshift of the source. The approach of comparing the flux in adjacent broadband filters to identify drop-outs has been a successful method and found the first star-forming galaxies at $z \sim 3$ in the mid-1990s (Steidel et al., 1996a,b) and has since been pushed to longer wavelength filters and higher redshifts.

Deep surveys have utilised this method over the past decades to identify high-redshift Lyman-break galaxies (LBGs), many utilising the Hubble Space Telescope (HST). In 1995 the Hubble Deep Field (HDF, Williams et al. 1996) allowed Lyman-break galaxies to be detected at $z \sim 3 - 4$ (Steidel et al., 1996a). The addition of the Advanced Camera for Surveys (ACS) to the Hubble Space Telescope allowed the identification of the Lyman-break to longer wavelengths (e.g., $z \sim 6$ in Stanway et al. 2003) and in 2004 the Hubble Ultra Deep Field (HUDF, Bunker et al. 2004; Beckwith et al. 2006) pushed the detection of galaxies out to $z \sim 6$. Subsequent additions to

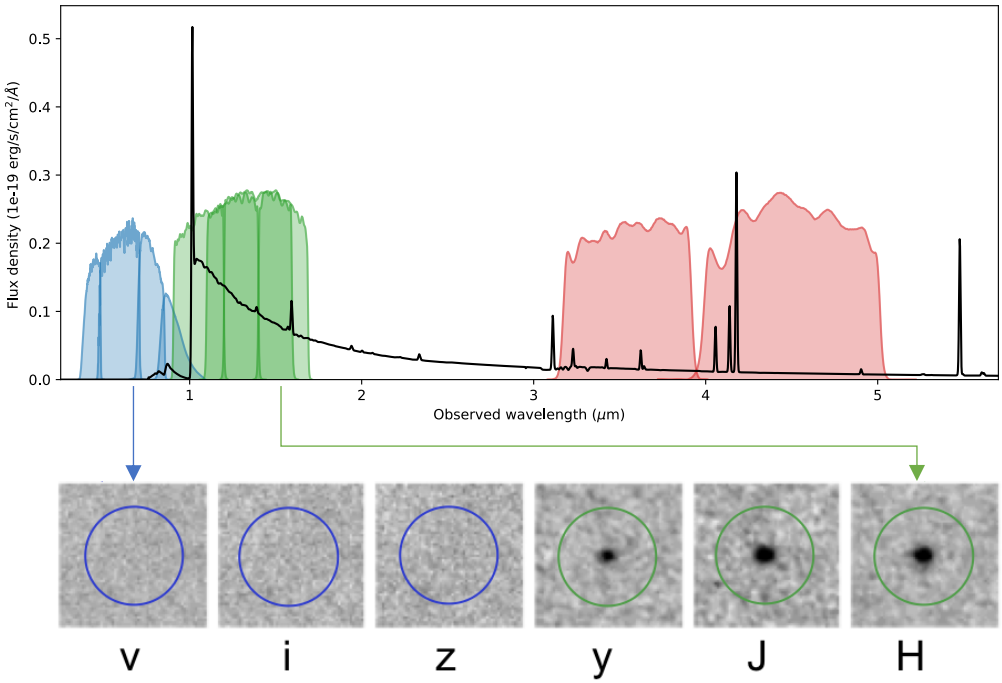

Figure 1.1: A synthetic spectrum of a young star-forming redshift $z \sim 7$ galaxy (taken from the JAGUAR catalogue of Williams et al. 2018) showing a clean Lyα break, corresponding to the suppression of shorter wavelength flux due to absorption by neutral hydrogen along the line of sight. Top: The spectrum over-plotted with HST ACS (blue, F435W, F606W, F775W, F850LP), WFC3 (green, F105W, F125W, F140W, F160W) and spitzer/IRAC channel 1 and 2 filters (red) often used in high redshift galaxy observations. Bottom: Imaging of an actual $z \sim 7$ galaxy from my Chapter 4 work shown in 6 filters across the Lyman break. The galaxy disappears at wavelengths below 1μm (the v-, i-, z-bands) due to absorption by the Lyα forest.

the Hubble Space Telescope improved its infrared capabilities, the Wide-Field Camera 3 (WFC3) allowed longer wavelength filters to push detections in the HUDF out to $z \sim 7-8$ (Wilkins et al., 2011; Lorenzoni et al., 2011; Bouwens et al., 2010; Oesch et al., 2010b). The highest redshift candidates currently known were identified with this technique (sometimes boosted by gravitational lensing) with photometric candidate redshifts around $z \sim 9-11$ (e.g., Coe et al., 2013; Oesch et al., 2014; Zheng et al., 2012). With the launch of JWST, NIRCam filters in the Near-Infrared should allow detection of the Lyman break to longer wavelengths and are anticipated to allow LBG samples to be selected out to redshifts > 10.

However, one draw back of identifying the Lyman-break through broadband pho-

tometric drop-out is that the same characteristic red colour between two adjacent filters can be mimicked by other spectral features, including the 4000Å and Balmer spectral breaks in the spectra of galaxies (created by metal-line absorption in older stellar populations and the Balmer break dominated by A-type stars), and complex SEDs of local brown dwarf stars due to molecular absorption in their cool photospheres. Cleaner selection of LBGs has been achieved by also considering the colour from two longer wavelength filters, the addition of the longer wavelength colour distinguishes high redshift LBGs (typically expected to exhibit a blue colour due to the intrinsic UV slope) from low redshift interlopers such as red elliptical galaxies (which would exhibit a redder colour at longer wavelengths). However, spectroscopic follow-up is still important to unambiguously confirm the redshifts of candidate LBGs, through the detection of emission lines and the spectrally resolved shape of the SED.

1.2.3 Galaxies within the Epoch of Reionisation

The observed suppression of flux below the Lyα line is greatest in the spectra of high-redshift galaxies before the end of the epoch of reionisation (EOR, $z > 6$), the transition of the atomic hydrogen in the IGM from neutral to a mainly ionised state (in which it becomes less efficient at absorbing the UV-ionising photons from lower-redshift galaxies). The prediction of an optically-thick Lyα forest (i.e. near-complete absorption at wavelengths shortward of Lyα) due to a large IGM neutral fraction was made by Gunn & Peterson (1965), and this was first seen observationally in the spectra of $z \sim 6$ quasi-stellar objects (QSOs) found in the SDSS survey (Fan et al., 2001; Becker et al., 2001), with temperature-polarisation measurements from the CMB also providing constraints on the EOR from free electrons (optical depths τ from WMAP, Hinshaw et al. 2013, and Planck, Planck Collaboration et al. 2020). Before the EOR, the hydrogen in the Universe had been neutral ever since the expansion of the Universe had allowed the temperatures to cool sufficiently for the first atoms to form (at around 370,000 years after the Big Bang during the epoch of recombination, Peebles 1968; Zel'dovich et al. 1969; Seager et al. 2000). The beginning of the transition in the state of atomic hydrogen was driven by a new ionising radiation field, probably associated with the formation of the first stars and galaxies in the Universe ($z > 15$). The progression and spatial distribution of reionisation is therefore dependent on the ionising sources. Local bubbles of ionised hydrogen surrounding the ionising sources may grow and become interconnected, leaving only small "islands" of neutral hydrogen by the end of the epoch. By $z \sim 5 - 6$ the fraction of neutral atomic hydrogen

had dropped to $< 4\%$(McGreer et al., 2015), marking the end of the EOR.

At low and intermediate redshifts ($z < 3$), Active Galactic Nuclei (AGN) are observed to dominate the production of UV photons, however constraints from observations and simulations indicate that too few QSOs existed during the epoch of reionization to match the required UV photon budget (e.g., Haardt & Madau, 2012; Richards et al., 2006; Faucher-Giguère et al., 2008). The source for the ionizing radiation field currently favours a population of star forming galaxies (Bunker et al., 2008, 2010; Stark, 2016; Boylan-Kolchin, 2018) with hot young massive stars providing the high energy UV photons, although debate remains as to whether the bright and faint QSO populations provide a non-negligible contribution (e.g., Giallongo et al. 2015; Grazian et al. 2018; Sulentic et al. 2014; c.f., Dijkstra et al. 2004). However, there remains uncertainty in the underlying assumptions associated with whether SFGs are the dominant ionizing sources, which depends on the initial mass function (affecting the ionising photon production efficiency), escape fraction (f_{esc}, the fraction of HI ionising photons that reach the inter-galactic medium) and the galaxy UV luminosity function (the integral of which is related to the production rate of ionising photons, and which in particular depends on the faint-end slope, of the Schechter luminosity function).

1.2.4 Low-redshift analogues of potential EOR ionising sources

One current approach for exploring the nature of galaxies during the EOR is the study of low-redshift analogues with similar properties. This provides larger samples for population analysis, and cover a broader range of luminosities and masses, than the small number of known high-redshift galaxies. At local and moderate redshifts, the current state of observatory facilities allows sensitive study of the properties of these low-redshift analogues, which will not be possible at higher redshifts until the longer-wavelength coverage and sensitivity of JWST is available.

Over the last decade, considerable effort has focused on the study of extreme emission line galaxies (EELGs) as low-redshift analogues of the galaxies that may have reionised the Universe, exhibiting nebular emission line equivalent widths consistent with what has been inferred at high redshifts. These systems are identified through their large [OIII], Hβ or Hα equivalent widths and have been studied in detail both locally $z \sim 0$ (Cardamone et al., 2009; Amorín et al., 2010; Izotov et al., 2011;

Brunker et al., 2020) and in comparable populations at redshifts $z \sim 1-2$ (e.g., van der Wel et al., 2011; Atek et al., 2011; Amorín et al., 2015; Maseda et al., 2018; Tang et al., 2019). Although rare at the current epoch, EELGs are thought to represent a significant fraction of the SFG population at $z > 6$ (e.g., Smit et al., 2015; De Barros et al., 2019; Endsley et al., 2021). They are characterised by a combination of strong nebular line emission and weak rest-optical continuum (i.e. high equivalent width), as expected for a galaxy powered by a very young stellar population with moderately low metallicity.

SFGs are expected to contribute the bulk of the ionising photon budget during the reionisation epoch (e.g., Bunker et al. 2004, 2010; Bouwens et al. 2015b; Robertson et al. 2015; Stanway et al. 2016; Stark 2016; Boylan-Kolchin 2018; Naidu et al. 2020; Finkelstein et al. 2019; c.f., Madau & Haardt 2015) and with a large fraction of early galaxies exhibiting extreme [OIII]+Hβ EWs, it is likely that a significant proportion of the ionising output responsible for reionising the IGM comes from SFGs in an EELG or burst phase. Galaxies may also be very effective at producing globular clusters during these intense star formation episodes (Vanzella et al., 2020; Endsley et al., 2021). It is clear that EELGs are likely to play an important role in galaxy growth and reionisation. While existing data hints at the EELG phase becoming more common toward higher redshifts, we currently do not have quantitative constraints on how the prevalence of this population evolves with redshift or varies with galaxy luminosity. This not only hinders our ability to track the contribution of galaxies to reionisation, but it also impedes our understanding of how bursty star formation may be changing in the galaxy population.

In this thesis, I will start by studying galaxies selected directly on their emission lines, using HST/WFC3 slitless spectroscopy from two projects: in Chapter 2 I follow-up a sample of emission line galaxies at $z \sim 0.5-2$ from the parallel-time WISPS survey (Atek et al., 2010) with ground-based optical spectroscopy, with the goal of confirming their redshifts and studying the physical conditions (such as metallicity, dust reddening and ionisation) as a function of the emission line equivalent width. In Chapter 3 I use another slitless survey (3DHST, Brammer et al. 2012) in the well-studied CANDELS fields (Grogin et al., 2011) to select a sample of star-forming galaxies at $z \sim 2$ to measure the distribution of emission-line EWs and to study if there are any evolutionary changes with redshift.

In the second half of this thesis, I look to expand on this work on star-forming galaxies (in particular EELGs) to higher redshifts, including in the Epoch of Reionization. This will be made possible by the forthcoming James Webb Space Telescope, in particular the near-infrared spectrograph (NIRSpec) and camera (NIRCam) which will identify LBGs at $z \gg 6$ down to low luminosities, and study their rest-frame optical spectra. I am a member of the JWST Advanced Deep Extra-galactic Survey (JADES, a GTO project between the NIRSpec and NIRCam Instrument Science Teams), and in Chapter 4 I describe how a list of potential targets for NIRSpec spectroscopy has been drawn up from LBGs in the JADES fields (including the HUDF, and the wider GOODS fields, Giavalisco et al. 2004). In Chapter 5 I simulate the NIRSpec spectra for typical high redshift targets which we will observe, to determine whether the signal to noise is sufficient to achieve some key science goals (in particular redshift confirmation, and metallicity measurements from line ratio diagnostics).

Chapter 2

Emission-line galaxies at $z \sim 1$ from near-IR HST Slitless Spectroscopy: metallicities, star formation rates and redshift confirmations from VLT/FORS2 spectroscopy

2.1 Introduction

In this Chapter I study galaxies seen in Hα emission across "cosmic noon" ($z \sim 0.5 - 2$), the era when the SFR comoving density peaks. In recent years there has been significant effort in slitless spectroscopic surveys from HST, such as the WFC3 Infrared Spectroscopic Parallel Survey (WISPS) in the near-IR (Atek et al., 2010), and in future this will greatly expand with space-based slitless spectroscopy such as JWST-NIRISS and Euclid.

Slitless spectroscopy disperses all the light across a 2-dimensional field on the sky, usually at a low spectral resolution, to provide short spectra. Since each pixel will receive a background flux from all the wavelengths covered (unlike in a long-slit spectrum or fibre spectroscopy, where the light is highly apodised). This method is most suited to a low-background environment, such as space-based observatories (e.g. HST). The advantage of slitless spectroscopy is the large volume surveyed (a 2-dimensional area on the sky, and a significant depth in redshift space due to the wavelength coverage), and the fact that all objects in the field have a spectrum without the need to pre-select targets for a slit mask or a fibre configuration. The field of view of slitless spectroscopy is also typically much larger than that for integral

field spectroscopy (where each spatial pixel/resolution element has a separate spectrum). The main disadvantage of slitless spectroscopy is the higher background flux than slit/fibre spectroscopy, meaning reduced sensitivity, as well as potential overlap of spectra from different targets causing confusion. One advantage of slitless spectroscopy is that it selects directly on emission line strength (which is often a good proxy for the star formation rate), and is sensitive to high equivalent width sources. These extreme emission line objects, with potentially high specific star formation rates, may well be missed in traditional multi-object spectroscopic surveys which are based on broad-band photometric selections.

However, many WISPS spectra contain only single emission lines or are low signal to noise (S/N) where line designation may be in error. To address this concern, I analyse VLT/FORS2 spectroscopic optical follow up on selected WISPS galaxies. A key goal is redshift confirmation, affirming WISPS line identifications and improving redshift measurements with higher spectral resolution. The optical spectroscopy also enables the study of line ratio diagnostics, to measure the gas-phase metallicity of the WISPS galaxies and to identify potential AGN.

In this work I describe the reduction and analysis of the VLT/FORS2 spectroscopy, and combine this with the WFC3 spectra and photometry across a wide wavelength range (including Spitzer 3.6 μm imaging) to study the nature and evolution of emission line galaxies at high redshift.

2.2 Observations

The initial results of the WFC3 Infrared Spectroscopic Parallel Survey (WISPS, see Section 2.2.1) are reported in Atek et al. (2010) with subsequent data releases being made available through MAST[1] as the survey expanded. In this section, I report the optical spectroscopy follow-up performed at the VLT on selected WISPS fields, providing complementary 0.5 to 0.9μm wavelength coverage, ideal for rest-optical emission lines (e.g., [OII], Hβ and [OIII]) in our anticipated redshift range, and offering up to an order of magnitude greater spectral resolution that the WFC3 grisms. First I will briefly discuss the WISPS HST/WFC3 slitless spectroscopy, then I will discuss follow-up target selection, observing strategy and observation data reduction.

[1]https://archive.stsci.edu/prepds/wisp/

Finally, I will discuss the complimentary broadband photometry.

2.2.1 HST/WFC3 slitless spectroscopy

WISPS is a purely parallel field program on the Hubble Space Telescope, using the HST/WFC3 G102 and G141 infrared grisms to detect emission line galaxies through slitless spectroscopy from 0.7 to 1.8μm in $\sim$ 1500 arcminutes^2 of blank fields. Sensitive to Hα emission across a broad redshift range, $0.5 < z < 1.6$, WISPS detects emission line galaxies whose continuum may otherwise be too faint to appear in standard broadband wide field photometric surveys. Selecting on emission line strength rather than broadband luminosity is ideal for targeting low mass systems exhibiting high specific star formation rates (sSFR) which are expected to be abundant above $z > 1$ (e.g., van der Wel et al., 2011) but are below the broadband photometric threshold for standard spectroscopic surveys. Slitless spectroscopy offers the advantage over broad-band pre-selection for spectroscopic follow-up in that we are selecting directly on the quantity of interest (the star formation rate, indicated by the Hα flux), hence reducing any observational biases in a survey of star forming galaxies. Atek et al. (2010) provide the data reduction method and detail the identification and flux measurements of the observed emission lines ([OII]$\lambda 3727, 29$, Hβ, [OIII]$\lambda 4959, 5007$, Hα, [SII]) from the WISPS HST/WFC3 slitless spectra, with accompanying redshift estimates. I make use of the latest data release.

2.2.2 FORS2 Observation and Target Selection

Follow-up optical spectroscopic observations were conducted for a sub-sample of WISPS galaxies using the Focal Reducer/low dispersion Spectrograph 2 (FORS2, Appenzeller et al. 1998), a multi-object spectrograph on the Very Large Telescope UT1 (Antu), as part of program 093.A-0893. FORS2 uses two red-sensitive MIT/LL $2k \times 4k$ CCDs, with a native pixel scale of $0.125''\,\mathrm{pixel}^{-1}$. To reduce the readnoise the pixels are binned 2×2 (hereafter I refer to the binned pixels, 0.25"), which still Nyquist-sampled the seeing and spectral resolution. The observations are detailed in Table 2.1, and were taken at low airmass (1.0–1.35) and in good seeing ($\sim$0.6" FWHM). A slit width of 1" is used across all of the masks. To disperse the light the 600RI grism (with a central wavelength of 6800 Å) and the GG435 order-blocking filter are used. Each slit mask is observed twice, each with a 1400s exposure. The

masks are nodded by 3" between the two exposures to place the targets first in the upper half of their slit and then in the lower (±1.5" from the centre of the slit), in order to perform local background subtraction (discussed in Section 2.2.3). Acquisition images of the field were taken in the R-band before the slit mask was moved into the focal plane. The field-of-view of FORS2 is $6.8 \times 6.8\,\mathrm{arcmin}^2$ and since WISPS fields are smaller (the HST/WFC 3 detector is only 2.2 arcmin across) all the targets are placed in just one of the two FORS2 detectors.

Four WISPS fields were chosen for observation which were equatorial or in the Southern hemisphere with RAs appropriate to the observing time. Two of the WISPS fields (309 and 236) were observed twice with different slit mask designs. The emission line catalogue from the WISPS HST/WFC3 spectroscopy (Section 2.2.1) has between 24 and 48 candidate galaxies per HST field with detected line emission. However, all the candidates in each field could not be accommodated on a single FORS2 slit mask, since a minimum slitlet length of 8" was desired to facilitate sky subtraction by nodding at two positions along the slit. Over the 2' HST/WFC3 field up to ~ 15 targets could be allocated to the slit mask, and each galaxy was given a score based on the WISPS line emission (typically Hα, unless unreported then [OIII][2]), considering the equivalent width, S/N of the WISPS line and the redshift. The EW was measured as the ratio of the line flux to the continuum flux density (measured from the HST/WFC3 broadband reference image for the grism containing the emission line, after appropriate subtraction of the line flux contribution). Specifically, the scores favour:

- high signal to noise ratio in the WISPS WFC3 spectroscopy, with $S/N > 10$ scoring 3, $5 < S/N < 10$ scoring 2, and $S/N < 5$ scoring 1;
- high observed-frame equivalent width emission line sources, with EW$>$ 300 Å scoring 3, 100 $<$EW$<$ 300 Å scoring 2, and EW$<$ 100 Å scoring 1.

The scores for equivalent width and S/N were multiplied together to obtain an overall score between 1 and 9, and if the redshift based on the WISPS/WFC3 grism spectroscopy lay beyond $z = 1.25$ the overall score was down-weighted by a factor of 4, since few bright emission lines would fall in our FORS2 wavelength range at higher redshifts. In the WISPS catalogues about 20-30% of galaxies per field lie at these higher redshifts. 15 galaxies beyond this redshift are selected for follow-up to check if

[2]such as when Hα was out of grism coverage due to location or redshift

Observation mask	RA (Deg)	Dec (Deg)	Date	Airmass	Seeing
309_1	324.79799	-38.419686	2014-08-03	1.0655	0.55”
309_2	324.79799	-38.419686	2014-08-03	1.0615	0.6”
64_2	219.36889	-1.8316702	2014-07-18	1.2465	0.6”
62_1	195.318858	-0.03223	2014-07-18	1.374	0.575”
236_1	231.20360	0.41788568	2014-07-01	1.129	0.675”
236_2	231.20360	0.41788568	2014-07-29	1.3515	0.625”
std_star	28.710728	-27.47780	2014-07-25	1.33	0.625”

Table 2.1: Observation conditions for the 6 FORS2 masks and the standard star.

conflicting emission lines appear, this can provide confirmation on whether or not the HST/WFC3 grism detected lines were identified correctly. The UCSC-LRIS mask design software, developed by D. Phillips and collaborators for LRIS on the Keck telescope, is used to maximise the sum of the overall scores of the objects placed on the slit mask, optimising the centre and position angle for this. Of 138 galaxies in the WISPS emission line catalogue in these 4 fields, 85 have slits placed over them (a completeness of 62%). I will discuss the redshift distribution in section 2.3.2 with the distribution of spectroscopic redshifts presented in Figure 2.3. In Figure 2.2 I show the distribution of the rest-frame V-band Absolute magnitudes[3] ($\sim$5500Å) for the WISPS galaxies within the sample that have observed photometric coverage (observed-frame F110W-F160W), and I note the wide range of galaxy luminosities in our emission line selected sample.

Two slit mask configurations were created for fields 236 and 309 to accommodate the larger number of targets. As part of these masks design three targets appeared on both masks (and these are indicated in our tables of targets). Two observations allowing longer exposure times to be achieved and I will discuss this further in the next section.

2.2.3 FORS2 data reduction

The European Southern Observatory (ESO) provide a reduction pipeline for the FORS2 instrument - EsoReflex (Freudling et al., 2013), however this pipeline reduces individual exposures and does not combine the nodded observations at the different

[3]In this thesis all magnitudes in the AB system (Oke & Gunn, 1983).

positions that were taken. Hence I do my own data reduction, using standard techniques in the Image Reduction and Analysis Facility (IRAF). I now briefly outline the process.

Each exposure first had the bias removed using the overscan regions using the `linebias` package. For each slit mask I averaged several spectroscopic flat fields taken during the day with the same instrumental configuration. Then I normalised the flat field for each slitlet by dividing by the spectral shape of the flat field lamp (obtained by collapsing the 2D spectrum spatially, along the long axis of the slit), leaving the pixel-to-pixel sensitivity variations. I then flat fielded the science integrations for each 2D slitlet through division by the appropriate flat field.

I performed cosmic ray rejection through two methods. I first used `LACOSMIC` (van Dokkum, 2001) on the individual 2D science spectra for each slitlet. I also used `crreject` within the IRAF `imcombine` package, rejecting outliers at the 4σ level when the two spatially-offset spectra were aligned (I used the CCD gain of 1.43e/DN and detector read noise of 2.9 electrons so that the Poisson noise was correctly calculated). The cosmic rays found were added to a mask, which also included bad pixels and regions not illuminated by the slitlet.

Finally, I subtracted one nod position from the other, and this "$A - B$" spectrum had the sky emission subtracted out although residuals due to time variation were still present. I combined the 2D "$A - B$" spectrum with the inverted "$B - A$" applying a spatial offset to reverse the effect of the nod along the slit, so that the spectrum of the target galaxy added at the same location. Bad pixels, unilluminated areas and cosmic rays were excluded in this combination.

The resulting 2D combined spectra for each slitlet (i.e. targeted galaxy) had not yet been corrected for spatial curvature, or wavelength and flux calibrated. However, at this point each pixel was independent (no interpolation had yet been applied), so the noise could be measured directly and was found to agree well with the expected Poisson noise (with the readout noise added in quadrature) derived from the spectrum of the sky emission.

I then extracted the spectra of each object using the `apextract.apall` package in IRAF. For the brighter objects, where the spectral continuum was easily seen, I

traced how the position of the spectrum varied with wavelength across the detector. For fainter objects, where no continuum or just individual emission lines were visible, I used the edge of the slit (which was readily seen in the flat field exposures) to map the spatial distortion. I use a 1" extraction width, corresponding to 4 pixels centred on the target, in combination with the 1"-width slits this creates a 1"×1" extraction aperture. Some sources were spatially extended, so I also performed a second extraction over a wider 10-pixel (2.5") height along the slit. In both cases I applied background subtraction using the `IRAF.Background` package to remove any residual sky emission which remained after the differencing of the offset exposures, by subtracting the clipped average counts in pixels between 6 and 10 pixels from the object position (which avoided self-subtracting the object flux, and also avoided the ends of the slitlets). For each extraction width I also generated a 1D noise spectrum from the Poisson noise model of the object and sky counts (taking into account the gain of the detector).

Wavelength calibration for each slit mask was done using NeArHgHe arc lamps observed during the day with the same instrument configuration. I extracted the arc spectrum for each slitlet using the same trace as the object, but without the background subtraction. I fit a cubic mapping of pixel to wavelength using about 50 arc lines with a scatter of 0.3 Å, and calculated the average scale to be $1.62\,\text{Å}\,\text{pix}^{-1}$. The wavelength calibration was checked against sky emission lines in our spectra to confirm there had been no shift in the grism central wavelength. I then produced two versions of the wavelength-calibrated spectrum, the first involving interpolation onto a uniform wavelength scale of $1\,\text{Å}\,\text{pix}^{-1}$, and the other preserving the original pixels but allocating a wavelength to each pixel on a non-linear scale (so that the pixels are independent). For slitlets close to the centre of the CCD, the wavelength coverage was $5150 - 8470\,\text{Å}$, although slits placed on targets towards the edge of the field (offset along the wavelength axis) can have the wavelength coverage shifted by up to ±300 Å. I computed the spectral resolution from the FWHM of arclines and unblended sky lines, and found this to be 5.6Å, equivalent to a resolving power of $R = \lambda/\Delta\lambda_{FWHM} = 1200$ at our central wavelength. However, I note that for objects which do not fill the 1" slit the spectral resolution will be better. This spectral resolution is far greater than the $R = 210$ and $R = 130$ that the G102 and G141 HST/WFC3 grism achieve at ∼1.1 and ∼1.4μm respectively.

As part of the FORS2 observing program, four standard stars were obtained to flux calibrate the science images, however these were not necessarily observed on the same nights as their target masks. Only one of the standard stars (LTT1020) was taken in similar seeing to our slit mask observations, so I used this to determine the flux calibration. The extraction and wavelength calibration were performed as described above. I determined the conversion of counts to flux density by comparison with the reference values for the standard star (Hamuy et al., 1992, 1994). For each slit mask about 4 additional brighter compact/point sources were added as a check of the spectro-photometry. These objects have photometry from Sloan Digital Sky Survey (SDSS DR12) (Fukugita et al., 1996) or the VLT Survey Telescope ATLAS (VHS-ATLAS DR3) (Shanks et al., 2015). The literature flux in the r and i bands (within our FORS2 wavelength coverage) was compared to the FORS2 spectrum continuum flux (convolved with the r- or i-band filter transmission function) averaged across the same wavelength range. The FORS2 observed flux consistently falls short of the anticipated flux based on the flux calibration from the single standard star. The discrepancy is seen to be 30% in the r-band and 15% in the i-band[4]. The origin of this flux discrepancy may be due to a number of factors: different seeing (which may be wavelength-dependent); some slight mis-alignment in the mask acquisition; telescope tracking drift or changes in atmospheric transparency. I apply the appropriate scaling factor (for the mask and wavelength) to correct the emission line fluxes in the FORS2 spectroscopy. Finally, for the three galaxies that were each assigned to two masks, allowing them to be observed twice, the 1D wavelength and flux calibrated spectrum from each mask are averaged together to achieve greater S/N.

2.2.4 Multi-band photometry

In addition to the HST WFC3 grism slitless and VLT/FORS2 spectroscopy, these four WISPS fields (62, 64, 236 & 309) have been observed with ground- and space-based telescopes to provide complimentary imaging (described below). However, not all fields have coverage in all filters and the imaging available to each WISPS field is

[4]The factor of 2 difference (15% vs 30%) in correction factors between the r-band and the i-band regions of the spectra does not have a significant impact on the spectral diagnostics I wish to explore: for example a difference of 15% in the [OII]/Hβ would result in an offset of $log_{10}1.15 = 0.06$ in the x-axis Figure 2.14 (which shows the metallicity tracks in [OIII]/Hβ vs. [OII]/Hβ), which is comparable to the error bars and also the bin size of the SDSS comparison dataset. The [OIII]/Hβ ratio is unaffected by the correction factor since these lines are close in wavelength to each other. A larger potential impact is on the Hβ flux, and hence the Balmer decrement - perturbing the Balmer decrement Hα/Hβ by 15% changes the reddening of A(Hα) by 0.04mag

given in Table 2.2. I will briefly describe the imaging and photometric analysis.

As part of the WISPS Survey (Atek et al., 2010) HST/WFC3 grism slitless spectroscopy was obtained in combination with direct imaging in typically two HST/WFC3 broadband filters, F110W and one of either F140W or F160W (apart from field 236 which only had F140W obtained). The near-infrared bands are observed to provide reference images for wavelength calibration of the grism slitless spectroscopy. As part of the WISPS program, HST/UVIS direct imaging was observed for certain WISPS fields, this include F475X and F600LP for field 64 and F814W for field 309. Here multiple exposures of the reduced imaging were drizzled into a final science image that retains the HST/WFC3 native 0.128" pixel scale. Due to the variable number of HST orbits that each WISPS field was observed for, the exposure times for each direct imaging observation vary and I measure 5σ limit depth in a 0.4" radius aperture in the range 26.05 to 24.74, full details given in Table 2.2.

To compliment the HST imaging, the WISPS program obtained follow up ground-based Palomar/WIYN Sloan u, g, r, i and Spitzer/IRAC 3.6μm observations for WISPS fields 62, 64 and 309. The IRAC imaging is drizzled to a 0.6" pixel scale (1.2" pixel native scale) and has 5σ 1.2" radius aperture depths in the range 23.35 to 23.58. The AB magnitude distribution for the F160W "H-band" (F140W "JH-band" for WISPS field 236) is given in Figure 2.1.

From the available imaging, I determine the photometry using IRAF.phot using apertures fixed at the location of the emission line galaxies for each WISPS target to provide complimentary analysis to existing SExtractor Bertin & Arnouts (1996) derived photometry (see Atek et al. 2010 for discussion of SExtractor parameter details). The SExtractor photometry was measured by training on each filter image separately (i.e., without a reference image), which meant galaxies would not have a flux measurement in a particular band if they were too faint to be detected in that image. In these cases our application of fixed-position apertures allows targets with faint continuum emission to have photometric measurements obtained when they were undetected above the SExtractor specified thresholds. Across the HST direct imaging, 0.4" radius apertures are laid on the coordinates determine from the F160W or F140W reference image of each WISPS target. For our aperture photometry, I apply an aperture correction determined from point sources to account for the flux falling outside of the aperture and to return an approximate total magnitude (which

is appropriate for compact sources, but will underestimate the total flux if the source is significantly extended). Due to the lower resolution of the Spitzer/IRAC imaging I measure total fluxes using 1.2" radius apertures with an infinite aperture zeropoint and a corresponding 0.7 magnitude aperture correction from Eyles et al. (2005) appropriate for a compact source. The lower resolution of Spitzer/IRAC additionally means that for a small number of WISPS targets the measured flux within an aperture is confused with the contribution of close neighbours. In each of these cases, I utilise the WISPS photometry which models the contribution of multiple sources to reduce the confusion and will be presented in a future paper by the WISPS collaboration.

For the majority of objects, consistency is found between the photometry derived from both the SExtractor and fixed-aperture photometric analysis methods. However, disparity in the measured photometry is found in extended sources, when the target extends beyond the fixed aperture. For extended sources the variable radius employed by SExtractor recovers a more reliable total flux estimate. For faint sources, which were not necessarily detected above the required SExtractor thresholds (see Atek et al. 2010 for details), fixed aperture photometry provides reliable measurements using coordinates matched to the HST/WFC3 reference images. Therefore, upon inspection of each galaxy, the preferred choice of photometric method is dependent on whether the galaxy is considered to be extended in comparison to the PSF of the images and the size of the fixed aperture (these are given in Table 2.3 and are available in electronic form[5]).

2.3 Results

The combination of HST/WFC3 slitless grism and VLT/FORS2 provides spectroscopic coverage over a broad observed-optical to near-infrared range, with complimentary multi-band photometry constraining the broadband continuum from the observed-optical into the near-infrared. This breadth of data provides coverage of key rest-optical emission lines over our redshift range (e.g., Hα, [OIII]$\lambda 4959 + 5007$, Hβ and [OII]$\lambda 3727, 29$) which I will use to assess the validity of HST/WFC3 grism WISPS line identifications and redshifts, correct WISPS Hα derived star formation rates (SFRs) by estimating the dust extinction, and utilising line diagnostics and photometry-derived stellar masses to assess the gas-phase metallicity and Interstellar

[5]https://github.com/Kitboyett/Supplementary-Thesis-material

Filter	$\lambda_{\rm central}$ (μm)	Galaxy field			
		Par-309	Par-236	Par-62	Par-64
U	0.383	$\sim 26.0^a$	-	-	$\sim 26.0^a$
G	0.487	$\sim 26.0^a$	-	-	$\sim 26.0^a$
F475X	0.490	-	-	-	25.39^c
R	0.625	$\sim 25.3^a$	-	-	-
F600LP	0.719	-	-	-	24.88^c
I	0.768	-	-	-	$\sim 25.3^b$
F814W	0.806	25.17^c	-	-	-
F110W	1.152	26.05^c	-	25.38^c	25.95^c
F140W	1.392	-	25.29^c	24.74^c	-
F160W	1.540	25.13^c	-	-	24.97^c
IRAC 3.6μm	3.557	23.58^d	-	23.58^d	23.35^d

Table 2.2: HST UVIS2, WFC3 and ground-based Sloan-like ancillary photometric data available for each of the four WISPS fields observed. The 5σ 0.4" radius-aperture depths are given for each, with the IRAC given for a larger 1.2" radius-aperture due to the lower resolution. Depths in the Sloan bands was provided by the WISPS collaboration. HST and IRAC depths were measured by myself. Imaging from: *a*) Magellan-Megacam; *b*) WIYN-MiniMosaic; *c*) HST; *d*) Spitzer/IRAC

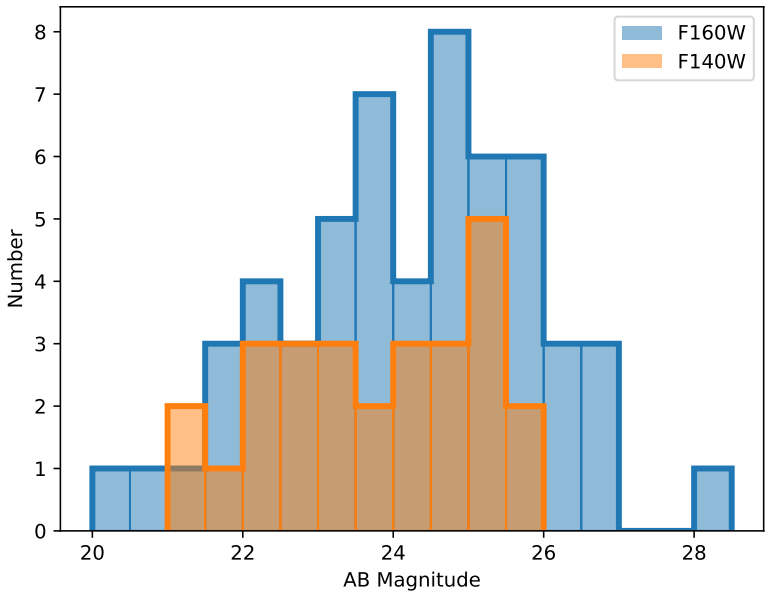

Figure 2.1: The H-band and JH-band AB magnitude distribution for the 85 objects in our sample. JH-band is given instead of the H-band in WISPS field 236 due to the availability of imaging, see Table 2.2. 51% of galaxies have magnitude fainter than AB=24 mag.

id	U	G	F475X	R	F600LP	I	F814W	F110W	F140W	F160W	IRAC
64_2_10	0.18±0.03	0.19±0.03	0.27±0.05	-	0.45±0.08	-	-	0.51±0.03	-	0.54±0.07	1.46±0.33
309_1_16	2.77±0.04	3.09±0.05	-	4.42±0.08	-	-	4.57±0.13	5.12±0.08	-	5.02±0.25	7.94±0.19
...											

Table 2.3: Ancillary photometry (mirco Jansky), available for the full sample as a machine readable table.

id	redshift[a]	[OII]$\lambda 3727, 29$[b]	Hβ[b,c]	[OIII]$\lambda 4959, 5007$[b]	Hα[b,c,d]	[SII][b]
64_2_10	0.6588±0.001	1.47±0.12 e-16	7.07±0.26 e-17	3.12±0.10 e-16	1.82±0.36e-16	-
309_1_16	0.8123±0.0001	2.15±0.37 e-15	6.11±1.37 e-16	3.15±0.13 e-15	1.57±0.05 e-15	1.26±0.28 e-16
...						

Table 2.4: Emission line flux measurements (erg/s/cm2), available for the full sample as a machine readable table. a. spectroscopic redshift based on FORS2 detected emission line. b. Corrected for seeing and reddening. c. Corrected for stellar absorption. d. Corrected for NII contribution Hα

id	SFR(UV)	SFR(Hα[a])	SFR(SED)	M(SED)	Mv	Hα[a] EW$_0$	metal(O32)	metal(R23)
64_2_10	1.70±0.33	1.49±0.27	1.01±0.29	8.03±0.23	-16.85	300.0±58.0	8.33±0.02	7.88±0.25
309_1_16	24.54±0.76	27.99±1.34	29.27±2.65	9.07±0.11	-19.69	306.2±9.4	8.41±0.04	< 8.44
...								

Table 2.5: Derived galaxy properties from emission line measurements and photometric SED analysis, available for the full sample as a machine readable table. Star formation rates are given in $M_\odot/yr$, BEAGLE SED derived masses in $\log_{10}(\mathrm{Mass}/M_\odot)$ and rest-frame equivalent widths given in Å. a. Hα corrected for stellar absorption and NII contribution

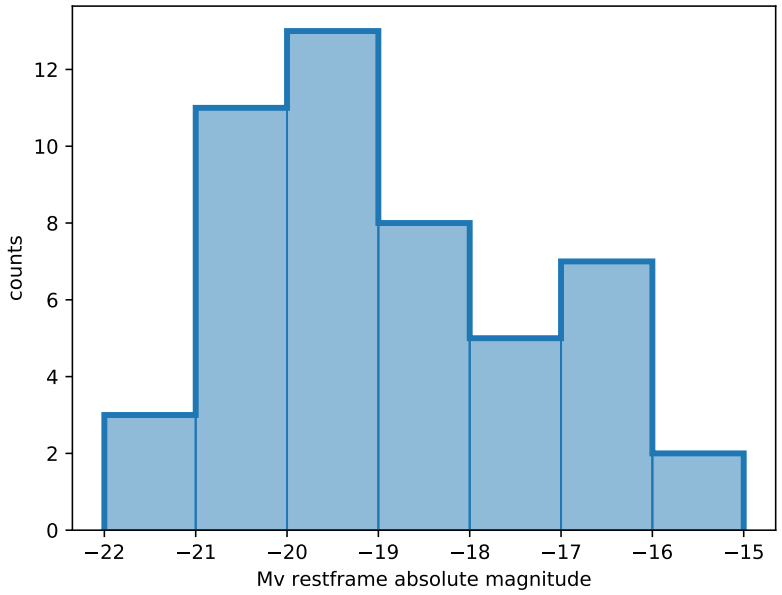

Figure 2.2: The distribution of the rest-frame V-band absolute magnitudes (∼5500Å) for the sub-set of targeted WISPS galaxies with observed photometric broad-band coverage (observed-frame F110W-F160W).

medium (ISM) conditions for our galaxies.

2.3.1 Emission line identification and flux measurement

With the 2D and 1D FORS2 spectrum for each galaxy extracted, I visually inspect each to identify all significant emission. Visual inspection establishes 38 of 85 unique WISPS targets displayed FORS2 emission lines (the breakdown by field and mask is given in Table 2.6). I note that this FORS2 emission line detection rate is low and I emphasise that many of the single line emitters followed-up were low S/N and FORS2 is being used to test the reality of these (see discussion in Section 2.3.1.1). As a preliminary check before a more sophisticated redshift determination, a simple overlay is created to mark the locations of expected [OII], Hβ and [OIII] emission lines on the FORS2 2D spectra based on the WISPS spectroscopic redshift estimates for each galaxy. This provides immediate visual confirmation that 36 out of these 38 galaxies have observed emission lines consistent with the expected redshift, whereas 2 show emission lines inconsistent with the WISPS redshift. I will discuss redshift validation further in Section 2.3.2. The FORS2 observed emission lines are typically

the [OII]$\lambda 3727, 29$ doublet and often Hβ+ [OIII]$\lambda 4959 + 5007$.

The remaining 47 targets without obvious emission lines in the FORS2 spectrum can be further separated into two categories. First, those where no emission lines were predicted to lie in the FORS2 wavelength range based on the WISPS redshift estimates (15/85). Here the lack of contradictory line detections in FORS2 supports the WISPS redshift estimate and line identification by ruling out alternative redshift/line-identification solutions that would have placed emission in the FORS2 wavelength coverage. Secondly, those where we had expected emission lines to be coincident with the FORS2 range but no detections were made (32/85), either due to the emission line flux being too faint to be detected or due to mis-identification of the WISPS emission line.

The 1D science and noise spectra of the 38 targets with visually identified FORS2 emission line detections is processed through the Penalized Pixel-Fitting (PPXF) spectral fitting package (Cappellari, 2017) to fit a continuum and emission line model to the spectra and to obtain emission line flux measurements. Here the galaxy spectra are brought to the rest-frame using the HST/WFC3 grism WISPS redshift estimate. The galaxy continuum in these emission line selected targets is usually non-dominant and a fourth order additive polynomial is used to model the continuum, the individual emission lines are modelled as either a single gaussian or a pair in the case of the [OII]$\lambda 3727, 29$ doublet. The flux ratio between this pair is tied to constraints set from atomic physics (Osterbrock & Ferland, 2006). Any velocity offset exhibited by the emission lines allows the HST/WFC3 grism WISPS redshift estimate to be refined by the FORS2 spectroscopy. The corrected emission line fluxes are given in Table 2.4.

2.3.1.1 Undetected emission lines

Given that a significant fraction of the sample (32/85 galaxies) did not display emission lines in their FORS2 spectroscopy, despite the sufficient wavelength coverage, I now consider whether this was expected. In turn I will examine whether the expected signal to noise of the three strongest rest-optical emission lines ([OII], Hβ and [OIII]) was below a 3σ detection threshold. I will explore whether these non-detections can be attributed to the line emission being too faint or to the WISPS HST/WFC3 emission lines being mis-identified.

To determine the expected observed flux for each undetected emission line, I will utilise the line ratio between the average detected emission line flux of Hα and the average detected flux of the line in question, for the sub-sample where both lines were detected. I remove two sources which were extended compared to the FORS2 slit width, as these would artificially increase the measured line ratio due to slit losses. I require detections in both emission lines and a detection in the FORS2 spectroscopy to confirm the redshift and within the sample there are 34 galaxies that met this criterion for the Hα and [OII] lines. The Hα and [OII] line ratio of the average observed line fluxes is 3.6 ± 0.7. For Hβ there are 15 galaxies that meet these criteria with a measured observed line ratio to Hα of 6.0 ± 1.0 (this is consistent with Balmer decrement presented in Section 2.3.3.2 where we consider the [NII] contribution and stellar absorption). For [OIII]λ4959 + 5007, 24 galaxies meet these criteria with a measured observed line ratio to Hα of 1.5 ± 0.2.

To calculate the expected signal to noise of each line, the WISPS measured Hα flux for each galaxy is divided by the chosen measured observed emission line flux ratio above to estimate the corresponding observed flux. Then the associated noise spectrum for each galaxy is used to estimate the noise over a 500km/s aperture centred on the expected wavelength, determined from the WISPS grism spectroscopic redshift.

Out of the 32 galaxies with WFC3 emission line determined redshifts that predict emission lines to fall in the FORS2 coverage but without FORS2 detections, 29 were expected to exhibit [OII] with a S/N estimate ranging between 4 and 43 (the remaining 3 galaxies were at redshifts or slit-mask locations where [OII] did not fall in the spectral coverage). A sub-set of 17 galaxies were expected to exhibit [OIII] in FORS2 and had estimated S/N ranging between 5 and 57. Finally for Hβ, the same 17 galaxies are estimated to exhibit a S/N in the range of 2 to 21 for the observed line ratio, or up to a S/N between 5 to 44 for the intrinsic line ratio (1:2.86 Osterbrock 1989). Therefore, I would have expected to observe significant line emission in the FORS2 spectra for the majority of these objects, following the typical line ratios of the FORS2 detected objects. I note that all of these 32 galaxies had WISP redshifts based on single-emission line detection in WFC3. Hence, for these galaxies, I believe the WFC3 emission line may have either been spurious (e.g., a mistaken artefact within the grism imaging), have had the emission line mis-identified such that no lines should have been expected to fall in the FORS2 coverage or were genuine but

were associated to wrong object in the direct image (hence the FORS2 slit was placed on the wrong target).

As a check, I stack the FORS2 spectra for the galaxies without FORS2 emission line detections on the assumption that the single line tentatively observed in WFC3 are Hα (the most conservative assumption). The stacking is performed by averaging the linearised 1D FORS2 spectrum of each object. Due to the lower spectral resolution of the WFC3 grism the redshift precision means the expected location of the non-detected emission line may lie over a broad pixel range (rest-frame $\sim$ 30Å, the typical uncertainty from the spectral resolution, which improves at higher S/N). I examine evidence for a flux excess over a $\pm$15Å wavelength range centred on the expected position, after subtracting a fit to the continuum emission and I find no evidence for a flux excess in the stacked [OII], [OIII] or Hβ spectra. I note that due to the redshift uncertainty in WFC3 being much larger than that due to the FORS2 spectral resolution, the undetected emission line may fall over a large wavelength (and pixel) range and this increases the noise in the stack and can mask the benefits of improving the S/N of the individual spectra by stacking the data. This stacking result supports that the WFC3 detected single-line emission of these galaxies may not be genuine or that line identify or the direct image associated object was mis-identified. Within our complete sample there are 49 galaxies with only single emission line detections in WFC3, with 17 (35%) having their redshift confirmed. The inverse of this sets a maximum false-detection rate of galaxies identified in the WFC3 grism with only a single emission line to 65%

I note that on further inspection of these 32, one galaxy (FORS2 id:62_1_7) has an implausibly high Hα EW, i.e., the emission line would produce more than the total flux observed in the broadband filter (see Section 2.3.7), implying again that perhaps the wrong object was associated with the source of this emission line or that the emission line was spurious.

2.3.2 Redshift validation

When a galaxy in a spectroscopic survey only has a single emission line detected, determination of the line identification and redshift is ambiguous. One goal of the optical spectroscopy follow up is to validate the WISPS redshifts, especially for the

49/85 galaxies that only had a single emission line detection in the HST/WFC3 slitless spectroscopy.

Visual inspection of the 2D and 1D FORS2 spectra identified 38 of the 85 unique galaxies with significant line emission ($> 3\sigma$). Of these 38, 36 galaxies had FORS2 emission line detections that supported their WISPS designated spectroscopic redshift, whilst 2 galaxies had FORS2 significant line emission that was inconsistent with the expected redshift. Hence, in the sub-set of cases where there was significant line detection in FORS2 (38/85, 45% of targetted objects) the tentative redshift from WFC3 was confirmed 95% of the time (36/38). Where FORS2 was able to detected emission lines, there was a very high success rate in confirming that the WISP redshifts are accurate, although due to the low WISP spectral resolution compared to the FORS2 resolution, the FORS2 redshift is more precise.

Of the 38 galaxies with significant FORS2 line emission, 17 were cases when the WFC3 redshift was based on only a single WFC3 line detection (attributed to Hα, although in one case [OIII]). Here, the reliability of the WISPS spectroscopic redshift is less robust than cases when multiple emission lines were detected in WFC3 which would further constrained the redshift. The identification of the WFC3 line was confirmed in 88% of the cases where FORS2 detected other lines (15/17 objects). With the remaining two single WFC3 line galaxies with FORS2 detections presenting catastrophic WISPS mis-identification.

These two galaxies had emission lines in FORS2 that were inconsistent with their WISPS spectroscopic redshift and from the detection of multiple FORS2 emission lines I determine new line identifications and redshifts. FORS2 id `236_2_12` had a WISPS spectroscopic redshift of $z \sim 0.36$ based on a single emission line assumed to be Hα. However, FORS2 spectroscopy identified line emission of Hβ, [OIII] and Hα consistent with z=0.12. With no standard emission line expected at the WISPS line wavelength (rest-frame 0.89μm based on the FORS2 spectroscopic redshift), the WISPS line detection (signal to noise = 2.9) is determined to be spurious and may have been caused by a cosmic ray or some detector artefact coincident with the dispersed slitless spectrum of the galaxy. FORS2 id `62_1_13` similarly had a single line detection attributed to Hα at $z \sim 0.62$ however, a clear FORS2 [OII] doublet is identified which determines a $z = 1.13$ spectroscopic redshift. The WISPS detection (signal to noise = 6.1) lies coincident with a rest-frame wavelength of 4990Å

based on the FORS2 redshift, which I identify as being consistent with the blended [OIII]λ4959 + 5007 doublet.

Within the WISPS catalogue I note three incidences where indexing errors had caused individual emission lines to be mis-identified and given redshifts inconsistent with other detected emission lines. Firstly, FORS2 id `309_1_13` had multiple emission lines detected by WISPS (Hα at $z = 0.35$ and [OIII], Hα, [SII] at $z = 1.02$), but by error two of these were determined to be Hα at different redshifts. Observation of a FORS2 [OII] doublet confirms the redshift as $z = 1.03$ and the first Hα line is re-identified to be consistent with the [OIII]λ4364 emission line. Secondly, FORS2 id `62_1_14` had three emission lines detected, however, the redshift determined from the identification of each was inconsistent with the others (Hα at $z \sim 0.6$, Hβ at $z \sim 1.8$ and another Hα at $z \sim 1.14$). No lines were detected in the FORS2 spectroscopy and re-inspection of the observed wavelengths of each HST/WFC3 WISPS emission line revealed that they are consistent with [OII], Hβ and [OIII] at $z = 1.8$. Finally, FORS2 id `62_1_9` is recorded to have two Hα detections at similar observed wavelengths of 1.22 and 1.24 microns. Observation of a FORS2 [OII] doublet confirms the redshift is consistent with this emission feature being Hα. Inspection of the 2D slitless spectroscopy and direct imaging reveals two components to the emission line which I attribute to the extended nature of the galaxy which exhibits two spatially offset Hα emitting regions along the dispersion axis. The emission line flux from both components is summed to determine the total Hα emission.

In Figure 2.3 I first present the WISPS spectroscopic redshift distribution (left panel) for the complete WISPS sample of galaxies in the four target fields and the sub-sample that were followed up with our optical spectroscopy. In the right panel of Figure 2.3, I present the redshift distribution updated considering the FORS2 spectroscopy, identifying how robustly each sub-group has its redshift validated. In Figure 2.4, I present the Near-IR magnitude distribution, again highlighting how robustly each sub-group has its redshift validated.

2.3.3 Emission line flux corrections

In this sub-section I will consider the necessary corrections for the observed emission line fluxes to recover line luminosities. The sub-set of the final emission line fluxes

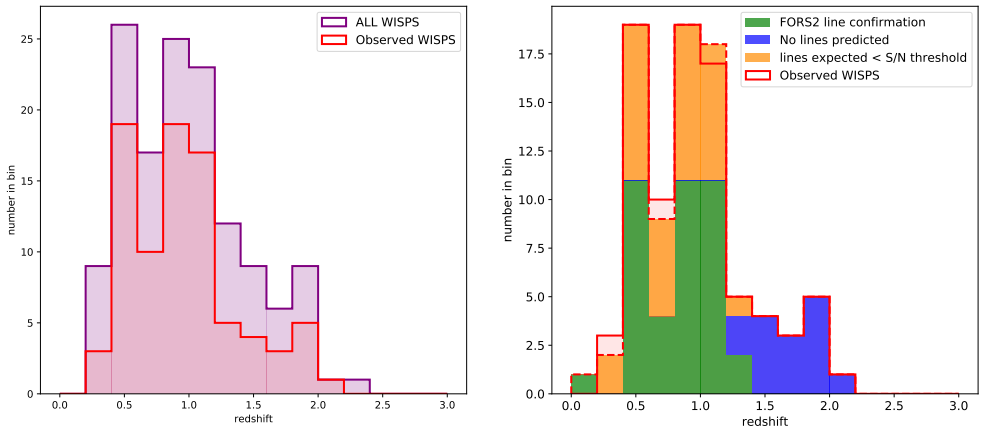

Figure 2.3: Left: The HST/WFC3 grism slitless spectroscopic redshift distribution of the 85 galaxies (red), out of the 138 WISPS emission line detected sources (purple), that we follow up with optical spectroscopy. Right: The updated redshift distribution based on the FORS2 follow up (solid red, with updates shown in dashed). 38 galaxies (green) had FORS2 detected emission lines allowing their spectroscopic redshifts to be validated or corrected. 32 galaxies (orange) are predicted to exhibit emission lines within the FORS2 wavelength coverage but at a signal to noise (S/N) below a 3σ detection threshold, the lack of contradictory lines helps rule out alternative redshift solutions. 15 galaxies (blue) were not predicted to exhibit emission lines within the FORS2 wavelength coverage, the lack of contradictory lines help rule out lower redshift solutions.

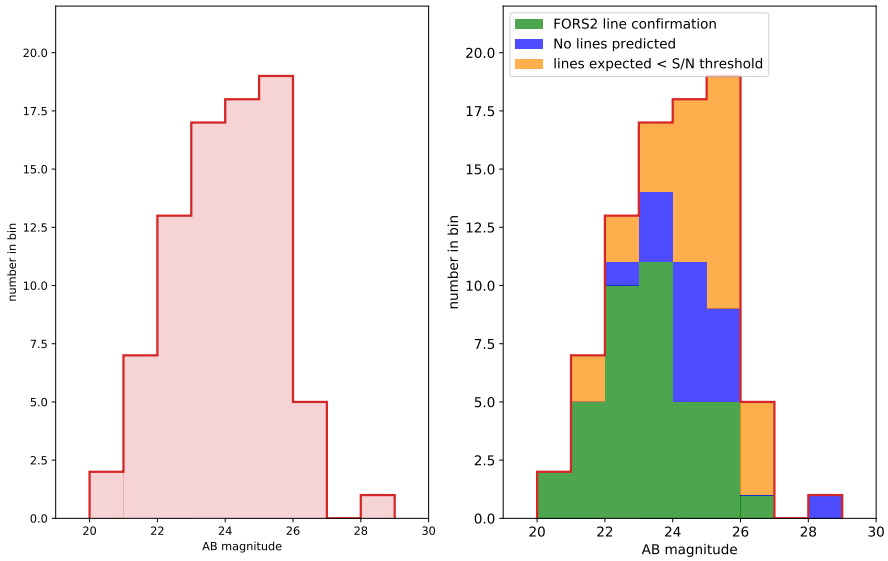

Figure 2.4: Left: The NIR AB magnitude distribution of the 85 galaxies in our sample (red), using either the H-band or the JH-band depending on available imaging. Right: The NIR AB magnitude distribution coloured by redshift the same validation as in Figure 2.3. Galaxies (green) that had FORS2 detected emission lines are typically brighter than average, but still cover a broad $20 < ABmag < 27$ range in F160W/F140W.

are presented in Table 2.4, and are available electronically[6].

2.3.3.1 [N II] contribution correction for Hα flux

The low spectral resolutions of the WFC 3 grisms means the Hα, [NII]λ6548 and [NII]λ6584 emission lines are blended and the WISPS flux measurement therefore provides an upper limit to the Hα emission. To obtain an estimate for the contribution from the two [NII] emission lines (which have a theoretical flux ratio of 3:1 between [NII]λ6584 and [NII]λ6548, Osterbrock & Ferland 2006), the [NII]λ6584 over Hα ratio is estimated from the star-forming abundance sequence in the redshift-dependent BPT diagnostic diagram from Kewley et al. (2013b, equation 5). The star-forming abundance sequence provides a [NII]λ6584/Hα flux ratio as a function of the [OIII]λ5007/Hβ flux ratio under the assumption that our sample consist of star forming galaxies. The mean value for the [NII]λ(6548 + 6584) contribution to the total Hα + [NII]λ(6548 + 6584) flux is $18 \pm 10\%$ for the sub-sample of 19 galaxies which had [OIII]λ5007, Hβ and Hα detections, exhibiting a mean redshift of $z = 0.69 \pm 0.34$. We also consider a plausible upper limit on the [NII]λ(6548 + 6584) (hereafter [NII]) contribution to Hα + [NII] flux for this sub-sample, which we determine to be $26 \pm 10\%$, following the upper boundary on the star forming abundance sequence provided by Kewley et al. (2013a). For the remaining galaxies in the sample, the Hα flux is corrected for the [NII] contribution using the mean from this sub-sample (where [NII] contributes a fraction 0.18 to the blended flux). This correction provides an updated estimate to the [NII] contributions adopted in previous WISPS papers (Atek et al., 2010, 2011; Domínguez et al., 2013; Colbert et al., 2013) which lie in the range $4 - 20\%$, dependent on the Hα equivalent width and stellar mass of the galaxy. Our value for the [NII] contribution is marginally larger than some previous estimates, due to the availability of a redshift-dependent BPT star-forming abundance sequence. Higher [NII] contributions are found at higher redshifts which may be due to a larger ionisation parameter, evolution of metallicity or a different N/O abundance ratio (Faisst et al., 2018), whereas the previous computations were all reliant on $z \sim 0$ galaxy diagnostics.

field & mask	FORS2 line detections	without FORS2 detections (high-z)	without FORS2 detections ($< S/N$)	total targets
309_1	11	1	5	17
309_2	3	7	4	14
62_1	6	2	5	13
64_2	5	4	4	13
236_1	8	0	8	16
236_2	5	1	6	12
Totals	38	15	32	85

Table 2.6: FORS2 follow-up detection rate (number of galaxies) split between each of the six observed mask configurations.

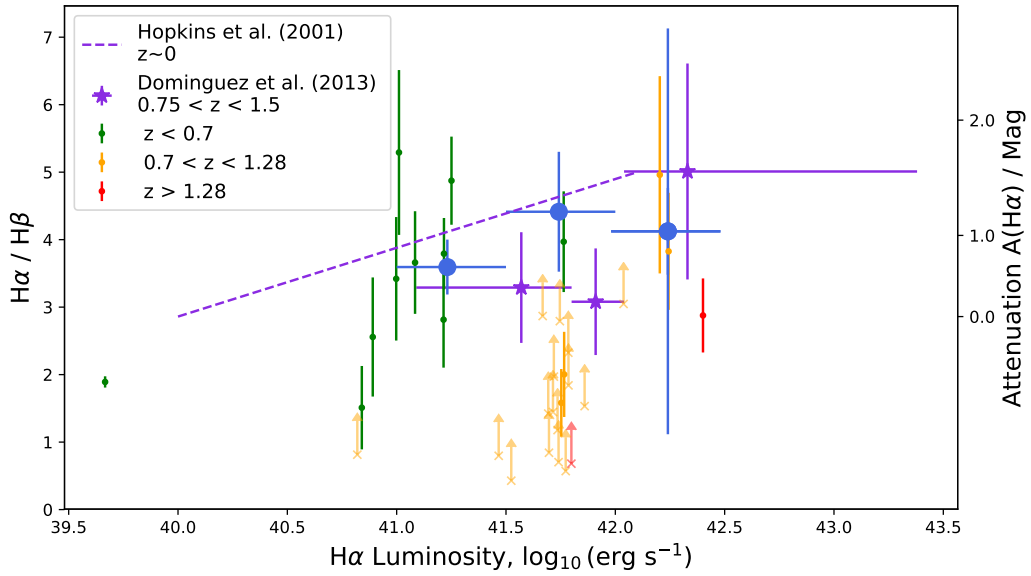

Figure 2.5: Balmer decrement - Hα luminosity relation, corrected for [NII] contribution and stellar absorption. Purple dashed line shows Hopkins et al. (2001) SDSS ($z \sim 0$) work and purple stars show the results of Domínguez et al. (2013) ($0.75 \leq z \leq 1.5$). Our detections are spilt into low (green, $z < 0.7$), medium (orange, $0.7 < z < 1.28$) and high (red, $z > 1.28$) redshift bins, with galaxies that have Hβ detections below 2σ are plotted as 2σ lower limits in grey. Binned data points in filled blue show the luminosity ranges 41.0-41.5, 41.5-42.0 and 42.0-42.5, while the open blue in the last bin shows the stack with the two high balmer decrement limits removed (which showed imaging artefacts around the Hβ emission line).

2.3.3.2 Extinction correction and the Balmer Decrement

Observation of the Hα emission line in WISPS allows galaxy properties including star formation rates (SFRs) to be measured. However, measurements of the SFR based on Hα luminosity alone may be underestimated due to dust attenuation, which I wish to correct for. For the majority of the sample I have wavelength coverage of the Hα emission line in the HST/WFC3 grism spectroscopy and also the Hβ emission line, which falls in the FORS2 wavelength coverage at $z \lesssim 0.7$, and in the G102 WFC3 grism at $0.7 < z < 1.4$. The intrinsic flux ratio between the Hα and Hβ emission lines, known as the Balmer decrement, is set by atomic physics and for Case B recombination the flux ratio is $f(\mathrm{H}\alpha)/f(\mathrm{H}\beta) = 2.86$ (Osterbrock & Ferland, 2006). The flux ratio observed in galaxies is typically larger than this due to wavelength dependent differential extinction, with the shorter-wavelength Hβ line typically more attenuated. In this section, I will use the observed Balmer decrement from galaxies in the sample along with a Calzetti extinction law (Calzetti et al., 2000) to determine and correct for the dust extinction. Alternative laws include the SMC, LMC and Milky Way laws and the extinction curves for each are shown in Figure 2.6. However, these foreground dust screen models are probably less appropriate than the Calzetti et al. (2000) law for starburst galaxies such as those in our WISP sample, where the gas and dust are likely intermixed within the star forming region[7]. I report the extinction values for different dust laws for key wavelengths in Table 2.7[8]

I note since the Hβ emission line flux is typically more than three times weaker than Hα it is frequently undetected (see Section 2.3.1.1). This is seen even in the cases where I confirm the putative WISPS redshift from a single emission line in the slitless WFC3 WISP spectrum with another line (typically [OII] or [OIII]) in the follow-up FORS2 spectroscopy.

To determine the Balmer decrement within the sample the measured Hα and Hβ emission line fluxes must be corrected for two effects. First, the Hα flux is corrected

[6]https://github.com/Kitboyett/Supplementary-Thesis-material

[7]the estimates for the star formation rates from the Hα luminosity (discussed in Section 2.3.4) would change by a maximum of 30% if I used the SMC law. However, the O32 and [OII]/Hβ line ratios (discussed in Section 2.3.6) would only change by a maximum of 9% and 8% respectively, were I to swap to a LMC law, and accounts for < 0.04dex in Figures 2.14 and 2.15 which is smaller than the typical uncertainties or the size of the binned-SDSS regions.

[8]The extinction at a given wavelength, as adapted from Domínguez et al. (2015), is given by $A(\lambda) = \frac{2.5*k(\lambda)}{k(H\beta)-k(H\alpha)} \log_{10}([\mathrm{H}\alpha/\mathrm{H}\beta]_{\mathrm{obs}}/[\mathrm{H}\alpha/\mathrm{H}\beta]_{\mathrm{int}})$, where the intrinsic Balmer decrement is taken to be 2.86 following Case B recombination and $k(\lambda)$ is given in Table 2.7 for key wavelengths.

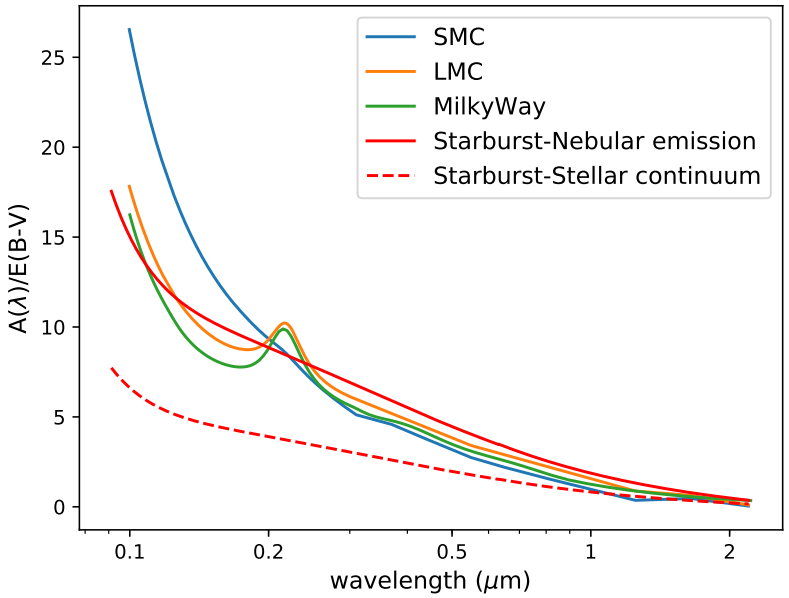

Figure 2.6: The extinction curves of 4 common extinction laws including the SMC and LMC from Gordon et al. (2003); the Milky Way from Cardelli et al. (1989); the Calzetti et al. (2000) star burst for both the nebular emission and stellar continuum (discussed further in Section 2.3.4.3).

Dust law	[OII]-3727μm	Hβ-4863μm	[OIII]-5007μm	v-5500μm	Hα-6563μm
SMC[a]	4.549	3.334	3.200	2.741	2.172
LMC[a]	5.146	3.988	3.858	3.410	3.025
MW[b]	4.770	3.609	3.475	3.100	2.535
Starburst[c] (Gas)	5.846	4.586	4.454	4.038	3.317
Starburst[c] (Stars)	2.575	2.020	1.962	1.779	1.461

Table 2.7: Table of magnitude attenuation per E(B-V) colour excess at key wavelengths ‘k(λ)’ for 4 dust extinction curves from Figure 2.6. Extinction curves taken from *a*) Gordon et al. (2003), *b*) Cardelli et al. (1989) or *c*) Calzetti et al. (2000). I note for Calzetti et al. (2000) that E(B-V)[gas] = E(B-V)[star]/0.44.

for contamination from the [NII] doublet, as described in Section 2.3.3.1. Second, I correct for stellar absorption, the intrinsic Balmer line absorption that occurs in the photospheres of stars in these galaxies. The strength of this absorption depends on the stellar population and we follow Domínguez et al. (2013) and adopt correction values for the emission line equivalent width of 3Å for Hβ and 2Å for Hα, which are appropriate for systems with stellar masses $M_* \approx 10^{8.5}\,M_\odot$ (which is consistent with the mean stellar mass of our sample, described in Section 2.3.4.3).

The Balmer decrement is measured for the sub-sample of galaxies that have detections $> 2\sigma$ in both Hα and Hβ emission lines. For galaxies with a robust redshift (i.e., confirmed through a FORS2 line detection or multiple emission line detections in WISPS) but with a Hβ signal to noise below our detection threshold, a 2σ lower limit to the Balmer decrement is derived using the 2σ upper limit to the Hβ flux and I plot these limits for individual galaxies in Figure 2.5. I also stack the data in bins of Hα luminosity by adding the measured line fluxes from different galaxies (even if undetected in individual cases) to get the average Balmer decrement for a sub-sample of galaxies. I do not consider three galaxies that clearly have extended morphology beyond the FORS2 1" slit-width, where the slit-losses would lead to an overestimate of the Balmer decrement (these are noted in Table 2.4[9]). Together the average Balmer decrement for the sub-sample of galaxies with robust redshifts is 4.08 ± 0.45. In Figure 2.5, the Balmer decrement measurements and lower limits are plotted against their Hα luminosity (corrected for [NII] contribution and stellar absorption). The individual galaxies are colour coded by redshift and are also binned (closed blue circles) into three Hα luminosity regimes ($\log_{10}(L_{H\alpha}$, erg/s) = 41.0-41.5, 41.5-42.0 and 42.0-42.5). A second binned measurement is made for $42.0 < log_{10}(L_{H\alpha}) < 42.5$ where two galaxies are removed, whose WFC3 spectra exhibit strong negative counts around Hβ due to data reduction artefacts[10]. The binned data lie slightly below the local Balmer decrement - Hα luminosity relation (Hopkins et al., 2001) and are in broad agreement with the moderate redshift ($0.75 < z < 1.5$) observations made by Domínguez et al. (2013).

When stacking into bins of Hα luminosity, I note a trend that galaxies with higher Hα emission line luminosity tend to have higher Balmer ratios and hence more dust extinction. However, I note that our lowest luminosity bin ($\log_{10}(H\alpha) = 41.0 - 41.5$)

[9]FORS2 id:236_1_10, 62_1_16 and 309_1_5
[10]FORS2 id:64_2_15 and 236_2_16

is almost exclusively comprised of galaxies at $z < 0.7$ with Hβ falling in the FORS2 spectroscopy, but the higher luminosity bins are mainly the higher redshift galaxies with Hβ from the slitless WFC3 spectroscopy. Hence the trend may either be due to line luminosity, or instead a trend with redshift. The former is more likely, since most models predict that dust extinction should increase with time (i.e. decrease with redshift). Indeed the Balmer decrement results, binned in Hα luminosity, are slightly below the $z \approx 0$ work of Hopkins et al. (2001) from SDSS, who also fit an extinction dependence on Hα luminosity.

Although I find tentative evidence for a correlation between Hα luminosity and extinction, I also note that each luminosity bin is consistent within 1σ with an extinction $A_{H\alpha} = 1$ mag, consistent with the findings of Sobral et al. (2009), corresponding to an observed Balmer decrement of 4.27. I note that the average Balmer decrement stacking our full sample of galaxies with robust redshifts is 4.08 ± 0.45. In order to correct the emission line fluxes, later used in line diagnostic analysis (Section 2.3.6), I assume a fixed extinction corresponding to this standard value of A(Hα) = 1. For a Calzetti et al. (2000) extinction law this corresponds to A([OII]) $\sim$ 1.77 mag and A(Hβ), A([OIII]) $\sim$ 1.36 mag for the other nebular emission lines. I note that the continuum might be affected by a different level of attenuation than the nebular lines (Calzetti et al., 2000), and I consider this further in Section 2.3.4.2.

2.3.4 Star Formation Rates and Stellar Masses of the WISPS galaxies

The star formation rate and stellar mass are two fundamental galaxy properties that influence the observational characteristics of a galaxy, including the luminosity, comparative broadband colour and nebular emission line strength. Several indicators of the star formation rate have been used (see for example the review by Kennicutt 1998) for a range of redshifts and galaxy samples, and these have been combined to trace the evolution of the star formation rate density in the Universe (e.g., Lilly et al., 1996; Madau et al., 1996; Hopkins et al., 2003; Madau & Dickinson, 2014). The sample selection from the WISPS HST/WFC3 slitless spectroscopy favours galaxies with high luminosity emission lines and it is the expectation that these will exhibit high specific star formation rates (sSFR, star formation rate per unit mass). The reliance of the sample selection on the detection of strong emission lines without the requirement for any continuum detection is expected to allow a large range of stellar masses to

be observed, including low mass systems potentially missed in spectroscopic surveys following up of broad-band magnitude-limited samples. In this section I compare the star formation rate estimates derived using three techniques: the measured Hα flux; the luminosity in the rest-frame UV; and through SED fitting to the full broadband photometry. I also derived stellar mass estimates from the SED fitting. The derived properties are shown in Table 2.5 and are available electronically[11].

2.3.4.1 Spectroscopic star formation rate analysis

Hα is one of many nebular emission lines whose luminosity is sensitive to the star formation rate of a galaxy. Hα is a recombination line of atomic hydrogen which arises from the integrated stellar light from photons below the Lyman-limit ($\lambda < 912$Å) which photo-ionise neutral hydrogen in the ISM. The Hα luminosity therefore provides a probe of the ionising flux and is sensitive to the population of young massive stars, which have hot photospheres and short lifetimes. Taken with a population synthesis model and assumptions of the underlying initial mass function, a calibrated scaling relation can be constructed between the luminosity of the emission line and the star formation rate.

For the sample I derived star formation rates using the Hα fluxes corrected for [NII] contribution, stellar absorption and reddening (see Sections 2.3.3.1 and 2.3.3.2). The Hα fluxes are converted to luminosities using the FORS2 emission line measured redshift or HST/grism emission line redshift when FORS2 had no detections. I adopt the Kennicutt (1998) SFR - Hα luminosity relation and apply a correction factor to account for the different choice in IMF. Kennicutt (1998) assume a Salpeter (1955) IMF whereas I adopt a Chabrier (2003) IMF throughout this Chapter and in our stellar mass measurements. I follow Madau & Dickinson (2014) and apply a multiplicative 0.63 factor to the Kennicutt (1998) relation to adjust the measured star formation rate to a Chabrier (2003) IMF.

2.3.4.2 Star Formation Rates inferred form the rest-UV

The luminosity of the non-ionising UV continuum is sensitive to the stellar population of a galaxy and towards shorter wavelengths it is increasingly dominated by the

[11] https://github.com/Kitboyett/Supplementary-Thesis-material

emission from younger stellar populations. The rest-frame UV continuum luminosity can be used as a probe of the underlying star formation rate (e.g., Kennicutt 1998). I adopt the rest-frame 2800Å UV continuum luminosity (L_{UV}) as a probe of the star formation rate, available across the majority of our redshift range. I utilise the Kennicutt (1998) L_{UV} - SFR scaling relation, which assumes a constant star forming history (SFH) and a Salpeter (1955) IMF. I again apply a correction to the SFR to account for the change in IMF, between Salpeter (1955) and Chabrier (2003). I note that the non-ionising rest-UV continuum is sensitive to the star formation rate integrated over longer timescales ($\sim$100Myr) than that probed by the Hα (since the OB stars which dominate the ionising flux have lifetimes of <10Myr, e.g., Sullivan et al. 2001). Hence scatter between the L_{UV}- and Hα-derived SFRs (see Figure 2.7) could be attributable to different recent star formation histories.

Across the sample the rest-frame 2800Å has broadband filter coverage spanning from the ground-based r-band for the lowest redshift galaxies to the HST/WFC3 F110W band for the highest. To estimate the stellar continuum luminosity ($L_{\rm UV}$) from the broadband photometry, I first correct the flux density for any contribution from measured emission lines (e.g., [OII]λ3727) measured in either the WISPS HST/WFC3 grism or VLT/FORS2 spectroscopy. The flux from any emission lines is subtracted from the filter flux density, weighted by the filter transmission profile at the respective location of each line. For each galaxy in the sample I determine $L_{\rm UV}$ from the broadband magnitude of the filter that contains the rest-frame 2800Å based on the spectroscopic redshift. I remove galaxies from this sub-sample if the rest-frame 2800Å did not fall within an observed filter or if it lies within 100Å of the edge of the filter where the filter response is minimal. The SFR is then computed using the Kennicutt (1998) relation for these 41 galaxies out of the 85 observed with FORS2.

The observed $L_{\rm UV}$ measurements will underestimate the intrinsic luminosity due to attenuation by dust. I correct the 2800Å continuum for dust extinction. In Section 2.3.3.2 I corrected the nebular emission line flux for reddening by adopting a 1 magnitude attenuation ($A_{H\alpha} = 1$) along with a Calzetti et al. (2000) extinction law. Like Wuyts et al. (2013), I note the need for extra attenuation in nebular emission lines (e.g., Hα) compared to the continuum and I adopt the Calzetti et al. (2000) parameterisation $E(B-V)_{star} = 0.44E(B-V)_{gas}$. This parameterisation accounts for the young O/B stars responsible for the UV continuum being within their birth

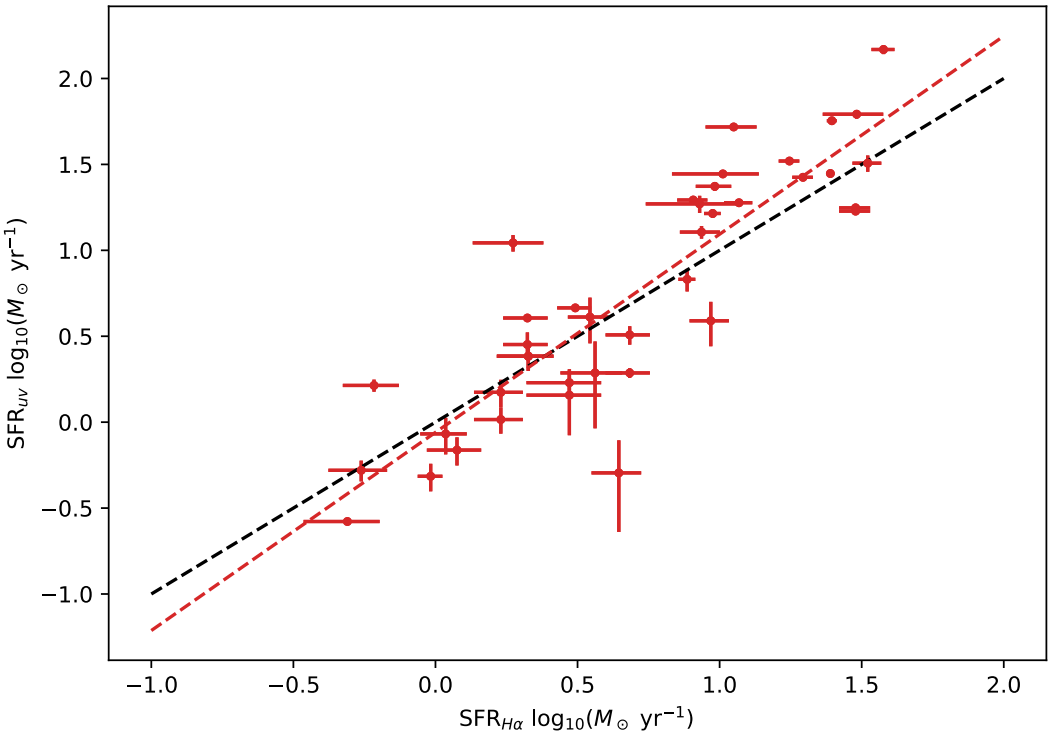

Figure 2.7: The Hα-derived SFR compared to the $L_{\rm UV}$ (rest-frame 2800Å) -derived SFR. The black curve shows the 1:1 line. The best fit model has a log slope of 1.15 ± 0.10.

cloud and generates $\rm A_{2800} = 1.29 A_{H\alpha}$ as given by Equation 14 of Calzetti (2001).

For 39 galaxies, both Hα-derived and $L_{\rm UV}$-derived star formation rates are available, and I present their comparison in Figure 2.7. I find good agreement between the star formation rates derived from each method, with a fitted slope of SFR($L_{\rm UV}$) $\propto$ SFR(Hα) raised to the power of 1.15 ± 0.10, close to a linear relation. A similar power law slope is identified in Wuyts et al. (2013) where, as in this work, a linear relation between A_{cont} and $A_{H\alpha}$ is assumed. The effects of this different dust obscuration are also reported in the $L_{\rm UV}$- and Hα-derived SFRs of Reddy et al. (2015).

2.3.4.3 Stellar population fits

The available broadband photometry and emission line flux measurements allows each target's spectral energy distribution (SED) to be sampled, from which I can constrain

galaxy properties including the stellar populations, stellar mass and star formation rate. The composite spectrum of a galaxy is dictated by several factors including the galaxy's star formation history, initial mass function (IMF) and dust extinction law. In this section I utilise the Bayesian analysis of Galaxy SEDS (BEAGLE, version 0.24.5, Chevallard & Charlot 2016) to model the SED of the subset of our sample with sufficient broadband coverage. We therefore do not consider WISPS field 236 which only has photometry in the HST/WFC3 F140W filter and is unable to place constraints on the stellar templates.

I fix the galaxy redshift to the spectroscopic redshift measured from either the FORS2 or WISPS HST/grism emission lines. I assume a two-component star formation history that is comprised of a declining exponential component and a 10Myr constant-SFR burst. The constant-SFR burst component can vary over a large dynamic range, $-4 < \log(\mathrm{SFR}/\mathrm{M}_{\odot} yr^{-1}) < 4$, and allows a directly sampling of the SFR independent of the previous SFH unlike in a delayed/exponentially declining SFH model. This reflects that the emission line galaxies identified through the WISPS HST/grism slitless spectroscopy are actively star forming galaxies. I assume a Chabrier (2003) IMF and a Calzetti et al. (2000) dust attenuation law. I input flux densities and filter transmission curves for each broad-band, along with the emission line fluxes and wavelengths from our spectroscopy. The flux contribution from emission lines is not removed from the broadband photometry as this is considered as part of the modelling.

A total of seven parameters are fitted in BEAGLE: stellar mass, stellar age, characteristic star formation timescale (the exponential component), star formation rate (the burst), stellar metallicity, effective dust attenuation, and effective galaxy-wide ionisation parameter. The ionisation parameter is freely-varied so the emission line fluxes could better constrain the spectral fits. A burst component was included for physical reasons while also enabling better identification of multi-modal solutions. Within SED fitting the derived stellar mass acts as free parameter used to constrain the normalisation of the composite synthetic galaxy stellar population spectrum to the observations. In Figure 2.8 the BEAGLE SED derived mass distribution for the 56 galaxies with sufficient broadband photometry to constrain the stellar template is presented (excluding field 236 which only had photometry available in F140W). In particular, the availability of Spitzer/IRAC channel 1 photometry (3.6μm) for three

of our four fields gives us the rest-frame continuum at $> 1\mu$m, which is more sensitive to the underlying stellar mass than recent star formation (unlike at shorter wavelengths), and improves our measurement of the stellar mass. This is reflected through a re-running the BEAGLE SED analysis on our sample without the IRAC 3.6μm photometry. In both analysis, consistent stellar mass estimates are found (presented in Figure 2.10), albeit with the uncertainty on the estimates more tightly constrained when the IRAC data is utilised. The average uncertainty on the stellar mass decreasing from 0.3 to 0.2dex. I note that of the 56 galaxies covered by Spitzer, 14 are undetected down to 2σ limits of AB=24.2-24.5mag, and these are consistent with being very low mass systems ($M_{\rm stellar} < 10^8 M_{\odot}$).

With a median mass of $log_{10}(M/M_{\odot})$ =8.94 and a dynamic range of $7 < log_{10}(M/M_{\odot}) < 11$, the sample reaches lower masses and is typically fainter on average than broadband-magnitude-limited spectroscopic surveys e.g., VMOS, DEEP (see Section 2.3.7). I note that due to the requirement for the galaxies to be detected in the WISPS direct imaging, to calibrate the wavelength of the emission lines, the lowest mass galaxies may still be missing from our sample.

I additionally use our SED fitting to estimate the SFRs of the sample, and in Figure 2.9 I present their comparison to our Hα-derived SFRs. I find reasonable agreement between the two methods, with a fitted power law slope of 1.05$\pm$0.08. I also determine an offset from the 1:1 line of 0.18$\pm$0.05dex compared to the Hα-derived SFRs.

2.3.4.4 Star forming main sequence

There is a relation between the stellar mass - star formation rate, commonly known as the star forming main sequence, which has been studied in great detail from local redshifts out to beyond $z > 4$ (e.g., Speagle et al., 2014; Renzini & Peng, 2015; Schreiber et al., 2015). Most commonly the main-sequence is parameterised with a log-space slope and intercept, with the redshift evolution mainly effecting the normalisation of the relation in line with the increasing star formation rate density with redshift (e.g., Madau & Dickinson, 2014). I present the stellar mass - Hα derived star formation rate 'main-sequence' in Figure 2.11 for the subset of our sample which have measured Hα fluxes. I over-plot the main-sequence from three papers over a redshift range $0 < z < 2.5$, Speagle et al. (2014); Schreiber et al. (2015); Santini et al. (2009).

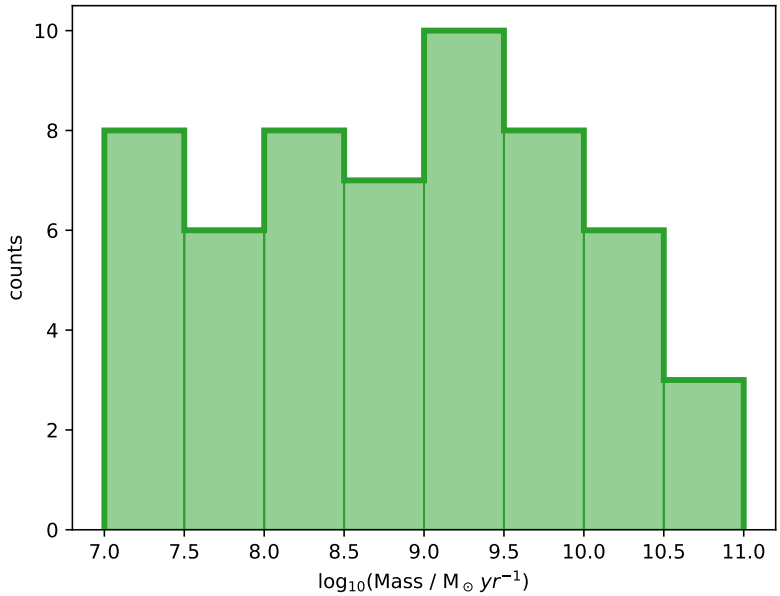

Figure 2.8: Stellar mass distribution, derived using BEAGLE SED photometric fitting code.

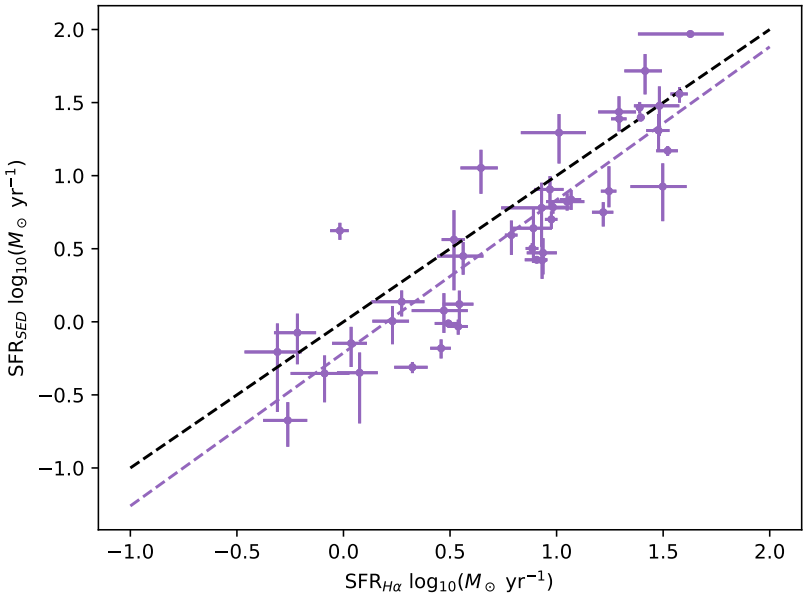

Figure 2.9: The Hα-derived SFR compared to the SED-derived SFR. The black curve shows the 1:1 line. The best fit model has a log slope of 1.04 ± 0.08 with an offset of 0.18dex. Two galaxies have been removed due to having significantly underestimated SFRs which may indicate AGN contamination, see section 2.3.5

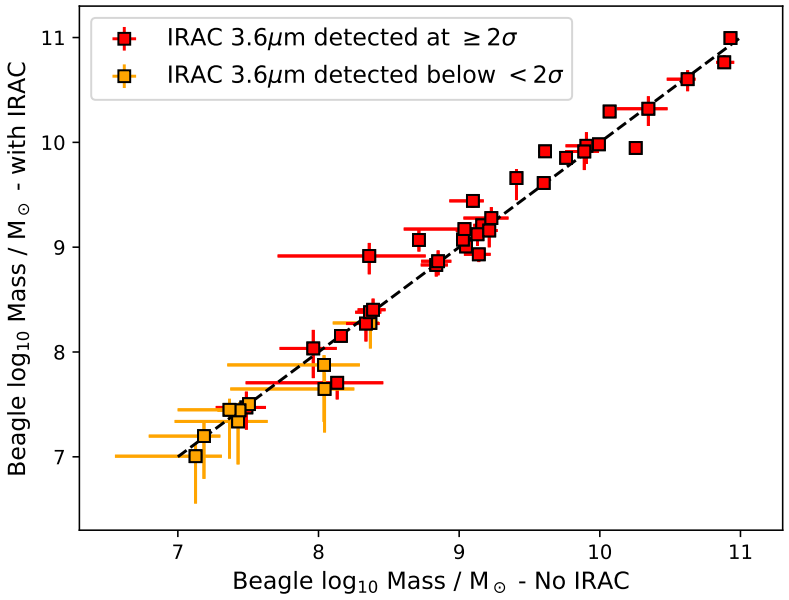

Figure 2.10: Comparison of the BEAGLE SED-derived stellar masses with and without the inclusion of IRAC 3.6μm photometry. While consistent masses are found, the use of IRAC photometry reduces the estimated uncertainty.

Galaxies within the sample lie above the main-sequence of the literature curves at the corresponding redshift, matching the expectation that the emission line selected galaxies in the HST/WFC3 slitless spectroscopy exhibit high specific star formation rates, as one would expect with an increasing star formation rate, such as a burst. The overall trend in the sample is flatter than the literature main-sequence due to the Malmquist bias imposed by the selection on strong Hα emitters. At low masses, only those galaxies with the highest SFR produce sufficient Hα luminosity to make it into the selection. This selection-driven flattening of the main sequence has been reported for surveys that select on SFR-sensitive proprieties, such as surveys selecting on strong emission lines or UV continuum selections (e.g., Cochrane et al., 2018; Rodighiero et al., 2014, 2011; Erb et al., 2006).

2.3.5 Identifying potential AGN in the sample

Emission line galaxies can be powered by star formation and/or AGN, and although I do not have X-ray data by which to select AGN, I can still address the relative contribution by looking at the line ratios of the emission lines which relate to the

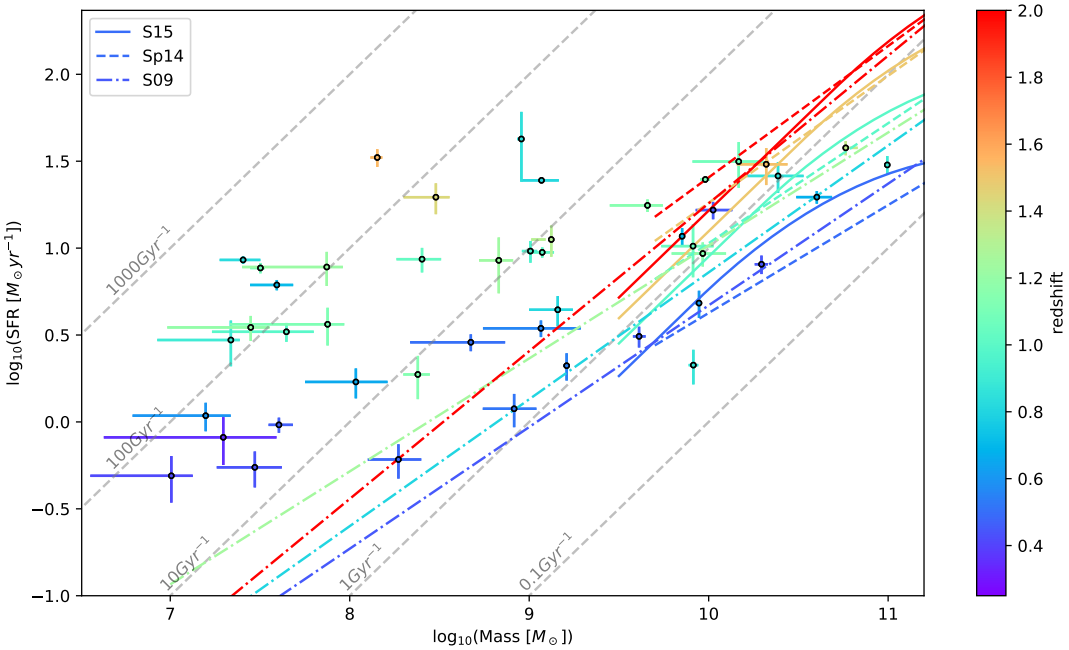

Figure 2.11: Hα-derived star formation rate - stellar mass main sequence. Hα luminosity derived star formations rates, adjusted for [NII] contribution, stellar absorption and reddening corrections. Stellar masses come from BEAGLE SED fitting. Grey dashed lines indicated lines of constant specific star formation rate. Over a range of redshifts I over-plot the literature main-sequence from Schreiber et al. (2015) (solid), Speagle et al. (2014) (dashed) and Santini et al. (2009) (dot-dashed). These emission line selected galaxies, colour coded by redshift, lie above the main-sequence indicating they have large specific star formation rates.

hardness of the ionising spectrum. A BPT diagram (Baldwin et al., 1981; Veilleux & Osterbrock, 1987) traditionally uses [NII] and [OIII] forbidden lines in ratio with their counterpart (close in wavelength) recombination lines Hα and Hβ to discriminate between star formation and AGN as the source of photoionisation. However, for this dataset, [NII] is unusable in the low spectral resolution WFC 3 grism as it is blended with Hα. Hence I use [SII]$\lambda 6717, 6731$ (hereafter [SII]) as an alternative diagnostic to [NII] (e.g., Kewley et al., 2006). A soft ionising spectrum indicating a star forming radiation field consists of low [OIII]$\lambda 5007$/Hβ and [SII]$\lambda\lambda 6717, 31$/Hα line flux ratios whilst Seyfert galaxies and LINERs with harder ionising spectra occupy the high ratio region. In Figure 2.12 I present the BPT diagnostic diagram where the $z \sim 0$ AGN/star-formation separation line diagnostic from Kewley et al. (2001, 2006) is plotted in red with the 0.1dex uncertainty in pink.

There are 35 galaxies with coverage of all the lines in the [SII] BPT diagram. This breaks down to 11 galaxies with ($> 2\sigma$) detections in each of Hα, [OIII], [SII], Hβ. There are 10 galaxies that have only [SII] undetected and 6 galaxies with only Hβ undetected. The remaining 8 are undetected in both [SII] and Hβ. I plot 2σ limits on the flux ratios in the upper panel of Figure 2.12. In the lower panel of Figure 2.12 I replace the limits on undetected Hβ with an inferred flux based on the Hα flux, assuming a case B flux ratio and an assumed dust attenuation of $A(H\alpha) = 1$ mag with a Calzetti et al. (2000) extinction law (Section 2.3.3.2), corresponding to $f(\mathrm{H}\alpha)/f(\mathrm{H}\beta) = 3.573$ (where the Hα flux has had the estimated [NII] removed, and both Hα and Hβ have been corrected for stellar absorption, see sections 2.3.3.1 and 2.3.3.2 respectively).

From this sub-sample, 29 of the 35 galaxies on our [SII]-BPT diagram lie below the SFG/AGN demarcation line at $z \sim 0$, although it should be noted that 10 of these 29 have lower limits on Hβ that mean they are conceivably still consistent with the AGN region (this falls to 3 if I use Hβ fluxes inferred from the measured Hα emission line), whilst 19 (54%) are confirmed as inconsistent with being AGN. The remaining 6 galaxies lie above the diagnostic demarcation line in the region consistent with being dominated by AGN, although 4 are consistent with the star forming region within the uncertainties. I therefore determine that 33 of the 35 galaxies (94%) are consistent with being star forming galaxies (either falling below the demarcation line for $z \sim 0$, or with limits consistent with the star forming region). Of the galaxies above the dividing line, inspection of the F110W and F160W H-band WFC 3 images reveals that the two galaxies inconsistent with being SFGs appear to be spatially unresolved

(309_1_2 & 309_1_6). I note that 309_1_6 also exhibited [Ne III]λ3869 emission, further evidence of a hard radiation field (although I note, 2 additional galaxies that are consistent with being SFGs also had [Ne III] detected).

In recent years it has been suggested that there is evolution with redshift in the dividing line between SFG and AGN in the BPT diagram, in the sense that the demarcation rises with increasing redshift, and this is particularly prominent in the [NII]-based BPT (e.g., Kewley et al., 2013b, who note that this evolution may also be due to a larger electron density or a harder ionising radiation field). However, Shapley et al. (2019) study the [SII]-based BPT diagram for a sample of galaxies from the MOSDEF survey at z$\sim$1.5-2.3 (slightly higher redshift on average than in our sample), and find that the evolution is less extreme than when using [NII], which they argue is attributable to two competing effects: a less significant contribution from Diffuse Ionised Gas (DIG) leading to a lower [SII]/Hα ratio at higher-redshift; and an increased ionisation parameter which pushes this line ratio in the opposite direction (higher [SII]/Hα). Hence the net result is minimal overall evolution in the [SII]-BPT diagram, and I adopt the z$\sim$ 0 dividing line as our AGN criterion.

The measurements of [SII] from our WISP WFC3 spectroscopy are often low S/N, and so I want another check on the presence of AGN. I also consider the mass-excitation (MEx) diagnostic proposed by Juneau et al. (2011), where the [NII]/Hα ratio of the original BPT diagram is replaced by the stellar mass (on the grounds that the average stellar mass of a galaxy depends on the metallicity, from the mass-metallicity relation, see Section 2.3.6.4). This also allows the inspection of the ionising conditions of the highest redshift galaxies within the sample, where Hα no longer fell within the HST Grism coverage. Plotting the stellar mass against [OIII]λ5007/Hβ allows SFG to be separated from AGN, and I show a MEx diagram in Figure 2.13, where I plot the low-redshift dividing line, along with another division which may be more appropriate at higher redshift (due to evolution in the mass-metallicity relation e.g., Newman et al. 2014; Coil et al. 2015). I adopt the AGN/star-formation separation in the MEx diagram from Henry et al. (2021) who also consider a sample of WISP galaxies.

Within the MEx diagram, there are 6 galaxies with Hβ detections (diamonds in Figure 2.13) that lie in the $z \sim 0$ AGN region, although each of these lies either inside or is consistent within their uncertainties of the modified $z \sim 2$ SFG region.

When undetected Hβ flux limits are replaced with the Hα flux divided by 3.573 (that consistent with a Hα attenuation of 1 magnitude), 5 further galaxies lie above the $z \sim 0$ AGN/SFG separation line, although 4 are at least consistent with the SFG region on the modified MEx diagram. Only one galaxy (FORS2 id 309_1_2) is clearly an AGN considering both MEx diagrams, this galaxy is also identified as an AGN in the [SII]-based BPT diagram.

In Table 2.8 I present the AGN candidates identified by the [SII]-BPT and MEx diagnostics, and report that only a sub-set of 2 are identified by both methods. These 2 are also found to be unresolved in the F110W and F160W imaging, and in one we detect the high ionisation [Ne III] emission line, suggesting that these are indeed AGN contaminants of the desired star forming sample in this work and I remove them from the sample. The remaining AGN candidates are identified as being SFG in at least one of the methods with many also being spatially resolved. I conclude that star formation is the dominant ionising source in most of the emission-line-selected galaxies, with only 2 out of 41 galaxies (which have sufficient data to be plotted on at least one of the [SII]-BPT or MEx diagrams) likely being AGN. For the overwhelming majority of the sample, the Hα emission is most likely dominated SFG rather than AGN.

2.3.6 Determination of Metallicity from Emission Lines

One of the key ISM properties that can be inferred from these observations is the gas-phase metallicity, and in this section I will derive the gas-phase oxygen abundance from two different line-ratio diagnostics. Using this, I will investigate the relation between the metallicity and the stellar mass of the galaxies in the emission-line selected sample.

The observed metallicity as measured from the gas-phase oxygen abundance is sensitive to the galaxy's stellar population, star formation history and history of gas inflows and outflows. The chemical enrichment of the ISM reflects the star formation history, with metal-enriched gas returned to the ISM over time through stellar ejecta and explosions. The degree of enrichment of the ISM can be diluted by the flow of cold gas (typically of lower metallicity, and perhaps pristine) from the Inter-Galactic or Circum-Galactic Medium into the galaxy. Outflows of chemically-enriched gas being ejected from the galaxy driven by supernovae or black hole feedback may also alter the ISM metallicity (e.g., Lilly et al., 2013)

FORS2 id	[SII]-BPT $z \sim 0$	MEx $z \sim 0$	MEx Modified	[Ne III] detection	imaging inspection
309_1_2[a]	AGN	AGN	AGN	No	Compact
309_1_6[a]	AGN	AGN	AGN*	Yes	Compact
309_1_13	AGN	SFG	SFG	No	Resolved
309_2_13	AGN*	SFG	SFG	No	Resolved
309_2_1	AGN*	SFG	SFG	No	Compact
64_2_10	AGN*	SFG	SFG	No	Resolved
236_1_14	AGN	-	-	No	Resolved
309_1_3	SFG	AGN*	SFG	No	Resolved
309_2_4	-	AGN	AGN*	No	Compact
309_2_5	-	AGN	AGN*	No	Resolved
309_2_7	-	AGN*	AGN*	No	Resolved
64_2_5	SFG	AGN	SFG	No	Resolved
64_2_9	-	AGN*	SFG	No	Compact
64_2_15	SFG	AGN	SFG	No	Resolved
64_2_16	-	AGN*	AGN*	No	Compact
62_1_14	-	AGN	SFG	No	Resolved

Table 2.8: A table of potential AGN candidates meeting various selection criteria. I consider the BPT diagram using the [SII] line rather than [NII], and also the mass-excitation (MEx) diagram (where I indicate if it meets the AGN threshold at z$\sim$ 0 and also a modified threshold which may be more appropriate at high redshifts). I also indicate those sources which have [NeIII] emission and the $z \sim 0$ and modified MEx diagram. AGN candidates marked with (*) were consistent with the SFG region within their uncertainties or had limited consistent with the SFG region due to non-detections in the [SII] emission line. Two galaxies, marked by (^{a}), are consistent with being AGN in both diagnostics and are removed from the sample.

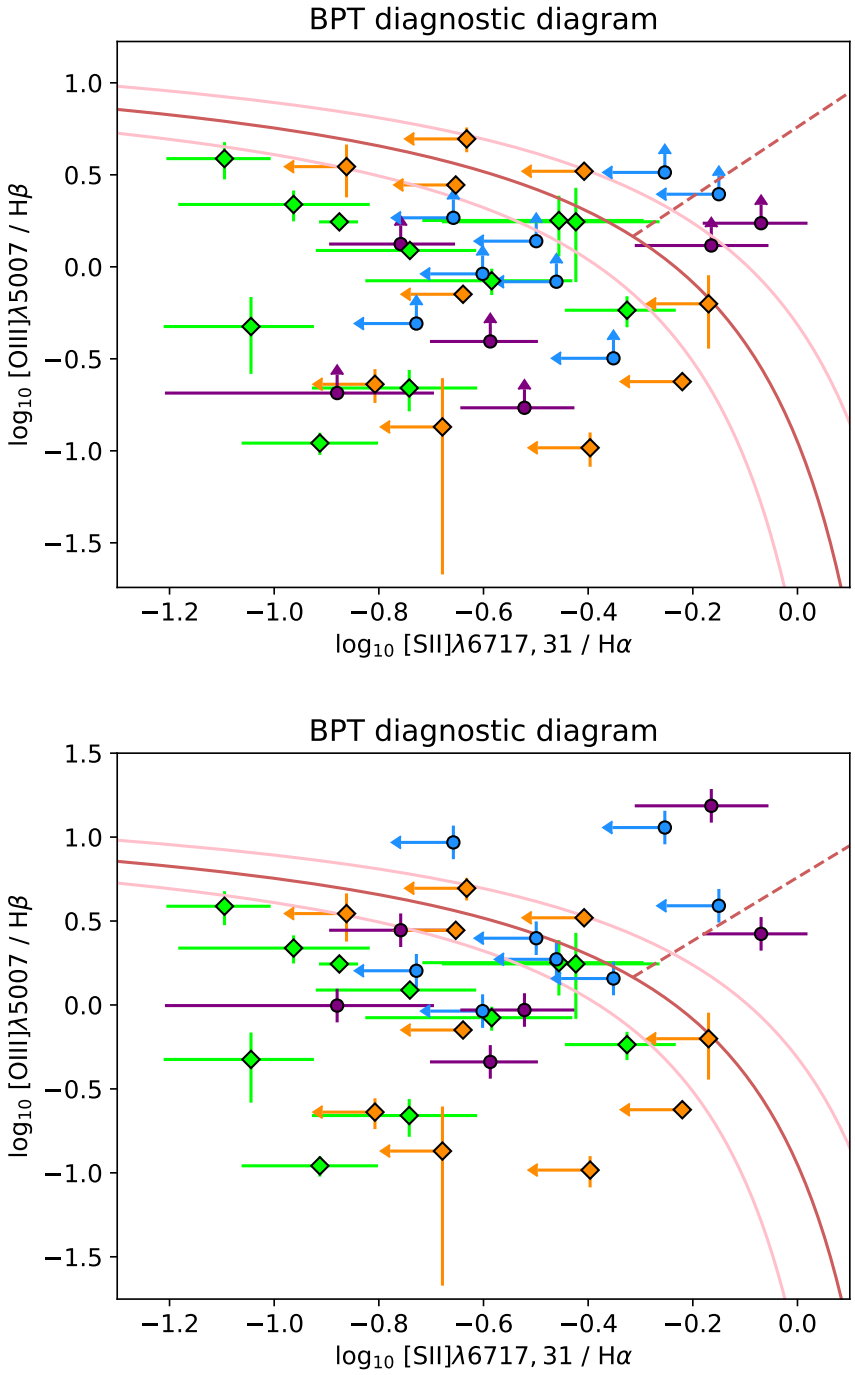

Figure 2.12: The [SII]-modified BPT diagram to identify AGN candidates (which lie in the region above the curve), using the Kewley et al. (2006) separation $z \sim 0$ curve. The pink lines show the typical demarcation curve uncertainties of 0.1 dex. Top: Galaxies without Hβ detections ($\geq 2\sigma$) are treated as 2σ lower limits on the flux ratios. Bottom: Galaxies without Hβ detections are plotted using Hα/3.573. Galaxies with Hβ detections are shown in diamonds (green or orange), whilst galaxies without detections in Hβ are shown in circles (blue or purple). Unlike Hβ, those galaxies without [SII] detections are always shown as a 2σ upper limit (blue or orange).

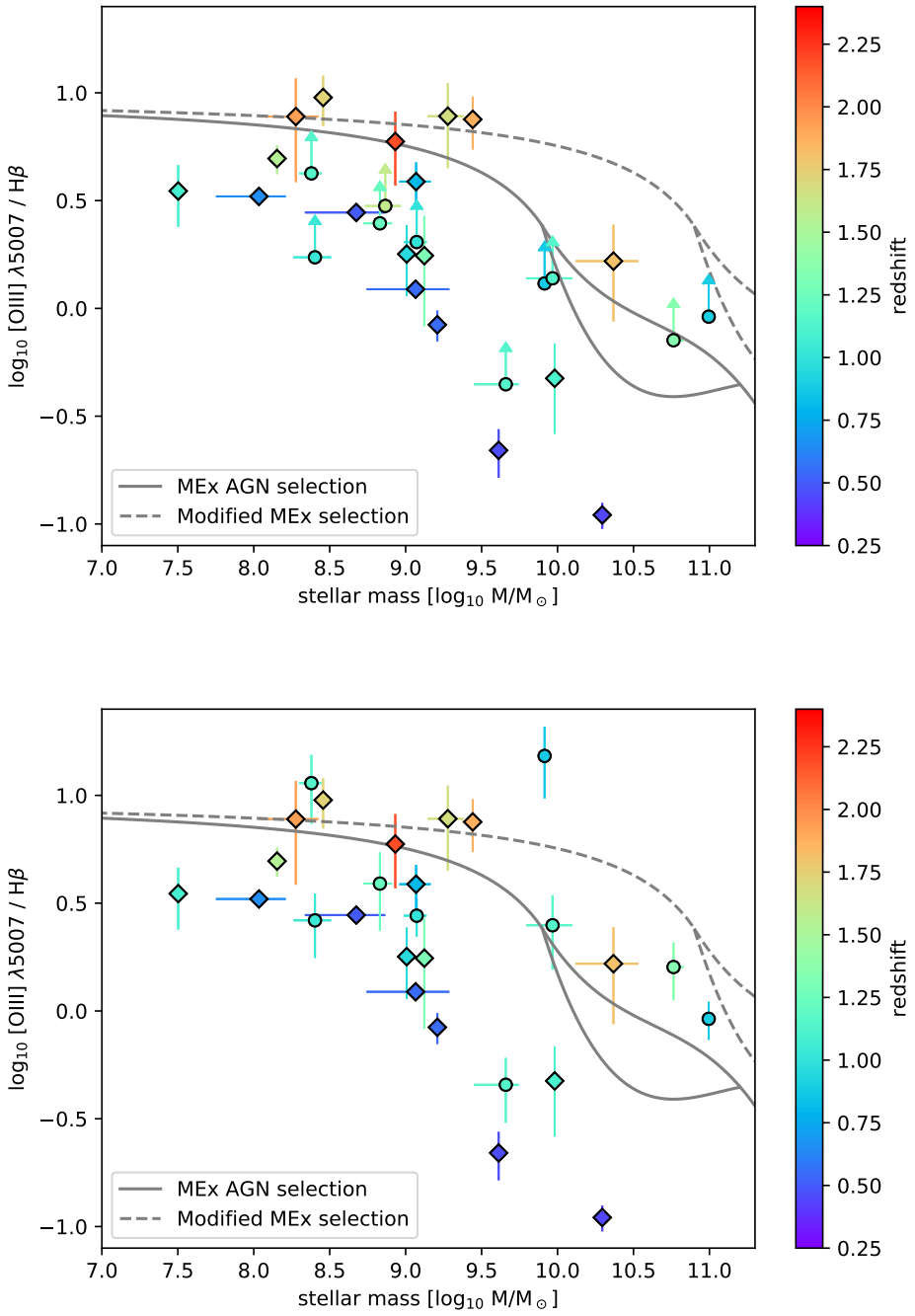

Figure 2.13: The mass excitation (MEx) diagnostic diagram, which divides the AGN dominated region (above the curves) and the SFG dominated region (below the curves), shows that the ionising radiation field in the majority of our sample is consistent with star formation, rather than AGN activity. Top: Galaxies without Hβ detections ($\geq 2\sigma$, circles) are treated as 2σ low limits on the line flux ratios. Bottom: Galaxies without Hβ detections are plotted using Hα/3.573.

2.3.6.1 Metallicity Determinations using the R23 and O32 Diagnostics

The wavelength range available from the combined WFC3 and FORS2 spectroscopy provides coverage of metallicity-sensitive nebular emission lines, in particular the [OII]λ3727 and [OIII]λ4959, 5007 doublets. In this section I will utilise these strong oxygen emission lines along with empirical calibrations of the gas-phase oxygen abundance in star-forming galaxies to derive the metallicity of the sample. Alternative approaches include the measurement of stellar metallicity rather than the gas-phase (often using absorption lines, e.g., Cullen et al. 2019) or "direct methods" to determine gas-phase metallicity based on electron temperature measurements using auroral emission lines (e.g., Sanders et al., 2016). However, the spectra from WFC3 and FORS2 are insufficiently deep to achieve good detections of absorption lines or weak auroral emission lines, and hence I can only use strong-line metallicity diagnostics for the sample.

The flux ratio of recombination emission lines (e.g., Hα, Hβ) to forbidden collisional emission lines (e.g., [OIII]λ5007, [OII]λ3727, [NII]) is sensitive to the gas-phase metallicity and ionisation conditions of the ISM. Standard nebular line flux ratios R_2 = f([OII]λ3727, 3729)/f(Hβ) and R_3 = f([OIII]λ5007)/f($H\beta$) and the combination of these by Pagel et al. (1979) into R_{23} = f([OII]λ3727, 3729 + [OIII]λ5007, 4959)/f(Hβ) are frequently used as strong-line metallicity indicators. However, these empirically show non-monotonic behaviour (i.e., multiple metallicities can exhibit the same diagnostic value) and traditionally a second line diagnostic is introduced to break the degeneracy (e.g., Alloin et al. 1979; Pagel et al. 1979; Kewley & Dopita 2002; Maiolino et al. 2008; Sanders et al. 2016; Strom et al. 2017). Many works have noted that the excitation conditions in high redshift galaxies are very different from galaxies and H II regions at $z \approx 0$ (e.g., Masters et al., 2014; Strom et al., 2017), and the strong-line metallicity calibrations depend on the ionisation conditions (e.g., Kewley et al., 2013b). Typically, the metallicity indicator O32 = f([OIII]λ5007)/ f([OII]λ3727, 3729) or the f(Hα)/f([NII]λ6583) line flux ratios are used as they are sensitive to the ionisation conditions of the ISM. Since [NII] is blended into the Hα emission line at the spectral resolution of the HST/WFC3 grism, and the nearby [SII]λ6717, 6731 doublet is often at very low signal to noise in our WFC3 spectra, I use the O32 diagnostic (rather than [NII]) to break any degeneracy of the R23 metallicity indicator.

I utilise the Curti et al. (2017) empirically-calibrated metallicity diagnostics for R23 and O32 to derive the Oxygen abundance for galaxies in our sample. I use

this recent calibration in preference to older once because their sample combines individual low-metallicity galaxies with binned-stacks of SDSS galaxies to achieve the sensitivity in the [O III] λ4363 and [O II]$\lambda\lambda$7320, 7330 auroral lines required to calibrate the strong-line diagnostics using the direct-temperature method (based on the electron temperatures of the different ionisation zones) over a large metallicity dynamic range. The calibration of traditional strong-line diagnostics to the direct-temperature method establishes robust metallicities since the electron temperature, which can be determined from the line ratios of auroral to strong-lines, is known to be strongly correlated with metallicity. Where higher Oxygen abundances trend with lower electron temperatures, because forbidden emission lines from metals are the primary coolants in HII regions (Curti et al., 2017).

The metallicities for the galaxies in the sample are presented in Table 2.5. I present the line diagnostic R2-R3 in Figure 2.14 and R23-O32 in Figure 2.15 for the individual galaxies within the sample (colour coded by redshift), and compare these with the low redshift results from SDSS, and the empirical metallicity calibration from Curti et al. (2017). Henry et al. (2013, 2021) also analysed the metallicity of a different sub-sample of galaxies from the WISPS survey, based on the WFC3 spectra alone and focusing on higher redshifts than in this Chapter where all the lines [OII], Hβ and [OIII] are covered by the HST grism(s). This current work can explore the metallicities of WISPS galaxies down to lower redshift thanks to our VLT/FORS spectroscopic follow-up at shorter wavelengths.

The diagnostics diagrams in Figures 2.14 & 2.15 show measurements from individual galaxies where the [OII], [OIII] and Hβ emission lines are all detected at $S/N > 2$. I note that I have removed one galaxy (FORS2 id:309_2_18) which has a large spatial extent and where the FORS2 slit spectrum would not capture the full flux from the [OII] emission line, and after removing this one object I have 23 galaxies with individual measurements, of which 18 also have Hα flux measurements. These individual data points largely agree within 2σ of the region occupied by SDSS galaxies, with few lying much further away than this. Each individual galaxy presented in these figures has corrections based on the general properties of the sample (e.g., average dust attenuation and Hb absorption corrections) which may show variation on a galaxy-by-galaxy basis and be responsible for some of the data points lying away from the SDSS region. The uncertainties presented represent the random errors on the emission lines but do not include the potential systematic errors from the correction terms, such as

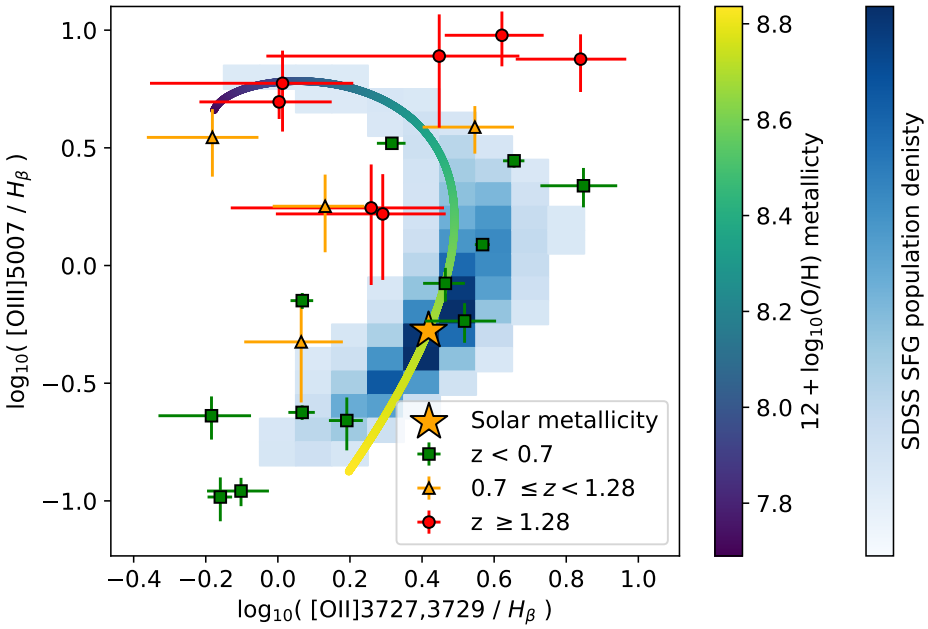

Figure 2.14: Line diagnostic plot of [OII] vs [OIII] normalised by Hβ, where the sub-sample of 23 galaxies that have detections in all of [OII], [OIII] and Hβ are split into three redshift bins. The over-plotted Curti et al. (2017) metallicity curve (colour coded by the colour-bar to the right of the plot) indicates that the WISPS galaxies generally lie at sub-solar metallicities, with a trend of decreasing metallicity with increasing galaxy redshift. A heat map of SDSS SFG density at $z \sim 0$ is under-plotted, taken form Curti et al. (2017).

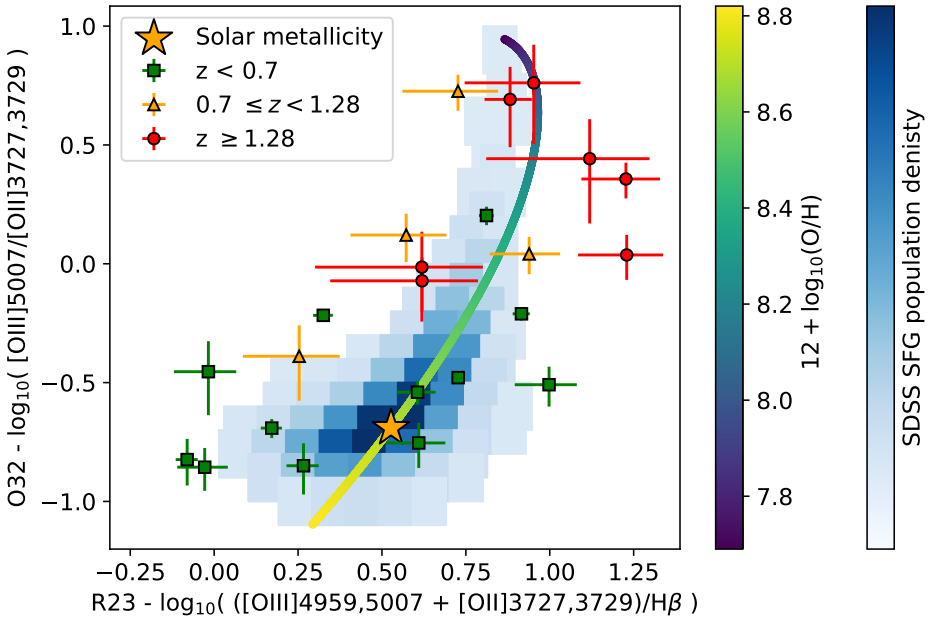

Figure 2.15: Line diagnostic plot of O32 vs R23, where the sub-sample of 23 galaxies that have detections in all of [OII], [OIII] and Hβ, are split into three redshift bins. The over-plotted Curti et al. (2017) metallicity curve (colour coded by the colour-bar to the right of the plot) indicates most lie at sub-solar metallicities, with a trend of decreasing metallicity with increasing galaxy redshift.

for the slit losses, and I will place greater emphasis on stacking data points which should average over the scatter of the individual galaxies. This additionally means I also consider galaxies where individual lines are undetected ($< 2\sigma$) by combining the emission line fluxes from several galaxies together in a stacking analysis. I generate several sub-samples and scaling schemes for the stacking, and these are shown in Figures 2.16 & 2.17. First, I perform a straight average of the emission line fluxes (which would typically minimise the noise, but would give equal weight to low-luminosity galaxies at lower redshift and higher luminosity galaxies at greater redshift with the same observed line flux). Secondly, I perform a straight average of the emission line luminosity, so as not to penalise higher redshift sources. Next, I considered a stack where I normalise the line luminosities by the stellar mass before averaging (requiring mass measurements and reducing some of the sample sizes for this stack). Finally, to ensure that the stacks are not dominated by a small number of very bright sources, I normalise the individual line luminosities before averaging such that the integrated line luminosity from Hα was the same (where the Hα luminosity is a proxy for the star formation rate, and has been corrected for [NII], reddening and stellar absorption, as described in Section 2.3.3.2).

In this stacking, I only include galaxies with faint emission line measurements ($< 2\sigma$) if an accurate redshift is available from the higher-spectral-resolution FORS2 spectrum, which enables the wavelength of the emission line to be accurately located in the extracted spectra. For each emission line of interest, I sum the line fluxes, luminosities or the luminosities after normalising by the stellar mass or Hα luminosity, and take the ratios of the summed fluxes for different samples to plot on the diagnostic diagrams. For inclusion in the Hα luminosity-normalised stacked spectrum I require each galaxy to have Hα, Hβ, [OII] and [OIII] coverage across our FORS2 or WFC3 spectroscopy, which results in a sample of 30 galaxies, 15 of which have $S/N < 2$ in one or more of these emission lines (typically Hβ). The other 15 galaxies entering the sample for the stacking analysis are a sub-set of the 23 individual objects plotted in Figures 2.14 and 2.15 with five galaxies excluded as Hα was not covered by the slitless spectroscopy at their redshift and three excluded as they were spatially extended and the [OIII], Hβ & [OII] line fluxes determined from FORS2 will be subject to slit losses compared to the Hα line measured from the WFC3 slitless grism (see Section 2.3.3.2). The sample covers a broad redshift range and to study any evolutionary trend I consider sub-samples of objects binned by redshift (low $z < 0.7$ and medium $0.7 < z < 1.28$). I note that there are only two galaxies in the sample at

$z > 1.28$ that meet our criteria for the stacked sub-samples and so I do not consider this range. I additionally split the stacking sub-samples by Hα rest-frame equivalent width, which is sensitive to the presence of bursty star formation and young stellar populations. I wish to test if the ISM conditions depend on the Hα rest-frame equivalent width, EW_0(Hα), and I create sub-samples[12]of galaxies with EW_0(Hα)$<$ 100Å and EW_0(Hα)$>$ 100Å(corrected for [NII] and stellar absorption, with further details given in Section 2.3.7). I note that the high-equivalent-width galaxies identified in the WISPS slitless spectroscopy may have been missed in traditional broad-band selected spectroscopic galaxy surveys, which I will discuss further in Section 2.3.7.

The medium redshift - low Hα equivalent width sub-sample of 8 galaxies exhibited no Hβ detections, even in the stack, so I plot instead 2σ limits for Hβ. The stacks of these sub-samples are shown in Figures 2.16 and 2.17, with the results of Curti et al. (2017) at low redshift shown for comparison. The stacks of the galaxies in each of these various sub-samples all lie on or near the locus of SDSS $z \sim 0$ galaxies. I note that each of these sub-samples is consistent with being sub-solar metallicity.

In recent years concern has been raised over the contribution of line emission from the Diffuse Ionised Gas (DIG) affecting the metallicity inferred from the strong-line diagnostic ratios (e.g., Sanders et al. 2017; Vale Asari et al. 2019). In local galaxies the DIG may be responsible for 30-60% of the Hα line emission (e.g., Zurita et al., 2000) and from the observation available, I am unable to measure the DIG contribution in our WISPS galaxies. However, at the high redshifts of our WISP galaxies (z$\sim$ 1) Sanders et al. (2017) measure that the contamination from the DIG drops to $<$20% and it is likely to only be a small contribution to the Hα fluxes in this work. Sanders et al. (2017) present a correction for DIG contamination involving the [NII] emission line but since I do not recover the [NII] line emission flux in either the HST/WFC3 or FORS2 observations, I do not apply this comparatively small DIG correction. Additionally, the recent study by Mannucci et al. 2021, who consider the influence of aperture effects in spectroscopic studies, report that the effect of DIG on the spectra of SFGs could be even less significant than previously thought.

[12]There are 7 galaxies in the low-redshift low-Hα EW stack, 2 galaxies in the low-redshift high-Hα EW stack, 8 galaxies in the medium-redshift low-Hα EW stack, and 11 galaxies in the medium-redshift high-Hα EW stack

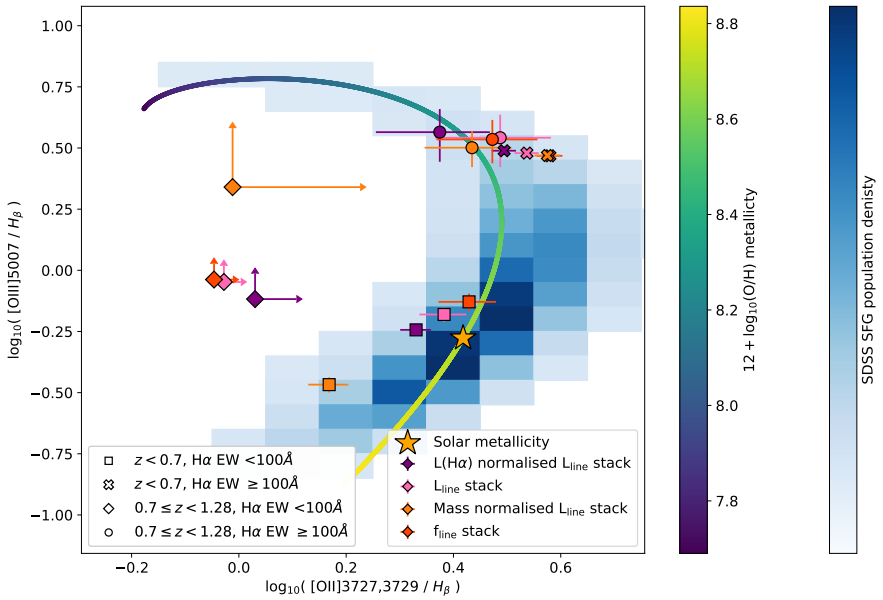

Figure 2.16: As in Figure 2.14, the line diagnostic [OII] vs [OIII] normalised by Hβ plot for sub-samples of galaxies binned by redshift and Hα rest-frame EW. Four different weighting schemes are plotted, as in the legend. Since the medium-z low-EW sample of 8 objects had no Hβ detections, even in the stack, we present the Hβ 2σ limit.

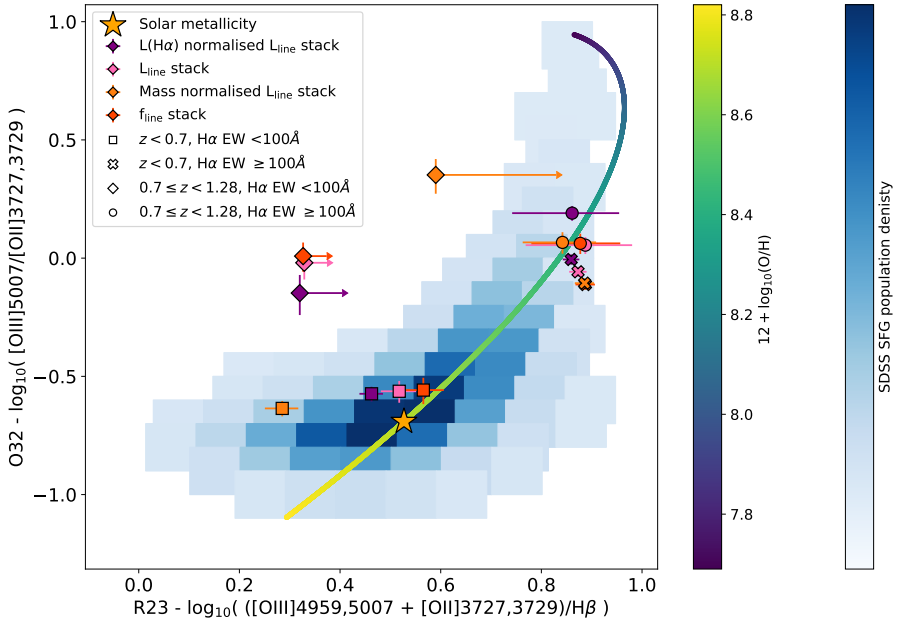

Figure 2.17: As in Figure 2.15, the line diagnostic O32 vs R23 plot for sub-samples of redshift and Hα rest-frame EW (as in Figure 2.16).

2.3.6.2 Metallicity trend with redshift

As apparent from Figures 2.14-2.17, I find a trend that metallicity, as measured from the Curti et al. (2017) calibration, decreases with increasing redshift. This redshift evolution reflects changes in the conditions of HII regions, although a changing contribution of the DIG at different redshifts may also contribute to apparent evolution of the diagnostic ratios. This trend with redshift is supported by previous surveys: the low redshift sample lies consistently within the R23 and O32 region occupied by the $0.5 < z < 1$ sample of Lilly et al. (2003) and the medium and high redshift galaxies are consistent with the higher redshift $z \sim 2 - 3$ sample from Cullen et al. (2014), which exhibit a higher ionisation parameter (higher O32 and R23 values) indicative of a harder ionising radiation field than local galaxies. This supports the conclusions of Cullen et al. (2014), Hainline et al. (2009) and Nakajima et al. (2013) whose higher-redshift samples (z$\sim$ 2) are systematically offset to higher O32 than low-redshift SDSS galaxies. Strom et al. (2017) and Maiolino et al. (2008) at even higher redshift $z \sim 3$ show offsets to still larger values of R23 and O32. These results at higher redshift are in broad agreement with the highest redshift WISPS galaxies. The rise of [OIII]/Hβ with redshift is often attributed to a rise in the ionisation parameter, which could be driven by the changing metallicity, age and geometry of the stellar population in HII regions with redshift (e.g., Kewley et al., 2015; Jaskot et al., 2019).

2.3.6.3 Metallicity trends with Hα Equivalent Width

I find that galaxies exhibiting a high rest-frame equivalent width of Hα (> 100Å) typically have higher O32 values (and hence lower metallicities on the Curti et al. 2017 calibration) than the low-EW galaxies at similar redshifts, which agrees with previous studies who find a positive trend between the equivalent width of Balmer lines and the O32 line ratio (e.g., Kewley et al. 2015 at $0.2 < z < 0.6$ and Reddy et al. 2018 at $1.6 < z < 2.5$). As can be seen in Figure 2.16, there is a dramatic difference in the [OIII]/Hβ line flux ratio (and similarly in both the O32 and R23 ratios in Figure 2.17) going from low-EW of Hα to high-EW in the low redshift sub-samples, with the higher-ionisation [OIII] line becoming more dominant compared to [OII] for the galaxies with high EW Hα. This trend is driven by a higher ionisation parameter at higher EWs, indicative of young stellar population and high sSFR due to the relative abundance of young ionising stars to older non-ionising stars (Mingozzi et al., 2020;

Kaasinen et al., 2018; Kewley et al., 2015)

2.3.6.4 Metallicity trends with stellar mass

The metallicity of star forming galaxies is found to increase with their stellar mass. This trend with mass, the "mass-metallicity relation", has been well studied over a broad redshift range (e.g., Tremonti et al. 2004 at z$\sim$ 0.1; Yabe et al. 2014 at z$\sim$ 1.4; Henry et al. 2013 at z$\sim$ 2; Sanders et al. 2018 at z$\sim$ 2.3; Maiolino et al. 2008 at z$\sim$ 3.5). The mass-metallicity relation may reflect different levels of star forming chemical enrichment and regulation driven by secular processes including gas inflows and outflows, such as in the bathtub model of Lilly et al. (2013), with outflows more efficiently removing material at lower galaxy stellar masses. At a fixed mass, galaxies at higher redshifts are typically observed to exhibit lower metallicities (see for example the review by Maiolino & Mannucci 2019). Within this redshift evolution the observed shape of the mass-metallicity relation remains roughly constant.

Here I compare the derived stellar masses (see Section 2.3.4.3) to the metallicity of the galaxies within our sample. I present the mass-metallicity relation for the two gas-phase metallicities derived using the R23 and O32 line diagnostics, shown in Figure 2.18 colour coded by the derived star formation rate, and in Figure 2.19 colour coded by the redshift. I over-plot three local observed relations derived from SDSS samples, first by Tremonti et al. (2004) who derived metallicities using strong-line ratios, Curti et al. (2020) who derived metallicities using direct temperature methods and Sanders et al. (2017) who also use a direct temperature method and adjust their relation to correct for DIG. In this work the metallicities come from the O32 and R23 strong-line method which are calibrated against the direct temperature method by Curti et al. (2017, 2020). Additionally I over-plot two higher redshift samples; Ly et al. (2016) at $0.5 < z < 1.0$ who use direct temperature methods to derive their metallicities, and the binned data of Henry et al. (2021) at $z \sim 1.9$ who use strong-line derived metallicities (who themselves find consistency with Sanders et al. 2018 at z$\sim$ 2.3 who use direct temperatures methods).

The mass-metallicity relation in the sample becomes very apparent when I bin the galaxies by stellar mass (Figures 2.18 and 2.19), and individually I find that the galaxies lie typically in between the z $\sim$ 0.1 and z $\sim$ 1.9 mass-metallicity trends from Tremonti et al. (2004) and the WISPS sample of Henry et al. (2021). Within the

mass–metallicity scatter I find a trend that higher redshift galaxies exhibit a lower metallicity at a given mass, as shown by the colour-coding of the individual data points in Figure 2.19. This trend is found in both the O32 and R23 diagnostic derived metallicity values.

Many studies have probed dependencies on the scatter within the mass–metallicty relation, which led to the development of the Fundamental Metallicity Relation (FMR, Mannucci et al. 2010) where the scatter was seen to correlate primarily with the star formation rate of the galaxies (see also, Tremonti et al. 2004, Lara-López et al. 2010, Hunt et al. 2012). At a constant mass, galaxies with larger SFRs show lower metallicities and vice versa. This correlation is thought to be driven by the reserves of pristine gas for each galaxy, where a greater abundance of pristine gas lowers the metallicity of ISM and provides fuel for star formation. Whereas after a period of star formation has ended the metallicity has increased due to chemical enrichment from the stellar population and the depletion of the pristine gas, which in turn also decreases the SFR. In Figure 2.18 I colour code the data by the derived SFR (similar to Maiolino & Mannucci 2019 figure 22), using the Hα-derived SFRs for galaxies with detected Hα and the $L_{\rm UV}$-derived SFR for those at higher redshifts where Hα was not available (which we have shown to be comparable methods in Figure 2.7).

In the mass-metallicity diagram based on the O32 diagnostic, colour-coded by SFR in Figure 2.19, I find a clear trend in the mass-metallicity relation, in that low-SFR galaxies have higher metallicities than high-SFR galaxies of the same stellar mass. The trend is less obvious when I use R23-based metallicities, because many of the Hβ detections (which go into the R23 diagnostic) are often low S/N.

The FMR defines a surface that galaxies occupy in the 3D space of stellar mass, metallicity and SFR. Hence the scatter in the mass-metallicity relation can be reduced by scaling the mass as a function the star formation rate. I adopt the Mannucci et al. (2010) modified mass-metallicity scaling parameter $\mu = log_{10}(M) - \alpha\, log_{10}(SFR)$ where $\alpha = 0.32$ to inspect whether the mass-metallicity scatter decreases. I determine the scatter by considering the RMS of the residuals after fitting the data with a standard mass-metal relation parameterisation (e.g., Sanders et al., 2017)

$$12 + log_{10}(O/H) = 12 + log_{10}(O/H)_{asym} - log_{10}(1 + \frac{M_{TO}}{M}^{\gamma}). \quad (2.1)$$

Diagnostic	$asym^{a}$	M_{TO}^{b}	γ
Mass-metallicity (O32)	8.55±0.06	8.19±0.26	0.69±0.29
Mass-metallicity (R23)	8.72±0.06	8.31±0.19	1.14±0.24
$\mu_{0.32}$-metallicity (O32)	8.55±0.07	8.19±0.30	0.69±0.29
$\mu_{0.32}$-metallicity (R23)	8.74±0.07	8.67±0.24	1.02±0.26

Table 2.9: The best fit parameters (a. asymptotic metallicity, b. turnover $\log_{10}$ mass) for the mass-metallicity and modified $\mu_{0.32}$-metallicity diagnostics.

Where each term defines the asymptotic gas-phase metallicity, the turn-over mass (M_{TO}) and a power slope (γ). Plotting metallicity against $\mu_{0.32}$ in Figure 2.20 shows a slightly tighter relation than seen when plotted against mass, with an RMS scatter of 0.145 compared to 0.155 when plotted against mass for the O32 metallicity (and 0.165 and 0.190 for $\mu_{0.32}$ and mass using R23). This effect is subtle, but I do note that I find $\alpha = 0.32$ tightens the scatter to a greater extent than the best fit $\alpha = 0.17$ measured by Henry et al. (2021). The best fit asymptotic metallicity, turn over mass and γ are given in Table 2.9

2.3.7 High equivalent width Hα sample

The slitless spectroscopy from the WISP survey selects galaxies on the basis of their line emission. This is in contrast to the usual broad-band magnitude-limited surveys, which select on the continuum emission. Hence, while WISPS may miss galaxies which have very low star formation rates (and hence weak line emission), it is more sensitive to galaxies with high equivalent width emission lines and weak stellar continuum - these low-mass but actively star-forming systems would typically not enter a broad-band selection. To examine this I consider deep spectroscopic surveys targeting $z \sim 1$ galaxies. These typically extend to optical magnitudes of $AB = 22.5$ mag over wide fields and $AB = 24$ mag over smaller regions, for example: VVDS-wide with $I_{AB} < 22.5$ (Garilli et al., 2008), VVDS_deep with $I_{AB} < 24.0$ (Le Fèvre et al., 2005); DEEP2 with $R_{AB} < 24.1$(Newman et al., 2013); zCOSMOS-wide $I_{AB} < 22.5$, zCOSMOS_deep with $I_{AB} < 24.0$ (Lilly et al., 2007); VUDS $I_{AB} < 25.0$ (Le Fèvre et al., 2015). Many of our WISPS sources with reliable detections of emission lines have $H_{AB} \sim 24 - 25$ (see Figure 2.1). A typical star forming galaxy with moderate extinction $E(B-V) = 1$ at $z \approx 1$ has a colour of $(I-H)_{AB} \approx 1$ mag (e.g., figure 1 of Doherty et al. 2005, where $(I-H)_{AB} \approx (I-H)_{\rm Vega} - 0.9$). About half (51%) of the WISPS emission line galaxies that are followed-up with FORS2 spectroscop-

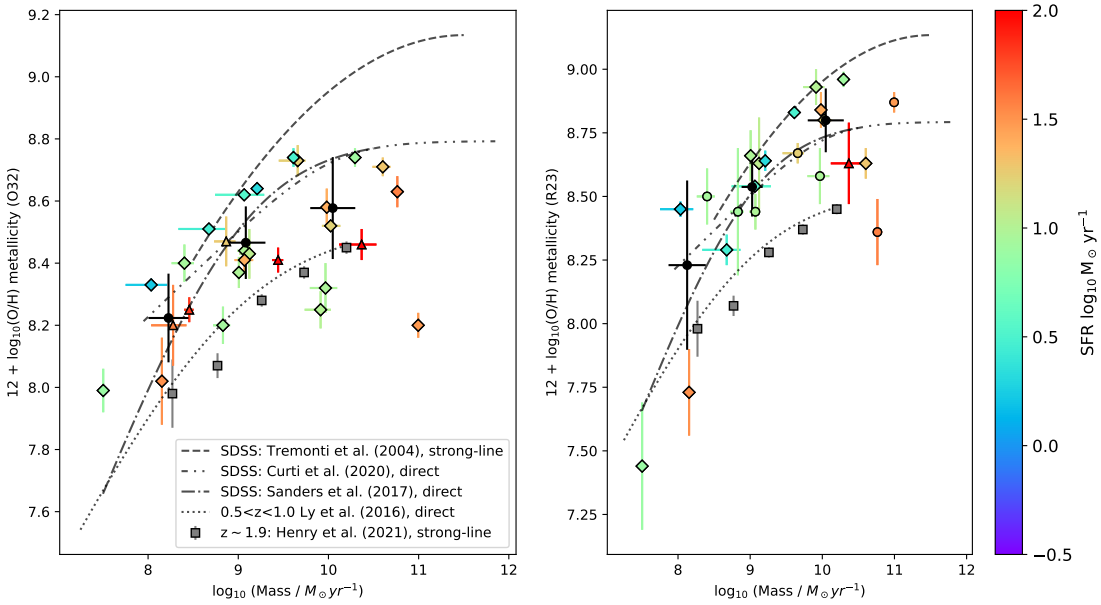

Figure 2.18: Mass metallicity relation for R23 and O32 derived metallicities, colour coded by star formation rate (Hα, unless unavailable then SFR-UV is used, these are shown as triangles). circles are the locations of galaxies with undetected Hβ where I instead infer the Hβ flux from the measured Hα flux, as in Figures 2.12 and 2.13. Black circles show the data binned by mass for $\log_{10}$(M) = 7.5-8.5, 8.5-9.5 and 9.5-10.5.

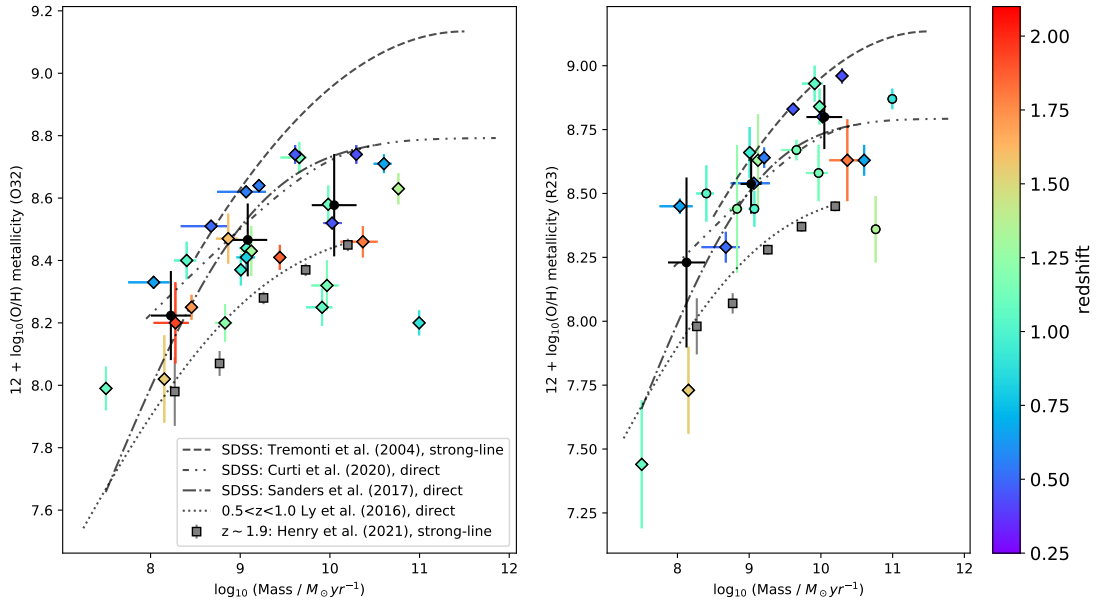

Figure 2.19: Mass metallicity relation for R23 and O32 derived metallicities, colour coded by redshift. circles are the locations of galaxies with undetected Hβ where I instead infer the Hβ flux from the measured Hα flux, as in Figures 2.12 and 2.13.

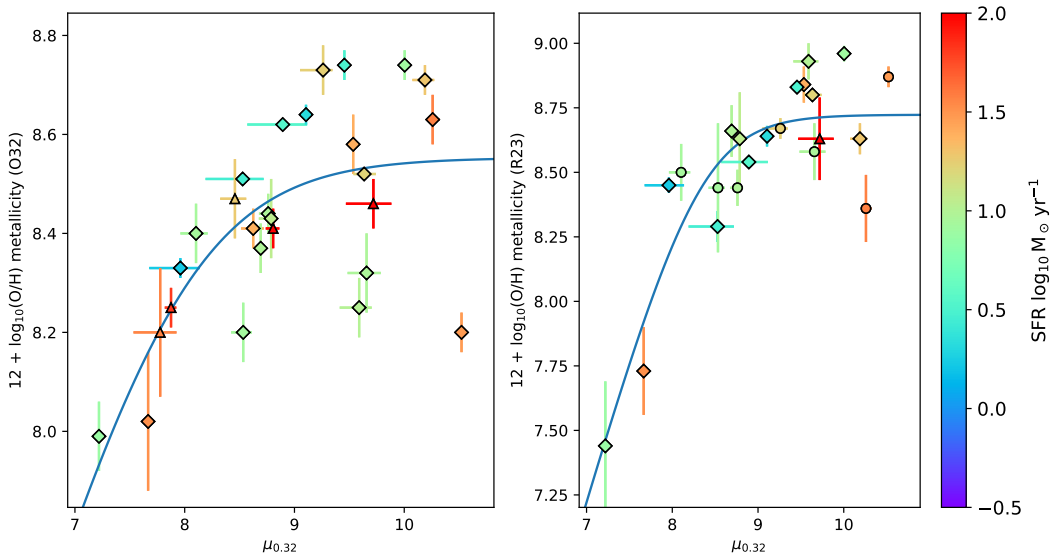

Figure 2.20: modified mass-metallicity diagram, with μ=log$_{10}$(M)-αlog$_{10}$(SFR) and $\alpha = 0.32$ from Mannucci et al. (2010). The best fit parameterisation is given by the blue curve.

ically in this work, are fainter than $H_{AB} = 24\,\mathrm{mag}$ ($I_{AB} \sim 25\,\mathrm{mag}$) and will have escaped previous spectroscopic surveys, with 30% of our WISPS galaxies fainter still ($H_{AB} > 25\,\mathrm{mag}$).

I determine the Hα equivalent width of the galaxies in the sample through the ratio of the Hα emission line flux, corrected for [NII] contribution and stellar absorption (see Sections 2.3.3.1 and 2.3.3.2), and the continuum flux density determined from the broadband magnitude of the photometric filter the line fell in. I remove the contribution of the emission line to the flux in the broad-band filter when calculating the stellar continuum, using the transmission profile of the filter and assuming a spectral slope of $f_\lambda \propto \lambda^\beta$ with $\beta = -2$ (a slope flat in f_ν appropriate for ongoing star formation in the absence of significant reddening, e.g., Wilkins et al. 2011, and I note that in Section 3.3.1 I test how an EW estimate would change if I instead assumed a reddened slope with E(B-V)=0.2 with a Calzetti et al. (2000) extinction law and find a less than 1% change). I convert all the observed-frame equivalent widths to the rest-frame values (EW_0) using $EW_0 = EW_{obs}/(1+z)$. A distribution of the Hα rest-frame equivalent widths is shown in Figure 2.21, and I also compare our distribution of Hα rest-frame equivalent widths with that determined from a broad-band-selected survey from Mouhcine et al. (2005). I note that a tail of high-EW_0 galaxies is picked up in the slitless spectroscopy that is missing from the broad-band selection. The high-EW_0 tail will also be enhanced compared to the z$\sim$ 0.06 Mouhcine et al. (2005) sample due to the evolution of Hα EW with redshift.

I examine the distribution of rest-frame Hα equivalent widths across our three redshift bins. The median (and mean) rest-frame Hα equivalent widths for the low ($z < 0.7$), medium ($0.7 \leq z < 1.28$) and high ($z \geq 1.28$) redshift bins are 78Å (mean 115 ± 23Å), 112Å (mean 211 ± 47Å) and 126Å (mean 265 ± 101Å) respectively, from bins of 27, 36 and 6 galaxies with Hα observations, where I quote the standard error on the mean. I show this data binned by redshift in Figure 2.22, and parameterise the growth of rest-frame EW with redshift as

$$EW_0 \propto (1+z)^P \tag{2.2}$$

where I determine the best-fit value of P to be 1.88 ± 0.32. One important question is whether this strong evolution in rest-frame equivalent width is real, or is a product of the way these galaxies have been selected (potentially introducing biases). The WFC3 slitless spectroscopy selects on emission line flux, and in terms of placing

galaxies on the FORS2 slit masks for follow-up spectroscopy we prioritised those with higher S/N in the WFC3 emission line, and also those galaxies with emission lines showing observed frame EWs >100Å with those above 300Å as top priority. I note that the sensitivity to lines *vs.* continuum (i.e. EW) is boosted at high redshift due to a fixed observed-frame EW limit dropping in rest-frame EW_0 by $EW_{obs}/(1+z)$, but most of the sources are well above the EW threshold for line identification in slitless spectroscopy, and the main selection effect is the Hα S/N. Hence it seems that the strong evolution in the equivalent width of galaxies with redshift is real (the large power law, P, in Equation 2.2), with any biases introduced by the observational selection likely to underestimate the true evolution (P) since we would be including progressively lower EW galaxies at higher redshifts.

The sample shows a trend of increasing Hα restframe EW with redshift , in line with the picture of increasing specific star formation rate (e.g., Mármol-Queraltó et al. 2016). Similar results on the redshift evolution of the Hα equivalent width are obtained by the 3D-HST survey (Fumagalli et al., 2012), who also use WFC3 slitless spectroscopy. For their $10 < log_{10}(M/M_{\odot}) < 10.5$ sample, Fumagalli et al. (2012) determine an evolution of rest-frame Hα EW[13] over the range $0 < z < 2.2$, characterised by $P = 1.79 \pm 0.18$ for their sub-sample of Hα detected sources using the same parameterisation as Equation 2.2, which agrees with the determination of $P = 1.88$ from the typically lower mass sample in this work. I note that the galaxy selection used to create the sample in this Chapter is different to that used by Fumagalli et al. (2012) in their complete galaxy sample, who select a sample based on multi-colour imaging in the well-studied CANDELS fields and hence also include galaxies with undetected Hα line emission (i.e. low star formation rates, below the sensitivity of WFC 3). Such galaxies are not included in the emission-line-selected sample in this Chapter, where I prioritise spectroscopic follow-up of high equivalent width sources. The specific star formation rates in my emission line selected sample are higher than the reported stacked average sSFRs in the Fumagalli et al. (2012) complete sample, due the bias against low-SFR systems in emission-line selected samples such as in this Chapter, and that the broadband selection from Fumagalli et al. (2012) limits their sensitivity to low stellar masses systems.

[13]In the HST Grism the Hα emission line is blended with the [NII] doublet and Fumagalli et al. (2012) do not correct for the contribution from [NII]. The value of the power law evolution will remain comparable to the results of this Chapter unless there is significant evolution in the [NII]/Hα ratio.

In Section 2.3.6.1 I compared two stacks of high and low Hα EW and found that galaxies with $EW_0 > 100$Å, which may be missed by broadband selected spectroscopic surveys (e.g., Mouhcine et al., 2005), had higher [OIII]/Hβ and O32 line ratios than $EW_0 < 100$Å galaxies. This indicates that these more extreme emission line galaxies have lower metallicity and/or higher ionisation parameters than galaxies with lower EW (see Figures 2.16 & 2.17). This supports the contention that the population of galaxies captured by broadband photometric selection criteria may not represent the full variety of star forming galaxy properties, and may miss low stellar mass galaxies with high specific star formation rates.

2.4 Conclusions

In this Chapter I have followed-up galaxies identified through line emission in the near-infrared in the slitless HST/WFC3 WISPS survey, using VLT/FORS2 optical spectroscopy to confirm the redshifts and to study the reddening and metallicity of this emission line population. Half of the WISPS galaxies in our sample are fainter than $H_{AB} = 24$ mag, and would not have been included in many well known surveys based on broad-band magnitude selection. Over 4 WISPS fields, 85 out of 138 line emission objects were targeted, identified in the WFC3 slitless spectra over a redshift range $0.4 < z < 2$. I confirm 95% of the initial WFC3 grism redshifts in the 38 cases where I detect lines in the FORS2 spectra. Spectroscopic confirmation from FORS2 is important because in many cases the WFC3 detected only a single emission line, usually assumed to be Hα. For these single-line WFC3 sources, I confirmed the redshifts of 15 out of 17 galaxies (88%).

I measure the Balmer decrement (the Hα/Hβ flux ratio, after correcting for stellar absorption and for [NII] emission blended with Hα at the resolution of WFC3 grism), and find that the extinction of the WISPS galaxies is consistent with $A(\mathrm{H}\alpha) = 1$ mag with some evidence for an increase in reddening with Hα luminosity, and less reddening than seen in $z \sim 0$ samples. After correction for reddening, I find good agreement between star formation rates derived from the Hα emission line and those from the rest-frame UV continuum (L_{UV}) with a near-linear relation of $SFR(L_{UV}) = [SFR(H\alpha)]^{1.15\pm0.10}$. I obtain comparable star formation rates to those from the dust-corrected rest-UV when doing SED-fitting of the stellar population with BEAGLE on multi-band photometry including Spitzer 3.6 μm. I find that stellar masses derived

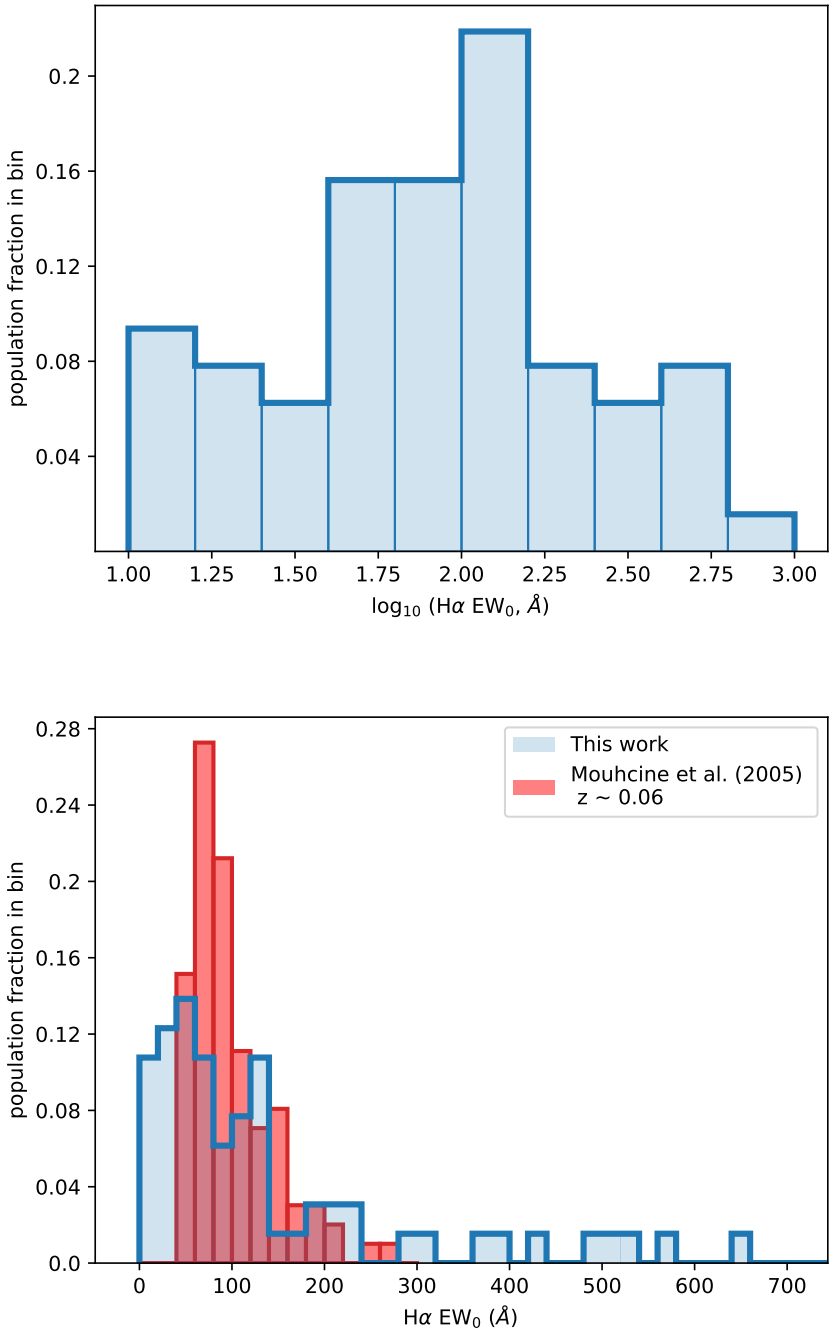

Figure 2.21: Upper panel: Hα restframe equivalent width distribution of the WISP selected galaxies with follow up FORS2 observations. Corrected for [NII] contribution and stellar absorption, two AGN candidates have been removed (see Section 2.3.5). Lower panel: I compare our EW distribution (blue histogram) with that determined from the broad-band selected survey of Mouhcine et al. (2005) in red, and note the tail of high-EW galaxies which is missed in the broad-band selection (the Mouhcine et al. 2005 sample has selected on $EW_0(H\beta) > 0$ Å , which results in the sharp decline in the red histogram at $EW_0(H\alpha) < 40$,Å).

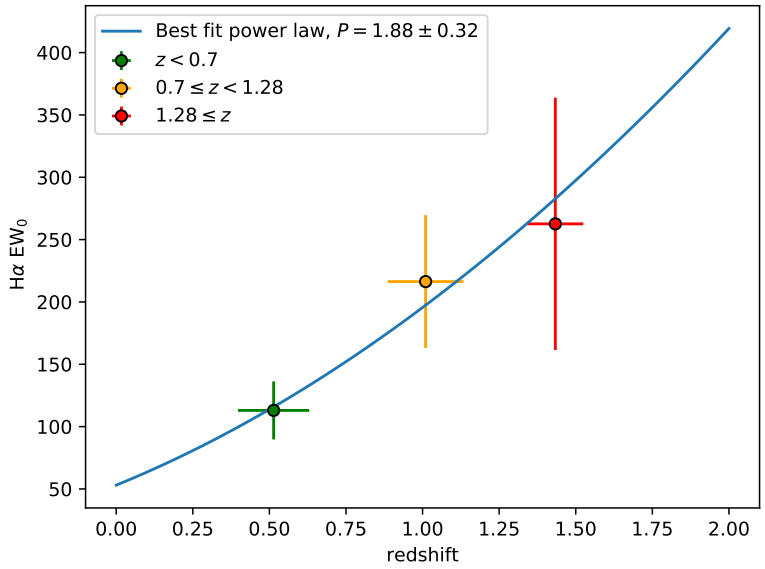

Figure 2.22: Mean Hα rest-frame equivalent width against mean redshift of the low, medium and high redshift samples. A power law trend of the form $EW \propto (1+z)^p$ is fit with a best fit power law of $p = 1.88 \pm 0.32$, consistent with the findings of Fumagalli et al. (2012) at higher masses ($\log_{10}(\mathrm{M/M_\odot})$ = 10-11.5).

from this fitting have a median mass of $\log_{10}(M/M_\odot) = 8.94$, and the emission-line-selected galaxies tend to lie above the star-forming main sequence when plotting star formation rate against stellar mass (i.e. they have higher specific star formation rates than the comparison samples at similar redshifts).

I use emission line ratios to identify two likely AGN (∼5% of the sample) from the BPT diagram (modified to use [SII] rather than [NII]) and the mass-excitation (MEx) diagnostic. For the star-forming galaxies, I use the [OIII], [OII] and Hβ lines to derive gas-phase metallicities using the strong-line O32 and R23 diagnostics and the calibrations from Curti et al. (2017). Individual galaxies detected in these lines lie within the region of the diagrams occupied by the low-z SDSS galaxies and typically have sub-solar metallicity, with a trend of metallicity decreasing with redshift. The WISPS galaxies exhibit a mass–metalicity relation, and lie below the $z = 0$ relation (i.e. the WISPS galaxies have lower metallicity) and these results are consistent with the evolution seen in other high redshift studies. I find a trend that for galaxies of the same mass, those with higher star formation rates have lower metallicity, consistent with the existence of a Fundamental Metallicity Relation between SFR, stellar mass

and metallicity.

Finally, I consider the evolution of the Hα rest-frame equivalent width of galaxies in the sample, and find a strong dependence on redshift of $EW_0(H\alpha) \propto (1+z)^{1.88\pm0.32}$. When I split our sample by Hα equivalent width at $EW_0(H\alpha) = 100\,\text{Å}$, I find that higher EW galaxies have a larger [OIII]/Hβ and O32 ratio on average, suggesting a lower metallicity or higher ionisation parameter in these extreme emission line galaxies.

Chapter 3

The [OIII]λ5007 equivalent width distribution at $z \sim 2$: The redshift evolution of the extreme emission line galaxies

3.1 Introduction

In the last few years, spectroscopic studies at z $\sim 0-2$ have shown that extreme emission line galaxies (EELGs, identified by large nebular emission line equivalent widths[1]) are more efficient ionising agents than typical star forming galaxies at these epochs. The photon production efficiency of ionising radiation increases with an increasing [OIII]λ5007 EW, reaching its largest values in the most extreme systems within the EELG population (e.g., Chevallard et al. 2018; Tang et al. 2019). Many EELGs also show evidence of large ionising photon escape fractions (e.g., Izotov et al. 2016; Fletcher et al. 2019), making them potentially good analogues of the galaxies that may have reionised the Universe at higher redshifts. Nebular gas under very high ionisation conditions has been proposed as a necessary but not sufficient criterion for large $f_{\rm esc}$ (Nakajima et al., 2020; Jaskot et al., 2019; Izotov et al., 2018). This is commonly parameterised using the O32 index (the flux ratio of [OIII]λ5007 and [OII]λ3727,3729), a quantity that will soon be measurable at z > 6 with JWST. The O32 values that appear required for large $f_{\rm esc}$ (O32>6) are uniquely found in

[1] As I will discuss later in Section 3.3.2, there is no set definition for what EW threshold (or even which emission line, e.g., Hα or [OIII]λ5007) is required for a galaxy to be termed an EELG, and in this study I will investigate EELG sub-samples of galaxies with [OIII]λ5007 EWs above 200, 500, 750 and 1000Å. Special focus will be given to EELGs above 750Å, as these have the potential for large $f_{\rm esc}$ of ionising photons in addition to having higher ionisation photon production efficiencies that typical galaxies at $z \sim 2$.

EELGs, in particular those systems with [OIII]λ5007 EW $>$ 750Å. At z $\sim$ 3, Pahl et al. (2021) measure an average $f_{\rm esc}$ for SFGs to be $\sim$ 6%. In contrast, individual EELGs with [OIII]λ5007 EW well above 1000Å have been observed to exhibit escape fractions up to an order of magnitude greater than these typical systems (Vanzella et al., 2016; Rivera-Thorsen et al., 2017; Izotov et al., 2018; Fletcher et al., 2019). These observations suggest that when galaxies are in an EELG (or burst) phase, they are likely to contribute more to the ionising background than a typical SFG at z $\simeq 2-3$. However the fraction of EELGs in the star forming population is not well constrained at these redshifts. As a result, it is not clear that these systems make a significant contribution to the z $\simeq 2-3$ ionising background.

At higher redshifts (z $>$ 5), broadband spectral energy distributions (SEDs) suggest that EELGs may be fairly ubiquitous within the SFG population. This inference comes from the presence of strong Spitzer/IRAC flux excesses in filters that are contaminated by [OIII]+Hβ emission lines. (e.g., Labbé et al., 2013). The flux excesses imply substantial equivalent widths, often placing galaxies in the EELG regime. While for some of these z $>$ 5 galaxies the flux excess may also have a contribution from a Balmer break (e.g., Eyles et al., 2005, 2007; Roberts-Borsani et al., 2020), over some redshift ranges (e.g., 6.6 $<$ z $<$ 6.9, Endsley et al. 2021; Smit et al. 2014, 2015) the flux excess can unambiguously be linked to rest-optical emission lines. This has enabled the first glimpse at the [OIII]+Hβ EW distribution in the reionization era. At z $>$ 6, typical [OIII]+Hβ rest-frame EWs are $\sim 600-700$Å (Endsley et al., 2021; De Barros et al., 2019; Labbé et al., 2013). Endsley et al. (2021) find that 20% of the SFG population at z $\sim$ 7 exhibits yet more extreme EWs with [OIII]+Hβ EW $>$ 1200Å (see also Smit et al., 2014, 2015; Roberts-Borsani et al., 2016; Castellano et al., 2017). Like EELGs at lower redshifts, these large EWs imply the presence of extreme radiation fields, which is further supported by observations of strong line emission from high-ionisation rest-UV metal lines, such as CIII] λ1909Å, CIV λ1549Å and HeII λ1640Å (Stark et al., 2017, 2015a,b; Mainali et al., 2017; Laporte et al., 2017; Schmidt et al., 2017; Mainali et al., 2018; Hutchison et al., 2019).

EELGs at high redshift may play a key role in the reionisation of the Universe. During the epoch of reionisation, the once neutral hydrogen in the inter-galactic medium (IGM) is ionised by a new source of ionising UV photons (the Lyman continuum photons, $\lambda \leq 912\mathring{A}$). The source of this Lyman continuum emission originates within galaxies in hot young stars and the super-heated accretion disks around

SMBHs, with the observed abundance of QSOs at high redshifts favouring that SFGs are the more dominant source (as discussed in Chapter 1.2.3). If, as seems likely, EELGs are very common at high redshift and have large escape fractions of ionising photons, then they may be a key population in achieving reionisation. When Lyman continuum photons are able to escape from the galaxies the photons can begin to ionise the neutral hydrogen in the IGM, with the galaxies sitting at the centre of newly created ionised bubbles. As time progresses the size of the ionised regions around galaxies expands and the bubbles from multiple sources join up to create large regions of ionised hydrogen. By the end of the EOR, the abundance of neutral hydrogen has diminished, with only small pockets remaining between the interconnected-ionised bubbles.

In this Chapter, I seek to provide a robust measurement of the [OIII]λ5007 EW distribution in SFGs at $z \simeq 2$. By selecting systems in the same manner as those at higher redshifts (i.e., UV-selected dropouts), I aim to provide a baseline measurement which allows the evolution of the EELG population (and its implied duty cycle) to be established as a function of redshift into the epoch of reionization. For this study I require a robust photometric redshift (to ensure the [OIII] line is within the Grism G141 wavelength coverage), a large enough sample to perform the Bayesian statistical analysis (to reduce the effect of small number statistics on the results and to allow the fitting of sub-sets of the sample to test for evolution – e.g., high vs low redshift) and sensitivity to both high and low EWs. However, the WISP survey, used in Chapter 2, whilst being an effective slitless spectroscopic survey is limited by only certain fields having multi-wavelength broadband photometry available for constraining the photometric redshift, and was designed to study the properties of the strongest line emitters with a selection based on their line flux, and hence the WISP survey isn't sensitive to low EW systems which typically have faint line fluxes and which are crucial for constraining the EW distribution. Instead I select galaxies in the GOODS North and South field at $z \sim 1.7 - 2.3$ using the HDUV photometric catalogues and redshifts (Oesch et al., 2018), creating a sample sensitive to a broad EW range, and I characterise the [OIII]λ5007 emission line properties using 3D-HST slitless spectra (Momcheva et al., 2016) (described in Section 3.2). I determine whether the fraction of the strongest line emitters increases with redshift by comparing these results at $z \sim 2$ with existing measurements at higher redshifts (described in Section 3.3). I discuss implications of these results for reionisation (in Section 3.4).

3.2 Sample Selection

3.2.1 A photometric sample of z $\simeq 1.7 - 2.3$ galaxies

This work is motivated by recent studies $z \sim 7$ that have revealed intense rest-optical nebular emission (e.g., median [OIII]+Hβ EW $\sim 600 - 700$Å, see Endsley et al. 2021; De Barros et al. 2019; Labbé et al. 2013). Whilst examples of such objects have been identified at lower redshifts ($z \sim 1-3$ Fumagalli et al., 2012; Atek et al., 2010; Maseda et al., 2018), the fraction of star forming galaxies with extreme line emission at these redshifts has yet to be quantified. In this Chapter I combine the HST/WFC3 G141 grism slitless spectroscopy from 3D-HST (Momcheva et al., 2016) with the Hubble Deep UV legacy survey photometry (HDUV; Oesch et al., 2018) to measure the EW distribution of [OIII]λ5007 of 672 galaxies at redshift ~ 2 ($1.700 < z < 2.274$). I describe the selection criteria that leads to this sample below.

To facilitate comparison to higher redshift [OIII]+Hβ EW distributions (e.g., De Barros et al. 2019; Endsley et al. 2021), I select a parent sample from the HDUV catalogue (Oesch et al., 2018) using their photometric redshifts which mimic a rest-UV Lyman break dropout colour selection that is similar in nature to those used at $z > 4$. The HDUV catalogue adds UV photometry in the F275W and F336W filters over ~ 100 arcmin^2 of the CANDELS GOODS North and South fields. The addition of UV photometry to existing optical and near infrared (NIR) data in these fields allows selection of z$\sim$2 galaxies using their characteristic Lyman break (Steidel et al., 1996b,a) which provides robust photometric redshifts. The two UV filters have average 5σ magnitude depths (in 0.4" diameter aperture) of 27.4(27.6) and 27.8(28.0) for F275W and F336W across GOODS North(South) (Oesch et al., 2018). These two UV filters are combined with the high quality HST ACS optical and WFC3 near-infrared photometry as well as the Spitzer/IRAC and ground-based filters. Oesch et al. (2018) use this photometry to generate photometric redshifts for the 30,561 galaxies in the HDUV catalogue using EAZY (Brammer et al., 2008). As I describe below, I construct a sample using these photometric redshifts as my initial selection, similar to that often used to identify $z > 4$ galaxies (e.g., Finkelstein et al. 2015; McLure et al. 2011). At the redshifts I am interested in for this analysis, the photometric redshifts are primarily driven by the Lyman break probed by the HDUV photometry. I note that at high redshifts the high abundance of neutral hydrogen along the line of sight creates complete suppression of the Lyman continuum below the Lyman break. Whereas, at more moderate redshifts ($z \sim 2$), the abundance of neutral hydrogen

along the line of sight is lower and potentially more patchy, creating less complete suppression (this is seen for example in the Lyman forest region of QSO spectra). The level of suppression, however, does remain sufficient to create a distinctive break at Lyα at z=2, even if the Lyα forest does not produce completely suppression, and there is still near-complete absorption below the Lyman limit (912Å), the ionisation edge of hydrogen. The Lyman break technique for selecting galaxies has been used at this redshift for many years (e.g., Oesch et al. 2010a has a colour selection for $z \sim 2$ drop-outs in the F275W/F336W-band) as the level of neutral hydrogen along the line of sight is still sufficiently prominent to secure a continuum break.

Since the goal is to characterise the strength of the [OIII]λ5007 emission in these galaxies, I must pick objects that have photometric redshifts which place the [OIII] doublet confidently within the G141 grism spectral window ($\sim$1.0755 to 1.6999 μm). This translates into a redshift range of $1.148 < z < 2.395$. However there is an additional constraint that limits the selection further. Below $z \sim 1.7$, the Lyman limit begins to shift blueward of the F275W and F336W filters, making dropout identification somewhat less reliable without bluer filters (i.e., F225W). I thus adopt $z = 1.700$ as my lower redshift bound. At the high redshift end, I need to choose objects that are confidently within the redshift range ($z < 2.395$) where I can measure [OIII] doublet with the G141 grism. Accounting for the typical photometric redshift uncertainty in this sample, I conservatively adopt an upper redshift bound of $z = 2.274$ for photometric selection, minimising the inclusion of sources with true redshifts above the $z = 2.395$ threshold. I select all galaxies in the HDUV catalogues with photometric redshifts between 1.700 and 2.274. As I will show below, sources in this redshift range have SEDs that show strong breaks associated with IGM attenuation, driving the solution of the photometric redshifts in HDUV catalogue. This redshift cut results in a sample of 4026 galaxies, with the photometric redshift distribution of the final sample shown in Figure 3.1.

I next apply a brightness cut on the rest-UV magnitudes of the photometric sample. This serves two purposes. First, it ensures consistency with higher redshift dropout samples which are traditionally selected in the rest-frame UV. Second, the magnitude threshold guarantees that this sample is well-matched to the sensitivity of the grism spectra, enabling useful constraints (or upper limits) on the [OIII]λ5007 EW. I adopt a fixed cut on M_{UV}, the absolute magnitude measured near rest-frame 1500Å. To calculate M_{UV} for this sample, I adopt the apparent magnitude in the

filter closest to rest-frame 1500Å. I use either the observed F435W (B-band) magnitude below a redshift of z = 2.2 or the observed F606W (V-band) magnitude above $z = 2.2$. To convert apparent to absolute magnitude, I use the grism-based redshift if the [OIII] doublet is detected at S/N>5 and the photometric redshift otherwise. I will show below that the grism redshifts and photometric redshifts are highly-consistent. I choose $M_{UV} = -19$ as the magnitude cut, ensuring that galaxies are detected at significantly greater than 5σ in both F435W and F606W filters. This reduces the sample to 766 galaxies. The exact choice of the M_{UV} threshold is arbitrary and does not significantly change the best fit parameters for the best fit EW distribution, as discussed further in section 3.3.4. The M_{UV} distribution for my final sample is shown in Figure 3.2.

I use the latest grism catalogue (V4.1.5) from 3D-HST (Momcheva et al., 2016; Brammer et al., 2012). This catalogue contains spectra extracted for all galaxies within the field with a near-infrared (NIR) JH_{IR} magnitude brighter than 26 (see Momcheva et al., 2016). There are 28 galaxies within the sample that do not satisfy this NIR threshold and hence do not have available spectroscopic data. To retain these targets within the sample I locate each within the grism slitless spectroscopy and inspect their 2D spectrum, determining that no emission lines were visible in any of the 28 systems. The lack of any visible emission lines is confirmed by utilising an alternative line detection procedure (with no requirements on NIR magnitude) described in Maseda et al. (2018)[2]. I will treat each as a non-detection in the following analysis. Keeping these targets within the sample ensures that the NIR magnitude never directly enters the selection, which is important owing to the influence that emission lines can have on the NIR broadband flux if equivalent widths are large.

I make two final cuts to the photometric sample. First, I remove a small number of sources with very red (B-V) colours. Such objects are generally kicked out of Lyman break selections and would not feature in higher redshift samples I wish to compare to. To remove these objects, I utilise a colour cut of $B - V < 0.8$ (using the F435W and F606W HST ACS filters). This colour threshold is very close to the Lyman break colour cut used at similar redshifts by Oesch et al. (2018). This specific colour is chosen to correspond to select sources with E(B-V) < 0.4, equivalent to UV slopes with $\beta < -1.0$ (where $f_\lambda \propto \lambda^\beta$). Here I have assumed the dust attenuation law derived from typical $z \sim 2$ galaxies (Reddy et al., 2015). This B-V threshold reveals 4 very

[2]This specific check was carried out by Dr. M. Maseda

red sources which I remove from the sample. I note that adopting a slightly different colour cut does not significantly alter the results. I also wish to remove sources that may host active galactic nuclei (AGNs), as my goal is to establish the [OIII]λ5007 EW distribution in star forming galaxies. I cross-match the sample against deep *Chandra* X-ray imaging across GOODS-North (Alexander et al., 2003; Xue et al., 2016) and GOODS-South (Xue et al., 2011), identifying sources that match the coordinates of my sample using a 1.0" search radius. There are 30 targets within the sample that show X-ray counterparts and are removed. Together these two cuts reduce the sample to 732 galaxies.

The goal is to establish the [OIII]λ5007 EW distribution in this photometric sample. To do so, I first need to ensure that I have removed any galaxies with grism artefacts from the sample, and second I need to quantify the scatter between the photometric and grism redshifts. I visually examine the grism spectra of the remaining sample to characterise data quality. I identify spectra that have artificial features created by edge effects where the dispersed light of the galaxy falls partially outside the illuminated region of the detector. These artificial features may be mistaken for emission lines, while regions of un-illuminated spectra may contain genuine features that would be missed. The 3D-HST catalogue provides a flag `'f_cover'` describing the fraction of dispersed light that falls within the illuminated region of the detector. I find that removing all sources where the `f_cover` parameter is below 0.65 effectively eliminates these incidences in the sample. This removes 51 targets.

I also identify targets that display a negative spectrum on average, where poor contamination subtraction of the contributed light from overlapping spectra has compromised the individual extractions. The 3D-HST catalogue flag `'f_negative'` describes the fraction of the spectrum that has a negative flux and I determine that a cut on the `f_negative` parameter at 0.7 effectively removes these compromised spectra from the sample, eliminating a further 4 galaxies. I additionally review and remove 1 further system (3D-HST ID: S24717) identified to have incorrectly-associated grism emission lines, due to the dispersed light of other galaxies lying coincident with that of the target. I deem the target spectrum to be irretrievable behind the dominant contamination of the neighbour and remove it from the sample. I also individually review all targets with SExtractor `'class_star'` value greater than 0.5. This inspection results in 3 targets being removed (S20271, S23225, S29694) after being identified as either stars or for having their photometry or slitless spectroscopy compromised

by lying in the wings of stellar diffraction spikes. I also remove one object (S24312) as it is associated with one component of a larger galaxy that is already in the sample (S24365). These cuts leave 672 galaxies.

3.2.2 Photometric redshifts and contaminants

Now that I have a cleaned sample of grism spectra, I can quantify the reliability of the photometric redshifts used to select the parent sample and assess the contamination level among those objects without spectroscopic redshifts. To do so, I take two different approaches. First I identify objects with robust grism redshifts in the photometric sample. I define these as those with confident emission line detections ([OIII] doublet detected at a greater than 5σ significance) following work in Tang et al. (2021b). There are 293 galaxies that satisfy this emission line cut in the photometric sample. In this sub-sample, I see that the photometric redshifts do a very good job of reproducing the grism redshifts. To quantify this, I define the typical scatter between photometric and grism redshift using the the normalised median absolute deviation, defined as $\sigma_{\rm NMAD} = 1.48 \times {\rm median}(|\Delta {\rm z} - {\rm median}(\Delta {\rm z})| / (1 + {\rm z_{spec}}))$, where $\Delta z = z_{\rm spec} - z_{\rm phot}$(e.g., Brammer et al., 2008). I find a normalised median absolute deviation of $\sigma_{\rm NMAD} = 0.037$ for the sub-sample with robust grism redshifts, suggesting good agreement between photometric and grism redshifts. I will assume this dispersion is characteristic of the photometric redshifts in the sample, including those systems lacking grism redshifts. This latter subset primarily includes objects with lower equivalent width emission lines. The HDUV photometric redshift 68% confidence intervals of these sources (median $\Delta {\rm z} = 0.063$) are comparable to those objects in the sample with grism redshifts (median $\Delta {\rm z} = 0.053$), likely reflecting their similar continuum magnitudes which in turn enable robust characterisation of the Lyman break (which again is what primarily drives the photometric redshift solution). The average strength of the Lyman break is consistent between the robust grism redshift sub-sample and the sub-sample without significant line detections, both exhibiting a strong F275W-F435W mean break colour of 2.4 mag. Hence in spite of their lower emission line equivalent widths, we expect the photometric redshifts of these sources to be similar in their reliability as those with grism redshifts.

The typical dispersion between photometric and grism redshifts allows the fraction of the sample that is likely to be in-scattered from redshifts where the G141 grism is not able to constrain [OIII] emission ($z < 1.148$ or $z > 2.395$) to be calculated.

Given the value of $\sigma_{\rm NMAD}$, I can perturb the measured photometric redshifts of the sample to quantify this contamination rate. While the in-scatter rate from sources with $z < 1.148$ is expected to be negligible (owing to the significant buffer provided by my $z > 1.700$ selection), the dispersion between grism and photometric redshifts suggests that 3.4% of the photometric sample will have true redshifts of $z > 2.395$. These sources will appear as non-detections in the photometric sample even though they could have strong nebular line emission. This is easily accounted for in the derived EW distribution, as I will discuss in Section 3.3.

In addition to the typical scatter described above, I expect a small number of catastrophic outliers, where the derived photometric redshift is substantially offset from the true redshift of the object. Such objects are generally not included in the dispersion implied by a Gaussian distribution with $\sigma = \sigma_{\rm NMAD}$, so they must be considered separately. Contaminants can be identified in the G141 grism via detection of strong rest-optical lines (Hα, [OII], or [OIII]) at redshifts well outside of this works selected range (1.700< z <2.274) or through the extensive ground-based spectroscopy that has been conducted in the GOODS fields. I first consider the latter and focus on the GOODS South field where many public redshift surveys have been conducted (e.g., Le Fèvre et al. 2005; Vanzella et al. 2008; Balestra et al. 2010; Kurk et al. 2013). I cross-match these surveys with the sub-set of 318 GOODS-South galaxies studied here, finding 75 unique matches. The spectra in these catalogues find only one catastrophic outlier with a confident redshift identification (3D-HST ID: 19233, matched to Balestra et al. 2010 ID: J033227.25-274919.2 with $z_{\rm spec} = 0.5568$), indicating a catastrophic outlier fraction of 1.3% in the ground-based spectra and suggesting a fraction of at least 0.3% in the total GOODS-South sub-sample. The WFC3/IR grism spectra provide an independent check. The G141 grism is able to detect Hα down to z = 0.6, providing a window on low-z interlopers in the sample. Here I define a catastrophic outlier as a source with a redshift that is further than $5\sigma_{\rm NMAD}$ from the lower redshift bound of the photometric redshift selection, corresponding to z = 1.2. I identify 10 sources with Hα detections, but none fall below z = 1.4. These redshifts are consistent with the Gaussian distribution implied by the calculation of $\sigma_{\rm NMAD}$, hence the grism sample is also suggestive of a low catastrophic outlier rate. In the following section, I will conservatively assume a catastrophic outlier rate of 1.3% within the sample. I will add this catastrophic contamination fraction to that derived for more typical source-to-source redshift scatter. The total contamination

fraction (3.4%+1.3%=4.7%) will be modelled when deriving the EW distribution.

To summarise, I am left with a final sample of 672 galaxies, with 354 in GOODS North and 318 in GOODS South. The total photometric sample includes 293 systems with $\geq 5\sigma$ detections of the [OIII] doublet. The photometric redshift distribution is presented in Figure 3.1 with an average value of $z = 2.1 \pm 0.2$. The absolute M_{UV} magnitude distribution is shown in Figure 3.2 and spans $-21.6 < M_{UV} < -19.0$, with 75.6% of targets fainter than $M_{UV} = -20.0$. These values are well-matched to those of z $\simeq$ 7 galaxies that have been used to infer [OIII]+Hβ EWs via *Spitzer*/IRAC excesses (De Barros et al., 2019; Endsley et al., 2021).

While this selection is initially based on the photometric redshift and not on a colour cut as is used by Endsley et al. (2021), the selection still uses the Lyman break as the main feature to determine the photometric redshifts. This choice may allow galaxies that might not enter a purely colour-criteria selection to enter the sample, for example, galaxies that are very red (dusty or quenched). However, since I apply $B - V$ colour criteria to remove red objects that sit apart from the SFG region of colour space, this sample mimics the same selection as Endsley et al. (2021). So, whilst the difference in method does initially create selections that are not identical (in terms of the types of galaxies that can enter), effort is made to mimic the selection function of high redshift surveys and will allow the results drawn from this work to be compared to higher redshift studies. I note that the overall SFG population at $z \sim 2$, and that are represented in this sample, are probably not analogues of high redshift SFGs, but the high EW objects within the $z \sim 2$ population with elevated ionisation conditions are likely to have ISM conditions similar to galaxies at high redshift, and this sub-set may be good analogues of the high redshift population. It will be these EELGs that will be the focus in this study.

3.3 [OIII]λ5007 Equivalent Width Distribution at z$\sim$ 2

In this section, I compute the [OIII]λ5007 EW distribution at $z \sim 2$ from the selected sample. I first discuss measurements of individual EWs in Section 3.3.1 and then describe how I characterise the functional form of the EW distribution in Section 3.3.2. From this distribution I measure the fraction of galaxies caught in an extreme EW phase (the EELG fraction), corresponding to very large sSFRs expected when

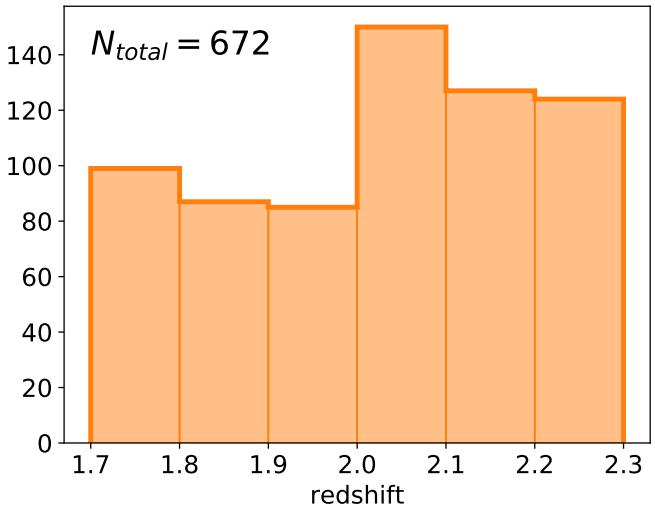

Figure 3.1: Redshift distribution of the 672 dropout galaxies in the combined GOODS North and South UV selected sample. The photometric redshifts presented here are taken from the HDUV survey (Oesch et al., 2018) and restricted to $1.700 < z < 2.274$ to ensure that the [OIII]λ5007 emission line, which will constrain the EW distribution, is visible within the HST WFC3 G141 grism spectrum.

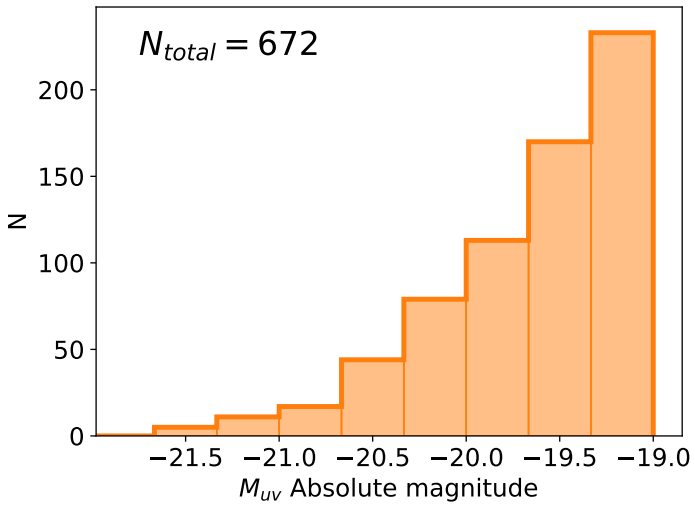

Figure 3.2: Absolute magnitude $M_{\rm UV}$ distribution of the $z \sim 2$ sample of 672 galaxies. The individual $M_{\rm UV}$ magnitudes are measured using the observed B-band magnitude below $z = 2.2$ and V-band magnitude above $z = 2.2$. The absolute magnitude is restricted to $M_{\rm UV} < -19.0$ to ensure a sufficiently bright sample to observe a full range of [OIII]λ5007 EWs.

galaxies experience bursts of star formation. I characterise the redshift and luminosity dependence of the EELG fraction in Section 3.3.3 and Section 3.3.4 respectively.

3.3.1 Individual equivalent width measurements

The first step in deriving the [OIII]λ5007 EW distribution is to robustly measure the individual EWs for each of the 672 galaxies in the final sample. As described in Section 3.2, I create a sub-sample of galaxies with significant [OIII] doublet detections ($\geq 5\sigma$) and determine their [OIII]λ5007 EW. For the remaining sample I derive upper limits on the EW. I describe this procedure below.

This approach is similar to that taken in Tang et al. (2019). For galaxies with a $\geq 5\sigma$ [OIII] doublet detection in the grism spectra of Momcheva et al. (2016), I use their measured line flux as part of determining the EW. I note that the [OIII]λ4959, 5007Å doublet is unresolved at the spectral resolution of the G141 grism and the total [OIII] doublet flux is reported in Momcheva et al. (2016). I correct the total line flux of the doublet to the expected line flux of [OIII]λ5007 alone, assuming the theoretical line flux ratio of 2.98 between [OIII]λ5007Å and [OIII]λ4959Å (Storey & Zeippen, 2000). For the estimate of the stellar continuum at the observed wavelength, I derive the continuum flux density from the broadband photometry rather than using the spectral continuum measured from the grism spectra by Momcheva et al. (2016). In many objects in the sample, the continuum is often very low S/N. This approach provides a uniform method for the entire sample, and as I show later in this section the two approaches give consistent EW measurements. To compute the photometric broadband flux density in the filter covering the [OIII] doublet, I re-measure the broadband photometry using IRAF.phot with apertures matched to the size of the grism spectral extraction aperture to ensure consistency in the EW measurement. The F125W broadband filter is used to determine the continuum for galaxies below z=1.8, the F140W filter is used in the range z=1.8-2 and the F160W filter is used above z=2 (or above z=1.8 when F140W is unavailable). In determining the continuum flux density from the broadband photometry, I correct the flux within the filter for the contribution of emission lines. I consider the contribution from all lines detected in the grism spectra, weighted by the filter transmission profile at the respective location of each line. For the majority of sources in the sample, this is a very small correction that does not significantly impact the EW inference. I verify that systems with grism non-detections have minimal emission line contribution to the broadband flux (<5%). I find that three sources in the sample are sufficiently

line-dominated that the the derived continuum flux density (after line subtraction) is unreliably beneath the flux density corresponding to 5σ in that filter. In these cases (S19339, S30532, N16381), I utilise the average of neighbouring broadband filters without line contamination to measure the continuum flux density.

In order to compute the [OIII]λ5007 EW, I must make a small correction to convert the continuum flux density at the effective wavelength of the chosen filter (i.e., F125W, F140W, F160W) to that at the rest-wavelength of [OIII]λ5007. Given the small wavelength baseline involved, I assume that the stellar continuum is flat in f_ν, as is appropriate for unreddened stellar populations at the range of ages spanned by the sample. But this correction changes by less than 1% if I consider galaxies with more reddening (i.e., selective extinction of E(B-V)=0.2 with a Calzetti reddening curve). The [OIII]λ5007 EW is then taken as the ratio of the line flux to the continuum flux density and corrected to the rest-frame using the grism-measured spectroscopic redshift ($\mathrm{EW_{rest}} = \mathrm{EW_{obs}}/(1+z)$).

I note that taking this broadband approach may lead to an overestimate in the continuum flux density if there is significant contribution from close proximity neighbours to the measured photometry. I inspect by eye all galaxies with on sky neighbours where the Skelton et al. (2014) half-light radii of the target and neighbour overlap. Two targets of concern are identified ($<$ 1% of the sample), and I employ Galfit (Peng et al., 2002) to model and subtract the contribution from the neighbour and re-compute the EW accordingly.

For systems lacking [OIII] doublet detections with S/N$\geq$5, I derive upper limits on the [OIII]λ5007 EW. For each non-detection, I adopt the 5σ grism flux upper limit using the line sensitivity equation, described in Momcheva et al. (2016). This is an empirical parameterisation of the flux uncertainties determined through 2D model fitting of the grism spectra, acting as a function of the filter transmission throughput at the observed wavelength and the aperture size required to span the spatial extent of the galaxy (for each object I adopt the broadband flux radius from Skelton et al. 2014). The EW upper limits are then produced by combining the line flux upper limit with the broadband continuum (derived as discussed above) and corrected to the rest-frame using the HDUV photometric redshifts.

Within the photometric sample, the sources with [OIII] doublet detections in the grism spectra have rest-frame [OIII]λ5007 EWs ranging between 40 and 1800Å with a median of 214Å. For sources that are sufficiently bright in the continuum ($JH_{\rm IR} < 23$ mag) the sample is sensitive to low EWs (< 50Å), providing a broad [OIII]λ5007 EW range. The bulk of the [OIII] doublet non-detections are fainter sources where the grism spectra are not sufficiently deep to reach low [OIII]λ5007 EWs. I find a median 5σ [OIII]λ5007 EW upper limit of 93Å. The dynamic range of the sample's NIR magnitudes means the distribution of EW measurements and upper limits overlap. A histogram of the resultant [OIII]λ5007 EWs is shown in Figure 3.4. The detected sources (blue) are assigned to their appropriate EW bin while the contribution to the histogram from each EW upper limit source (orange) is spread over the EW parameter space below the 5σ upper limit, following the best fit log-normal distribution (discussed in Section 3.3.2). The sum of the probability across all bins below the 5σ upper limit equals 1 for an individual galaxy.

In Figure 3.3, I present the distribution of [OIII]λ5007 EWs for the sample against the observed H-band magnitude and the inferred $M_{\rm uv}$ magnitude. As expected, the fainter systems with weaker continuum flux densities exhibit the largest EWs. Due to the line sensitivity of the grism there is a minimum [OIII] doublet flux that achieves the required 5σ detection for EW measurement, and towards weaker continuum flux densities (fainter magnitudes) the EW detections are not sensitive to the lowest EWs. This can be seen clearly in the blue EW data points in the top panel of Figure 3.3, especially fainter than 24.5 magnitude. However, the sample also includes non-detections which place upper limits on the EW (again, based on the line sensitivity of the grism). Towards lower magnitudes our sample is increasingly incomplete in detections at low EW, but any potential bias driven by this are alleviated by the EW upper limits which constrain the population and are included as part of the Bayesian analysis in Section 3.3.2

3.3.2 Equivalent width distribution

As outlined in the introduction, the primary goal is to derive the [OIII]λ5007 EW distribution. In doing so I seek to quantify what proportion of the $z \sim 2$ population is in an extreme EW phase, as is believed to be common $z > 7$. Equipped with robust measurements and upper limits for the EW for the described sample I can now characterise the distribution of EWs. I will model the sample, inclusive of non-detections, with a log-normal EW distribution. This functional form has been shown to be a

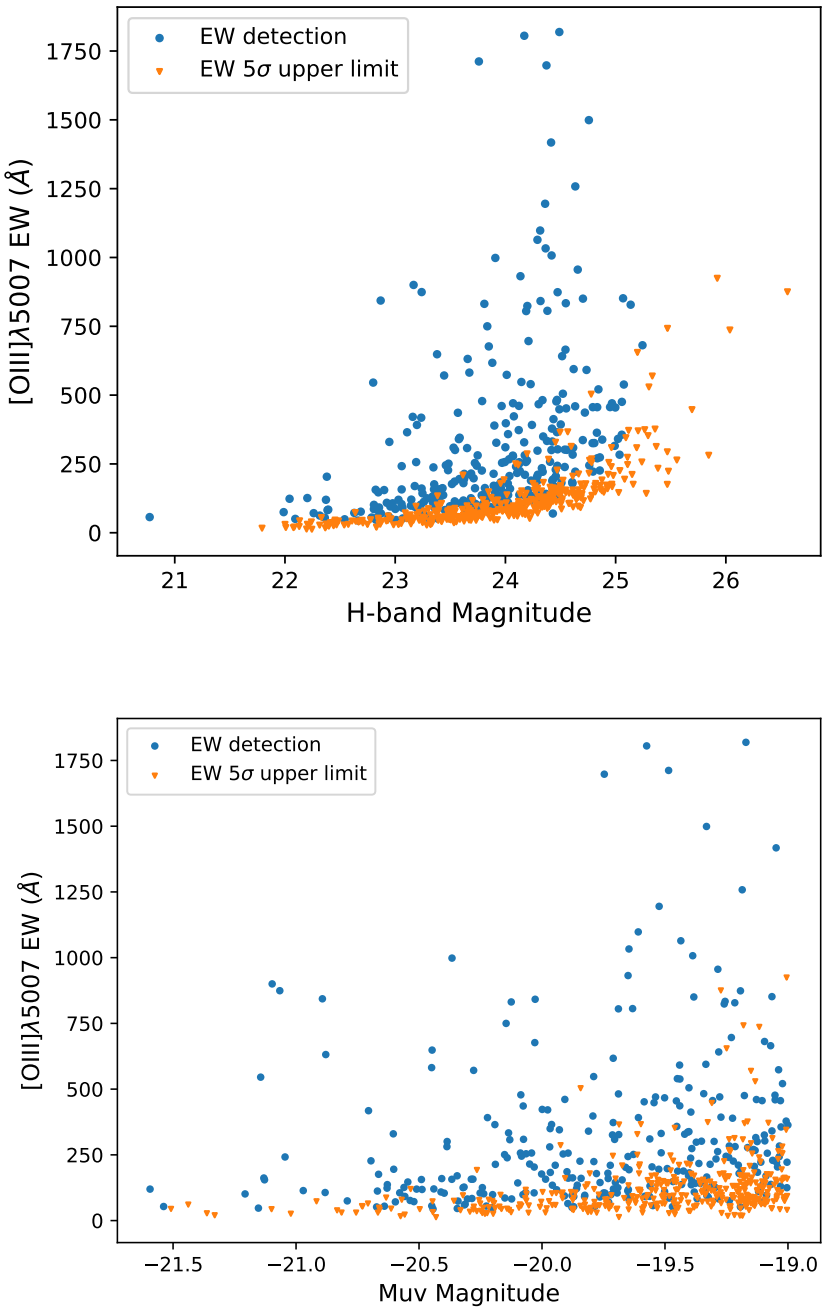

Figure 3.3: The [OIII]λ5007 EW (blue) or 5σ upper limit on the EW (orange) for the sample against the H-band magnitude (Top panel) and the $M_{\rm uv}$ magnitude (Bottom panel). Due to the signal-to-noise requirement I place on the [OIII] doublet line flux to ensure a detection, at faint H-band magnitudes the EW detections become incomplete at low EW. However, the EW upper limits place constraints on the EW distribution, removing the potential for bias. The $M_{\rm uv} < -19$ selection ensures that even at faint $M_{\rm uv}$ magnitudes the detections still reach low EWs.

good fit to other EW samples (see Lee et al., 2007, 2012; Ly et al., 2011; Schenker et al., 2014; Stark et al., 2013; Endsley et al., 2021).

To infer the underlying [OIII]λ5007 EW distribution from the observed sample I follow the Bayesian method set out by Schenker et al. (2014) which preserves information on each galaxy's EW measurement uncertainty, while removing the need to bin the equivalent width measurements. The EW distribution is modelled as a log-normal function $\theta = [\mu_{\rm LN}, \sigma_{\rm LN}]$[3]. I follow Schenker et al. (2014) and place a flat prior $P(\theta)$ over both the log-normal location $\mu_{\rm LN}$ and variance $\sigma_{\rm LN}$ parameters allowing the posterior to be determined directly as the model likelihood from the observed sample.

For a set of model parameters $[\mu_{\rm model}, \sigma_{\rm model}]$ the model log-normal probability distribution is given by

$$P(EW|\theta)_{\rm model} = \left(2\pi\,\sigma^2_{\rm model}\,EW^2\right)^{-\frac{1}{2}} e^{-\frac{(ln(EW)-\mu_{\rm model})^2}{2\sigma^2_{\rm model}}} \tag{3.1}$$

and the Gaussian measurement uncertainty on the measured equivalent width is given by

$$P(EW)_{\rm obs_i} = \left(2\pi\,\sigma^2_{\rm obs_i}\right)^{-\frac{1}{2}} e^{-\frac{(EW-\mu_{\rm obs_i})^2}{2\sigma^2_{\rm obs_i}}}. \tag{3.2}$$

Where $\mu_{\rm obs_i}$ and $\sigma_{\rm obs_i}$ are the determined EW and observational uncertainty for the i$^{\rm th}$ system. The likelihood over the complete dataset is taken as the product of the individual likelihoods of each galaxy within the sample. The individual likelihood for each detected source (i) is defined as

$$P(obs_{\rm i}|\theta)_{\rm detect} = \int_0^\infty P(EW)_{\rm obs_i} \cdot P(EW|\theta)_{\rm model}\; d\,EW. \tag{3.3}$$

The combination of the true EW distribution model with the Gaussian profile describing the EW measurement within the likelihood integral addresses observational noise to avoid overestimating the number of EELGs, where noise would preferentially scatter sources from the bulk of the distribution (with low EWs) towards extreme EW and broaden the observed EW distribution (up-scatter).

[3]Equivalently this is the same as setting a normal distribution in logarithmic space with parameters $\theta = [\mu_{\rm N}, \sigma_{\rm N}]$. Both forms have been used in the literature and the relation between the normal distribution parameters and the log-normal parameters is given by; $\sigma_{\rm N} = \sigma_{\rm LN} \times log_{10}(e)$ and $\mu_{\rm N} = (\mu_{\rm LN} - \sigma^2_{\rm LN}) \times log_{10}(e)$ and I will provide the best fit results from the analysis in both formats.

Table 3.1: Best fit model parameters for the rest-frame EW(Å). I show the results for the log-normal distribution (LN) and normal distribution in logarithmic space (N).

Number	$\mu_{\rm LN}$	$\sigma_{\rm LN}$	$\mu_{\rm N}$	$\sigma_{\rm N}$
672	4.24 ± 0.07	1.33 ± 0.06	1.08 ± 0.10	0.58 ± 0.03

For sources which are undetected, the individual likelihood is defined by

$$P(obs_{\rm i}|\theta)_{\rm non\_detect} = P(EW < EW_{5\sigma_{\rm i}}|\theta) + P(EW > EW_{5\sigma_{\rm i}}|\theta) \cdot C_{1,{\rm i}} + C_2 \qquad (3.4)$$

where $C_{1,{\rm i}}$ is the proportion of the i$^{\rm th}$ spectra that is unilluminated due to its location on the detector. C_2 is the photometric redshift in-scatter fraction, evalutated in Section 3.2.2 to be 4.7%. The probability is determined as the sum of: the likelihood that the galaxy has a EW below the 5σ limit; the likelihood that the galaxy has an EW above this threshold multiplied by $C_{1,{\rm i}}$; and C_2. Due to the inclusion of the in-scatter term (C_2), the probability $P(obs_{\rm i}|\theta)_{\rm non\_detect}$ may exceed 1 and so to avoid this a maximum value is enforced set equal to 1.

A Markov Chain Monte Carlo (MCMC) approach is taken to efficiently cover the parameter space using `emcee` (Foreman-Mackey et al., 2013). The marginalised posterior distributions over the log-normal parameters are used to determine the best fit model, which are presented in Table 3.1. I over-plot the best fit model for the sample on the EW distribution in Figure 3.4 with the 2σ model uncertainties indicated by the grey shaded region.

From the best fit results in Table 3.1 I report a mean (with standard error on the mean) and median EW of 168 ± 1Å and 70 ± 5Å, with the EELG population skewing the mean EW higher than the median. This mean is within the expected [OIII]λ5007 EW range (80-250Å) for $\log_{10}(\frac{M}{M_\odot}) = 9 - 10$ stellar mass galaxies based on the $z \sim 2$ MOSDEF empirical relation by Reddy et al. (2018). The median is significantly lower than the ~ 450Å median [OIII]λ5007 EW inferred for $z > 7$ samples (Endsley et al., 2021; De Barros et al., 2019; Labbé et al., 2013) (when converted from [OIII]+Hβ to [OIII]λ5007 EW assuming the assumptions detailed in Section 3.3.3). I note that the median [OIII]λ5007 EW in the sub-sample where the [OIII] doublet is detected ($\geq 5\sigma$) was 214Å (see Section 3.3.1), whereas taking the whole sample and treating upper limits as described I measure a lower median [OIII]λ5007 EW of 70Å. This should be expected since intrinsically low EW sources would be more likely to have

[OIII] doublet non-detections.

Through fitting a functional form, the proportion of SFGs with an EW above a given threshold can be easily calculated and I shall call this the EELG fraction. For each set of model parameters θ of the MCMC run the EELG fraction is recorded and the resultant posterior density function (PDF) over all models is then used to estimate the best fit overall EELG fraction and uncertainty for the population (see Figure 3.5, discussed below).

Within the literature there is no set definition for the threshold [OIII]λ5007 EW a galaxy must have to be classified as an EELG and the quoted threshold varies from author to author. Commonly taken threshold values range from [OIII]λ5007 EW $\sim 100 - 1000$Å. At low redshift, Amorín et al. (2015) employ a ≥ 100Å threshold to construct an EELG sub-set from a $0.11 < z < 0.93$ SFG sample, and in the distribution this EW threshold results in an EELG fraction of 39^{+2}_{-3}% at $z \sim 2$. At intermediate redshifts considerable attention has been focused on photometric selection of EELGs, for example, van der Wel et al. (2011) who identify $z \sim 1.7$ galaxies through HST J-band (F125W) flux excess. These selected EELGs at $z \sim 1.7$ tend to have [OIII]λ5007 EWs above 500Å, which is comparable to the typical [OIII]λ5007 EW found at $z > 7$. Adopting a threshold of 500Å yields an EELG fraction of $6.8^{+1.0}_{-0.9}$% in my EW distribution at $z \sim 2$.

More recently, spectroscopic work at $z \sim 2$ exploring the stellar population and gas properties as a function of [OIII]λ5007 EW (e.g. Tang et al., 2019, 2021a) has focused on the most extreme line emitters, those with [OIII]λ5007 EWs above 750 or 1000Å. These are the galaxies at $z \sim 2$ found to have the highest $\xi_{\rm ion}$, O32 values, and the potential for large ionising escape fractions. In my $z \sim 2$ distribution these are rare, accounting for only $3.6^{+0.7}_{-0.6}$% above a threshold of 750Å and $2.2^{+0.5}_{-0.4}$% above a threshold of 1000Å.

In Figure 3.5 I present the EELG fraction posterior density function (PDF) for four [OIII]λ5007 EW thresholds. These correspond to the rough mean [OIII]λ5007 EW of SFGs at $z \sim 2$ (200Å), the typically EW of SFGs at $z > 7$ (500Å) and the EW seen in the most extreme line emitters at $z \sim 2$ (750 and 1000Å). The 200Å threshold accounts for roughly a fifth of SFGs at $z \sim 2$ with the higher EW thresholds recovering diminishing fractions. The 500Å threshold highlights that the

Sample	EW$\geq$ 200Å	EW$\geq$ 500Å	EW$\geq$ 750Å	EW$\geq$ 1000Å
full sample	$21.2^{+1.7}_{-1.6}$	$6.8^{+1.0}_{-0.9}$	$3.6^{+0.7}_{-0.6}$	$2.2^{+0.5}_{-0.4}$
$1.70 < z < 2.01$	$19.7^{+2.1}_{-2.1}$	$5.4^{+1.2}_{-1.1}$	$2.6^{+0.8}_{-0.9}$	$1.5^{+0.6}_{-0.4}$
$2.01 < z < 2.274$	$22.8^{+2.6}_{-2.3}$	$8.2^{+1.6}_{-1.5}$	$4.7^{+1.2}_{-1.1}$	$3.0^{+0.9}_{-0.8}$
$-19.5 < M_{\rm UV} < -19$	$20.1^{+2.4}_{-2.1}$	$6.7^{+1.4}_{-1.3}$	$3.6^{+1.0}_{-0.9}$	$2.3^{+0.8}_{-0.7}$
$-21.6 < M_{\rm UV} < -19.5$	$22.3^{+2.4}_{-2.3}$	$7.1^{1.5}_{-1.3}$	$3.7^{+1.0}_{-0.8}$	$2.2^{+0.7}_{-0.6}$

Table 3.2: The fraction of star forming galaxies in an extreme emission line phase (the EELG fraction) with [OIII]λ5007 EW above four rest-frame EW thresholds. The EELG fractions are presented as a percentage (%) for the full $z \sim 2$ UV-selected sample, the sample split into two redshift bins and the sample split into two bins of UV luminosity.

SFGs common at $z > 7$ are rare at $z \sim 2$, with the most extreme candidates effectively absent from the $z \sim 2$ population. I present the measured EELG fractions for each [OIII]λ5007 EW threshold in Table 3.2.

3.3.3 Redshift evolution of the EELG fraction

The [OIII]λ5007 EW distribution produced in the previous section provides a baseline to probe the redshift evolution of EELGs from $z \sim 2$ out into the EOR. The best fit distribution for $z \sim 2$ SFGs produces a mean and a median EW of 168Å and 70Å whereas recent work at $z > 7$ show a median EW of $\sim$ 450Å (Labbé et al., 2013; De Barros et al., 2019; Endsley et al., 2021), suggesting significant evolution in the typical EW in the two billion years between these two epochs. This trend likely reflects evolution in the sSFR and metallicity (a topic I will come back to in Section 3.4). In what follows, I seek to use my EW distribution to quantify the redshift evolution in the fraction of extreme emission line galaxies, using the various EW thresholds as discussed in the Section 3.3.2.

I will compare the $z \sim 2$ measurements to studies of galaxies at higher redshift which also select on rest-frame UV luminosity. I consider three higher redshift studies which characterise rest-optical EW distributions: Stark et al. (2013) at $z \sim 4-5$; Rasappu et al. (2016) at $z \sim 5$; Endsley et al. (2021) at $z \sim 7$. These three studies are all based on Spizter/IRAC colours of Lyman break galaxies, where the flux excess between two adjacent filters is attributed to the presence of strong nebular lines

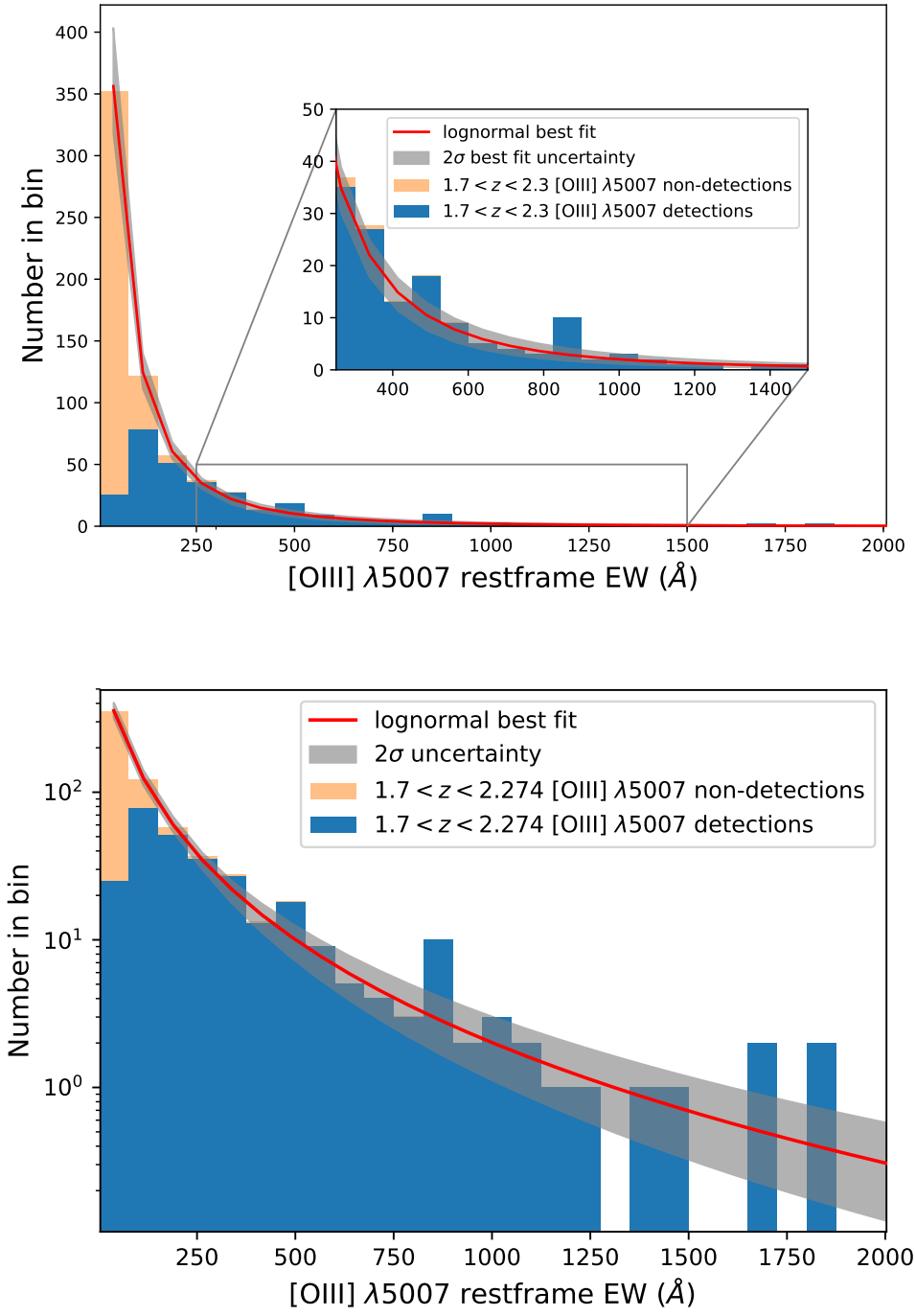

Figure 3.4: The EW distribution of [OIII]λ5007 for star forming galaxies at $1.700 < z < 2.274$. The best fit log-normal model (red line) and 2σ uncertainties (grey) along with the EW histogram in 75Å bins for the $M_{\rm UV}$ selected sample constructed from 5σ [OIII] doublet detections (blue) and 5σ upper limits (orange), where the histogram contribution from each [OIII] doublet non-detection is assigned following the best fit model below the associated 5σ [OIII]λ5007 EW upper limit. Top: linear y-axis with cut-out to show high EW region. Bottom: logarithmic y-axis

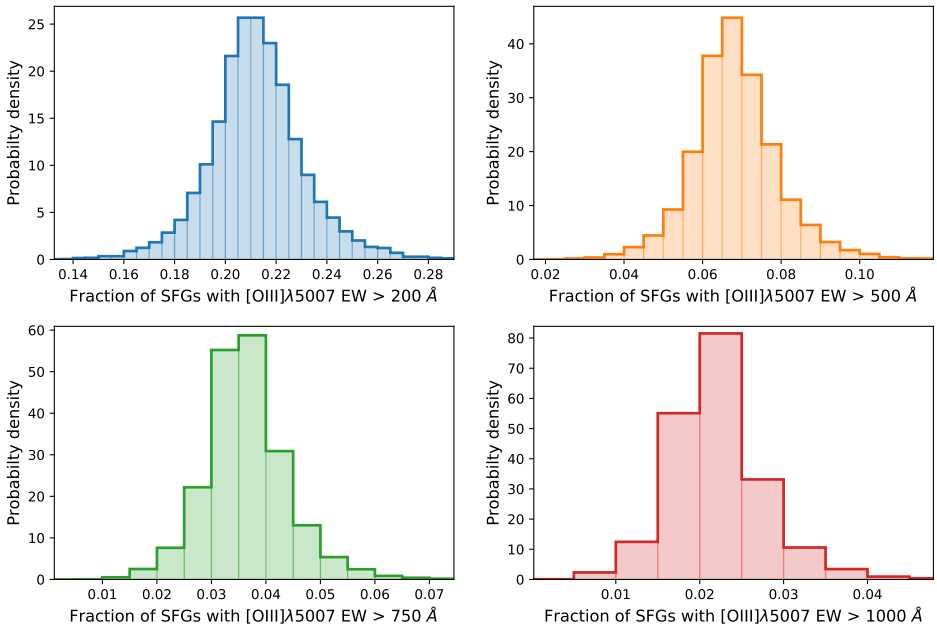

Figure 3.5: The MCMC posterior density function for the fraction of star forming galaxies at $z \sim 2$ with extremely large [OIII]λ5007 EW. The MCMC posterior distributions for the fraction of SFGs above four different [OIII]λ5007 EW thresholds are shown in blue (200Å, top left panel), orange (500Å, top right panel), green (750Å, bottom left panel) and red (1000Å, bottom right panel).

(either [OIII]λ4959, 5007+Hβ or Hα depending on the redshift and filter) allowing the rest-optical nebular EWs to be measured for samples of SFGs. My primary comparison will be to Endsley et al. (2021) who model the [OIII]λ5007, 4959 + Hβ EW distribution from 22 Lyman break dropouts at $6.63 < z < 6.83$.

To compare against EELG fractions from Endsley et al. (2021), I scale the [OIII]λ5007 EW thresholds into appropriate [OIII]λ5007, 4959 + Hβ thresholds. As described previously, I obtain the [OIII]λ5007, 4959 threshold through a 2.98:1 flux ratio between [OIII]λ5007 and [OIII]λ4959 (Storey & Zeippen, 2000). For Hβ, I infer the EW contribution using an Hβ:[OIII]λ5007 EW empirical relation

$$\log_{10}(\mathrm{H}\beta\,\mathrm{EW}) = 1.065 \times \log_{10}([\mathrm{OIII}]\lambda5007\,\mathrm{EW}) - 0.938 \tag{3.5}$$

obtained from the Tang et al. (2019) results for a comparable sample of $1.3 < z < 2.4$ EELGs covering a sufficiently broad [OIII]λ5007 EW range ($\sim 100 - 2500$Å). Here the 500, 750 and 1000Å [OIII]λ5007 EW thresholds are equivalent to 754, 1135 and 1516Å [OIII]+Hβ EW thresholds.

In Figure 3.6, I present the $z \sim 2$ [OIII]λ5007 EW distribution (as in Figure 3.4) alongside the Endsley et al. (2021) $z \sim 7$ [OIII]+Hβ EW distribution for comparison (with the latter scaled to the [OIII]λ5007 EW). It is clear that whole SFG population at the higher redshift $z \sim 7$ exhibits larger EWs than the typical $z = 2$ SFG in my work. Since the two EW distributions are determined from samples of SFGs that have similar selection criteria (LBGs selected through a colour cut at $z \sim 7$ or using photometric redshifts at $z \sim 2$ with the addition of a $B - V$ colour cut to mimic the removal of red dusty galaxies, see details in Section 3.2) the difference in the galaxy population at these two epochs can be seen clearly with an obvious evolution in the EW distribution. While subtle selection differences may influence the two distributions, such as photometric redshifts potentially selecting galaxies with relatively weak Lyman breaks, the clear offset between the two cannot be put down to a selection-based bias alone and evolution in the galaxy population is required.

The comparison sample also includes two Hα EW studies: Stark et al. (2013) at $3.8 < z < 5$; and Rasappu et al. (2016) at $5.1 < z < 5.4$. In order to convert the [OIII]λ5007 EW thresholds into that appropriate for the Hα studies, I apply a conversion factor from the linear relation found by Tang et al. (2019) between Hα and [OIII]λ5007 EW in EELGs. A scaling factor EW(Hα/[OIII]λ5007) = 1.0 for

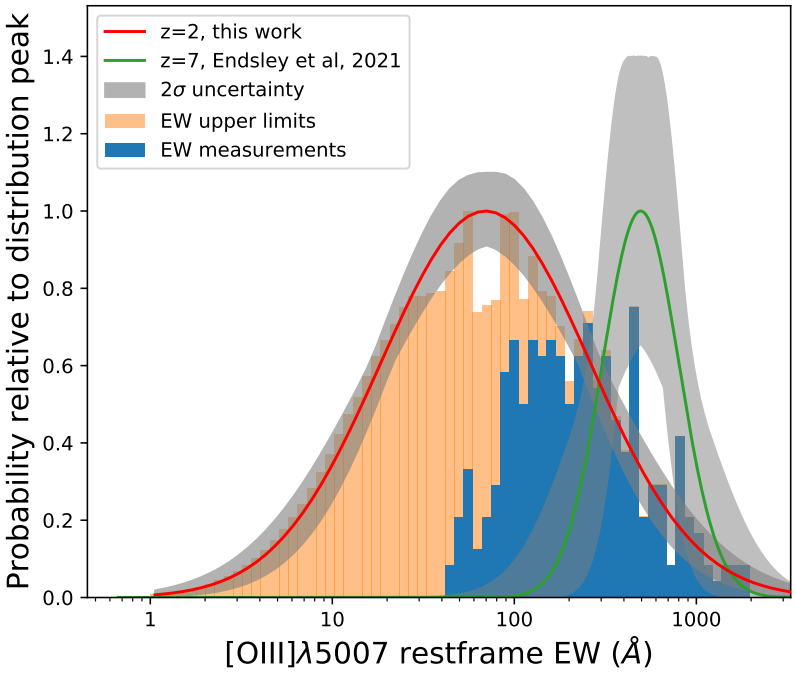

Figure 3.6: The $z \sim 2$ [OIII]λ5007 EW distribution (as in Figure 3.4) alongside the Endsley et al. (2021) $z \sim 7$ [OIII]+Hβ EW distribution, with the x-axis scaled to the [OIII]λ5007 EW. The two distributions are normalised so the maximum probability of both distributions is equation to unity and the histogram of EWs is set in bins of equal width in logspace. A clear distribution shift can be seen with the higher redshift distribution sitting at higher EWs.

[OIII]λ5007 between 450-800Å and 1.1 between 800-2500Å. This mapping suggests that the 500, 750 and 1000Å [OIII]λ5007 EW thresholds are roughly equivalent to 500, 750 and 1100Å Hα EW thresholds. These conversions are comparable to what has been used in the literature previously (e.g., Labbé et al. 2013; Rasappu et al. 2016).

To characterise the redshift evolution within the dataset, I divide the $z \sim 2$ sample into two redshift bins, $1.70 \leq z \leq 2.01$ and $2.01 < z \leq 2.274$ containing 329 and 343 galaxies respectively (using spectroscopic redshifts for [OIII] doublet detections and photometric redshifts for non-detections). I report EELGs fractions for the two redshift bins in Table 3.2. Figure 3.7 shows the EELG fractions calculated at [OIII]λ5007 EW thresholds of 500 and 750Å and compares to results in the literate at higher redshift.

It is clear from Figure 3.7 that at higher redshifts a greater proportion of star forming galaxies are observed in an extreme emission line phase. Not only are the typical SFGs at z$\sim$7 ([OIII]λ5007 EW $\sim$ 500 Å) rare at z$\sim$2, representing $5.4^{+1.2}_{-1.1}$% and $8.2^{+1.6}_{-1.5}$% of the population in the $1.70 < z < 2.01$ and $2.01 < z < 2.274$ bins, but conversely the SFGs typical of z$\sim$2 ([OIII]λ5007 EW $\leq$ 200Å) are rare at z$\sim$7, making up only $\sim$ 3% of SFGs at these high redshifts (Endsley et al., 2021). It has been argued that objects with [OIII]λ5007 EW above 1000Å lie above the star forming main sequence (the relation between the SFR of a galaxy and the stellar mass, see e.g. Speagle et al. 2014). Such intense line emitters encompass $\sim$ 20% of the population at $z > 7$, but at $z \sim 2$ these objects are practically insignificant, with only $1.5^{+0.6}_{-0.4}$% ($1.70 < z < 2.01$) and $3.0^{+0.9}_{-0.8}$% ($2.01 < z < 2.274$) of SFGs in such a phase in the two intermediate redshift bins. I consider a power law fit to the redshfit evolution of the EELG fraction ($\mathrm{frac(z) = frac_0\,(1+z)^P}$) and find z = 0 fraction and power law slope parameters ($\mathrm{frac_0}$=$0.47^{+0.12}_{-0.10}$%, P=$2.42^{+0.18}_{-0.18}$) for an EW threshold of 500 Å and ($\mathrm{frac_0}$=$0.22^{+0.11}_{-0.07}$%, P=$2.51^{+0.27}_{-0.32}$) for an EW thresholds of 750 Å. This evolution with redshift may reflect changing star formation histories, particularly the presence of bursty star formation in a galaxy population that can elevate the sSFR. Different ionisation conditions within galaxies at low- and high-redshift, perhaps related to the evolution of metallicity with redshift, can also help drive the evolution of the EW distribution. This EW distribution evolution will be discussed further in Section 3.4.

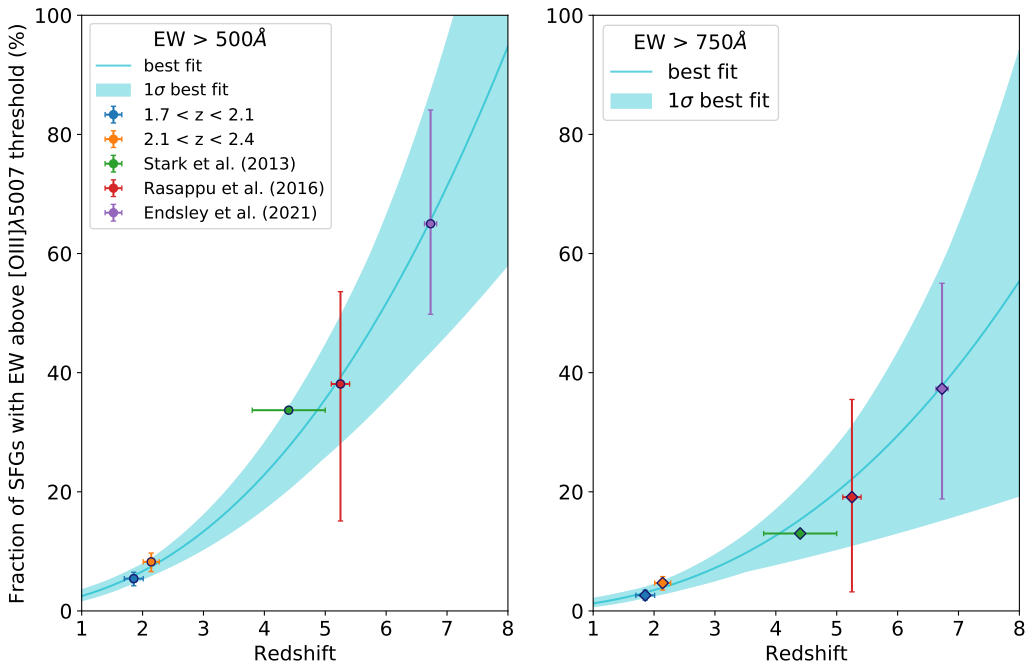

Figure 3.7: The evolution of the fraction of star forming galaxies with extremely large [OIII]λ5007 EW. The fraction for two [OIII]λ5007 EW thresholds shown in circles (Left plot - 500Å) and diamonds (Right plot - 750Å) across five redshift epochs shown in blue ($1.70 < z < 2.01$), orange ($2.01 < z < 2.274$), green ($3.8 < z < 5.0$), red ($5.1 < z < 5.4$) and purple ($6.63 < z < 6.83$). This works $z \sim 2$ data points are combined with the Hα studies at $z \sim 5$ and the [OIII]+Hβ study at $z \sim 7$ assuming conversions to [OIII]λ5007 EW. A fitted power law slope $\propto (1+z)^{P}$ and associated 1σ uncertainty are shown in light blue.

Table 3.3: Best fit model parameters for the rest-frame EW(Å). I show the results for the log-normal distribution (LN) and normal distribution in logarithmic space (N) for the two redshift sub-samples.

z-range	N	$\mu_{\rm LN}$	$\sigma_{\rm LN}$	$\mu_{\rm N}$	$\sigma_{\rm N}$
$1.70 - 2.01$	329	$4.26^{+0.09}_{-0.09}$	$1.21^{+0.08}_{-0.07}$	$1.21^{+0.12}_{-0.11}$	$0.53^{+0.03}_{-0.03}$
$2.01 - 2.274$	343	$4.26^{+0.11}_{-0.12}$	$1.43^{+0.11}_{-0.10}$	$0.97^{+0.18}_{-0.18}$	$0.62^{+0.05}_{-0.04}$

3.3.4 The dependence of the EELG fraction on UV luminosity

Here I characterise the luminosity-dependence of the [OIII]λ5007 EW distribution in the range sampled by the dataset ($-21.6 < \mathrm{M_{UV}} < -19$). At $z \simeq 7$, an analysis using Spitzer/IRAC flux excesses as a probe of rest-optical line strengths found no evidence for a significant [OIII]+Hβ EW trend with $\mathrm{M_{UV}}$ (Endsley et al., 2021). Given the close connection between [OIII]λ5007 EW and the ionizing efficiency (see discussion in Section 3.1), this result has implications for the $\mathrm{M_{UV}}$-dependent contribution of galaxies to reionisation. Physically I may expect the [OIII]λ5007 EW to be stronger towards lower UV luminosities given the observed correlation between $\mathrm{M_{UV}}$ and stellar mass at $z \simeq 2$ (e.g., Reddy & Steidel 2009) and the relationship between mass and metallicity (e.g., Sanders et al. 2021). The larger electron temperature in lower metallicity systems can act to boost collisionally-excited emission lines such as [OIII]λ5007 (Reddy et al., 2018). The [OIII]λ5007 EW additionally depends on the sSFR (e.g., Tang et al., 2019). This is especially true at very large sSFR, where the [OIII]λ5007 EW is enhanced by the weak underlying rest-optical continuum associated with very young stellar populations. If the large sSFR phase is more common in galaxies with lower UV luminosities (as might be expected if bursts are more common in lower luminosity and lower mass systems), I would expect to see larger EELG fractions at the faint end of the luminosity function.

To investigate whether the [OIII]λ5007 EW distribution varies with UV luminosity, I first separate the sample into a UV-bright ($-21.6 < \mathrm{M_{UV}} < -19.5$, 337 galaxies) and UV-faint sub-sample ($-19.5 < \mathrm{M_{UV}} < -19$, 335 galaxies). I recompute the best-fit log-normal parameters for the [OIII]λ5007 EW distributions in both magnitude bins. The results reveal broad consistency in the model mean and also the median of the two $\mathrm{M_{UV}}$ bins: the mean EW values of the UV-faint and UV-bright samples are $165.1^{+2.0}_{-1.5}$ and $174^{+1.4}_{-1.1}$Å respectively (where I quote the standard error on the mean), and the median values are 63^{+8}_{-7} and 74^{+7}_{-6}Å. The full set of best-fit parameters for both sub-samples is presented in Table 3.4. As can be seen in the table, both the average and width of the EW distributions are consistent within 2σ.

I also consider specifically the luminosity-dependence of the EELG population, computing the fraction of galaxies that have [OIII]λ5007 EWs above four physically motivated thresholds (200, 500, 750 and 1000Å , see Table 3.2). The EELG fraction posterior density functions for both UV bins are shown in Figure 3.8. For

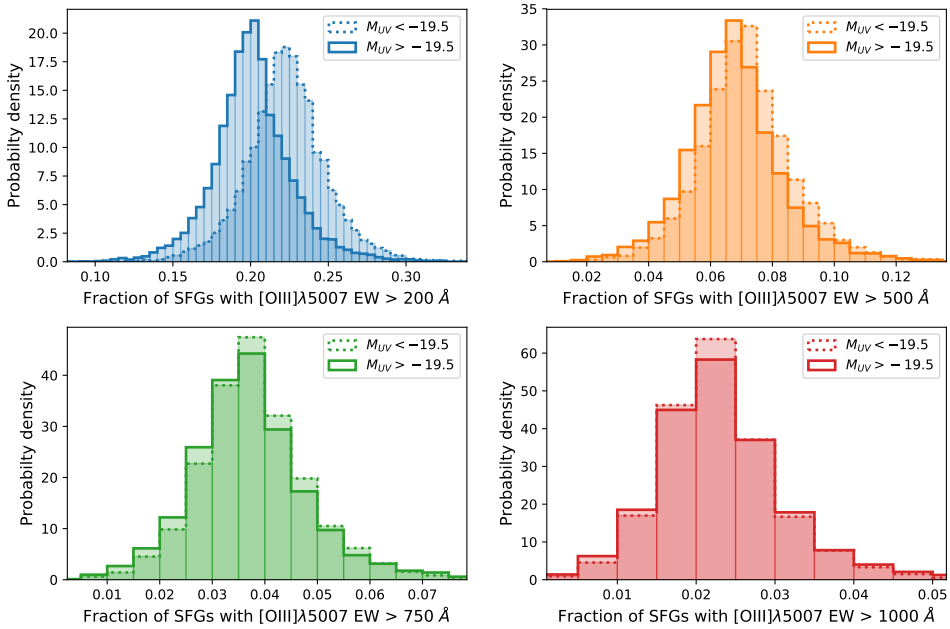

Figure 3.8: The MCMC posterior density function for the fraction of $M_{\rm UV}$ bright and $M_{\rm UV}$ faint star forming galaxies at $z \sim 2$ with extremely large [OIII]λ5007 EW. The MCMC posterior distributions for the fraction of bright $-21.6 < M_{\rm UV} < -19.5$ (solid lines) and faint $-19.5 < M_{\rm UV} < -19.0$ (dashed lines) sources above four different [OIII]λ5007 EW thresholds, shown in blue (200Å), orange (500Å), green (750Å) and red (1000Å). At each EW threshold the two UV bins are consistent within 1σ.

each threshold (each sub-panel in Figure 3.8) the derived fraction of SFGs with an [OIII]λ5007 EW above the given threshold is consistent between the two luminosity sub-samples. The fraction of galaxies with an EW above the typical [OIII]λ5007 EW at $z \simeq 2$ (200Å) is consistent between the fainter and brighter bins (from $20.1^{+2.4}_{-2.1}$% to $22.3^{+2.4}_{-2.3}$%), and the same is found for the relative abundance of the most extreme emission line galaxies (EW $\geq$ 1000Å) ($2.3^{+0.8}_{-0.7}$% and $2.2^{+0.7}_{-0.6}$% for the fainter and brighter bins).

The absence of significant variations in the [OIII]λ5007 EW distributions between the UV-bright and UV-faint bins is consistent with the findings of Endsley et al. (2021) at $z \simeq 7$.

Table 3.4: Best fit model parameters for the rest-frame EW(Å). I show the results for the log-normal distribution (LN) and normal distribution in logarithmic space (N) for the two $M_{\rm UV}$ sub-samples.

$M_{\rm UV}$	N	$\mu_{\rm LN}$	$\sigma_{\rm LN}$	$\mu_{\rm N}$	$\sigma_{\rm N}$
$-19.5 \rightarrow -19$	335	$4.13^{+0.12}_{-0.12}$	$1.39^{+0.12}_{-0.11}$	$0.95^{+0.19}_{-0.18}$	$0.60^{+0.05}_{-0.05}$
$-21.6 \rightarrow -19.5$	337	$4.31^{+0.08}_{-0.09}$	$1.30^{+0.08}_{-0.07}$	$1.14^{+0.13}_{-0.12}$	$0.57^{+0.03}_{-0.03}$

3.3.5 Grism-derived EW supplemented sample

As discussed in Section 3.2.2, within the sample of 672 galaxies I define a sub-set of 146 for which the Momcheva et al. (2016) EW based on the grism-derived stellar continuum is deemed to be reliable. I define this sub-set as those galaxies with a significant [OIII] doublet detection and EW measurement from Momcheva et al. (2016), both required to have a S/N $\geq 5\sigma$, where the low S/N below either criteria would compromise the EW measurements. These EW measurements made from the grism alone provide an alternative to the use of the broadband-derived stellar continuum flux density. In Section 3.2 this robust sub-set was used to establish that the broadband-derived stellar continuum provides a consistent EW estimate to the grism-derived stellar continuum EWs. In this work I elected to use the broadband-derived continuum method for all sources with an [OIII] doublet detection ($\geq 5\sigma$), to provide consistency with targets with significant line detections but without reliable grism-derived EW measurements. To review whether this choice would affect the EW distribution I determine the EW distribution for the sample of 672 galaxies where the EW measurements of the robust sub-set (146 galaxies) are supplemented by the grism-derived [OIII]λ5007 EWs. I find consistency between both approaches, those using the supplemented grism [OIII]λ5007 EWs and those using purely the broadband-derived method, with the best fit EW distribution parameters agreeing within 1σ. I further reproduce the EW distributions for the sub-samples that will be explored in Section 3.3.3 and Section 3.3.4 and find consistent best fit parameters between the grism supplemented sample and the sample used in this work. I provide the best fit [OIII]λ5007 EW distribution parameters for the grism-derived [OIII]λ5007 EW supplemented sample in Table 3.5.

Sample	N	$\mu_{\rm LN}$	$\sigma_{\rm LN}$	$\mu_{\rm N}$	$\sigma_{\rm N}$
full sample	672	4.25 ± 0.07	$1.32^{+0.06}_{-0.05}$	$1.09^{+0.10}_{-0.09}$	$0.57^{+0.03}_{-0.02}$
$1.70 < z < 2.01$	329	$4.29^{+0.08}_{-0.09}$	$1.22^{+0.08}_{-0.07}$	$1.22^{+0.12}_{-0.11}$	0.53 ± 0.03
$2.01 < z < 2.274$	343	$4.23^{+0.11}_{-0.13}$	1.43 ± 0.10	0.95 ± 0.17	0.62 ± 0.04
$-19.5 < M_{\rm UV} < -19.0$	335	$4.16^{+0.12}_{-0.13}$	$1.38^{+0.11}_{-0.10}$	$0.98^{+0.18}_{-0.17}$	$0.60^{+0.05}_{-0.04}$
$-21.6 < M_{\rm UV} < -19.5$	337	4.29 ± 0.09	$1.31^{+0.08}_{-0.07}$	$1.12^{+0.13}_{-0.12}$	0.57 ± 0.03

Table 3.5: Best fit model parameters for the rest-frame [OIII]λ5007 EW(Å). I show the results for the log-normal distribution (LN) and normal distribution in logarithmic space (N) for the grism-derived continuum flux density measured [OIII]λ5007 EW supplemented sample. Each parameter consistent with the corresponding best fit parameter using broadband-derived continuum flux densities for all detections.

3.4 Discussion

In this Chapter, I have derived the [OIII]λ5007 EW distribution in $z \simeq 2$ UV-selected galaxies, thereby quantifying the fraction of EELGs at $z \simeq 2$. Locally ($z \sim 0$) and at intermediate redshifts ($1 < z < 3$), EELGs have been shown to be extremely efficient ionisers, both due to their large ionisation production efficiencies (Chevallard et al., 2018; Tang et al., 2019; Nakajima et al., 2020; Emami et al., 2020) and their large escape fractions (e.g. Jaskot et al., 2019; Nakajima et al., 2020; Izotov et al., 2016; Vanzella et al., 2016; Fletcher et al., 2019). However the rareness of this population suggests they make a sub-dominant contribution to the ionising background from star forming galaxies at $z \simeq 2$. In this section, I estimate the fractional contribution from EELGs at $z \simeq 2$, combining [OIII]λ5007 EW distributions with nominal assumptions on the ionising efficiency of the population.

I first consider the ionising contribution of EELGs at $z \simeq 2$, focusing on those systems with [OIII]λ5007 EW > 750Å. While this subset comprises just 3.6% of the $z \simeq 2$ population (Table 2), they are thought to be very efficient ionisers. These objects have typical ionising photon production efficiencies of $\log_{10}(\xi_{\rm ion}$, erg s^{-1}Mpc^{-3}Hz$^{-1}) = 25.58$ (Tang et al., 2019), 3.3× greater than that in more typical star forming galaxies at $z \simeq 2$ (Shivaei et al., 2018). While not all EELGs show ionizing photon leakage, values are often significant in the population, with systems having the largest [OIII]λ5007 EWs (i.e., >750 Å) often found with estimated escape

fractions of up to 20-50% (Vanzella et al., 2016; Rivera-Thorsen et al., 2017; Izotov et al., 2018; Fletcher et al., 2019). For the purposes of this calculation, I will assume that this range of $20-50\%$ escape fractions is exhibited by half of galaxies with [OIII]λ5007 EW > 750Å, with the remaining half leaking no ionising radiation. While this f_{esc} distribution is clearly still very uncertain, the values are broadly consistent with known constraints on LyC escape fractions and indirect indicators of leakage in this extreme [OIII] emitting population (e.g., Izotov et al. 2018; Jaskot et al. 2019; Tang et al. 2021b). In what follows, I take these values and calculate the comoving emissivity of ionising photons ($\dot{n}_{\rm ion}$, s^{-1}Mpc^{-3}) for these intense EELGs, but I caution that improved distributions of escape fractions in this population are ultimately required for more confident inferences. I focus on galaxies in the luminosity range probed in this work ($-21.6 < M_{\rm UV} < -19$) and assume the Reddy & Steidel (2009) UV luminosity function. I multiply the far UV luminosity density by the fraction of galaxies with [OIII]λ5007 EW > 750Å (3.6%). After accounting for the ionising production efficiency and the range of escape fractions, I find that this population injects a comoving ionising photon emissivity of between 3 and 8×10^{49} s^{-1} Mpc^{-3} into the IGM at $z \simeq 2$.

I can now estimate the fractional contribution these EELGs make to the total ionising background produced by $z \simeq 2$ star forming galaxies. To do so, I use population-average estimates of the ionising photon production efficiency and escape fraction. For the escape fraction, I use the recently-derived value from Pahl et al. (2021), indicating an average of $f_{\rm esc} \sim 6\%$ for $z \simeq 3$ UV-selected galaxies (see also Steidel et al. 2018; Bassett et al. 2021). Here I assume that $z \simeq 2$ galaxies have a similar value. For the ionising production efficiency, I use the value derived for the the $z \simeq 2$ UV-selected population, taking the same attenuation law as I assumed for EELGs (Shivaei et al., 2018). The estimated ionising emissivity from UV-selected galaxies over my luminosity range is then $\dot{n}_{\rm ion} = 1.5 \times 10^{50}$ s^{-1}Mpc^{-3}. While the emissivities quoted above are nominal estimates with significant uncertainties, they illustrate that EELGs do indeed make a sub-dominant contribution to ionising output from galaxies at $z \simeq 2$. However if the large escape fractions assumed here for a subset of the most intense of EELGs are correct, it would indicate that even at $z \simeq 2$, this population makes a non-negligible contribution to the ionising background of star forming galaxies.

Further contribution to the ionising background comes from AGN and SFGs outside the UV luminosity range so far considered ($M_{uv} < -19$) and the emissivity of

the total ionising background from all sources at this epoch is estimated to be $\sim 10^{51}$ s^{-1} Mpc^{-3}(Becker & Bolton, 2013; Becker et al., 2015). This total background is measured from studies of the Lyα forest in QSO spectra and therefore contains the contribution from all ionising sources. If I extend the SFG luminosity function down to $M_{uv} < -17$ ($L > 0.033L^*$), then the estimated SFG (not only EELGs) contribution of $\dot{n}_{ion}[L > 0.033L^*] = 3 \times 10^{50}$ $s^{-1}Mpc^{-3}$ would make up $\sim 30\%$ of the total ionising background. This estimate of the total emissivity from SFGs is consistent with previous findings for the total emissivity contribution from AGN of $\sim 60 - 80\%$ at this epoch, as presented in Becker et al. (2015) from the emissivity UVB model by Haardt & Madau (2012) and the semi-analytical emissivity model by Giallongo et al. (2012).

The EELGs (with EWλ5007 $>$ 750Å) within the UV luminosity ($M_{uv} < -19$) range provide a sub-dominant contribution ($< 10\%$) to the total ionising background at this epoch. The majority of the total $\dot{n}_{ion}$ at $z \sim 2$ comes from a combination of AGN activity and SFGs able to leak ionising radiation in more typical modes of star formation than that seen in EELGs (e.g., Steidel et al., 2018). However, as I will now go on to discuss, the importance of EELGs to the ionising background changes dramatically with redshift.

The ionising contribution from EELGs is likely to increase substantially as we enter the reionisation era. Given current constraints on the [OIII]+Hβ EW distribution (and nominal assumptions about the contribution of Hβ; see Section 3.3.3), the percentage of star forming galaxies with [OIII]λ5007 EW $>$750Å is thought to increase by a factor of 10 between $z \simeq 2$ and $z \simeq 7$, from 3.6% ($z \simeq 2$) to close to 37% ($z \sim 7$) (Endsley et al., 2021). The percentage of those with an [OIII]λ5007 EW$>$500Å also increases by a factor of 10 between $z \sim 2 - 7$, reaching close to 65% of the population at $z \simeq 7$ (Endsley et al., 2021). So while the majority of the $z \sim 2$ star forming galaxy ionising background comes from more typical modes of star formation than EELGs, during the reionisation era, the bulk of the ionising photons will likely come from EELGs. Future work is required to test if the ionising efficiency of this population evolves with redshift. The first spectra of EELGs in the reionisation era suggest similarly intense radiation fields as are often seen at lower redshifts (e.g., Stark et al., 2015a,b, 2017; Mainali et al., 2017; Schmidt et al., 2017; Hutchison et al., 2019; Jiang et al., 2021; Topping et al., 2021), but JWST will soon

allow much-improved investigation of the ionising output of reionisation-era EELGs.

The rapid evolution in the EELG population is suggestive of a shift in the main star forming mode between $z \sim 2$ and $z \sim 7$. The most intense EELGs are likely in the midst of a burst or recent upturn in star formation. The increase in this population with redshift may suggest that such intense bursts are becoming more common in the reionisation era. This is consistent with the observed rise in the galaxy merger rate and specific mass accretion rate observed between $1 < z < 6$ (Duncan et al., 2019), both of which may spark and feed more frequent and stronger bursts of star formation. The nebular rest-optical line EW distributions (and the related sSFR distributions) encode useful information on the star formation history, with the tails of the distribution (both at high and low sSFR) constraining the strength and duty cycle of bursts. The evolution and mass-dependence of these distributions will soon be constrained in more detail by JWST. Direct comparison of these observations to simulations and semi-analytic models promises valuable insight into the presence of bursts in the earliest galaxies.

3.5 Summary

Recent years have seen increased interest in extreme emission line galaxies, owing to their efficiency as ionising agents and their apparent ubiquity in the reionisation era. The [OIII]λ5007 equivalent width distribution constrains the percentage of star forming galaxies at a given epoch caught in an extreme emission line phase. While efforts have begun to characterise the distribution of [OIII]+Hβ line strengths at $z \simeq 7$ (Labbé et al., 2013; Smit et al., 2014; De Barros et al., 2019; Endsley et al., 2021), similar measurements do not exist at $z \simeq 2$, impeding efforts to track the redshift evolution of the EELG population. I establish the best fit log-normal model for the [OIII]λ5007 equivalent width distribution in a rest-UV selected sample ($M_{\rm UV} < -19$) in the redshift range $1.700 < z < 2.274$, using the combination of HDUV photometry and the 3D-HST grism spectra. With the [OIII]λ5067 EW distribution, I quantify the fraction of $z \simeq 2$ galaxies with extreme line emission, providing the low redshift baseline necessary to characterise the evolution of this population. The fraction of UV-selected galaxies with an [OIII]λ5007 EW above 200, 500, 750 and 1000Å is found to be $21.2^{+1.7}_{-1.6}\%, 6.8^{+1.0}_{-0.9}\%, 3.76^{+0.7}_{-0.6}\%$ and $2.2^{+0.5}_{-0.4}\%$ respectively. I find no strong evidence that the EELG fractions vary with UV luminosity in the range considered in this

work ($-21.6 < M_{\rm UV} < -19.0$), consistent with results at $z \simeq 7$ (Endsley et al., 2021).

Comparison to results at higher redshift (e.g., De Barros et al. 2019; Endsley et al. 2021) reveals rapid redshift evolution, with the fraction of galaxies having [OIII]λ5006 EW$>$ 500Å increasing from 6.8% at $z \simeq 2$ to 65% at $z \simeq 7$ (for nominal assumptions about the Hβ contribution at $z \simeq 7$). I find a similar increase with a slightly higher [OIII]λ5007 EW threshold ($>$ 750Å), with 3.6% of the population in this regime at $z \simeq 2$ and 37% at $z \simeq 7$. Even accounting for their enhanced ionising efficiency, EELGs are too rare at $z \sim 2$ to dominate the ionising background, contributing 20-50% of the ionising emissivity from all SFG below $M_{\rm UV} < -19$ and less than 10% of the total ionising background from all sources (including AGN).. But a far greater percentage of galaxies will be in an extreme emission line phase at $z \simeq 7$, providing an ideal population for ionising the intergalactic medium. Future work will soon offer much-improved measures of the evolving EELG population, both in terms of their ionising efficiency and their mass-dependent contribution to the total galaxy population. These studies promise valuable insights into the contribution of galaxies to reionisation and the redshift and mass-dependence of bursts in early galaxies.

Chapter 4

JADES - Target selection

4.1 Introduction to JWST

The James Webb Space Telescope (JWST Gardner et al. 2006) is a joint NASA, ESA and Canadian Space Agency (CSA) observatory scheduled for launch in late 2021. This next generation telescope hosts a 6.5 metre segmented diameter mirror, providing some 6 times the photon collecting area of the Hubble Space Telescope. The science payload contains 4 instruments; NIRSpec, NIRCam, FGS-NIRISS, MIRI (their coverage of the focal plane shown in Figure 4.1). The wavelength range spans 0.6 to 28μm in the visible to the mid-infrared. There is overlap with current red and near-infrared coverage with HST (out to 1.6μm) and ground-based (sensitive out to $\sim$ 2.4μm, the K-band window), but critically JWST extends to much longer wavelengths, including regions of low transmission from the ground due to significant absorption by OH bonds in H_2O atmospheric water molecules. JWST will greatly extend the work of the previous mid-infrared Spitzer mission, which had only a 0.85m mirror (Werner et al., 2004; Fazio et al., 2004; Rieke et al., 2004). The orbit of JWST after launch will follow the 2$^{\text{nd}}$ Sun-Earth Lagrange point. Unlike HST, which is in low earth orbit with a orbital period of 90 minutes, the orbit of JWST means it will be thermally stable and will not experience earth occultation. Here the instrument package is always kept in the earth's shadow at $\sim 50K$.

The design of JWST was built around four key science themes (Gardner et al., 2006): the end of the dark ages (first light and reionization); the assembly of galaxies; birth of stars and proto-planetary systems; and planetary systems. My research focuses on the first two of these themes. Crucially, the longer wavelengths covered with JWST, in particular through spectroscopy with NIRSpec, enables the same key

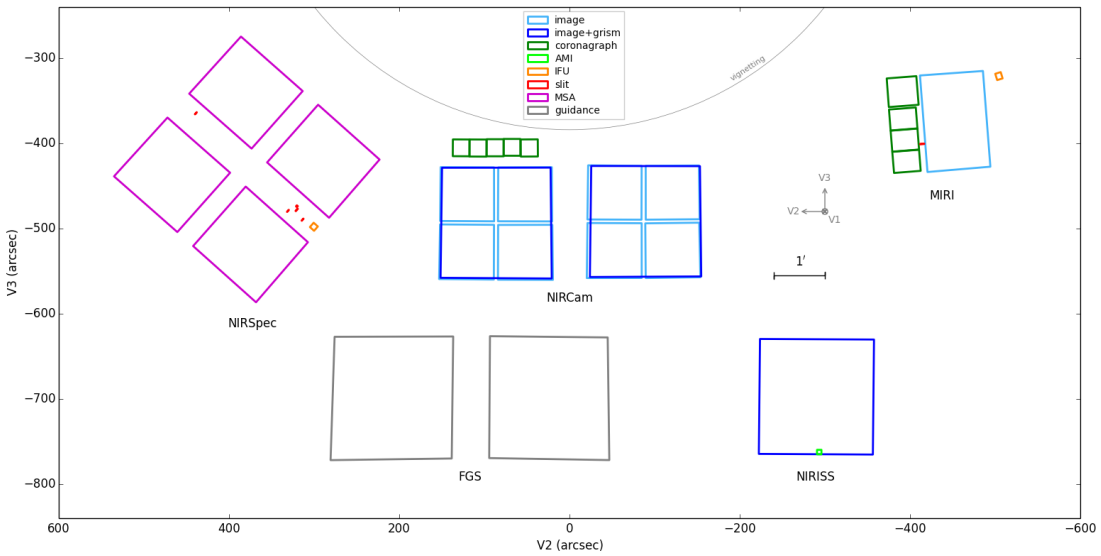

Figure 4.1: The area of the JWST focal plane that each instrument observes, given in the observatory's coordinate system (V2,V3). Each instrument observes a different portion of the focal plane, allowing parallel observations to be conducted where multiple instruments take exposures simultaneously. This image is taken from the James Webb Space Telescope User Documentation[2].

rest-frame diagnostics I used in Chapters 2 and 3 to characterise galaxies at $z \sim 0.5-2$ to be used to explore galaxies out to $z \sim 10$.

4.2 Introduction to JADES

The JWST Advanced Deep Extragalactic Survey (JADES, Bunker et al. 2020; Rieke 2020) is a guaranteed time survey between the NIRSpec instrument science team (IST) and NIRCam IST, with the science goals of determining galaxy evolution from redshifts $z \sim 2$ out to $z \geq 10$, including the star formation history, the build-up of stellar mass, and the chemical enrichment of galaxies over cosmic time. The JADES Guaranteed Time Observation (GTO) programme is allocated ∼790 hrs, which is the largest GTO programme. JADES combines the use of NIRCam photometry, NIRSpec spectroscopy and when available as a parallel, MIRI. The combination of using NIRSpec to target sources detected in NIRCam photometry allows galaxies at unprecedented redshifts to be studied. Through HST observing campaigns, some large samples of candidate high redshift galaxies have already been selected through their colours (e.g. the Lyman break technique) or photometric redshifts. However, only a

[2]JWST User Documentation, available at https://jwst-docs.stsci.edu/jwst-observatory-hardware/jwst-field-of-view

very small fraction of these galaxies at $z > 6$ (within the epoch of reionization) have spectra to confirm their redshifts. This is where NIRSpec spectroscopy with JWST should achieve a breakthrough in understanding.

The JADES team have identified various priority classes, covering a range of science goals in galaxy evolution (detailed in Table 4.2). At the highest redshifts, we are interested in spectroscopic confirmation of the most distant (and typically very faint) candidates, which is critical to understand the role of galaxies in the epoch of reionisation and to constrain the evolution of luminosity functions. I will consider the limiting magnitudes for which NIRSpec can measure redshifts in Section 5.6, which shapes our priority class selection criteria in JADES (Table 4.2). At lower redshifts, $2 < z < 7$, some galaxies will be sufficiently bright for line ratio work (such as I have conducted on lower-redshifts samples such as WISP and 3DHST in Chapters 2 & 3 using HST and ground-based data), and this is another key science goal - tracing the evolution of metallicity, dust and ionisation parameter for galaxies, and the fraction of the population which is in a highly-star forming phase (signified perhaps by extremely high equivalent width emission lines). In Section 5.6 I will consider the limiting magnitudes for which we can achieve this science through NIRSpec observations in the JADES programme.

I am a member of the NIRSpec Galaxy Assembly GTO team, and also a member of the JADES consortium (a joint NIRSpec-NIRCam GTO programme). In this chapter I will first describe the instruments used for the JADES survey, before detailing my work on refining the target selection for NIRSpec spectroscopy.

4.2.1 Introduction to NIRCam

The Near-InfraRed Camera (NIRCam, Rieke et al. 2005) is one of four scientific instruments on JWST and is the primary imager in the near-infrared, covering a spectral range of 0.6 to 5μm with a total of 29 narrow, medium and wide bandpass filters, with a field of view 9.7 arcminutes square. Two sets of 2×2 detectors at short wavelength (0.6-2.3μm), and simultaneously two long-wavelength detectors (2.4-5μm) survey the same area (each detector having 2040×2040 light sensitive pixels). JWST is diffraction-limited at $\sim 2\mu$m, so the full width at half maximum (FWHM) of the point spread function (PSF) will be 0.03-0.06 arcsec at $< 2\mu$m (3x better than HST), rising to 0.16 arcsec at 5μm (comparable to the HST PSF in the optical e.g., Dressel 2021 and 10x better than Spitzer at 5μm Fazio et al. 2004).

4.2.2 Introduction to NIRSpec

The Near-InfraRed Spectrograph (NIRSpec) on JWST represents the first multi-object spectrograph (MOS) in space and provides low, medium and high spectral resolution capabilities in the near infrared (0.6-5.3μm). NIRSpec also includes companion fixed slit and integral field Unit (IFU) spectroscopy modes. The primary MOS mode will allow $\sim$ 100 objects to be targeted during each exposure and is achieved through a multi-shutter assembly (MSA, Figure 4.3) constructed from a quarter of a million individually controllable micro-shutters spread over 4 quadrants (365 by 171 shutters), each aperture 0.43 arcsecond by 0.2 arcsecond in size with a 0.07 arcsecond support between every shutter. By using these shutters, the background (from zodiacal light and scattered light) is very much reduced compared to the slitless spectroscopy done by HST (e.g. the WISPS survey in Chapter 2) and hence NIRSpec spectroscopy will achieve unprecedented sensitivity. Figure 4.2 shows how the required sensitivity of NIRSpec is an improvement over the HST/WFC3 slitless spectroscopy from Chapter 2. The NIRSpec medium and high resolution gratings will have an expected $>$ 10 greater emission line sensitivity at $1 - 2\mu$m compared to the HST/WFC3 slitless spectroscopy (scaled to the same exposure time and S/N requirement).

The MOS achieves the 3 spectral resolutions through a Prism and a set of 6 gratings. The Prism allows a resolving power of R$\sim$ 100 (where R = $\lambda/\Delta\lambda$) across the full wavelength range (0.6-5.3μm). The Prism is powerful in that it observes a large spectral range in one shot, and is very sensitive to studying the shape of the spectral continuum. However, it is less sensitive to emission lines occupying a narrow range of wavelengths, and for this higher spectral resolution is needed. There are medium and high resolution gratings achieving higher resolving powers over a reduced spectral range. There are three medium spectral resolution gratings of R $\sim$1000, suitable for emission line work (including resolving the Hα and [NII] lines) and the full spectral range can be covered by observing with all three of these in turn. There are also three higher resolution gratings with R$\sim$2700, and these are useful for probing galaxy kinematics at a $\sim$100km/s velocity resolution.

The use of the MSA does bring limitations: whilst individual shutters are opened and closed magnetically between each exposure, a small proportion cannot be operated and remain either fixed closed ($\sim$ 15% of shutters) or fixed open ($<<$ 1%,

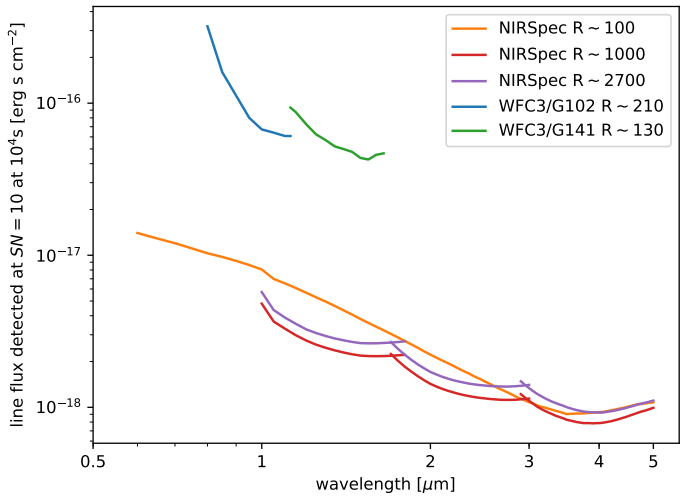

Figure 4.2: Comparative emission line flux sensitivity for a test S/N=10 and 10^4s exposure time. Showing the JWST-NIRSpec sensitivities for the R$\sim$ 100 Prism, and the R$\sim$ 1000 and R$\sim$ 2700 gratings as well as the sensitivity for the HST WFC3 G102 and G141 Grisms (Atek et al. 2010, adopting a 5px spatial $\times$ 3px dispersion aperture).

around $\sim$ 20 shutters in total) due to physical defects or electrical shorts during manufacturing. Fixed open shutters have the adverse effect of illuminating the detector and potentially contaminating target spectra while fixed closed shutters restrict the choice of apertures for exposures. Failed shutter maps therefore must be employed to address these constraints when target MSA configurations are generated. A key consideration for NIRSpec is the small shutter size (0.2x0.4arcsec). Although this is well matched to the typical size of high-redshift galaxies (e.g., Oesch et al., 2010a), the large variation in the PSF size with wavelength (from 0.03"-0.06" at $< 2\mu$m to 0.16" at 5μm) means that the slit losses change greatly with wavelength, and will also be a strong function of both the position within the micro shutter and also of the surface brightness profile of the galaxy (this motivates the work in Section 4.3.2 and 4.3.6 of this Chapter and also the work on mock NIRSpec observation simulations in Chapter 5). For line ratio work, it is critical to get this flux calibration correct.

[4]JWST User Documentation, available at https://jwst-docs.stsci.edu/jwst-observatory-hardware/jwst-field-of-view

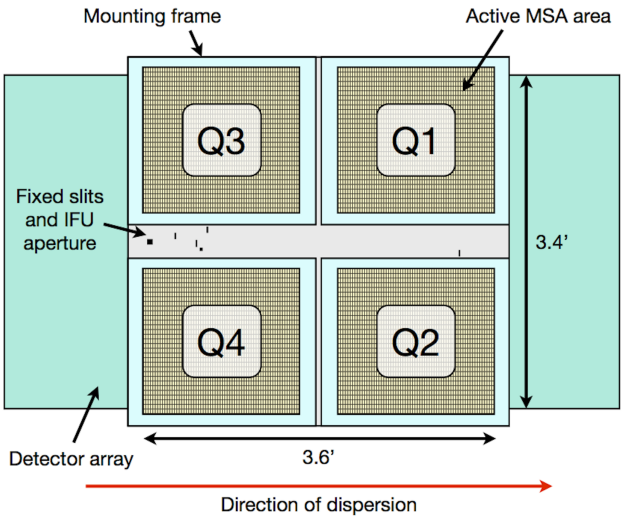

Figure 4.3: Plan of the NIRSpec Multi-shutter Assembly identifying the position of the four micro-shutter quadrants (Q1-Q4, totalling $\sim 250,000$ configurable 0.2"x0.4" aperture shutters), a series of five fixed slits (of varying width and length, permanently fixed open) and the NIRSpec IFU aperture. Two detectors are sensitive to the incident light and cover a larger collecting area than the aperture plane to account for the dispersion of light. Figure taken from the JWST User Documentation[4].

4.3 JADES strategy & Catalogue analysis for Target selection

Much of the JADES survey will use NIRCam images to select potential targets for NIRSpec follow-up spectroscopy. The JADES fields are the GOODS-North and GOODS-South fields(Giavalisco et al., 2004), and we use the existing HST data along with new NIRCam photometry to determine photometric redshifts, so that the highest redshift objects can be preferentially targeted for spectroscopy. The existence of HST data, particularly at $< 0.8\mu$m where we will not obtain JADES imaging with NIRCam, is crucial for a robust selection of Lyman break galaxies at $z \lesssim 7$ (with rest-frame imaging below 1216Å provided by HST).

As with many surveys designed to explore luminosity functions of galaxies, we wish to span a range of volume densities and brightnesses and to do this JADES will employ several "wedding cake" survey tiers. We will do two points of extremely long integration within GOODS-South. This "Deep" tier will be sensitive to extremely faint galaxies, which are likely to have the highest volume density. A "Medium" tier covers 12 pointings in both GOODS-North and South with intermediate duration

exposures. There is a separate "wide" tier to be done by the NIRSpec IST (distinct from the JADES collaboration) where existing known sources (primarily from HST) are observed over 31 NIRSpec pointings across the HST CANDELS fields, including the GOODS fields. This "wide" tier will target the brighter but rarer sources. Each tier can be seen to be probing a different region of the galaxy luminosity function, as shown in Figure 4.4.

To maximise the total achievable observing time, JADES will utilise parallel observations to effectively double the NIRCam + NIRSpec allocated time $\sim$ 790hrs. This means that whilst either NIRCam or NIRSpec is in use as the primary observing instrument (setting the observatory pointing) a secondary instrument can be observing simultaneously with the restriction that its position on the sky is fixed relative to the primary instrument's pointing and the roll angle of the observatory (see Figure 4.1 for the fixed relative positions on the focal plane). The optimum observing strategy allows efficient use of telescope time by scheduling NIRSpec or MIRI parallels during prime NIRCam pointings and NIRCam parallels during prime NIRSpec pointings. For the DEEP tier of the JADES strategy, it is anticipated that the first set of observations in GOODS-South will be the DEEP NIRCam primary with the first of two 100Ksec (10^5s) DEEP NIRSpec pointings in secondary (the primary position of NIRCam set to place the secondary position of NIRSpec over the HUDF, where targets can be selected from existing HST imaging). The second DEEP NIRSpec pointing is taken as the primary instrument, following-up the highest redshift candidates identified in the aforementioned DEEP NIRCam imaging, with NIRCam acting in parallel over the wider GOODS-South field. Figure 4.5 presents a possible layout of NIRCam, NIRSpec and MIRI observations for the DEEP and MEDIUM tiers over the GOODS-North and South fields. The exact layout is dependent on the the launch window of JWST and Cycle 1 scheduling.

As noted above we anticipate obtaining one deep spectroscopic GTO observation with NIRSpec early in the JWST mission before NIRCam imaging becomes available, in order to test the capabilities of the NIRSpec MSA. We intend to target currently-known galaxies in the Hubble Ultra Deep Field (HUDF, e.g., Bunker et al. 2004; Beckwith et al. 2006). HUDF is the deepest image yet obtained, and as such has a target density of candidate high-redshift objects that is well matched to the multi-object capabilities of NIRSpec. It is also likely that several of the NIRSpec observations in the MEDIUM and WIDE tiers of the survey will cover areas in and

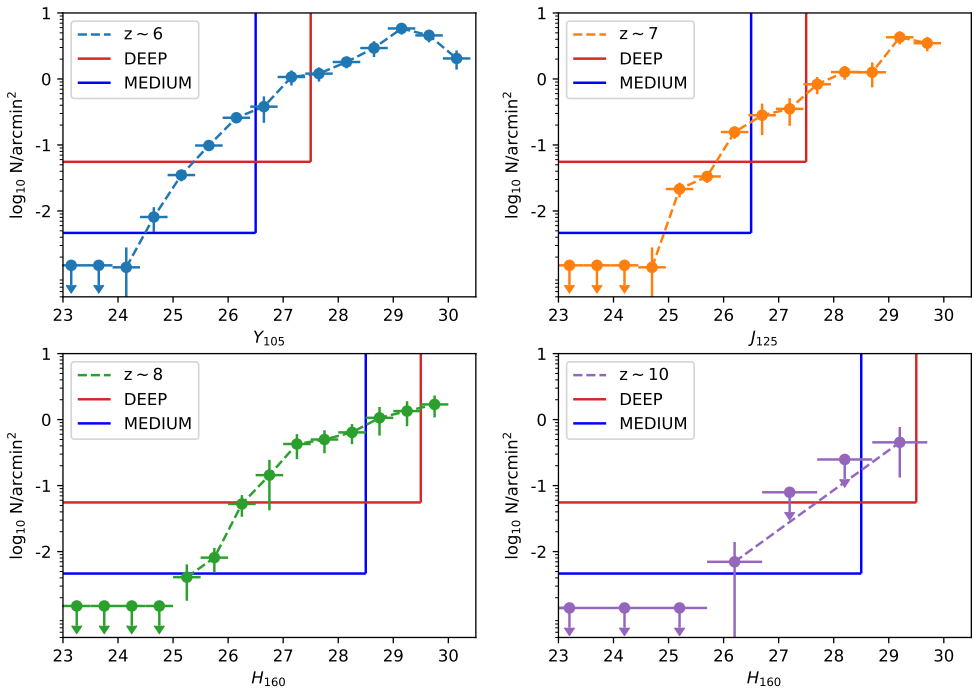

Figure 4.4: The surface densities of the i-, z-, Y- and J-band drop-out candidate Lyman break galaxies from Bouwens et al. (2015a) (corresponding to $z \sim 6, 7, 8\&10$), overlaid with the depth to which the DEEP (red) and MEDIUM (blue) NIRSpec survey tiers will probe. The AB magnitude limit in a band longward of the Lyman break for the $z \sim 6\&7$ panels is set by the priority Class 4 requirements of 27.5 in the DEEP and 26.5 in the MEDIUM tiers, whilst the AB magnitude limit for $z \sim 8\&9$ panels is set by the priority Class 1&2 requirements of 29.5 in the DEEP and 28.5 in the MEDIUM tiers. The horizontal edge to the survey box signifies the surface density required for 1 object to appear in the 18arcmin^2 DEEP tier and the 215arcmin^2 MEDIUM tier. The JADES tiered strategy allows the DEEP tier to observe the higher surface density fainter objects, the MEDIUM tier will observe the rarer brighter sources.

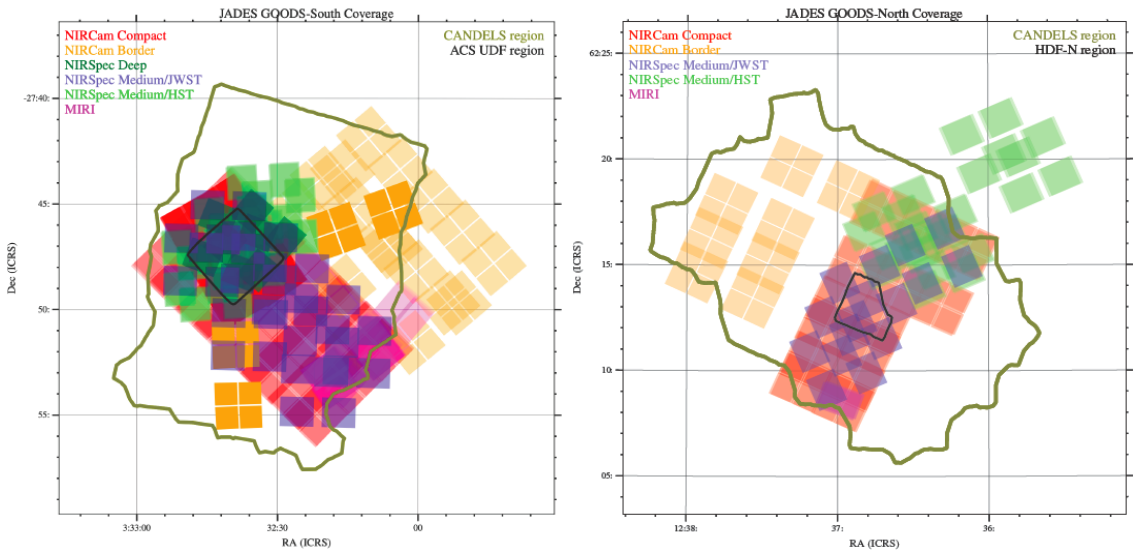

Figure 4.5: Possible layout for JADES observing plan, exact pointings will depend on the roll angle of JWST and according to the Cylce 1 schedule. Dark green and black borders identify existing HST fields including the GOODS North, South and deeper HDF-N and HUDF. The JADES DEEP and MEDIUM footprint is shown for the different components, NIRCam in red and orange, NIRSpec in light green and blue, and MIRI in purple. The use of parallels (observing with a second instrument simultaneous to the primary instrument) allows JADES to effectively double its allocated observing time. Credit to Chris Willott of the JADES team and NIRSpec IST for producing these plots.

around the GOODS fields that do not have prior NIRCam observations. Because of this, it is critical for the JADES team to have a catalogue of existing known targets so that MSA configurations can be built. In placing targets on the MSA, priority would be given to the most interesting for our science (i.e. the highest redshift candidates, in particular high redshift objects where the emission lines are likely to be bright enough for the line diagnostic work described earlier in this thesis, as well as those of particular scientific interest, e.g. those with longer wavelength emission line detections from ALMA or those that display AGN). The JADES team have agreed on a number of priority classes (detailed in Table 4.2), with the top-priority classes being the small number of candidate z >9 sources, along with highly unusual objects, followed by more numerous sources at z >6, and then the most numerous but lower-priority galaxies at z <6. I am concerned with the top 1-4 classes and sub-sets of classes 6 & 7 that are at high redshift. When designing an MSA configuration, we need to avoid spectra overlapping (although I note that in the low-dispersion R$\sim$100 Prism the spectra are quite short relative to the detector size, so that 3 or 4 may be placed along the dispersion direction). Which objects are selected for spectroscopic observation in an MSA configuration depends critically on the roll angle of the telescope, which is set by the date of observation. This has not currently been decided (the Space Telescope Science Institute is still developing the schedule), so the JADES team needs a comprehensive catalogue of known objects in the GOODS fields from which targets can later be selected.

The JADES team gathered together all the existing catalogues in the GOODS fields, and in 2017 a list of about 40,000 galaxies in the CANDELS GOODS-North and South fields was submitted to the Space Telescope Science Institute (STScI) as potential targets reserved for the JADES programme. This is done to avoid duplication of observations with other programmes in the early cycles of JWST science observations. However, this source list was built from a large number of published catalogues produced by a number of different groups. These groups often using different reductions of the HST data (which may be on slightly different astrometric frames) and included various supporting observations from other telescopes. In selecting objects for inclusion in these catalogues, the various groups often employed different selections (including different photometry schemes such as aperture magnitudes or "total" magnitudes, different magnitude or S/N cuts, and perhaps different photometric redshift fitting and/or different colour cuts for Lyman break selection).

My role within JADES has been to re-analyse the input catalogues and generate a single catalogue with photometry and astrometry re-done where we can easily compare every target. In particular, I focus on the higher redshift objects, specifically the Lyman break galaxies. With the available HST CANDELS filters, the shortest ACS waveband is the F435W b-band, which is sensitive to the Lyman break at z$\sim$ 4, and the redder filters extending into WFC3 can potentially select galaxies out to z$\sim$ 10 (e.g., Ellis et al., 2013). As a starting point for consistency, I take the re-reduction of all the CANDELS HST imaging done by 3D-HST (Brammer et al., 2012; Skelton et al., 2014). I begin by taking the original target coordinates from the input catalogues and the initial photometry as used in the original analyses from the different groups and I re-analyse all the targets using a uniform method across all catalogues. The ultimate goal is to allow galaxies on the reserved target list to be prioritised for NIRSpec spectroscopy on the basis of consistently measured photometry (and inferred photometric redshifts), and to obtain accurate relative coordinates for precise placement on the MSA.

4.3.1 Catalogue data

I focus on three large catalogues of Lyman break galaxies within the GOODS fields at $z \gtrsim 4$: Bouwens et al. (2015a) with 7892 galaxies in the range $2.5 < z < 10$, Finkelstein et al. (2015) with 7242 galaxies in the range $3 < z < 9$ and Harikane et al. (2016) with 8087 galaxies in the range $4 < z < 7$. I also cross-match with the 3D-HST catalogues from Skelton et al. (2014) which also have photometric redshifts, and while dominated by lower redshift source do include some of the high redshift Lyman break galaxies (although fewer than in the three core LBG catalogues that I consider, since the 3D-HST catalogues were not optimised for faint object LBG selection so have brighter magnitude cuts than specialised catalogues).

Each of the three groups initially ran SExtractor (Bertin & Arnouts, 1996) to identify objects within the GOODS-North and South imaging using varying composite detection images made from the WFC3/IR wavebands to improve the S/N of targets (although this has the potential counter effect of reducing the S/N of high-z objects if the composite image contains wavebands sensitive to wavelengths below their Lyman break, where only noise will be added). Bouwens et al. (2015a) measures the H-band 5σ depths from the uncertainties (corrected to total fluxes) of their faintest 20% of objects and determine these to be 26.8 in the GOODS-WIDE regions, 27.5 in the GOODS-DEEP regions and 29.4 in the HUDF . This is consistent with H-band 5σ

Tier	Field	Exposure Time Strategy	Depth	Area***
DEEP NIRSpec	HUDF, GOODS-S	1×200ksec pointing targeting HST imaging 1×200ksec pointing targeting JWST imaging (each 100ksec Prism + 25ksec x[G140M, G235M, G395M, G395H])	AB<29-30	18 arcmin^2
MEDIUM NIRSpec	GOODS-S, GOODS-N	12×43ksec pointings targeting JWST imaging (each 8.5ksec x[PRISM, G140M, G235M, G395M, G395H]) 12×24ksec pointings targeting HST imaging (each 3.5ksec x[Prism, G395M] + 2.8ksec x[G140M, G235M])	AB<27-28	215 arcmin^2
WIDE NIRSpec	GOODS-S, GOODS-N, AEGIS, COSMOS, UDS	31×6.3ksec pointings targeting HST imaging (each 24ksec Prism+ 18ksec x[G235H, F170LP]+ 18ksec x[G395H, F290LP])	AB<25	280 arcmin^2
DEEP NIRCam	HUDF, GOODS-S	9 filters, peak exposure time 120ksec in F115W, (F090W,F115W,F150W,F200W,F277W,F335M,F356W,F410M,F444W)	AB <30.5*	46 arcmin^2
MEDIUM NIRCam	GOODS-S, GOODS-N	10 filters, (F070W**,F090W,F115W,F150W,F200W,F277W,F335M**,F356W,F410M,F444W)	AB <29.5*	190 arcmin^2
DEEP MIRI	GOODS-S	F770W (167ksec)	AB = 27.4*	8 arcmin^2
MEDIUM MIRI	GOODS-S, GOODS-N	F770W(5.6ksec), F1280W(19.4ksec)	AB = 25.6, 25.0*	14 arcmin^2

Table 4.1: JADES DEEP and MEDIUM, and NIRSPEC GTO WIDE tiered survey strategy. The depths quoted for NIRSpec indicates the faintest objects we will target on the MSA.
$*$ Depth for a 5σ point source
$**$ over only 93 arcmin2 will be covered in these two filters $***$ taking the NIRSpec field of view to be $\sim 3 \times 3$arcmin^2. The unvignetted field is slightly smaller
.

Priority class	Redshift range	Brief description	Expected number of targets on MSA
1	$z >\sim 9$	Brightest rest-UV (AB* <29.5) or unusual candidates e.g., pop III candidates, galaxies with enormous breaks and those with potential line emission. (The pointing is fixed to maximise the largest number well-centred in MSA shutters.)	$\sim 1-5$
2	$z >\sim 9$	Rest-UV bright (S/N > 3 in R$\sim$ 100 continuum). For 100ksec in DEEP (AB<29.5) and MEDIUM (AB < 28.5-29.0) surveys.	$\sim 1-5$
3	$z >\sim 9$	Fainter high-z sources including those with strong emission lines but with weak continuum or lower likelihood z$\sim$ 9 candidates	<30.5
4	$z > 6$	Galaxies with sufficiently high S/N for line ratio work (requiring Hα or [OIII]5007 S/N > 25, e.g., at $z \sim 6$ anticipate F110W < 27.5**) or interesting AGN or ALMA sources	~ 30
5	$z > 2$	Very rare sources (AB < 23.5) allowing high S/N R=1000 spectroscopy for detailed population and absorption line analysis	<10
6	$z > 6$	Fainter high-z targets for redshift and emission line diagnostics. (or lower likelihood Class 4 candidates) Also including some interesting VLA/ALMA/X-ray/MUSE and high EW (selected from narrow- or broad-band colours) sources.	10-15% of remaining space
7	$1.5 < z < 6$	Broad range of galaxies with an ideal S/N ratio (Hα S/N > 25) for analysis over a range of redshift, mass, SFR. Favouring passive galaxies at high-z.	Remaining space
8	$z > 4$	Census sources above a 4.4μm limit (to achieve sufficient S/N in spectrum). Favouring sources undetected in the optical HST/ACS filters that are likely high-z	$\sim$ 20%

Table 4.2: Priority categories for the target Selection Strategy for NIRSpec MSA in NIRSpec Deep and Medium GTO surveys. High-redshift target selection will utilise JWST broadband 'colours'(Hainline et al., 2020). Anticipated numbers assume a 4$\sim$5.5sq.arcmin of NIRSpec shutter area and expected JWST surface densities(Williams et al., 2018).
∗Rest-frame magnitude (AB system)
∗∗Expected Hα line emission S/N from a well-centred source with SFR= $1 M_{\odot} yr^{-1}$, Salpeter IMF and Kennicutt (1998) recipe.

depths drawn using the uncertainties (corrected for aperture losses) of the faintest 20% of objects, measured during my photometric analysis (see Section 4.3.3), which are 27.5 in the GOODS region and 29.5 in the HUDF. Harikane et al. (2016) and Finkelstein et al. (2015) alternatively quote H-band 5σ depths derived by measuring the sky variation in 0.35" and 0.4" diameter apertures respectively, these are typically 0.5mag fainter than those calculated using the Bouwens et al. (2015a) method. To improve the target detection S/N, Finkelstein et al. (2015) use a J,H-band composite image, Harikane et al. (2016) use a Y,J,JH,H-composite image and Bouwens et al. (2015a) use a series of composite images for each drop-out filter sample using the WFC3/IR wavebands that lie above the Lyman break for that drop-out sample. The photometry measurements made by each group are subtly different: Harikane et al. (2016) use a fixed 0.35" aperture to measure their photometry, whilst Finkelstein et al. (2015) and Bouwens et al. (2015a) measure fluxes using small-scalable Kron apertures with corrections applied to estimate the total flux (Bouwens et al. 2015a additionally utilise a smaller 0.2" diameter flux aperture in ACS wavebands below the Lyman break in their selection criteria for determining non-detections). To arrive at a sample of Lyman break galaxies, Bouwens et al. (2015a) presents a set of 6 colour criteria to identify B-, V-, *i*-, *z*-, Y- and J-band drop-outs by comparing the flux in adjacent wavebands to identify the location of the Lyman break (as discussed further in Section 4.3.4). Bouwens et al. (2015a) goes on to apply additional constraints, for instance, a requirement for the galaxies to be not be detected in wavebands below the Lyman break (using a smaller fixed aperture), to improve the robustness of their selection. Harikane et al. (2016) adopt the Bouwens et al. (2015a) colour criteria in their selection of B-, V-, *i*- and *z*-band drop-outs. Finkelstein et al. (2015) alternatively determines their catalogue of high-redshift candidates from their measured photometric redshifts (utilising EAZY, Brammer et al. 2008). In their final published catalogues Bouwens et al. (2015a) and Finkelstein et al. (2015) do not give all the photometry (as described above) but instead give, in the case of Bouwens et al. (2015a), the total-magnitude corrected scalable Kron aperture estimate, and in the case of Finkelstein et al. (2015), the rest-frame 1500Å total magnitude estimate (based on the WFC3/IR photometry) Harikane et al. (2016) provides their 0.35" aperture magnitude for all wavebands.

The Bouwens et al. (2015a) and Finkelstein et al. (2015) catalogues are identified to contain repeated galaxies (where a catalogue ID appears more than once) and duplicates (where two galaxies with different catalogue IDs are determined to have

the same sky position to within 0.1", ~ 1.67 drizzled pixels). Instances of multiple entries of the same ID are errors seemingly produced when a galaxy's redshift lies on the border of two drop-out categories where the galaxy's photometry may lead it to appear in both, e.g., a $z \sim 4.5$ galaxy may have one entry classed as a B-band drop-out and a second as a V-band drop-out. This suggests the published catalogues are composites of individual drop-out band sub-catalogues. In these cases, the entry with the catalogue redshift closest in agreement to the BEAGLE photometric redshifts (see Section 4.3.5) is used. This accounts for 68 repeated galaxies in Bouwens et al. (2015a) and 21 in Finkelstein et al. (2015). For each of the three catalogues I check for duplicated galaxies (with different catalogue IDs) and look for galaxies with matched galaxy coordinates within a 0.1" radius aperture (~ 1.67 drizzled pixels in the 3D-HST reduced F160W H-band imaging). Within the Bouwens et al. (2015a) catalogue 62 galaxies are identified as duplicates, and I only keep the entry with the catalogue redshift closest to the BEAGLE photometric redshift. This leaves the Bouwens et al. (2015a) catalogue with 7761 objects and the Finkelstein et al. (2015) catalogue with 7221. The Harikane et al. (2016) catalogue shows no such repetition or duplication of galaxies, and remains with 8087 galaxies.

In addition to providing a uniform set of galaxy parameters for all $\sim 23,000$ galaxies in the three LBG catalogues, re-analysis allows for the input catalogues to be examined to determine whether any show systematic offsets in astrometry of photometry. A subset of galaxies in each of the three main catalogues overlap, allowing the original catalogues to not only be compared to the re-analysed results but also to each other. Across the three catalogues there are a total $\sim 14,500$ unique galaxies, and a sub-set of 2828 objects appear in all three of the catalogues. Bouwens et al. (2015a) and Harikane et al. (2016) reproduce over 50% of each other's galaxies, while Finkelstein et al. (2015) uses a different selection method (based on photometric redshifts) which allows the selection of objects not-obtained by the drop-out method in the other catalogues (e.g., those with weak breaks or very red slope) which lowers the fraction of galaxies in common between these three catalogues. The overall low reproducible rate between all three can also be put down to the low S/N nature of the highest redshift objects which are typically the faintest and that in the GOODS South field the area of coverage is subtle different depending on the inclusion of ERS regions. To validate this, in Table 4.4, I first show the fraction of galaxies in the Bouwens et al. (2015a) catalogue that overlap with the other two and then how the overlap fraction increases when I restrict the catalogues to the GOODS North region

(where all catalogues cover the same area) and to only galaxies detected at a high S/N ($> 10\sigma$ in the H-band). The fraction of objects in the Bouwens et al. (2015a) catalogue that appear in both the other catalogues increases from 36% to 55% when I apply the above restrictions. A break down of the full overlap between each catalogue is given in Table 4.3 where galaxies are matched at a 0.1" tolerance using the re-measured astrometry (see Section 4.3.2). A total of 2447 galaxies have further overlap between the three main catalogues and additionally the van der Wel et al. (2012) 3D-HST catalogue.

4.3.2 Astrometry

I re-determined the positions of each Lyman-break galaxy from the three main catalogues using the same 3D-HST imaging. I use the 3D-HST reduction F160W H-band imaging (Skelton et al., 2014; Grogin et al., 2011; Koekemoer et al., 2011) for both GOODS fields, except for the HUDF area where I use XDF (Illingworth et al., 2013) (which I determine to be on the same astrometric system), as this is typically the deepest band lying above the Lyman break for all objects.

Astrometry on the previously catalogued galaxies is made using `center` within `IRAF`, using the `centerpars.calgorithm = "centroid"` algorithm. The HST images have been gain-corrected but are in units of electron/sec. Hence within `Datapars`, `.readnoise` is set to exposure time (in sec) $\times$ the pixel-to-pixel standard deviation and `.epadu` (Gain) is set to the exposure time in sec. A minimum accepted Signal to noise ratio (S/N) value is set to 5 to eliminate centring on background noise. The recovered H-band change in position distribution of Right Ascension (RA) and Declination (Dec) relative to the literature position is then fitted by a Gaussian to establish the average offset and standard deviation (σ). Sources which return a ΔRA or ΔDec greater than 3σ from the average offset position are flagged in the Astrometric_Flag column of the final catalogue (see Table A.1 in Appendix A.2). I also looked for evidence of rotation and plate-scale change in the relative astrometry.

In IRAF "`center`" provides its own warning `A_CIER` for each target: where the change in position in either RA or Dec is greater than a chosen threshold of $1px$; where a low S/N is recorded; or where the coordinates are in fact off image. Where the re-measurement of the astrometry produced an error, I flagged this in my catalogue.

Drop-out Filter	Bouwens et al. (2015) total / in H16 / in F15 / in Both	Harikane et al. (2016) total / in F15 / in B15/ in Both	Finkelstein et al. (2015) total / in B15 / in H16 / in Both
B-band	4974 / 2916 / 2167 / 1653	5185 / 2029 / 2925 / 1651	4068 / 2194 / 2036 / 1667
V-band	1712 / 1008 / 1090 / 791	1821 / 1002 / 1022 / 813	2014 / 1054 / 960 / 765
i-band	613 / 347 / 373 / 265	653 / 297 / 319 / 242	666 / 381 / 334 / 276
z-band	332 / 156 / 183 / 111	428 / 156 / 175 / 122	341 / 162 / 138 / 109
Y-band	124 / 14 / 48 / 8	0 / 0 / 0 / 0	132 / 70 / 16 / 11
J-band	6 / 0 / 0 / 0	0 / 0 / 0 / 0	0 / 0 / 0 / 0
all	7761 / 4441 / 3861 / 2828	8087 / 3484 / 4441 / 2828	7346 / 3861 / 3484 / 2828

Table 4.3: The number of galaxies in each of the Bouwens et al. (2015a); Harikane et al. (2016); Finkelstein et al. (2015) catalogues in each of the B-, V-, i-, z-, Y- and J-band drop-outs, with the overlap number (matched at a 0.1arcsec radius in the re-measured astrometry) that also appear in the other catalogues also marked. The difference in overlap numbers between catalogues at the same drop-out filter highlights that the same galaxy in different catalogues can be reported to have different drop-out filters. The total number of entries across all three catalogues is 23,194 including 14,475 unique galaxies with a total of 2828 galaxies appearing in all three of the catalogue

Drop-out Filter	Bouwens et al. (2015) total / in H16 / in F15 / in Both	GOODS North only total / in H16 / in F15 / in Both	GOODS North + SN>10 total / in H16 / in F15 / in Both
B-band	4974 / 0.586 / 0.436 / 0.332	2479 / 0.604 / 0.475 / 0.370	762 / 0.743 / 0.591 / 0.496
V-band	1712 / 0.589 / 0.637 / 0.462	909 / 0.629 / 0.681 / 0.532	176 / 0.807 / 0.892 / 0.744
i-band	613 / 0.566 / 0.608 / 0.432	255 / 0.561 / 0.659 / 0.498	27 / 0.704 / 0.963 / 0.704
z-band	332 / 0.470 / 0.551 / 0.334	173 / 0.434 / 0.630 / 0.376	19 / 0.579 / 0.895 / 0.526
Y-band	124 / 0.113 / 0.387 / 0.065	53 / 0.170 / 0.433 / 0.113	3 / 0.333 / 0.666 / 0.333
J-band	6 / 0 / 0 / 0	3 / 0 / 0 / 0	1 / 0 / 0 / 0
all	7761 / 0.572 / 0.497 / 0.364	3872 / 0.593 / 0.541 / 0.413	988 / 0.748 / 0.660 / 0.545

Table 4.4: The fraction of galaxies in the Bouwens et al. (2015a) catalogue that are matched to galaxies in the Harikane et al. (2016) and Finkelstein et al. (2015) catalogues, split by the drop-out broadband filter. Progressively the catalogues are restricted to only the GOODS North field (where each study has the same area coverage) and then to only galaxies with a greater than 10σ detection in the H-band. When the catalogues are restricted to the same area coverage and to only the most confidently detected sources, the fraction of galaxies that overlap between the different studies increases.

These are removed from the calculations of the coordinate offset transformation between catalogues.

Across the catalogues there is good agreement between the re-centred results and input coordinates (see Figure 4.6 for the ΔRA and ΔDec), the exception being the Bouwens et al. (2015a) catalogue which is shown to exhibit a systematic astrometric offset in the GOODS North field. The mean offset and standard deviation of the Δposition distribution is given in Tables 4.5, 4.7 and 4.6. These have been calculated by fitting the distribution of ΔRA or ΔDec with a Gaussian model. Apart Bouwens et al. (2015a) catalogue in the GOODS North field, for each combination of catalogue and field, the re-measured position is found to be consistent within the measured uncertainty of the original position with no compelling evidence for errors in the plate scale or a relative rotation. Importantly all the offsets I report for these are $\ll$ 0.2arcsec, smaller than the MSA shutter size. However, the offset in the GOODS North Bouwens et al. (2015a) catalogue is significant and is greater than the extent of the MSA shutter size, but I note this offset does appear to be a genuine issue in the Bouwens et al. (2015a) catalogue and does not appear in the other catalogues. Figure 4.7 shows the astrometric offset relative to the 0.2" NIRSpec slit aperture (red). The average declination offset is found to be $\Delta\text{Dec} = (0.263 \pm 0.058)$ arcseconds, which would have led to the targets lying outside NIRSpec's micro-shutters. Hence it is important that I identified and corrected for the astrometry offset. I have also verified that this astrometric offset remains in the recently updated catalogue from the same group (Bouwens et al., 2021), this means it likely is a genuine error as part of their legacy reduction of the HST imaging, which is may not be particularly significant for ground-based spectroscopic follow up but is critical for the small microshutter of NIRSpec.

Ultimately the coordinates of each galaxy will be matched to the GAIA2 frame, using brighter objects within 3D-HST images to map the relative distortions. A re-reduction of CANDELS HST onto this revised astrometric frame by STScI or the 3D-HST team is not yet available. The GAIA2 frame will also be used for the alignment stars used to accurately register the MSA on the sky and it is critical that these are on the same astrometric system as the targets.

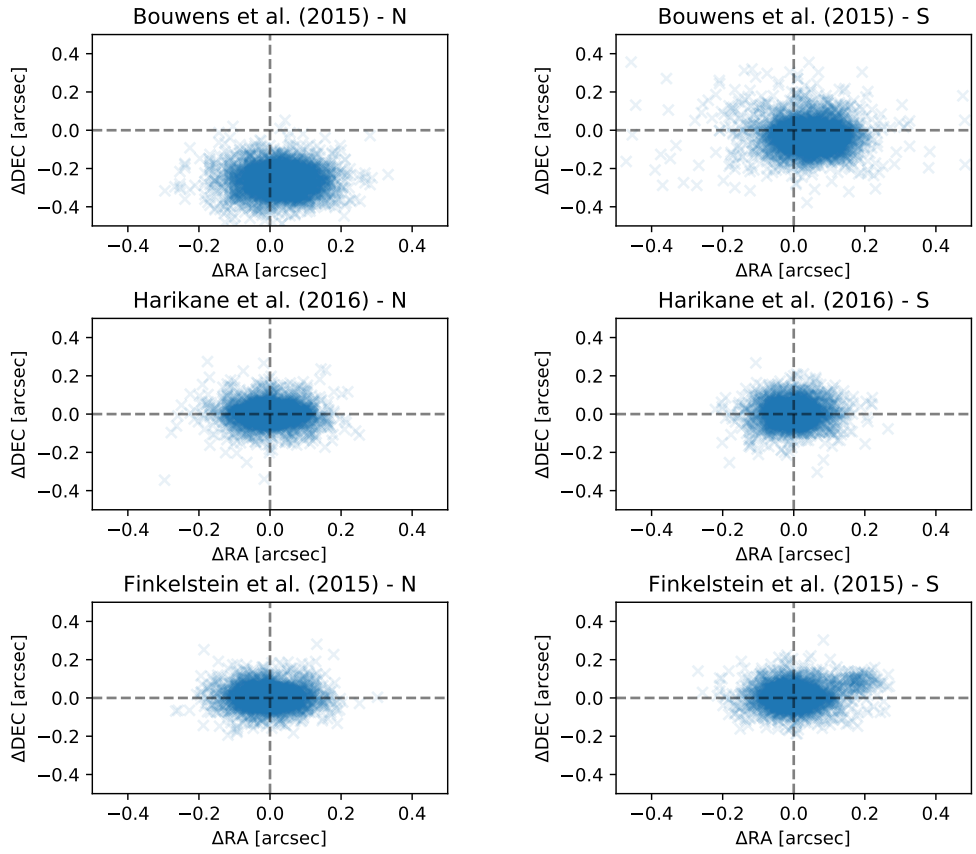

Figure 4.6: Measured positional offsets for the three Lyman break catalogues, re-determining the position on the 3D-HST F160W image. The offsets are mostly minimal with the exception of the Bouwens et al. (2015a) catalogue in GOODS North where there is a 0.26" offset in declination.

Table 4.5: The average positional offset in RA and Declination for sources in the Bouwens et al. (2015a) LBG catalogue, remeasured using the 3D-HST F160W. The standard deviation in the offset along each axis is also given (σ), fitting a Gaussian to the distribution of offsets in RA and Dec. I note significant offset in Declination in GOODS North for this catalogue.

	ΔRA	ΔDec	σ_{RA}	σ_{Dec}
North	0.0287	-0.2627	0.0640	0.0582
South	0.0529	-0.0388	0.0604	0.0550
XDF	0.0062	-0.0035	0.0137	0.0167

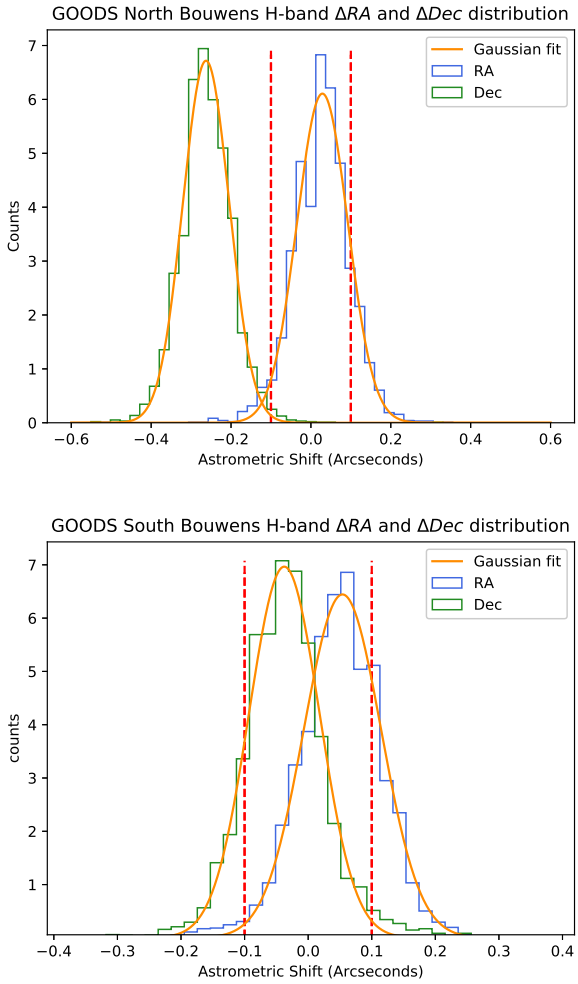

Figure 4.7: H-band astrometric ΔRA and ΔDec distribution re-analysis using IRAF *center*, comparing the astrometry from Bouwens et al. (2015a) Lyman break catalogue to remeasurement from the 3D-HST F160W image. Red dashed lines highlight the NIRSpec Microshutter 0.2arcsec width. Top: GOODS North field, a large systematic offset in the declination positions of the galaxies place them outside the NIRSpec Microshutter width. Bottom: GOODS South field, smaller offsets measured with the majority of the original catalogue positions lying within the Microshutter width.

Table 4.6: The average positional offset in RA and Declination for sources in the Harikane et al. (2016) LBG catalogue, remeasured using the 3D-HST F160W.

	ΔRA	ΔDec	σ_{RA}	σ_{Dec}
North	-0.0018	0.0015	0.0499	0.0342
South	-0.0038	0.0019	0.0381	0.0373
XDF	-0.0050	-0.0060	0.0195	0.0174

Table 4.7: The average positional offset in RA and Declination for sources in the Finkelstein et al. (2015) LBG catalogue, remeasured using the 3D-HST F160W.

	ΔRA	ΔDec	σ_{RA}	σ_{Dec}
North	-0.0050	0.0049	0.0504	0.0397
South	-0.0103	0.0080	0.0380	0.0371
XDF	-0.0053	-0.0050	0.0283	0.0306

4.3.3 Photometry

Using the H-band centred positions, `Phot` within `IRAF` is run to provide photometric measurements within a 3 and 5 pixel aperture radius (0.06"/px in the 3D-HST imaging), corresponding to circular apertures of diameter 0.36" and 0.6". A local measure of the sky background in an annulus between 0.6 and 1.2 arcsec was subtracted. The 3 pixel radii measurements correspond approximately to the average projection of a randomly-orientated NIRSpec micro-shutter on the sky (0.2"×0.4") and provide a useful estimate of the expected flux falling within a NIRSpec aperture for a well-centred source and will be used to determine the colours of objects (for photometric comparison between filters e.g., the Lyman break colour-colour selection in Section 4.3.4, while the larger 5 pixel measurements provide a more reliable measure of the total magnitude and are used to determine the SED fitting in Section 4.3.5. To enforce measurements centred on the H-band re-measured positions, I fix the coordinates and set `centerpars.calgorithm` to `"none"`. The `.readnoise, .epadu` and S/N conditions are the same as those used in the astrometric centring. The re-analysis uses where available the same 3D-HST (Skelton et al., 2014) imaging reduction as these catalogues and if data was not accessible it was taken from either the CANDELS (Guo et al., 2013) (the WFC3/F105W Y-band imaging which was not available from 3D-HST) or XDF (Illingworth et al., 2013) (for the HUDF) collaborations.

An appropriate aperture correction is made to the magnitudes to account for the proportion of the Point Spread Function (PSF) that falls outside the aperture. These aperture corrections are strictly only appropriate for point sources, but this

Filter	F435W	F606W	F775W	F850LP	F105W	F125W	F140W	F160W
Ap_cor	0.189	0.158	0.183	0.293	0.383	0.394	0.460	0.474

Table 4.8: Aperture correction for 3 pixel radius (0.36" diameter) magnitudes

is a reasonable approximation for the typical size of Lyman-break galaxies (certainly at z> 6) which are typically compact with intrinsic FWHM comparable to the HST PSF (Oesch et al. 2010a find an average half-light radius at z$\sim$ 7 of $\sim$0.7kpc, which corresponds to $\sim$0.1arcsec). The aperture photometry is corrected to approximate total magnitude through a fixed aperture correction, determined from bright compact sources in the field. For the 3px aperture, where standard literature corrections weren't available, fixed aperture corrections were determined for each filter using a set of bright objects (either unsaturated stars or compact galaxies). The correction is determined by comparing aperture magnitudes to an estimate of the total magnitude for this set of compact-sources and these are given in Table 4.8. For the 5px aperture I adopt the Bunker et al. (2010) magnitude corrections, determined in the same manner ($\sim$0.1 mag in the ACS filters, $\sim$0.2 mag in the WFC3 F105W filter and 0.25 in the redder WFC3 filters, reflecting the broader PSF at longer wavelengths). An alternative to a fixed magnitude correction would be to use an estimate of the "total" magnitude based on the curve-of-growth from the surface brightness of the galaxy, for example using SExtractor `MAG_AUTO`, but at faint fluxes this introduces large uncertainties (and this is something of a black box).

For these compact high-z sources a simple and reproducible aperture magnitude measurement is preferred. This is especially important in the preparation and ranking of potential NIRSpec targets, since the multi-shutter array has a narrow slit size of 0.2"$\times$0.4", so measuring the photometry using flux falling within a small aperture (as is done here) will be a better predictor of the spectroscopic signal ultimately detected than integrating the surface brightness profile out to large radii.

A magnitude zeropoint appropriate to each filter is used to convert the electrons/sec of the reduced image to an AB magnitude, such that

$$Mag(AB) = zeropoint - 2.5 \times log_{10}(elec/sec) \tag{4.1}$$

and the zeropoints from the WFC handbook[5] and the ACS calculator[6] for the Goods

[5]WFC handbook: `http://www.stsci.edu/hst/wfc3/documents/ISRs/WFC3-2009-30.pdf`, in particular Table 5

[6]ACS zeropoint calculator: `https://acszeropoints.stsci.edu`

fields, and from the STScI user documentation[7] for the XDF fields are used. All images used are themselves mosaics formed from a set of observations using the commonly used *drizzle* process (Fruchter & Hook, 2002; Koekemoer et al., 2003). This process allowed the pixels to be re-sampled to achieve a desired pixel scale resolution and recover some of the under-sampling of the PSF with the pixels sizes of the ACS and WFC3 (where compromises had been made between survey area and pixel sampling of the PSF), however this leads to the noise within each re-sampled pixel no longer remaining independent of its neighbours. To correctly estimate this correlated noise a correction factor is applied, taken from Roy Gals' "Notes on SExtractor"[8], which accounts for the output pixel scale as a fraction of the input (the input pixels are 0.13" for WFC3 and 0.05" for ACS), and the "droplet size" in drizzle. I confirmed the noise corrected for pixel correlations by placing many apertures on blank regions of sky (avoiding galaxies) in the image, and fitting a Gaussian to the histogram of apodized fluxes to obtain the standard deviation of background counts in an aperture.

The flux f (with the mean sky background subtracted), area A and standard deviation σ (corrected for correlated noise) parameters are also returned by `phot` for each target at each aperture and are used to determine the signal to noise ratio. S/N $= f/\sigma\sqrt{A}$, Note: the returned flux can be negative and hence so can the S/N. For those galaxies which are undetected ($< 2\sigma$) in a particular waveband, I also calculate the 2σ upper limit on the flux and this would correspond to a lower limit on the AB magnitude. It is preferred to work in flux density units, since negative fluxes are "undefined" on the magnitude scheme. Where a galaxy is undetected in a particular filter in the 5px radius aperture (0.6" diameter), I wish to be sure there is no flux down to faint limits. As most Lyman break galaxies are very compact, and the non-detection bands for Lyman break galaxies are typically at shorter wavelengths (often in the ACS optical instrument instead of the WFC3 IR channel) where the PSF is more compact, I re-measure the photometry in the undetected band using the smaller 3px radius aperture (0.36" diameter) to provide a more stringent constraint on the flux. A similar approach is adopted by Bouwens et al. (2015a) to minimise contamination by low redshift objects in their Lyman break selection. The 2σ limit is re-calculated by adding twice the estimated noise ($\sigma\sqrt{A_3}$) to the 3px aperture flux f_{3px} and then converting back to a magnitude and applying the same zeropoint as

[7] STScI User Documentation: `https://archive.stsci.edu/prepds/xdf/`

[8] "Notes on SExtractor": `http://www.ifa.hawaii.edu/$\sim$rgal/science/sextractor_notes.html`

before an aperture corrections for 3pix radius. If $f_{3px} < 0$ due to noise fluctuation, I instead take the flux to be 0 before adding twice the noise to obtain a flux limit. The photometry catalogues for the Y-band drop-outs is presented later in Table 4.16 and the full version is made available in a machine-readable format[9] and are described in Appendix A.2.

For galaxies which are essentially undetected in the 3D-HST image at the coordinates from the literature, and `IRAF.center` was unable to obtain an accurate fix on the centroid, I record the photometry at the nominal (literature) position, which is typically S/N$<$ 2 for these objects, and flag them as undetected. It should be noted that at low signal to noise, below $\sim$ 5, the uncertainty on the measured magnitudes are no longer symmetric. For the various SED fitting and photometric redshift codes (e.g. BEAGLE, see Section 4.3.5) I use the flux and flux error, since the flux can be negative (rather than "undefined" in the magnitude system) and the flux errors are typically symmetric.

The input catalogues use a variety of photometric methods, some use a SExtractor (Bertin & Arnouts, 1996) variable aperture approach (e.g., Bouwens et al. 2015a using Kron apertures to recover a total H-band magnitude) whilst others adopt a fixed aperture. While Harikane et al. (2016) and Bouwens et al. (2015a) provide their own measurements of the H-band magnitude (a 0.35" aperture magnitude in the case of Harikane et al. 2016 and a Kron total magnitude for Bouwens et al. 2015a), Finkelstein et al. (2015) instead provide the rest-frame 1500Å magnitude (derived from their NIR photometry). In Figure 4.8 I first present the comparison between the re-measured photometry (y-axis) and the Bouwens et al. (2015a) total magnitudes (where my H-band magnitude is for the 0.36"-diameter aperture corrected for aperture losses appropriate for a compact source). Strong agreement is found fainter than 25^{th} magnitude where galaxies are typically at higher redshift and are more compact, better fitting the aperture correction assumption treating galaxies as point-like sources. Around $\sim 24^{th}$ magnitude (typically low-redshift z$<$ 4) discrepancy is found where galaxies are beginning to be resolved and are poorly described as point-like. The aperture correction therefore under-estimates their total magnitude. Critically for the high-priority target groups (those at high-z) agreement is found to be good. In the bottom panel of Figure 4.8 I present the photometric comparison between the re-measured H-band magnitude and the Harikane et al. (2016)

[9]https://github.com/Kitboyett/Supplementary-Thesis-material

catalogue. While agreement was found between my re-measured photometry and the Bouwens et al. (2015a) catalogue, a systematic photometric offset is found with Harikane et al. (2016). This systematic offset is believed to be due to Harikane et al. (2016) not including an aperture correction to their fixed aperture photometry and therefore under-estimating the total magnitude. From Table 4.8, the aperture correction for the 0.35" aperture adopted by Harikane et al. (2016) would be about 0.5 mag in F160W H-band, which broadly agrees with the offset at the faintest magnitudes (dominated by compact galaxies). The offset is larger at brighter magnitude (and typically larger galaxies), where the small aperture captures less of the flux.

By re-measuring the photometry of the main catalogues, all galaxies have been brought onto a uniform photometric scheme which is suitable for the NIRSpec MSA target selection. I note that some of the Harikane et al. (2016) objects which at face value from their catalogue would be too faint for selection, after correction might be appropriate for targeting. In Section 4.3.4 I go on to check the colours with the revised and uniform photometry to see if high-z is still the preferred interpretation. The goal is to obtain a refined target list of uniformly-selected galaxies, divided into priority classes (see Section 4.3).

4.3.4 Colour - Colour redshift analysis

As discussed in Chapter 1, the comparison of a galaxy's colours across adjacent broad-band filters can be used to identify the presence of the Lyman break in the galaxy's spectrum and hence whether it lies within a certain redshift range. The primary colour across the Lyman break should be red (the magnitude in the longer wavelength filter above the break is brighter than that below the break). A second colour is used to minimise contamination by low-z galaxies. These contaminants are most often with an evolved stellar population producing a 4000Å break or dusty (reddened) galaxies. Some low-mass stars in our own Galaxy (L- and T-dwarfs) can also mimic the colours of Lyman break galaxies in some filters due to their complex absorption spectra (including molecular lines). Criteria combining these two colours create a selection window which is often a box in a the colour-colour diagram (e.g., see Figure 4.12) with a diagonal region removed to avoid the region occupied by stars and the redshift tracks of evolved and dusty lower-z galaxies (e.g., Figure 4.10, showing the redshift z$\sim$ 7 dropout colour-colour diagram with tracks of various low-redshift interlopers).

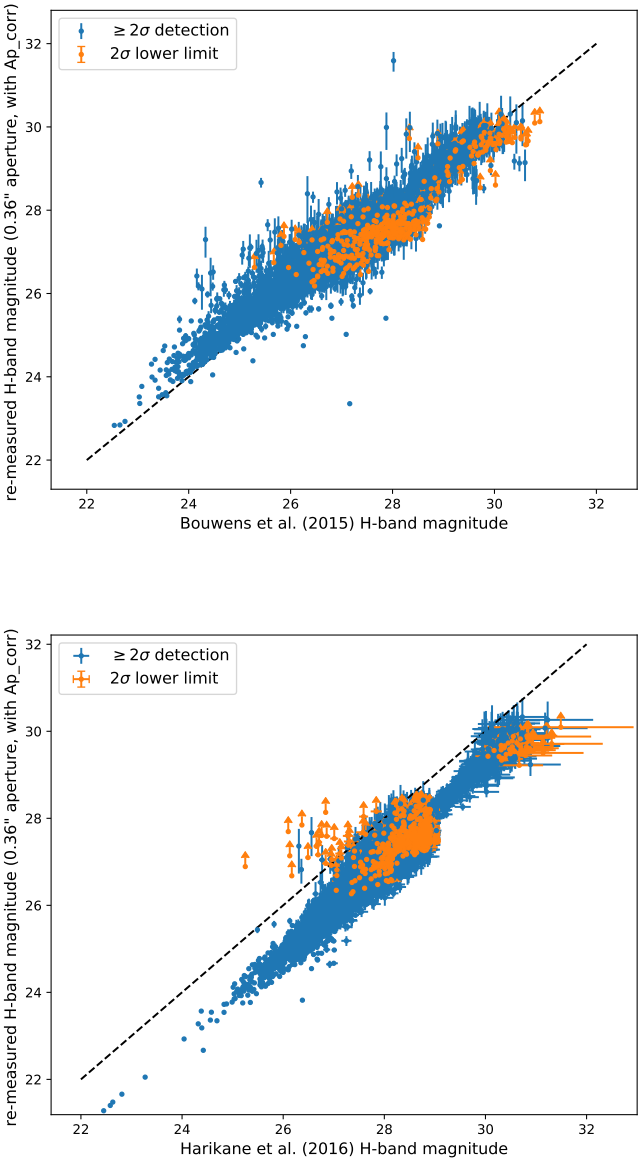

Figure 4.8: Comparison of the remeasured 0.36”-diameter aperture F160W H-band photometry corrected for aperture losses appropriate for a point source against the (Top) Bouwens et al. (2015a) catalogue total Kron magnitudes and (Bottom) Harikane et al. (2016) 0.35” aperture magnitudes. Top: good agreement in the photometry is found at fainter magnitudes (dominated by compact galaxies) with poorer agreement found for the brightest magnitudes (and typically larger galaxies), where the fixed aperture captures less of the flux. Bottom: A systematic offset is found in the Harikane et al. (2016) fluxes due to the addition of a correction for aperture flux losses in this work. In both panels those galaxies within the HUDF region, where deeper photometry is available, extend to fainter magnitudes and have tighter constraints at a given magnitude than the remaining sample outside the HUDF coverage.

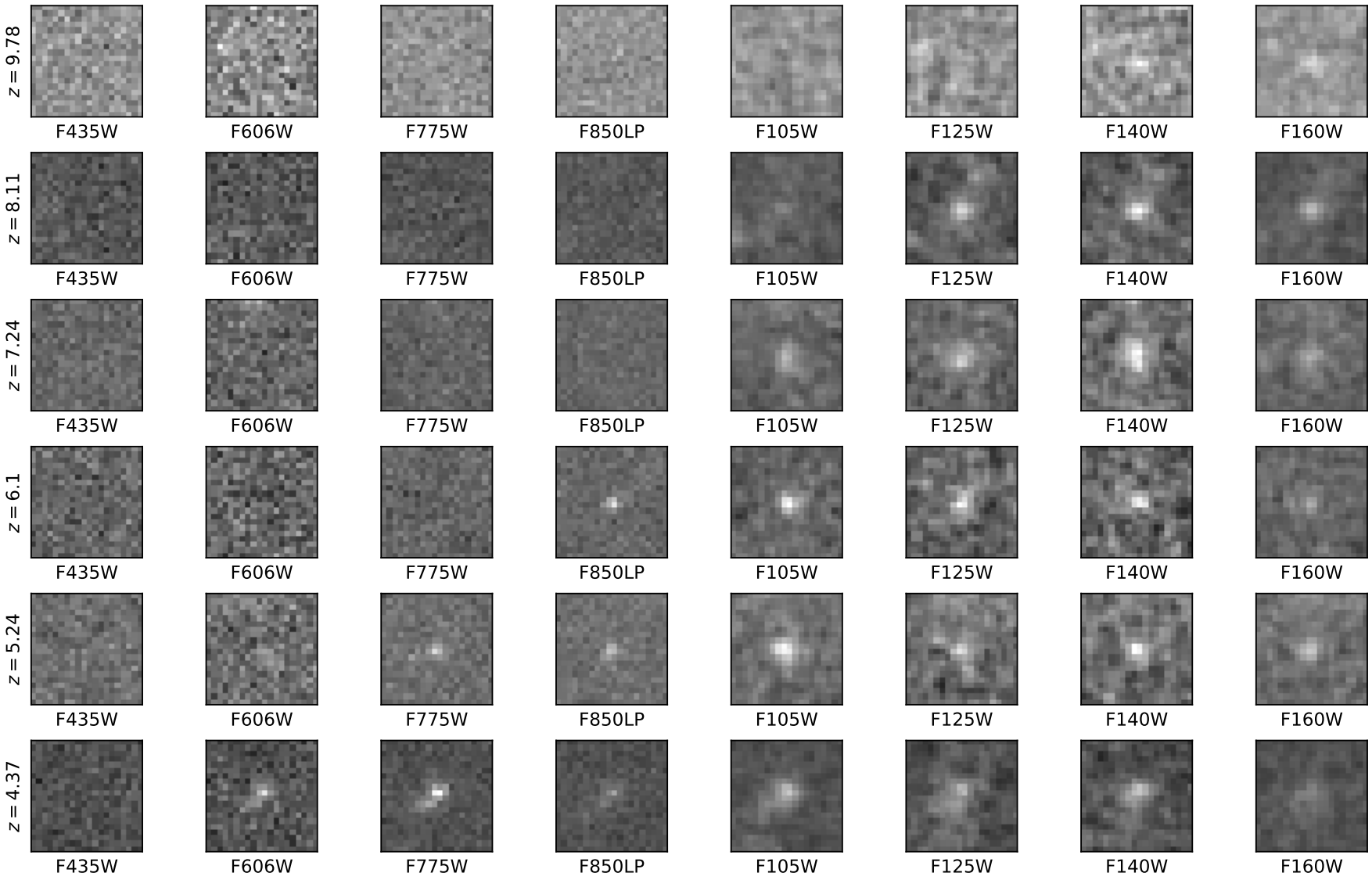

Figure 4.9: 3D-HST re-reduction imaging for galaxies at a range of photometric redshifts, highlighting the Lyman break dropout effect in the observed imaging. Photometric redshifts are indicated for these (bottom-to-top) B-, V-, i-, z-, Y- and J-drop outs.

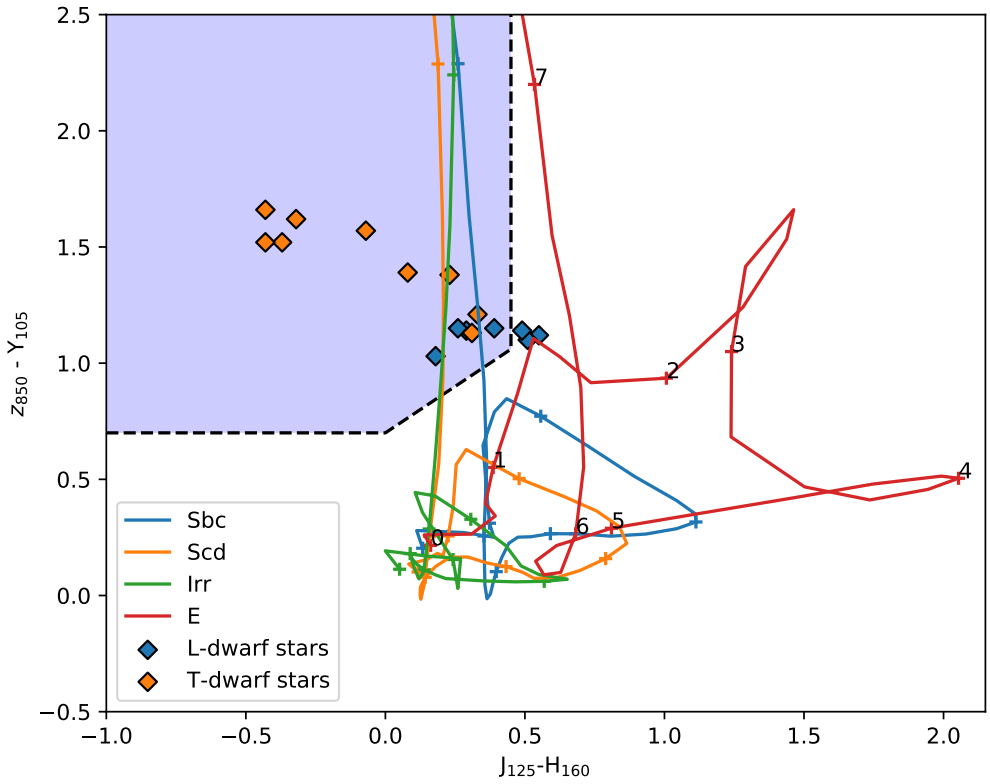

Figure 4.10: The $(J-H)$ vs. $(z-Y)$ colours used to select Lyman break galaxies, with the selection box from Bouwens et al. (2015a) indicated. Tracks for low-redshift templates from Coleman et al. (1980) are shown for several galaxy templates: Sbc (blue), Scd (orange), Irregular (green) and Elliptical (red), with tick marks at redshift intervals of $\Delta z = 1$. The Madau (1995) IGM opacity has been used at $z < 7$, and above this the Lyα forest is taken to be optically thick. Also plotted as diamonds are the colours for L- and T-dwarf stars from Wilkins et al. (2014).

Two of the three main LBG catalogues (Bouwens et al., 2015a; Harikane et al., 2016) take the same set of colour cuts to identify LBG at different redshifts (while Finkelstein et al. 2015 uses a photometric-redshift-based criterion). In my re-analysis I adopt a colour-colour selection based on the Bouwens et al. (2015a) colour regions, set out in Table 4.9, using the photometry re-measured in 0.36" diameter apertures for the colours (employing an aperture correction). For the undetected bands (at shorter wavelength) for each Lyman break selection, I also require S/N<2 in the 0.36" diameter aperture - a more stringent drop-out requirement.

Redshift range	y	x	break colour	slope colour	Cut out
$2.4 < z < 4.5$	$B_{435} - V_{606}$	$i_{775} - J_{125}$	y >1	x <1	y >1.6*x + 1
$4.5 < z < 5.5$	$V_{606} - i_{775}$	$z_{850} - H_{160}$	y >1.2	x <1.3	y >0.8*x + 1.2
$5.5 < z < 6.3$	$i_{775} - z_{850}$	$Y_{105} - H_{160}$	y >1	x <1	y >0.78*x + 1
$6.3 < z < 7.3$	$z_{850} - Y_{105}$	$J_{125} - H_{160}$	y >0.7	x <0.45	y >0.8*x + 0.7
$7.3 < z < 9.0$	$Y_{105} - J_{125}$	$J_{125} - H_{160}$	y >0.45	x <0.5	y >0.75*x + 0.525
$9.0 < z < 10.3$	$J_{125} - H_{160}$	-	y >1.2	-	-

Table 4.9: The Bouwens et al. (2015a) colour-colour criteria for B-, V-, *i*-, *z*-, Y- and J-band drop-outs, that I adopt for the Lyman break colour criteria. The expected redshift distribution for galaxies selected in each drop-out filter overlaps, see Figure 4.11, and I adopt the Bouwens et al. (2015a) redshift dividers to separate between drop-out filters. In addition to these criteria, non-detections are required in available the wavebands below the Lyman break. I require S/N(B) < 2 for V-band dropouts, S/N(B) and S/N(V) < 2 for *i*-band dropouts, S/N(B), S/N(V) and S/N(i) to be < 2 for *z*- and Y-band dropouts. For J-band drop-outs I do not have a longer wavelength filter beyond the H-band to constrain the spectral slope colour and I use the break colour alone, along with the condition that the S/N(B), S/N(V), S/N(i), S/N(z) and S/N(Y) are all < 2.

Using the re-measured photometric magnitudes, or 2σ magnitude limits when appropriate, colour-colour positions for each target are used to determine whether they meet the Bouwens et al. (2015a) criteria for each redshift bin. Figures 4.12 and 4.13 provides the colour-colour diagrams for i-, z- and Y-band drop-outs for the Bouwens et al. (2015a) GOODS and HUDF samples, the (Bouwens et al., 2015a) criteria set as the purple box (B- and V-band drop-out colour diagrams for Bouwens et al. 2015a and versions for the Finkelstein et al. 2015 and Harikane et al. 2016 samples are placed in Appendix A.1). I assign quality flags to the galaxies on the basis of whether the re-measured photometry meets the Lyman Break colour-colour selection requirement for each drop-out redshift range. Where the photometry sits within the colour

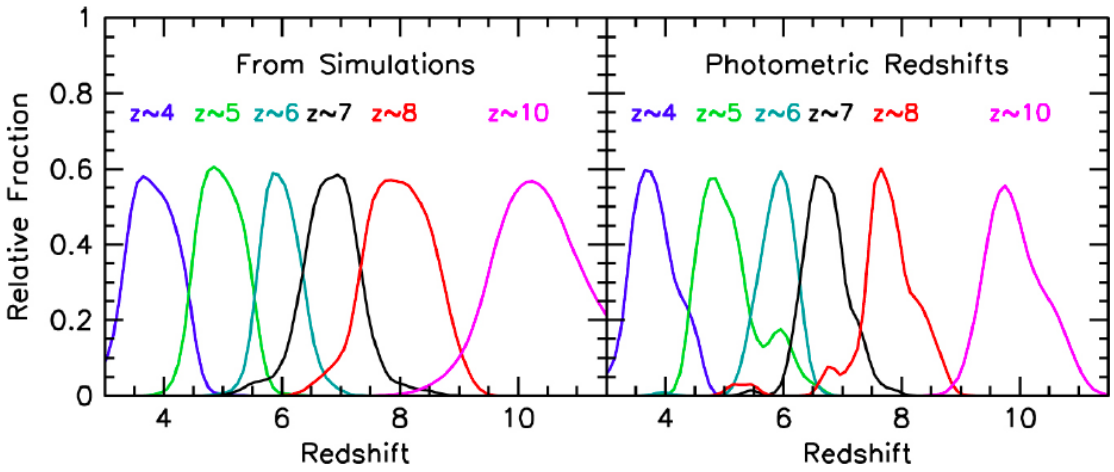

Figure 4.11: The expected redshift distribution (left) and measured photometric redshift distribution (right) for B-, V-, i-, $z-$, Y- and J- band drop-outs selected using Bouwens et al. (2015a) colour criteria. The agreement between their EAZY photometric redshift estimates and the simulated expectation distribution demonstrates the ability for the selection criteria to identify the redshift within a redshift window. Taken from Bouwens et al. (2015a)

selection box, these galaxies are flagged as "good" (including where the filter shortward of the break is undetected, and the colour cut is met using the 2σ limit in this waveband). I also flag as "possible high-z" those galaxies which are undetected in the band shortward of the putative Lyman break, but whose lower limit on the colour across the break falls outside the selection window (but where the limit means the photometry may still be consistent with the galaxy being in the colour selection box). Finally, I flag as "unlikely" those galaxies where the remeasured photometry places them outside the colour selection box but within 1σ of the demarcation line, and flag as "bad" those whose photometry is inconsistent at the $> 1\sigma$ level of being in the colour selection box. The number of good, possible high-z and unlikely galaxies is presented in Table 4.10 for each drop-out redshift range.

Across the three main catalogues I find that there is good agreement with the input catalogue redshift estimate (where Bouwens et al. 2015a and Finkelstein et al. 2015 each provide photometric redshift estimates, and Harikane et al. 2016 just subdivides into drop-out categories). In each of Bouwens et al. (2015a), Harikane et al. (2016) and Finkelstein et al. (2015), 68%, 73% and 71% of galaxies have re-measured photometry that agrees with the colour criteria for the photometric redshift bin from the input catalogues. In Section 4.3.5 I go further to check the photometric redshifts

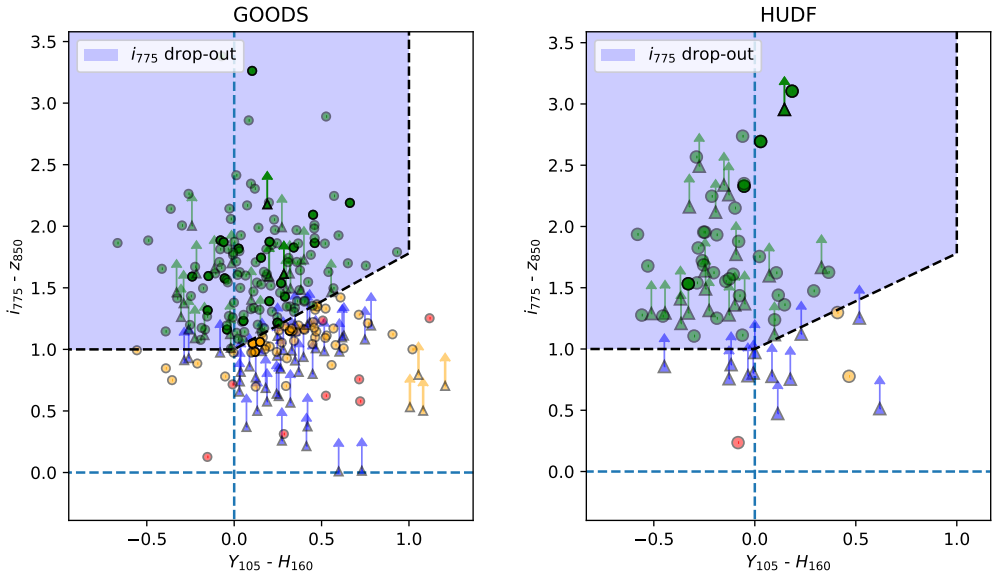

Figure 4.12: Colour-colour diagram from the remeasured photometry for i-band drop-out Lyman break candidates at $z \sim 6$ from the Bouwens et al. (2015a) catalogue. Those within the GOODS North and South fields are shown on the left, with those in the XDF/HUDF shown on the right. The purple shaded region displays the LBG colour criteria for drop-out selection adopted from (Bouwens et al., 2015a). I only plot those galaxies detected at 4σ in the H-band, and where the re-measured position did not significantly shift (i.e. I am analysing the same object as in Bouwens et al. 2015a), which form two of my selection criteria. As is customary with colour-colour plots (Bouwens et al., 2015a; Harikane et al., 2016), error bars have been removed to aid visualisation and due to the large number of sources. For clarity a S/N cut in the Y-band has been set at 5 for the GOODS plot (so that the figure is not swamped by low-significance points with large error bars), but all galaxies are retained as part of the analysis. Galaxies are colour coded: green circles indicates galaxies which are detected in all the filters plotted and which match the colour criteria (the purple shaded region); orange circles have photometry just outside the colour selection box, but lie within 1σ of it; and red circles indicate galaxies whose remeasured photometry places them significantly outside the Lyman break colour selection region, and hence these are no longer good high-z candidates. Where galaxies are not detected ($< 1\sigma$) in the i-band, I plot the $2\,\sigma$ lower limit on the $B - V$ colour. Green triangles are non-detections in the drop-out filter (i-band) where the lower-limit on the $B - V$ colour places them within the Lyman break selection region; and blue triangles are non-detections in the i-band where the limit on the colour may lie below the Lyman break selection, but as this is a lower limit on the colour they may still be consistent with being at high-z. Some i-band galaxies would be candidates for Priority class 4 in the JADES NIRSpec target selection, where we will give priority to galaxies with high enough star formation rates for emission lines to be detectable at high significance with NIRSpec and this translates to a magnitude limit on a rest-UV waveband above the Lyα break (in the case of the i-drops this would be the F105W Y-band). Those objects meeting this requirement of $AB = 26.5$ mag for the Medium pointings within GOODS, and 27.5 mag in the Deep NIRSpec pointing on the HUDF, are shown as bold symbols.

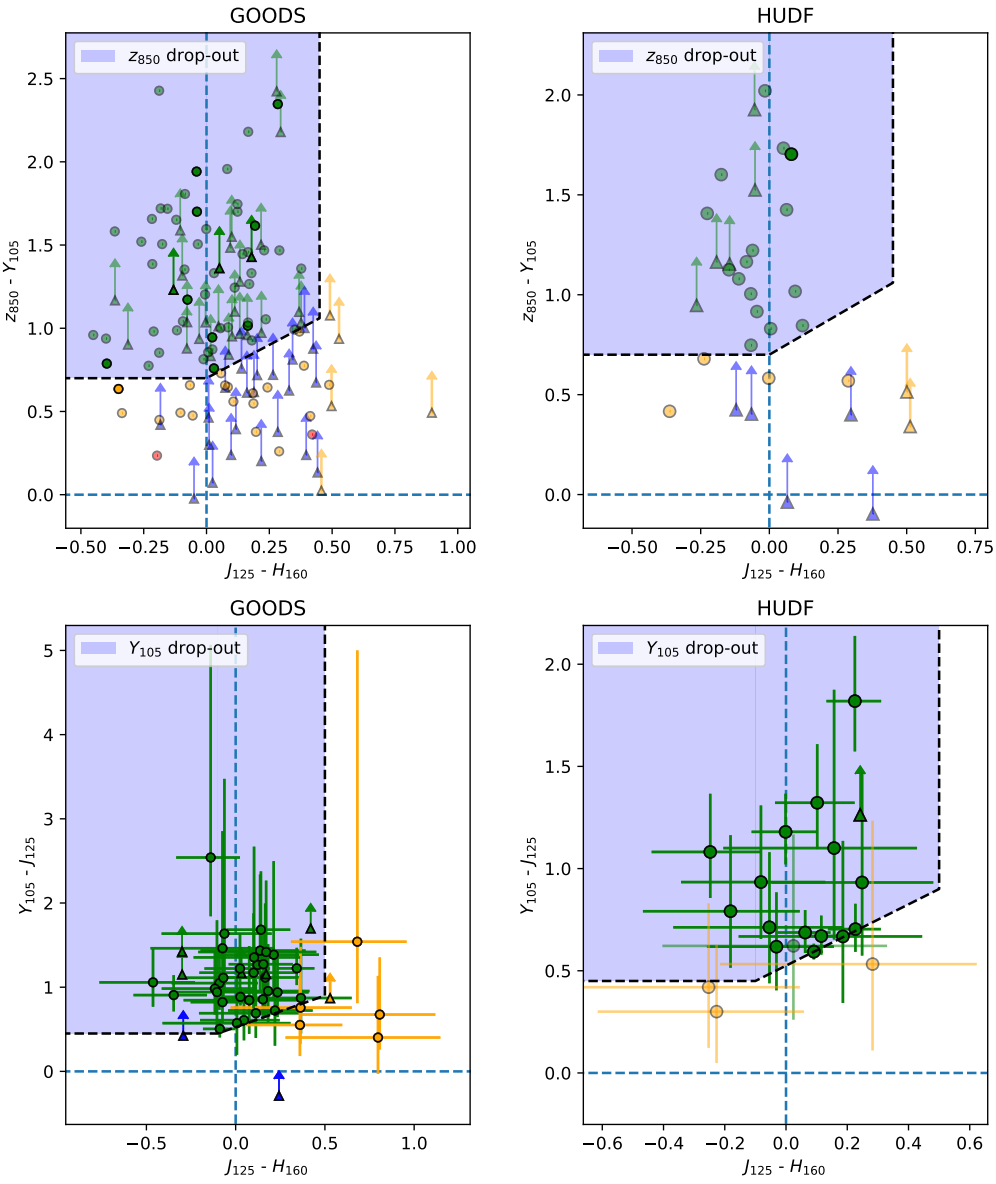

Figure 4.13: As for Figure 4.12, but the z- and Y-band drop-outs at z$\sim$ 7 & 8 are shown. For clarity a Y-band S/N cut has been set at 5 for the z-band drop-out GOODS plot, but all galaxies are retained as part of the analysis. Some z-drops would be candidates for Priority class 4 in the JADES NIRSpec target selection, where we will give priority to galaxies with high enough star formation rates for emission lines to be detectable at high significance with NIRSpec and this translates to a magnitude limit on a rest-UV waveband above the Lyα break (in the case of the z-drops this would be the J-band). Those objects meeting this requirement of $AB = 26.5$ mag for the Medium pointings within GOODS, and 27.5 mag in the Deep pointing on the HUDF, are shown as bold symbols. Some Y-band galaxies would be candidates for Priority classes 1 & 2, where we will give priority to the high-z galaxies that are sufficiently bright to confirm the redshift with NIRSpec — this translates to a magnitude limit for the Y-drops in the H-band. Those objects meeting this requirement of $AB = 28.5$ mag for the Medium pointings within GOODS, and 29.5 mag in the Deep pointing on the HUDF, are shown as bold symbols. Errorbars are presented for the Y-band drop-out panels where the numbers are sufficiently low to avoid over-crowding.

drop-out	Bouwens et al. (2015) [#Agree (1σ) /total]	Harikane et al. (2016) [#Agree (1σ) /total]	Finkelstein et al. (2015) [#Agree (1σ) /total]
$B-band$	3581 (665) / 4974	3918 (725) / 5185	3253 (285) / 4068
$V-band$	1181 (151) / 1712	1296 (144) / 1821	1271 (193) / 2014
$i-band$	365 (58) / 613	399 (56) / 653	300 (63) / 666
$z-band$	184 (31) / 332	271 (59) / 428	159 (21) / 341
$Y-band$	80 (12) / 124	0 (0) / 0	65 (21) / 132
$J-band$	5 (0) / 6	0 (0) /0	0 (0) / 0
All	5395 (918) / 7761	5884 (984) / 8087	5048 (583) / 7221

Table 4.10: The fraction of galaxies where the agreement of the re-measured photometry with the colour-colour criteria for the input catalogues redshift is considered to be good (either classed as "good" or "possible high-z") or "unlikely"(those lying within 1σ, given in brackets).

with the revised and uniform photometry and to see if high-z is still the preferred interpretation.

4.3.5 Photometric redshifts of Lyman break galaxies

As discussed in the previous Section, the photometry of a galaxy in several broadband filters can be used to identify candidate Lyman break galaxies in a colour-colour diagram, where the Lyman break falls between two adjacent filters for certain redshift ranges. However, a drawback is that some lower-redshift galaxies and local brown dwarf stars can mimic the colours of Lyman break dropouts in the selected filters. To place further constraints on the redshift and to aid the rejection of lower redshift interlopers, I make use of the additional re-measured photometry in all the available wavebands. So, in addition to a Lyman break selection based on a small number of colours (and non-detections in wave bands at wavelengths shortward of the putative spectral breaks), I also consider a full-SED fitting approach to determine the photometric redshift. Here measurements of the photometry in multiple broadband filters sample the SED of a galaxy, essentially providing a low resolution spectrum with sensitivity to the overall spectral shape (in particular continuum breaks such as the Lyman break and the Balmer and 4000Å break) and potentially extremely high equivalent width emission lines (see Chapter 3). The shape and intensity of a galaxy's rest-frame SED is sensitive to many of the galaxy's fundamental properties, including stellar mass, star formation history, dust content, initial mass function (IMF) and metallicity. By varying these properties, along with the redshift of a template spectrum (and altering the normalisation to find the best-fit stellar mass), we can

see what range of redshifts and galaxy properties are consistent with the photometry. This is the basis of "photometric redshifts" (e.g., Lanzetta et al., 1996; Wolf et al., 2001; Franx et al., 2003; Mobasher et al., 2004). Typically, simulated galaxy spectrum templates (e.g., Bruzual & Charlot 2003 population synthesis models) covering a larger parameter space of galaxy properties are used to find the most likely redshift and to identify the set of parameters that most closely replicate the observed SED. It is now standard practice in studies of galaxies to process their SEDs through fitting codes (e.g., BEAGLE, Chevallard & Charlot 2016; EAZY, Brammer et al. 2008; MAGPHYS, da Cunha et al. 2008) to identify the photometric redshift and other fundamental properties. Often these codes output probability density functions with redshift, which show where there may be secondary redshift solutions which are possible (e.g. the aliasing of the Lyman break at high redshift with the Balmer break at moderate redshift) and allowing the relative probabilities in these peaks to be assessed.

I provide a catalogue of the photometry flux densities and associated uncertainties for photometric redshift fitting. I make use of the Bayesian code BEAGLE (Chevallard & Charlot, 2016), which was previously used in Chapter 2. However, unlike in Chapter 2, where I knew the redshift of the sources from the emission line spectroscopy and wanted to fit the galaxy properties to the photometry and line fluxes, for this sample of candidate high redshift targets in the JADES fields we typically do not know the true redshifts (except for a very small number of Lyα emitters or emission line detections from ALMA), and hence I also treat the redshift as a free parameter for BEAGLE to fit. BEAGLE is set up adopting a Chabrier IMF (Chabrier, 2003), a linear-exponential star formation rate (SFR$\propto t * exp(-t/\tau)$) and a Charlot & Fall (2000) two-component dust extinction law (the details of the parameter ranges are given in Table 4.11). The combination of a linear and an exponential component allows for a star forming history parameterisation that includes both a rising SFH which is appropriate at high redshift (Salmon et al., 2015, e.g.,), and also a falling SFH as is more appropriate at lower redshifts. The two-component Charlot & Fall (2000) dust extinction model accounts for extinction on the continuum emission in the ISM of the galaxy and the additional extinction experienced by nebular emission which arises from the yet-to-be dispersed birth clouds that surround young-massive stars, the regions from where the nebular emission is created (further details on the application of this parameterisation are given in Chevallard & Charlot 2016). I utilise the latest version of the Bruzual & Charlot (2003) spectral population synthesis models (see Gutkin et al. 2016, section 2.1 for updates). A uniform prior is set

Parameter	Range	Description
τ	$6 < log_{10}(\tau/yr) < 12$	Star formation timescale
Z	$-2.2 < log_{10}(Z/Z_{\odot}) < 0.4$	Metallicity, $Z_{\odot} = 0.01524$
M	$4 < log_{10}(M/M_{\odot}) < 13$	Mass (integral of SFH)
max(Age)	$6 < log_{10}(max(Age/yr)) < 12$	Maximum stellar age
z	$0 < z < 15$	Redshift
z_{form}	$z_{form} < 15$	Maximum formation redshift*
U	$-4 < log_{10}(U) < -1$	Galaxy-wide ionization parameter
ξ_d	$0.1 < log_{10}(\xi_d) < 0.5$	Galaxy-wide dust-to-metal mass ratio
τv_{eff}	$0 < \tau v_{eff} < 2$	V-band attenuation optical depth
μ	$\mu = 0.4$	Relative V-band attenuation from diffuse ISM to total**

Table 4.11: Beagle (Chevallard & Charlot, 2016) parameter ranges set for photometric redshift fitting, with uniform priors set over each.
∗ No model age allowed to exceed the age of the Universe
∗∗ See Charlot & Fall (2000); Chevallard & Charlot (2016) for definition.

over each of the model parameters (which are listed in Table 4.11). For each galaxy BEAGLE returns a posterior distribution function (PDF, a probability distribution) for the redshift. The PDF sometimes favours a single unambiguous redshift solution, however instances do occur when multiple redshift solutions can fit the SED well. BEAGLE provides warning flags when the PDF is ambiguous (with two or more clear redshift solutions).

Across the three main catalogues of Bouwens et al. (2015a) (containing 7761 galaxies), Harikane et al. (2016) (containing 8087 galaxies) and Finkelstein et al. (2015) (containing 7346 galaxies) with an overlap of 2828 galaxies appearing in all three, BEAGLE was able to assign a single redshift solution to the majority of galaxies. When the BEAGLE `multinest` peak-finding feature (which considers the posterior density function of all parameters, not just the redshift) identifies only a single solution, the redshift is determined to be unambiguous and a second redshift solution isn't reported. This accounts for 73.8%, 73.0% and 78.7% of galaxies in the Bouwens et al. (2015a), Harikane et al. (2016) and Finkelstein et al. (2015) catalogues. The remaining galaxies all report two redshift solutions as well as the ratio of integrated probabilities between the two solutions. Here the redshift solution is ambiguous, between the primary (that with the higher integrated probability) and the secondary. I consider the primary redshift solution to still be constraining if it's maximum probability (P1) is over twice that of the secondary solution maximum probability (P2) e.g.,

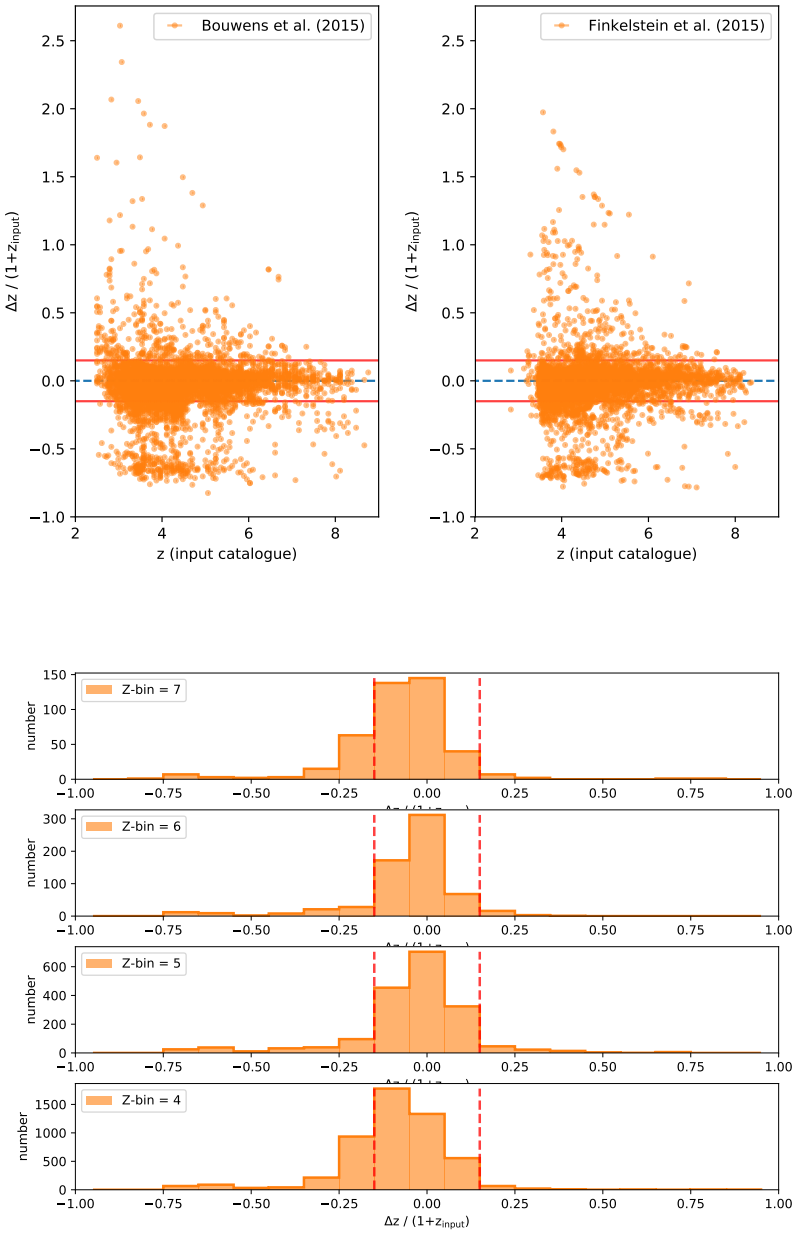

Figure 4.14: $\Delta z/(1 + z_{input})$ distribution for the three main catalogues, where $\Delta z = z_{beagle} - z_{input}$, red lines denote 0.15 outlier tolerance. Top: The continuous photometric redshifts of Bouwens et al. (2015a) and Finkelstein et al. (2015) allow the distributions to be plotted, highlighting the good agreement of the majority of galaxies and identifying a cloud of galaxies below $\Delta z/(1 + z_{input}) \sim -0.3$ that BEAGLE determines to be lower redshift interlopers. Bottom: The discrete redshift values of Harikane et al. (2016) at z=4, 5, 6 and 7 are presented as histograms, where again a similar low level cloud of galaxies can be seen. The galaxies in this low redshift solution cloud are flagged as potential interlopers.

Table 4.12: The fraction of galaxies that had a photometric redshift in the same drop-out filter redshift range as the input catalogue (designated either by the photometric redshift from Finkelstein et al. 2015 or from the drop-out filter allocation from Bouwens et al. 2015a; Harikane et al. 2016).

Redshift range	Bouwens et al. (2015)	Harikane et al. (2016)	Finkelstein et al. (2015)
$2.4 < z < 4.5$	4382 / 4974	4656 / 5185	3566 / 4068
$4.5 < z < 5.5$	1108 / 1712	1099 / 1821	1268 / 2014
$5.5 < z < 6.3$	344 / 613	358 / 653	378 / 666
$6.3 < z < 7.3$	155 / 332	197 / 428	171 / 341
$7.3 < z < 9.0$	69 / 124	0 / 0	92 / 132
$9.0 < z < 10.3$	5 / 6	0 / 0	0 / 0
all	5909 / 7761 (76%)	6310 / 8087 (78%)	5475 / 7221 (76%)

P2/P1 < 0.5. Galaxies with two redshift solutions with one dominating accounting for 22.4%, 22.4% and 18.1%. The redshift solution for galaxies with a probability ratio above 0.5 is considered to be ambiguous. This accounts for the remaining 3.79%, 4.65% and 3.18% of galaxies in the three main catalogues. Flags are assigned to the final galaxy catalogue reflecting the unambiguous, ambiguous yet constraining (P2/P1 < 0.5), ambiguous and no redshift solutions (which accounts for a total of 5 galaxies across the three catalogues). A more justified P1/P2 value could be obtained if I considered the model comparison from the Bayesian evidence calculations in BEAGLE but this is beyond the scope of this work and not necessary for the project goals.

I consider how the BEAGLE photometric redshifts compare to the input catalogue reported redshift and also the Lyman break selection. I would like to know whether galaxies that did not match the Lyman break criteria for their input catalogue drop-out filter redshift range have a BEAGLE photometric redshift that also disagrees with that redshift range. As can be seen in Tables 4.12, 4.13 and 4.14, where the fraction of objects with a BEAGLE redshift in agreement with the input catalogue redshift increases for objects with "good" Lyman break colour-colour agreement and is lower in galaxies which do not meet the colour criteria. This latter point highlights particularly those galaxies that are likely to be in a neighbouring drop-out band or those that are low redshift interlopers.

The majority of objects show consistency between the BEAGLE photometric redshifts and redshift ranges associated with the drop-out filter reported in the input catalogues of Bouwens et al. (2015a) (76% agreement) and Harikane et al. (2016)

Table 4.13: The fraction of galaxies that had a photometric redshift in the same drop-out filter redshift range as the input catalogue for the sources with Lyman break colour-colour agreement (either classed as "good", "possible high-z" or "unlikely"). This Lyman break colour-colour agreement sample displays a higher agreement fraction between the BEAGLE photometric and catalogue input redshift range than the complete sample in Table 4.12

Redshift	Bouwens et al. (2015)	Harikane et al. (2016)	Finkelstein et al. (2015)
$2.4 < z < 4.5$	3910 / 4246	4247 / 4643	3263 / 3538
$4.5 < z < 5.5$	930 / 1332	945 / 1440	1061 / 1464
$5.5 < z < 6.3$	279 / 423	277 / 455	246 / 363
$6.3 < z < 7.3$	123 / 215	163 / 330	115 / 180
$7.3 < z < 9.0$	61 / 92	0 / 0	69 / 86
$9.0 < z < 10.3$	4 / 5	0 / 0	0 / 0
all	5307 / 6313 (84%)	5632 / 6868 (82%)	4754 / 5631 (84%)

Table 4.14: The fraction of galaxies that had a photometric redshift in the same drop-out filter redshift range as the input catalogue for the sources with Lyman break colour-colour disagreement (classed as "bad"). This Lyman break colour-colour disagreement sample displays a lower agreement fraction between the BEAGLE photometric and catalogue input redshift range than the complete sample in Table 4.12

Redshift	Bouwens et al. (2015)	Harikane et al. (2016)	Finkelstein et al. (2015)
$2.4 < z < 4.5$	506 / 787	409 / 542	303 / 530
$4.5 < z < 5.5$	173 / 358	154 / 381	207 / 550
$5.5 < z < 6.3$	62 / 170	81 / 198	132 / 303
$6.3 < z < 7.3$	27 / 91	34 / 98	56 / 161
$7.3 < z < 9.0$	13 / 41	0 / 0	23 / 46
$9.0 < z < 10.3$	1 / 1	0 / 0	0 / 0
all	782 / 1448 (54%)	678 / 1219 (56%)	721 / 1590 (45%)

(78% agreement), or with the same redshift range as the Finkelstein et al. (2015) EAZY (Brammer et al., 2008) derived photometric redshifts (76% agreement). The agreement is greater in objects with Lyman break colour criteria agreement ($\sim 83\%$) and lower in galaxies which do not meet the colour criteria ($\sim 52\%$). I flag galaxies where the photometric redshift does not match the input catalogue drop-out filter (or respective redshift range). Photometric redshifts do not have the same limited ranges as the Lyman-break colours, which typically have a top-hat (tending to Gaussian) window function for selection with redshift (see e.g., Wilkins et al., 2011; Bouwens et al., 2015a), so are potentially sensitive to a wider range of redshifts (although much of the power will come from the dominant spectral feature, the Lyman break). Although a potential disadvantage of photometric redshifts is that the assumed templates may not properly match the SED of high redshift galaxies (which we won't really know until NIRSpec). Here, potential Population III stars and the line emission from EELGs may not be reflected in current template spectra, whereas the Lyman break is a property extrinsic to the galaxy (dependent on the optical depth of the IGM to Lyα) so may be more robust, but as stated, potentially less complete with redshift.

In addition to presenting the Lyman break colour selected drop-out filter, Bouwens et al. (2015a) also determines the photometric redshifts for each galaxy (using the SED fiting code EAZY Brammer et al. 2008). A comparison of the input catalogue photometric redshift and my BEAGLE photometric redshift is plotted in Figure 4.14, where the redshift difference ($\Delta z = z_{beagle} - z_{input}$) is normalised by the input catalogue redshift ($1 + z_{input}$). To accommodate the Harikane et al. (2016) catalogue I also present the histogram normalised redshift change for each drop-out filter subsample, the input catalogue redshift for each galaxy in the drop-out filter is taken as the redshift sub-division given by Harikane et al. (2016) (B-band is $z = 4$, V-band is $z = 5$, i-band is $z = 6$ and z-band is $z = 7$). In these figures, galaxies with a negative normalised Δz are those that BEAGLE allocates to lower redshift solutions than the input redshift estimate and I note the presence of a cloud of objects that BEAGLE reports as being at much lower redshifts compared to the input catalogues, although many of these have a secondary higher redshift solution. I also note the offset shift in the Harikane et al. (2016) histograms where the mean $\Delta z/(1 + z_{input})$ offset for the catalogue is -0.07. This indicates that the adopted redshifts of z= $4, 5, 6$ and 7 for each drop-out band are not accurate and slightly overestimate the typical redshift for each band, which is not unexpected given the redshift breadth sensitive to each

drop-out filter.

I note a small number of galaxies have been fitted with a primary redshift solution at $z_{\rm beagle} > 11$, a solution much higher than the input catalogue photometric redshift and would place these galaxies in the top priority class for target selection (see Section 4.3). These photometric redshift solutions are identified to be overestimates, generated by a negative flux measured in the F140W JH-band and mimicking a JH- Lyman break drop-out. Many of these galaxies have detections (S/N $>$ 2) in the Y- or J-band that contradict this redshift solution. In each of the $\sim$ 10 cases, the position of the photometric aperture (fixed to the H-band detection image position) was partly off image in the 3D-HST F140W JH-band (i.e., the 3D-HST JH-band imaging does not have as complete coverage as the H-band image with small regions missing).

The majority of galaxies form a locus around Δz $\sim$ 0 and for Bouwens et al. (2015a); Harikane et al. (2016) and Finkelstein et al. (2015) 84%, 75% and 86% agree within $|\Delta z| / (1 + z_{input}) < 0.15$ (marked as red horizontal dashed lines in the Figures). This is a tolerance that I adopt from galaxy surveys (e.g., Merlin et al., 2021), where a measured spectroscopic redshift is compared to a photometric redshift estimate and used to identify catastrophic outliers (when the photometric redshift is significantly different to the spectroscopic value). In galaxy surveys catastrophic outlier rates are typically found to be of order a few percent (e.g., Merlin et al., 2021), much lower than what I recover in this work. Harikane et al. (2016) presents a higher fraction of catastrophic outliers due to their sub-division of redshifts into discrete bins based on the drop-out band rather than on continuous photometric redshifts (as do Bouwens et al. 2015a; Finkelstein et al. 2015). If I restrict the catalogues to only those that found "good" agreement with the Lyman break colour-colour selection (see Section 4.3.4) the catastrophic outlier rate decreases to a reasonable 5%, 12% and 3% in Bouwens et al. (2015a); Harikane et al. (2016); Finkelstein et al. (2015) respectively, this effect can be seen in Figure 4.15.

In light of the photometric redshift fits, and the re-analysis of the Lyman break colour-colour selection, I am able to clean the target lists for JADES. I employ four criteria to arrive at a catalogue of the most robust sources:

1. Detection in the H-band at S/N$>$ 4 (0.36" diameter aperture)

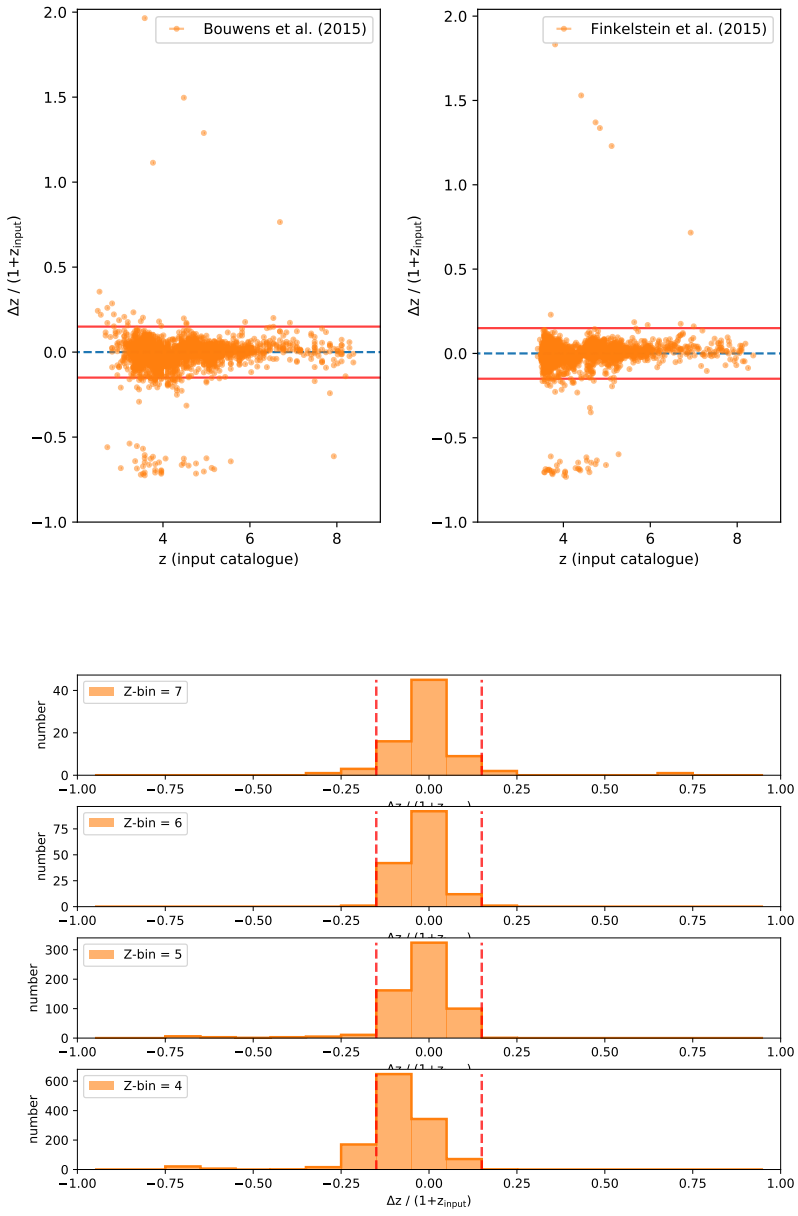

Figure 4.15: $\Delta z/(1+z_{input})$ distribution for the three main catalogues, where $\Delta z = z_{beagle} - z_{input}$, red lines denote 0.15 outlier tolerance. Sample restricted to those with "Good" Lyman break colour-colour agreement and shows fewer catastrophic outliers than the full sample in Figure 4.14. Top: The continuous photometric redshifts of Bouwens et al. (2015a) and Finkelstein et al. (2015) allow the distributions to be plotted, highlighting the better agreement of the majority of galaxies and a much reduced cloud of galaxies below $\Delta z/(1+z_{input}) \sim -0.3$ that BEAGLE determines to be lower redshift interlopers. Bottom: The discrete redshift values of Harikane et al. (2016) at z=4, 5, 6 and 7 are presented as histograms, where again a tighter agreement is found with a reduced lower redshift cloud of galaxies.

2. Not to be flagged for an astrometric offset[10], to ensure I have the same object

3. Agreement with the colour criteria to be classed as "good", "possible high-z" or "unlikely"(those lying within 1σ of the colour criteria)

4. The BEAGLE photometric redshift to agree with the catalogue reported drop-out filter redshift range (for Finkelstein et al. 2015 I require the catalogue photometric redshift and the BEAGLE redshift to lie in the same drop-out filter redshift range) to remove galaxies with lower redshift solutions (interlopers).

The clean criteria reduces the Bouwens et al. (2015a); Harikane et al. (2016) and Finkelstein et al. (2015) catalogues to 4402, 4537 and 4075 galaxies. Each criteria step reduces the sample: $\sim$20% is removed by the H-band S/N cut, this reflects the input catalogues source selection on a combined WFC3/IR detection image to select galaxies that may be lower S/N in just the H-band; $\sim$3% is removed by astrometric offset flag, noting cases when re-centring may have located on a nearby bright source; $\sim$11% is removed by the Lyman break drop-out colour criteria; and $\sim$ 10% is removed by the photometric redshift criteria. Table 4.15 presents the break down of the clean sample in each catalogue and the overlap between them, a total of 7221 unique objects. These clean objects are sorted into their relevant priority class, Table 4.16 and Tables A.2 and A.7 in the Appendix, present the priority class 1-3 and 4-6 objects.

I retain the other targets which did not meet the above four criteria, and these are placed in lower priority classes for potential targeting if there is space on the MSA - we are in particular interested in getting spectroscopy for some galaxies just outside the colour—colour selection windows used, or with ambiguous photometric redshifts, so that we can assess the low-redshift contamination rate and effectiveness of the selection. This will be important for other aspects of the JADES programme, in particular recovery of luminosity functions from Lyman break galaxies in the NIRCam imaging (many of which will not have NIRSpec spectra). The validation of photometric redshifts with our spectroscopy is also a key goal. For galaxies not meeting the four criteria for "robustness" (detailed above), I demoted more marginal sources potentially at the highest redshifts ($z >\sim 8$) from Classes 1 & 2 in Table 4.2 to Class 3. At $z > 6$, sources which are faint or less reliable are placed in Class 6 rather than Class 4. For the lower-redshift Lyman break galaxies ($z < 6$), those that are less reliable are moved from Class 7 to Class 8 where the chances of them being observed

[10]After correcting for the measured Bouwens et al. (2015a) systematic offset.

are significantly reduced (and more reliable sources will instead be favoured in the same region of sky competing for the same microshutters on NIRSpec).

4.3.6 Sizes and surface brightness profiles of Lyman break galaxies

As noted previously, not only are the brightness and photometric redshift of galaxies key considerations in the ranking of high redshift targets for observation with JWST-NIRSpec, but also the size and surface brightness profile will affect the amount of light entering a NIRSpec microshutter (along with how well centred the galaxy is within a shutter). Hence, as well as the accurate astrometry and multi-waveband photometry, I wish to measure the size and shape information for the potential targets - this will ultimately be used to assess whether the S/N of the spectrum would be sufficient for our science goals (i.e. determining whether an object is a worth targeting with NIRSpec), and also for targeted objects this information is crucial to determine the aperture corrections to the extracted spectrum which will be a strong function of wavelength (due to the PSF varying with wavelength) - this is necessary to achieve flux calibration and hence line ratios and spectral shape information.

GALFIT (Peng et al., 2002), is a surface brightness modelling and fitting tool which determines the best-fit model that (once convolved with the PSF) minimises the residuals in the model-subtracted image (e.g., see Figure 4.16). GALFIT is run on each galaxy's H-band image to provide measurements of its characteristic radius, position angle and axis ratio. Although the resolution of HST is better at shorter wavelengths, these Lyman break galaxies are often faint (or undetected if below Lyα) in the ACS filters, which probe far into the rest-frame UV. Hence I use the F160W H-band from WFC3 for determining the structural parameters. For the $z \sim 4$ Lyman breaks, the H-band corresponds approximately to the rest-frame B-band, but at the highest redshifts we are targeting, the H-band will sample the rest-frame UV. Hence the surface brightness profiles in this band may not fully reflect the underlying overall stellar population (and such work will await imaging from JWST/NIRCam at longer wavelengths), but the surface brightness profiles in the rest-UV will be indicative of the young stellar population which will power the emission lines which we are sensitive to with NIRSpec spectroscopy - and hence this is most suited to our JADES catalogue for NIRSpec target selection. Equally the position angle and axis ratio can also become useful parameters when designing the most efficient MSA configuration, because the individual shutters are 0.2×0.4arcsec (i.e. oblong) and so the flux falling

redshift range	Bouwens et al. (2015) total / in H16 / in F15 / in Both	Harikane et al. (2016) total / in F15 / in B15/ in Both	Finkelstein et al. (2015) total / in B15 / in H16 / in Both
B-band	3290 / 2227 / 1668 / 1336	3493 / 1633 / 2227 / 1336	2832 / 1670 / 1635 / 1337
V-band	747 / 500 / 538 / 414	739 / 521 / 501 / 415	903 / 538 / 519 / 414
i-band	221 / 139 / 139 / 102	202 / 133 / 136 / 101	205 / 138 / 133 / 101
z-band	91 / 56 / 49 / 38	103 / 56 / 58 / 38	83 / 48 / 56 / 38
Y-band	49 / 0 / 24 / 0	0 / 0 / 0 / 0	52 / 24 / 0 / 0
J-band	4 / 0 / 0 / 0	0 / 0 / 0 / 0	0 / 0 / 0 / 0
all	4402 / 2922 / 2418 / 1890	4537 / 2343 / 2922 / 1890	4075 / 2418 / 2343 / 1890

Table 4.15: The number of galaxies in each of the cleaned Bouwens et al. (2015a); Harikane et al. (2016); Finkelstein et al. (2015) catalogues in each redshift range (corresponding to b-, i-, v-, z,- and Y-band drop-outs), with the overlap number that also appear in the other catalogues also marked. The difference in overlap numbers between catalogues at the same redshift highlights that many galaxies has a different reported drop-out redshift in each catalogue. The total number of entries across all three catalogues is 13014 including 7221 unique galaxies with a total of 1890 galaxies appear in all three of the catalogue.

within the NIRSpec aperture also depends on the position angle and telescope roll angle at the time of observation.

I note that most of the input catalogues used to form our reserved target list have either no size information, or simply the FWHM output from SExtractor (Bertin & Arnouts, 1996) (typically from one of the HST wave bands). The SExtractor values also have the effect of the telescope PSF at that wavelength. I would prefer to recover the intrinsic size, accounting for the observed PSF, and this can be accomplished with GALFIT. The motivation here is that I would want to then re-convolve with the JWST PSF to simulate the future observations (which is done in Chapter 5).

GALFIT can fit several analytic functional forms. I adopt a variable "Sérsic" (Sérsic, 1968, 1963) profile with Sérsic index 'n'. Here the intensity at a given radius (R) is parameterised in terms of the half-light radius (R_e, that containing half the total light) and the intensity at that radius (I_e)

$$I(R) = I_e \, exp \left\{ -b_n \left[\left(\frac{R}{R_e} \right)^{(1/n)} - 1 \right] \right\}. \tag{4.2}$$

Standard values for the constant b_n include $b_1 = 1.678$ for a n=1 is exponential disk (Freeman, 1970) and $b_4 = 7.669$ for a n=4 de Vaucouleur profile (de Vaucouleurs, 1948) characteristic of bulges and elliptical galaxies (see e.g., Graham & Driver 2005 for discussion of b_n). The fact that these galaxies are high redshift and there is also size evolution (e.g., Oesch et al., 2010a) means the targets are small even at HST resolution and extend over only a few pixels. For these compact objects the Sersic shape index is typically poorly constrained. I fix $n = 1$, corresponding to an exponential disk (typical of a star-forming galaxy at low redshift). I note that Ravindranath et al. (2006) fit Sérsic profiles for galaxies in the GOODS fields at $3 < z < 5$ and find that most have Sérsic indices n$<$ 2 (with 40% having exponential profiles with n$\sim$ 1, and a further 30% with shallower profiles n$<$ 0.8 which may be related to mergers or multiple site of star formation within the same galaxy). van der Wel et al. (2012) analysed the Sérsic indices in the same 3D-HST images that I am using, although many of the faint Lyman break galaxies which I study here do not appear in their catalogue which is tuned to lower redshifts (z$\sim$0-3). van der Wel et al. (2012) find that the distribution of Sérsic indices peak strongly around $n \sim$1 (their Figure 3). I note that two other works on the surface brightness profiles of high redshift Lyman break galaxies also force a small Sérsic index similar or equal to an exponential profile

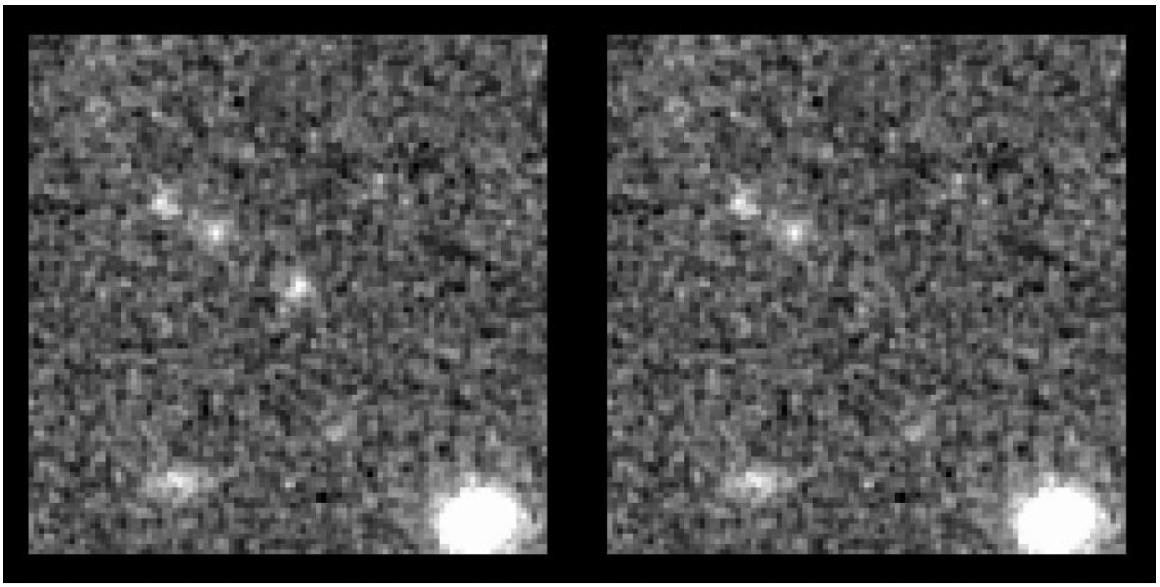

Figure 4.16: Left: original image of a centred high redshift target galaxy and right: the image after GAFLIT morphological fitting and subtraction. The light profile of the central galaxy has been modelled accurately and leaves minimal residuals after subtraction.

(Ono et al. 2013 take $n = 1$ for $7 < z < 12$, and Oesch et al. 2010a take $n = 1.5$ for $7 < z < 8$). Hence the choice of forcing an $n = 1$ profile for GALFIT (to help the fits converge) seems reasonable. To note, the conversion between the Sérsic effective radius (equal to the half-light radius, R_e) and the exponential characteristic radius (which is returned by GALFIT) is given by $R_{exp} = 1.678 R_{Sérsic}$.

GALFIT is run on all three catalogues with each galaxy image trimmed to 60" ×60" sub-image, and adopting the exponential light profile (Sérsic $n = 1$) and a uniform sky background determined by GALFIT for each sub-image. I used for a PSF an unsaturated star located in the same detector image as the galaxies in the GOODS field (i.e. coming from the same set of observations taken at the same time as the galaxy I wish to fit, so the roll angle between the PSF star and target will be identical). Across the three catalogues $\sim 30\%$ of sources recover GALFIT solutions whilst a further $\sim 50\%$ return the GALFIT convergence warning, indicating that the target covered too few pixels for the light profile to be modelled accurately, which is to be expected for high-redshift galaxies which are well described as point-sources. For 1410 galaxies in GOODS North and 1037 in GOODS South overlap is found between the 3 main catalogues and the 3D-HST sample of van der Wel et al. (2012) who also present a GALFIT shape analysis. In Figure 4.17, I compare my own results

of GALFIT on a sub-set of those of van der Wel et al. (2012). Here the half-light radius, GALFIT derived H-band magnitude, axis ratio and position angle all find good agreement when the Sérsic index of van der Wel et al. (2012) (which is left as a free parameter $0.5 < n < 8$) is close to 1, the fixed value for n I adopt. The scatter between my GALFIT shape analysis and that of van der Wel et al. (2012) is larger when the best fit Sérsic index does not agree with the $n = 1$ light profile adopted in this work. This potential different in the measured shape parameters between a free and fixed Sérsic index analysis may likely only be considerable for the lower-priority low-redshift bright sources which are resolvable and will be minimal for the key high-redshift targets which are more typically compact ($n = 1$).

4.4 Summary

In this Chapter I have looked at known existing targets falling within the JWST JADES survey fields for potential follow-up with NIRSpec. The goal has been to gather the Lyman break galaxies from the literature (and I focus on three large compilations done in the GOODS fields) and re-measure the photometry and astrometry for each using consistent well-reduced images (I use the 3D-HST reductions). This is critical to our JADES survey to ensure that enough galaxy light does indeed fall within an individual MSA microshutter of NIRSpec, and that we are targeting galaxies which are bright enough to achieve the science goals of our survey. I also check if the candidate Lyman break galaxies from the literature hold up as good candidates using the uniformly-measured photometry and photometric redshifts fits from BEAGLE.

I have identified an offset in the astrometry of one of the LBG catalogues (Bouwens et al., 2015a), which while small ($\sim$0.2arcsec) is significant in terms of the narrow shutter size of the NIRSpec MSA, and would lead to missing many of these targets if left uncorrected. I also identified that another of the catalogues (Harikane et al., 2016) was reporting photometry apparently uncorrected for aperture losses.

A total of 4402, 4537 and 4075 galaxies survive the re-analysis in the Bouwens et al. (2015a); Harikane et al. (2016); Finkelstein et al. (2015) catalogues which span $z > 3$ to $z \sim 10$. This produces a total of 13014 entries with 7221 unique galaxies. The distribution of galaxies with redshift is presented in Table 4.15. Galaxies that

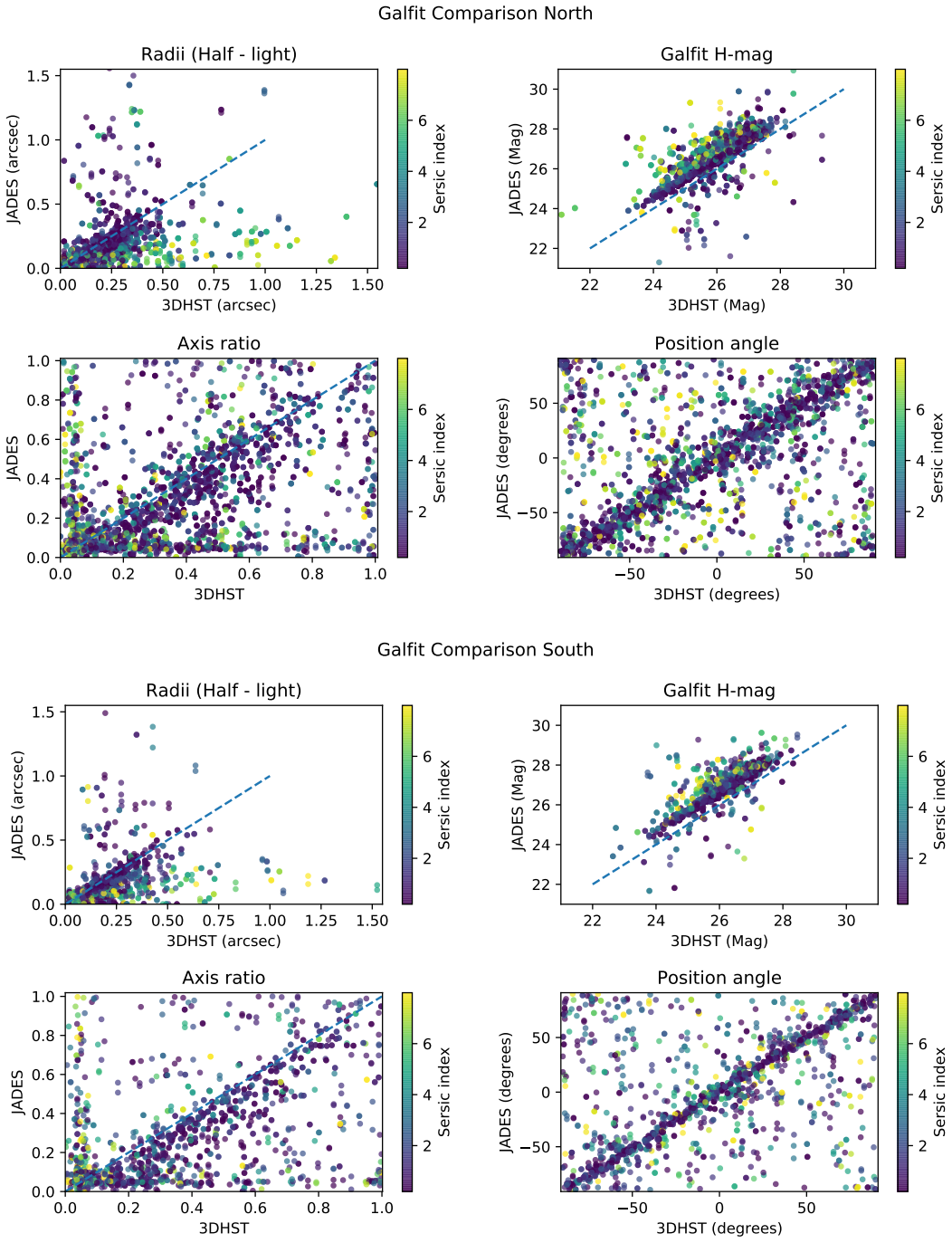

Figure 4.17: Comparison of GALFIT derived surface brightness parameters: Half-light radius (top-left panels), F160W H-band apparent magnitude (top-right panels), axis ratio (bottom-left panels) and position angle (bottom-right panels). Reported for the sub-set of galaxies matched to the 3D-HST van der Wel et al. (2012) sample for the GOODS North (Top) and South (Bottom) fields. van der Wel et al. (2012) fit the surface brightness profile with a Sérsic profile, allowing the Sérsic index (n) to be a free parameter (the colour bars present $0 < n < 8$ for the 3D-HST sample). Good agreement is found at n=1, where in this work the Sérsic index has been fixed to reflect the distribution of galaxies at high-z (e.g., Ravindranath et al., 2006).

do not make the cut will be retained for the target list but are down-weighted in the priority class (see Section 4.3.5 and Table 4.2). The cleaned galaxies can be separated into the priority classes. The Y- and J-band drop-outs are potentially at $z > 8$, and will be in priority Classes 1 & 2, and are among our highest priority targets which drive the choice of exact telescope pointing to maximise the number observed and ensure the highest priority ones fall close to the centres of microshutters. There are 44 of these $z > 8$ galaxies from the literature that survive the photometry checks and with a magnitude in the rest-frame UV filter just longward of the Lyman break brighter AB=29.5 in the XDF (6, for targetting in the NIRSpec DEEP tier of JADES) and AB=28.5 in the other portions of the GOODS fields (38, corresponding to Medium). A further 27 galaxies survive but have fainter magnitudes in their respective fields and are placed in priority Class 3 ($z > 8$ and brighter than AB=30.5), these are all presented in Table 4.16.

Appendix A.2 also presents the $z > 6$ candidates for spectroscopy from Class 4 of our JADES priority scheme — these objects have passed the "robustness" criteria above, and have rest-UV fluxes (indicative of star formation rates, albeit lower limits due to dust reddening) which would imply that we should be able to detect Hα with NIRSpec at $S/N > 25$, and other key lines (such as Hβ, [OII] and [OIII]) at $S/N > 8$. Detection of spectral lines at this significance would enable line diagnostics to be used to constrain the dust attenuation, metallicity and ionisation parameter (as I did in Chapter 2 for a lower redshift sample). For the XDF region (to be targeted with a DEEP NIRSpec exposure) I have 7 sufficiently-bright candidates ($AB < 27.5$), and for the rest of the GOODS fields (to be targeted with MEDIUM-duration JADES NIRSpec spectroscopy) I have 46 candidates at $AB < 26.5$. A further 358 objects enter the lower priority Class 6 (fainter $z > 6$ sources) with magnitudes brighter than 29.0 and 28.0 in the XDF/DEEP and GOODS/MEDIUM regions.

Details of the other existing targets (drawn from the three main input LBG catalogues) which number several thousand and which occupy our lower-priority classes (either because the Lyman break is in a short-wavelength filter, consistent with $z < 6$, or they do not pass all the robustness criteria for the higher redshifts) are available online in a machine-readable format[11], with similar columns to the tables 4.16, and tables A.2 and A.7 in Appendix. Previously in this Chapter I have shown plots of the distribution of these galaxies in colour—colour space (see Section 4.3.4 and Figures

[11]https://github.com/Kitboyett/Supplementary-Thesis-material

4.12 and 4.13) and the photometric redshift fits (Section 4.3.5 and Figures 4.14 and 4.15). A "read-me" column description for the machine-readable re-analysed catalogues containing all the galaxies in the input samples is given in Appendix A.2 and the additional colour-colour diagrams for the (Bouwens et al., 2015a; Harikane et al., 2016) catalogues are given in Appendix A.1.

As a result of the work done in this Chapter, I now have a target list of candidate high-redshift galaxies for the JADES NIRSpec survey. In the case of the XDF/HUDF, these existing targets (primarily selected from HST imaging) divided into our priority categories are likely to form the bulk of the targets for the JADES Deep spectroscopy on this particular field which is intended to be observed first by NIRSpec (before NIRCam imaging is done). For other parts of the survey, where NIRCam imaging will become available over the GOODS fields before we design our NIRSpec MSA configurations, we will be able to update the photometry of our existing with deeper and longer-wavelength NIRCam filters and refine the colour—colour selection and photometric redshifts of our targets, while critically adding new objects (fainter and redder) revealed in the NIRCam imaging which may potentially be at higher redshift. A key consideration as to whether one of these targets actually has a microshutter allocated is the amount of light entering this aperture, which depends no only on how well centred with in the microshutter the source is, but also the wavelength of interest and on the surface brightness profile of the source. In the next Chapter I simulate this effect.

ID(B15)	ID(F15)	ID(H16)	RA [Deg]	Dec [Deg]	Y-Flux/Err	J-Flux/Err	H-Flux/Err
GSDY-2499348180	z8_GSD_17938	-	53.2080661	-27.8050304	0.534±0.049	1.712±0.055	1.916±0.064
GNDY-7199315263	-	-	189.3330614	62.2572348	0.577±0.049	1.304±0.065	1.337±0.082
*GNDJ-2545743169	-	-	189.1060547	62.2420404	-0.01±0.092	0.041±0.055	1.313±0.074
-	z8_GNW_20826	-	189.4011959	62.3192411	0.473±0.089	1.053±0.117	1.23±0.131
-	z8_GND_34295	-	189.1591263	62.2057625	0.332±0.09	1.131±0.054	1.099±0.076
GNWY-6200412096	z7_GNW_15559	-	189.0834973	62.2025861	0.365±0.106	0.866±0.101	1.075±0.139
-	z7_GND_18323	-	189.3713783	62.2521495	0.404±0.05	0.781±0.06	1.066±0.075
GNDY-7048017191	z8_GND_8052	-	189.2700089	62.2885515	0.249±0.047	0.768±0.055	1.053±0.067
-	z7_GSD_3811	-	53.1334373	-27.7603004	0.432±0.048	0.741±0.063	0.908±0.086
-	z8_GNW_19912	-	189.2526986	62.3284036	0.493±0.094	0.767±0.085	0.843±0.097
GNWY-7183521367	-	-	189.3264590	62.3601044	0.286±0.103	0.688±0.121	0.813±0.13
-	z7_GNW_32502	-	189.2857997	62.3549749	0.364±0.118	0.463±0.147	0.796±0.14
GNWY-6458508231	z8_GNW_5376	-	189.1910543	62.1396941	0.242±0.13	0.675±0.096	0.787±0.119
-	z7_GND_7831	-	189.1773237	62.2910598	0.453±0.133	0.696±0.048	0.787±0.069
-	z8_GSD_2135	-	53.1786664	-27.7511864	0.226±0.043	0.636±0.059	0.743±0.079
-	z7_GND_8012	-	189.2604021	62.2894055	0.352±0.045	0.663±0.052	0.742±0.064
-	z7_GNW_14500	-	188.9201643	62.1949655	0.418±0.107	0.682±0.124	0.731±0.159
GNWY-7088719051	z8_GNW_21001	-	189.2870144	62.3180252	0.163±0.101	0.584±0.102	0.711±0.139
-	z8_GND_22233	-	189.2498287	62.2412296	0.283±0.081	0.617±0.059	0.694±0.074
-	z8_GNW_25541	-	189.5130591	62.2886848	0.42±0.097	0.725±0.127	0.663±0.129
*GNDJ-2273942274	-	-	189.3447379	62.2395665	-0.024±0.053	0.15±0.052	0.651±0.075
-	z8_GNW_2963	-	189.0922378	62.1223614	0.325±0.105	0.615±0.099	0.642±0.147
GNDY-7258112518	-	-	189.3575797	62.2143101	0.069±0.062	0.713±0.062	0.627±0.087
-	z7_GND_44109	-	189.1771675	62.2915142	0.364±0.156	0.527±0.048	0.62±0.065
GNWY-7247220496	z8_GNW_30497	-	189.3530225	62.3470180	0.262±0.103	0.571±0.12	0.612±0.12

Table 4.16: Photometric 0.36" aperture fluxes with a correction for aperture losses for the priority class 1,2&3 samples, constructed from Bouwens et al. (2015a); Finkelstein et al. (2015) (B15 and F15) Y- and J-band drop-outs that meet the re-analysis criteria. Fluxes and errors are given in [1xe-30 erg/s/cm2/Hz]. All objects are undetected in the B-, V-, i-, z-band ACS filters. Since JH is not used in the colour-colour work in Section 4.3.4 it is not reported here but is part of the online material made available, as are the ACS filter fluxes and the 0.6" diameter aperture photometry catalogues for all the galaxies in each catalogue. Galaxies that overlap have only been entered once with the ID's matched to the other catalogues. * J-band drop outs.

ID(B15)	ID(F15)	ID(H16)	RA [Deg]	Dec [Deg]	Y-Flux/Err	J-Flux/Err	H-Flux/Err
GNDY-6487514332	z8_GND_21784	-	189.2030709	62.2425019	0.304±0.071	0.649±0.054	0.607±0.077
GNWY-7379420231	-	-	189.4080671	62.3396823	0.074±0.101	0.799±0.116	0.606±0.129
GNWY-6336207437	z8_GNW_3806	-	189.1400941	62.1287132	0.336±0.095	0.889±0.104	0.581±0.123
*GSDJ-2697562835	-	-	53.1123988	-27.7745322	-0.031±0.038	0.214±0.058	0.578±0.082
GSDY-2181852456	z8_GSD_36195	-	53.0757610	-27.8793285	0.182±0.055	0.562±0.059	0.574±0.075
-	z8_GNW_27475	-	189.3737995	62.3363944	0.164±0.104	0.578±0.116	0.573±0.127
GSDY-2209748534	z8_GSD_21106	-	53.0874217	-27.8148500	0.106±0.049	0.5±0.053	0.569±0.071
XDFY-2388047071	z7_MAIN_3474	-	53.1616853	-27.7853216	0.297±0.008	0.513±0.011	0.558±0.01
-	z8_GSD_18901	-	53.0588854	-27.8080214	0.181±0.057	0.655±0.054	0.55±0.072
GSDY-2209651370	-	-	53.0873411	-27.8602938	0.147±0.039	0.476±0.052	0.549±0.067
GNDY-7092813358	-	-	189.2887020	62.2265341	0.205±0.045	0.451±0.054	0.519±0.074
-	z7_GND_6451	-	189.2219948	62.3157606	0.174±0.188	0.671±0.054	0.504±0.071
GSDY-2408551568	-	-	53.1702213	-27.8657943	0.22±0.117	0.524±0.061	0.476±0.086
GNDY-6355614172	-	-	189.1481773	62.2380442	0.199±0.088	0.387±0.058	0.474±0.072
-	z7_GND_41546	-	189.1596877	62.3105415	0.242±0.185	0.313±0.051	0.47±0.072
GNDY-7120316495	z8_GND_9408	-	189.3001370	62.2803536	0.18±0.057	0.501±0.058	0.47±0.065
-	z7_GND_34385	-	189.3167453	62.2054462	0.136±0.043	0.444±0.052	0.463±0.07
GSDY-2503746451	-	-	53.2098576	-27.7792190	0.111±0.041	0.207±0.059	0.435±0.073
-	z8_GND_23069	-	189.1094287	62.2387994	0.042±0.088	0.391±0.054	0.419±0.071
GSDY-2207551329	-	-	53.0864550	-27.8591485	0.053±0.05	0.22±0.052	0.412±0.068
GNDY-6556812087	z8_GND_35384	-	189.2319870	62.2023370	0.195±0.051	0.369±0.061	0.41±0.079
GNDY-6290917113	z7_GND_44524	-	189.1211819	62.2863984	0.244±0.043	0.563±0.048	0.409±0.068
GNDY-7193611417	z8_GND_37387	-	189.3306875	62.1948588	0.095±0.051	0.355±0.065	0.402±0.077
-	z8_GSD_9231	-	53.0455036	-27.7790181	0.048±0.051	0.31±0.059	0.401±0.075
-	z8_GND_17539	-	189.0451713	62.2545339	0.017±0.053	0.195±0.056	0.396±0.073
GNDY-7274212447	z8_GND_32082	-	189.3642899	62.2123279	0.164±0.052	0.43±0.054	0.395±0.071
GNDY-6507310134	-	-	189.2113762	62.1703162	0.018±0.052	0.361±0.063	0.372±0.085
GNDY-6480018111	-	-	189.2000091	62.3030129	-0.009±0.193	0.295±0.052	0.369±0.058
-	z8_GND_32588	-	189.3253255	62.2109598	0.093±0.042	0.37±0.053	0.364±0.069
GSDY-2180951184	z8_GSD_32912	-	53.0753801	-27.8551308	0.09±0.062	0.314±0.052	0.346±0.073
GNDY-7194815430	-	-	189.3311417	62.2618736	-0.043±0.047	0.211±0.06	0.343±0.08
GNDY-6474515254	z8_GND_16634	-	189.1977458	62.2569704	0.09±0.105	0.443±0.057	0.338±0.081
GNDY-7120113385	-	-	189.3000729	62.2272885	0.108±0.046	0.241±0.051	0.338±0.072
GSDY-2265446328	-	-	53.1105935	-27.7757868	0.075±0.038	0.277±0.054	0.325±0.072
-	z8_GSD_28457	-	53.1367213	-27.8373992	0.068±0.038	0.188±0.053	0.323±0.071

Table 4.17: Continuation of Table 4.16

-	z7_GSD_431	-	53.1677467	-27.7360749	0.22±0.039	0.374±0.055	0.319±0.075
GSDY-2144651485	z8_GSD_34461	-	53.0602642	-27.8634731	0.088±0.061	0.338±0.064	0.316±0.078
-	z7_MAIN_2203	-	53.1862729	-27.7789668	0.189±0.008	0.326±0.012	0.31±0.011
GSDY-2245251330	-	-	53.1022028	-27.8591904	0.023±0.042	0.396±0.054	0.3±0.07
GNDY-6542918162	z8_GND_42641	-	189.2262240	62.3044203	0.066±0.052	0.297±0.053	0.281±0.06
GSDY-2432246168	-	-	53.1800933	-27.7713666	0.108±0.04	0.179±0.03	0.249±0.044
XDFY-2431346284	z7_MAIN_1400	-	53.1797345	-27.7745789	0.118±0.008	0.218±0.011	0.242±0.011
XDFY-2395371744	-	-	53.1646920	-27.7881702	0.098±0.008	0.187±0.012	0.23±0.011
-	z7_MAIN_5721	-	53.1550594	-27.8017029	0.125±0.008	0.218±0.013	0.209±0.011
XDFY-2381245539	-	-	53.1588924	-27.7650021	0.031±0.008	0.165±0.011	0.203±0.01
XDFY-2428746345	-	-	53.1786534	-27.7762598	0.093±0.007	0.176±0.01	0.186±0.01
XDFY-2377946001	z8_MAIN_519	-	53.1574931	-27.7666950	0.053±0.008	0.157±0.011	0.157±0.011
XDFY-2376346014	-	-	53.1568058	-27.7670860	0.038±0.008	0.13±0.012	0.143±0.011
XDFY-2447446449	-	-	53.1864160	-27.7791743	0.056±0.009	0.098±0.014	0.096±0.011
XDFY-2430846276	z8_MAIN_1375	-	53.1795140	-27.7743622	0.042±0.009	0.115±0.012	0.091±0.011
XDFY-2424246136	-	-	53.1767896	-27.7704595	0.05±0.012	0.103±0.016	0.087±0.015
-	z8_MAIN_1318	-	53.1795271	-27.7738795	0.044±0.008	0.084±0.011	0.08±0.011
XDFY-2430746241	z8_MAIN_1224	-	53.1795062	-27.7733894	0.031±0.009	0.057±0.012	0.067±0.011
XDFY-2393447255	-	-	53.1639268	-27.7904300	0.02±0.009	0.054±0.011	0.062±0.012
XDFY-2392046322	-	-	53.1633597	-27.7756174	-0.001±0.008	0.048±0.01	0.06±0.011
*XDFJ-3811362435	-	-	53.1588140	-27.7734240	-0.006±0.008	0.012±0.011	0.053±0.01

Table 4.18: Continuation of Table 4.16. Galaxies below the single line have H-band magnitudes fainter than 28.5 and would only be considered for observation in the DEEP tier of the JADES survey based on the priority class 1&2 strategy. Galaxies below the double line have H-band magnitudes fainter than 29.5 and would be considered for lower priority class 3 DEEP observation based on the priority class strategy.

* J-band drop-outs.

Chapter 5

JADES Mini Data Challenge: Simulating NIRSpec spectra of high-z galaxies

In the previous chapter I outlined the selection criteria for candidate Lyman-break galaxies suitable for spectroscopic follow-up with NIRSpec. Where potential targets are split into priority categories. Similar priority classes are used for both existing known HST sources and for galaxies to be selected from future JWST-NIRCam imaging. The selection requirements for each priority class (in particular the redshift and luminosity of the sources) are set such that JADES sciences goals should be achievable (i.e, NIRspec spectroscopy should be sufficiently sensitive), as set out in Table 4.2. I now want to ensure that this is the case by simulating the spectra obtained by the Multi-Shutter Assembly (MSA) on NIRSpec. This is done as part of the JADES Mini Data Challenge (MDC), where the JADES collaboration practices the reduction and analysis steps of the JADES-DEEP campaign using simulated imaging and spectra in place of the future observations (discussed in the next section).

I wish to generate a realistic simulation of the JADES-DEEP MSA observation, and to do this I need an input catalogue which reflects the number densities of galaxies for a range of redshifts from which targets can be drawn according to the JADES selection criteria, and allocated to microshutters according to the priority class order. For the simulation of NIRSpec observations I use the JAGUAR mock catalogue produced by the JADES collaboration (Williams et al., 2018), which contains 10 independent realisations of 11'×11' fields, each containing galaxies over a $0.2 < z < 10$ redshift range and at masses $> 10^6 M_\odot$. The catalogue's number counts and galaxy properties reflect the observed mass and luminosity functions of both star-forming

and quiescent galaxies, and the redshift evolution of colours, sizes, star-formation and chemical properties of the observed galaxy population. JAGUAR also provides size information and the idealised spectra for each galaxy generated by Chevallard & Charlot (2016) based on their star formation history and redshift. Using this catalogue as an input allows the S/N with wavelength to be predicted for the NIRSpec observations using the throughput of the instrument, sensitivity of the detector with wavelength and other parameters such as dark current and read noise (many of which have been determined in ground testing), along with the anticipated sky background (predominantly from zodiacal light).

Importantly, during the real NIRSpec observations, objects will typically not be positioned at the centre of each microshutter, since the pointing is set by a few high priority objects, and the roll angle by the epoch of observation. Whilst the position of an object within the microshutter is taken into consideration during the MSA configuration optimisation process, targets may experience greater slit losses when they are not well-centred or are spatially extended. This can be seen in Figure 5.1, where extended objects and especially those that are not well-centred within the shutter will suffer from slit-losses. I therefore want to simulate a "real world" example of an MSA design to assess if the science goal objectives for each priority class (see Table 4.2) are achievable for the JADES spectroscopy. Work by the NIRSpec instrument science team in simulating NIRSpec spectra for the JADES observations has previously been presented in Giardino et al. (2019), which was restricted to simulating all the objects as point sources. The work presented here goes beyond that by treating objects as extended, using the intrinsic sizes from the JAGUAR catalogue.

5.1 Introduction to the JADES Mini Data Challenge

The "Deep" NIRSpec spectroscopy part of JADES involves two pointings, both in GOODS-South. The first will cover the HUDF to target existing HST sources (as discussed in Chapter 4) and then the second will follow up deep NIRCam photometric observations. The second pointing allows high priority galaxies that have not been identified in existing deep HST imaging to be targeted. The period separating the initial NIRCam DEEP observation and the follow up NIRSpec spectroscopy might be as short as 45 days if both are scheduled in the same visibility window, set by the pointing angles available to JWST during its orbit due to the required orientation

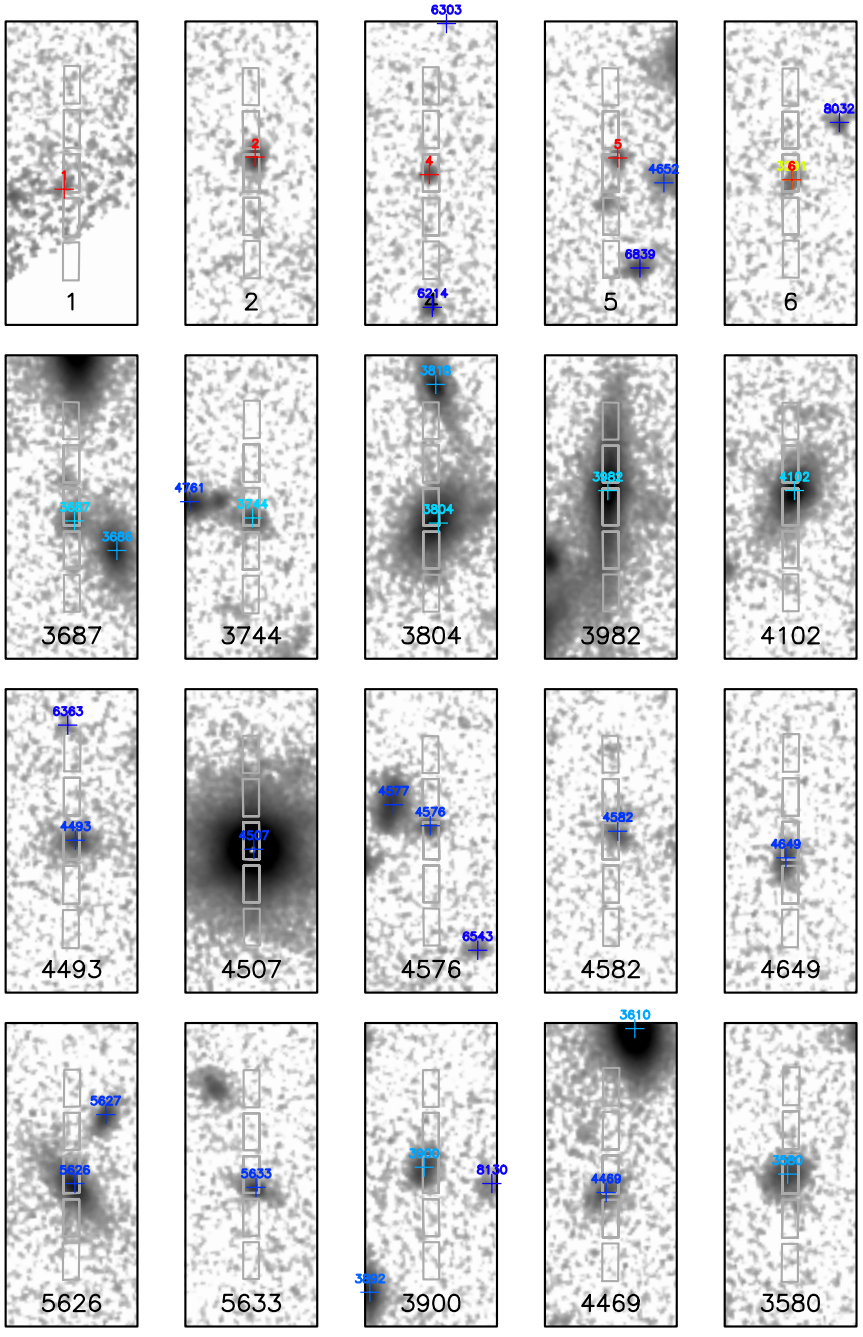

Figure 5.1: JAGUAR mock catalogue postage-stamps for a set of MDC targets, each in a 2.5" by 1" window with a set of micro-shutter slits (each microshutter is 0.46"by 0.2") overlaid on top. We show our observing mode of three open shutters, dithered up and down by 1 shutter, sampling 5 spatial positions in total. Targets are coloured based on their priority class, with red showing the highest priority objects ($z > 8$) and light and dark blue showing the lower priority class 4 and 7 objects (see Table 4.2). When two targeted objects are in close proximity (e.g., in 3687 and 3744) contamination may occur when the light from one source enters the shutter of another object.

of the solar-shield obscuring direct light from the sun[1]. Within this short window in time the complete NIRCam DEEP observational data would need to be downloaded from the telescope, reduced and calibrated, mosaiced into single images for each filter and analysed (photometric catalogues built, including photometric redshift fitting) to identify targets which are then to be prioritised into different classes of interest. The multi-slit configuration is then designed to maximise the number of high priority targets and the resulting MSA configuration passed on to STScI for checking prior to the NIRSpec observation. The time restriction presents a data challenge as how to effectively achieve each step and do so within the 45 day window.

In preparation for this objective, the JADES science group has set-up an internal project consisting of multiple stages to go from NIRCam images to NIRSpec spectra with the aim of testing the in-house pipelines and data product hand-over between sub-groups. This project is called the "Mini Data Challenge" (MDC), and is intended to replicate as closely as possible the full data reduction and analysis necessary on a timescale of less than 45 days, enabling potential bottlenecks to be identified and required pipeline improvements to be made before launch. The challenge is designed to test whether the JADES pipelines achieve the standard of reduction, calibration and analysis required, and whether the team can identify targets, prioritise them into classes and generate the multi-shutter array configuration that maximises the NIRSpec results. The Mini Data Challenge is then extended to test the NIRSpec reduction, calibration and analysis pipelines. The MDC is a blind-exercise in the sense that after creating the mock NIRCam imaging, the team does not know the JAGUAR catalogue identity of any galaxy in the imaging. The challenge on the data reduction strategy is to see how well we recover the ground truth.

Simulation of the NIRcam mock observation forms steps 1, and simulation of the NIRSpec mock observations forms step 8 of the 11 step Mini Data Challenge. The 11 steps are each handled by a different sub-group within the JADES science team and are briefly described in Table 5.1.

My role has been to lead step 8 of the Mini Data Challenge, where I am tasked with simulating the NIRSpec raw observational data from the MSA configurations

[1]NIRSpec and NIRCam are inclined at 45degrees in the focal plane, see Figure 4.1, and the telescope roll angle moves approximately 1 degree per day, so an interval of 45days means that the NIRSpec detector footprint will align with that of the previous NIRCam observation

generated in step 7 and passing the data products onto the analysis sub-groups. In the run-up to the Mini Data Challenge I have updated the step 8 simulation to allow galaxies to be treated as extended sources rather than as point sources in the mock observation, which had previously been the simulation default (see Giardino et al. 2019). Accurately simulating the NIRSpec spectra of the targets that have been allocated to MSA shutters gives the opportunity to assess whether the S/N of these spectra (particularly key spectral features such as emission lines) are sufficient to achieve the science goals. If this is not the case, it might be necessary to re-visit the selection criteria (Table 4.2) for the various priority classes.

This chapter will cover the work I undertook during my long term attachment at ESA-ESTEC, Noordwijk and the University of Leiden visiting JADES PI Pierre Ferruit and JADES science team members Giovanna Giardino and Marijn Franx (January-March 2020).

5.2 Mini Data Challenge strategy

The Mini Data Challenge follows the observational strategy of the DEEP part of the JADES survey. I simulate mock NIRSpec observations for the same set of MSA configurations, using the Prism ($\lambda = 0.6 \sim 5.3\mu$m) and the medium resolution G235M ($\lambda = 1.7 \sim 3.1\mu$m) and G395M ($\lambda = 2.9 \sim 5.1\mu$m) gratings (see Figure 5.2 for dispersion and resolution). The total exposure time of 100,828s for the Prism and 25,210s for each grating, is split between three different "dithers" (3 different MSA configurations). Each dither has a slightly offset pointing, to avoid bad pixels repeating. Such a strategy could be used to fill in the gap between the two NIRSpec detectors (to complete the wavelength coverage, particularly for the higher-dispersion gratings where the spectra are longer on the detector). When optimising the MSA configuration multiple successful configurations are created and three are selected. The pointing of each of the three MSA configurations is set by the same highest priority class targets in the field such that they will be always be allocated to microshutters and therefore received the maximum total exposure time. Lower-priority class targets may appear in 1, 2 or all 3 of the MSA configurations and may receive only one or two thirds of the total exposure time. This efficient method ensures the maximum exposure time for the highest priority targets whilst placing a greater number of lower-priority class targets on the shutters, which may not require the maximum integration time to achieve the desired science goals. The exposure time for each dither is then split into

Step	Title	Description
0	Jaguar catalogue	Mock catalogue of galaxies
1	Create raw images	simulate raw NIRCam photometry
2	Ramps to Slopes	reduce multiband photometry
3	Mosaic creation & source extraction	create source catalogue
4	Photometric redshifts & derived information	Value-added catalogue (derived physical properties)
5	Spectroscopic candidate selection	source lists for each target class
6	Image examination & to refine spectroscopic candidate list	revised source lists
7	MOS configuration files	generate MSA configuration
8	Create NIRSpec count-rate maps	simulate count rate maps
9	Process NIRSpec count-rate maps	calibrated 2D spectra for individual sources
10	Generate integrated spectra & line fluxes	calibrated 1D spectra & lines fluxes of individual sources.
11	Derivation of galaxy properties& from spectroscopy	spectroscopic redshifts & basic galaxy integrated properties

Table 5.1: Steps taken to undertake the Mini Data Challenge.

thirds and shared between three noddings, where the MSA configuration is shifted up and then down by one shutter to remove any shutter-to-shutter variation and to be used in local background subtraction (three shutters along the spatial direction are open for each object). Therefore a total of nine mock observations need to be simulated for each of the three disperser modes.

For the Mini Data Challenge, three pointings (dither positions) were created focusing on the same patch of sky. These contained 98, 102 and 104 targets in each pointing with 113 unique galaxies in total. Across the three dithers, 77.9% receive the total exposure time, being included in each of the three MSA configurations, 13.3% appear in 2/3 dithers and 6.8% appear in 1/3 of dithers (Table 5.2 breaks down the allocation per priority class). The second and third dither are centred roughly +3 horizontal shutters and +0 or +1 vertical shutters from the first dither.

One immediate improvement that will be made in future data challenges and in the real observations will be to increase the number of targets allocated to MSA microshutters for the Prism GWA mode. The low dispersion of the Prism produced relatively short spectra of $\sim$ 400px, allowing multiple microshutters to be opened on the same dispersion row across the two 2K detectors, which has not been taken advantage of to its full extent here.

For the simulations I want to emulate the read-out strategy that the DEEP observations will use (i.e., number of groups, integrations per exposure). The NIRSpec detectors enable a non-destructive up-the-ramp sampling approach (also called MULTIACCUM), where the charge in each pixel is read out multiple times ("frames") during a given integration. To reduce data volumes multiple frames can be averaged into a "group". At the end of the integration the accumulated charge in each pixel is then reset before the next integration begins. Each exposure can be made up of multiple integrations, which is not the case for CCDs where when reading the charge, the charge must be transferred from pixel-to-pixel during read out. Plotting the accumulated charge as a function of time (i.e., the gradient) enables a recording of the flux measured before a pixel saturates and for cosmic rays to be detected and potentially removed in post-processing (a cosmic ray strike would produce a discontinuity in the count rate with time). The simulations follow the JADES observation strategy and employ the NIRSpec readout mode "IRS2" (which offers the greatest noise reduction) and the readout pattern NRSIRS2 (5 frames per group, 72.944 seconds per group),

Priority Class	Unique targets	Triple exposed targets	Double exposed targets	Single exposed targets
1	6	6	-	-
2	0	-	-	-
3	4	4	-	-
4	2	2	-	-
5	0	-	-	-
6	4	3	-	1
7	39	35	3	1
8	34	27	4	3
9	24	11	8	5
Combined	113	88 (77.9%)	15 (13.3%)	10 (6.8%)

Table 5.2: Number of MSA allocated unique targets per priority class, with the number that appear in one, two or all three of the MSA configurations. These priority classes reported here align roughly to those given in Table 4.2.

with each observation constructed from 19 groups, 2 integrations per exposure and the required number of exposures to achieve the total exposure time, as mentioned above.

5.3 Mini Data Challenge - Step 8

I receive the MSA configuration files from the sub-group in charge of step 7 of the Mini Data Challenge. The MSA configuration placed the majority of slits in two out of the four MSA quadrants due to the layout of the target galaxies. In the simulations a sub-set of the galaxies will be treated as extended objects, whilst the rest will remain as point sources. For galaxies that are unresolved treatment as a point source is appropriate and achieves realistic slit-losses, however, this is not true for extended sources. In addition to examining the half-light radii of each target relative to the JWST resolution, a visual inspection of each target's realisation overlaid by the shutter mask is used to further identify and check which were appropriate to be treated as point-like. Figure 5.1 presents a selection of the target visualisations. Red, light blue and dark blue crosses identify the location of the top and lower priority class targets. Grey boxes in each panel present the location of the three open MSA shutters during noddings. Any additional coloured crosses within each panel identify close proximity neighbours which may contaminate the observation. Certain targets such as ID 4507, 4102 and 3804 can easily be seen to be extended sources, where treatment as a point-like source would significantly underestimate the slit losses. After visual

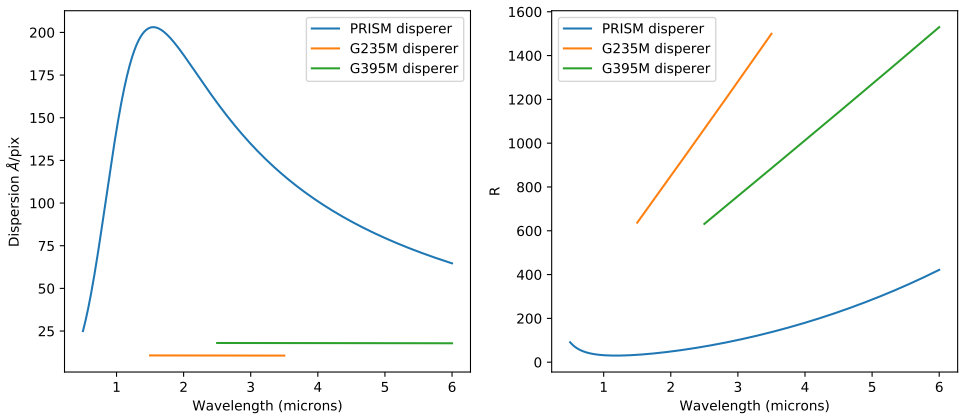

Figure 5.2: Left: Spectral dispersion of the PRISM, and the G235M and G395M gratings (with fixed values of 10.68Å/pix and 17.95Å/pix). Right: Spectral resolution of the same GWA modes. NIRSpec has a spatial resolution of 0.1" per pixel.

inspection, 37 of the 113 unique targets are chosen to be treated as extended, these include the 6 top priority class objects and 31 galaxies that are deemed to be resolvable.

Step 8 of the Mini Data Challenge takes the targets selected for the MSA configuration in step 7 and simulates the NIRSpec JADES observation. The simulation of the mock observation breaks down into 4 stages.

- **I. Inputs.** Using the generated MSA configuration, the Right Ascension and Declination of the selected targets are matched to the original JAGUAR catalogue to retrieve the galaxy properties for each object (specifically the size, shape and spectrum).
- **II. Scenes.** The retrieved properties and MSA configuration locations are used to create a scene for each galaxy (which is a 2D representation of the intrinsic light profile of each galaxy allocated to the MSA).
- **III. Instrument Performance Simulator.** The scenes are run through NIRSpec's Instrument Performance Simulator (IPS) to generate electron-rate maps of the mock observation, accounting for the instrument efficiency and the effect of the point spread function (PSF).
- **IV. Count-Rate Maps.** The electron-rate maps are converted into count-rate maps (including the effect of noise) using the desired observational strategy.

I will now go through each stage in more detail.

5.3.1 Stage 1 - Inputs

The outputs of step 7 of the Mini Data Challenge are the MSA configuration files which would be sent to JWST to define the NIRSpec observations (instructing which microshutters to open). These MSA configuration files are used as the input to step 8 and contain the measured coordinates of each selected object. The MDC is a blind-exercise and therefore I must first match the coordinates of each selected object back to the JAGUAR catalogue, from which the imaging simulation was based, to retrieve the galaxy information required to simulate the objects in the NIRSpec mock observation. This includes the galaxy size information and spectrum.

A galaxy property file is then created for the targets in the MSA configuration containing all necessary galaxy information including the galaxy's half-light radius (the radius containing half the target's total flux), redshift, Sérsic index and rest-frame spectrum. The ellipticity of the target, as given in the JAGUAR catalogue, can also be included in the simulation but for simplicity in the Mini Data Challenge this is not employed and the targets are treated as circular.

5.3.2 Stage 2 - Scenes

Using the galaxy property file created in stage 1, a scene is created for each galaxy in the MSA configuration to detail the spatial light profile of the source (before convolution with the telescope PSF). Galaxies can either be treated as a point source, where the intrinsic input light profile is restricted to just the input coordinate, or as an extended source, where the light is sampled over a 2-dimensional spatial grid following the luminosity profile of the target.

For many galaxies treatment as point-like sources for the JADES Mini Data Challenge would not provide an accurate estimate of the slit losses (the portion of target flux that does not reach the detector through the shutter aperture). At the angular resolution of JWST (0.06" at 2μm), many of the high redshift target sources will be spatially-resolved - as discussed in Chapter 4, the typical size of Lyman break galaxies (at $z = 7$ and F160W $M_{AB} < -18.7$) is 0.7kpc = 0.1". Hence using realistic input galaxy sizes and surface brightness profiles in simulating the NIRSpec spectra is important in assessing if the signal-to-noise achieved is sufficient for the science goals (a point source approximation would typically overestimate the S/N). Additionally,

quantifying the aperture slit losses as a function of wavelength for a particular galaxy is crucial for the flux calibration, and in particular for obtaining the true line flux ratios for use in diagnostic diagrams.

When sampling the light profile of an extended object, to minimise computational time the spatial extent on the focal plane over which the extended objects is sampled is restricted to twice the half-light radius (as given by the JAGUAR catalogue) up to a maximum size equivalent to 3 dispersion by 7 spatial shutters (there are 3 open shutters in each exposure, and nodding up and down by ± 1 spatial shutter means 5 shutters will be used and I consider ± 1 shutter beyond this). The light profile is sampled at above a Nyquist level ($> 2px$ per resolution element) and scaled to achieve the same integrated flux as a point source of the same brightness when interpolated by the IPS. Figure 5.3 shows a spatial visualisation of a scene (the light profile before convolution with the PSF), of a test galaxy at z=0.36 with a half-light radius of 0.2" (1.1kpc), first treated as a point source and then as an extended source highlighting that even before convolving with the PSF, a proportion of the total flux is outside the shutter leading to greater slit-losses.

For the Mini Data Challenge the JAGUAR catalogue provides the spectral continuum of each target and the flux information for various emission lines, which are treated as spectrally unresolved. Although the JAGUAR spectra contain emission lines, the resolution of these spectra is lower than that achieved with the NIRSpec gratings. Hence I use the JAGUAR spectra for the continuum flux, and add in lines of the appropriate flux with a FWHM of $\sim$100km/s. To simplify the simulation, only the emission lines of interest are included in each scene (given in Table 5.3), focusing on the emission lines used in rest-optical line diagnostics (such as those used in Chapters 2 and 3). These are typically the dominant lines in the spectrum and are of interest for much of the core science for JADES. The IPS then takes the assumption that the light profile of the emission lines is the same as the continuum, which is a simplification as line emission typically comes from more compact HII regions within a galaxy (although the rest-frame UV continuum may be a reasonable tracer of star formation, although effected by dust obscuration). This will be tested for a small number of galaxies using the integral field spectroscopy (IFS) mode of NIRSpec, which will comprise $\sim$ 300hours of the NIRSpec science team GTO (separate to JADES).

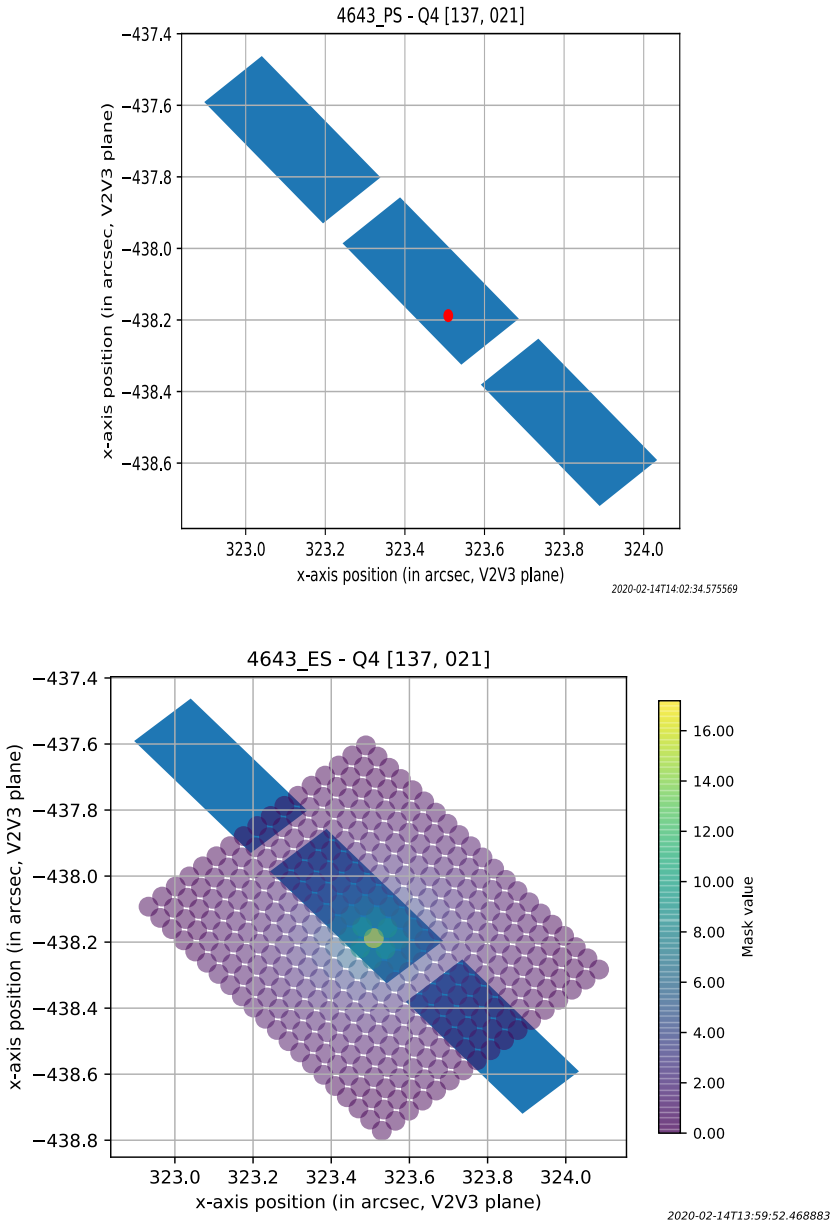

Figure 5.3: An example visualisation of a target's light profile within the central slit before being convolved with with telescope PSF, treated as a point-source (Top) and as an extended source (Bottom), with a half-light radius of 0.2" (1.1kpc at z=0.36). In both visualisations the galaxy can be seen to be offset from the centre of the central mirco-shutter, the two adjacent shutters open to allow the sky background to be measured as part of the background subtraction strategy. Top: As a point-source the light profile of the galaxy is treated as being a delta function at the input coordinate position. Bottom: When treated as an extended source the light profile is sampled over a grid extending to the point where the light profile would be consistent with the background noise. The sampling is weighted relative to the Sérsic profile of the galaxy, with the same total flux as the point-source. It can be seen that the extended source will suffer greater slit losses as a proportion of the total flux lies outside the shutter even before being convolved with the PSF.

Line	Wavelength λ_{vac} (Å)
Lyα	1215.17
[OII]	3727.32
[OII]	3729.23
Hγ	4340.47
Hβ	4861.33
[OIII]	4958.91
[OIII]	5006.84
[NII]	6548.05
Hα	6562.82
[NII]	6583.45
[SII]	6716.44
[SII]	6730.82
Paβ	12818.07
Paα	18750.98

Table 5.3: Rest-frame optical diagnostic and scientific interest emission lines including in NIRSpec IPS mock observation simulation.

The scenes also detail which shutters in the MSA are open for each object and this follows the JADES strategy to initially place each target in the centre of three open shutters along the spatial axis (perpendicular to the dispersion axis, 1×3, this layout can be seen in Figure 5.1). As mentioned earlier, in subsequent exposures the telescope is "nodded" to place the target in each of the two adjacent shutters. For compact sources the two adjacent shutters provide a measure of the local background, ideal for background subtraction (the background comes from various sources, such as zodiacal light, scatter light and the detector dark current). For extended sources, however care must be taken to avoid self-subtraction when the adjacent shutters contain non-negligible contribution from the source itself. The NIRSpec Instrument Science Team is also experimenting with "non-local" sky subtraction, where an average sky background spectrum for this telescope pointing can be used with an accurate instrument model at the location of each shutter.

5.3.3 Stage 3 - Instrument Performance Simulator

The NIRSpec Instrument Performance Simulator (IPS) is a ray tracing simulation that includes a geometrical model of NIRSpec and a Fourier optics treatment, which accurately computes the distribution of photons landing on the detector from a given light source on the focal plane (including diffraction effects). I note that the PSF

can change greatly with wavelength, particular for the Prism that covers the largest wavelength range (see Figure 5.6). A radiometric model of the throughput responses within NIRSpec converts the simulated distribution of photons landing on the detectors into an electron-rate map using wavelength-dependent quantum efficiency maps. The electron-rate map presents an effectively noiseless observation of the targets.

The design of the IPS considers the whole MSA configuration and allows for the contamination of a given target's designated open microshutter with light from other sources. However, in the simulation reported here I do not consider contamination from objects that were not allocated to MSA microshutters, for reason of computational resources.

NIRSpec's Grating Wheel Assembly (GWA) includes a prism, 6 gratings and a mirror for target acquisition. Across the whole JADES programme the Prism and a variety of gratings are used (see Table 4.1 for more details). The gratings each provide a greater spectral resolution over a short wavelength range compared to the Prism setting, the choice of GWA setting depending on the science goal in mind. The IPS can simulate the mock observation using any of the GWA available settings, with greater computational expense required by the higher resolution gratings than the Prism (because the spectra span more pixels). In the Mini Data Challenge the electron-rate maps of the Prism and two medium resolution gratings are simulated. JADES will actually use all three medium gratings and one high resolution grating in the DEEP strategy (see Table 4.1), but here I simulate a sub-set.

The electron-rate map for one such nodding of the MDC NIRSpec DEEP Prism is shown in Figure 5.4. In this effectively noiseless observation, emission lines can clearly be identified.

5.3.4 Stage 4 - Count rate maps

An observational strategy needs to be applied to the output electron-rate maps of the IPS to appropriately model the noise expected from the JADES observations. In the production of the count-rate maps the shot noise from the target's signal and the noise of the background as well as the detector's readout noise, dark current and gain are included and scaled to reflect the total integration time for each of the configuration count-rate maps (see Table 4.1 and Section 5.5.2, later in this Chapter, for more details). The appropriate treatment of the read-noise is set to be consistent with the

readout pattern chosen for JADES, of 19 groups, 2 integrations per exposure. Additionally, a representative spatially-uniform sky background is included which I adopt from Giardino et al. (2019). The background model includes a zodiacal light spectrum and a stray-light spectrum, from photons entering the telescope from Galactic emission, scattered zodiacal light and thermal emission from the optical telescope element (OTE). The dispersed light from the background will be present in all the MSA configuration open shutters as well as the fixed slits and any "failed open" shutters. I will show the extracted background from the IPS in Figure 5.9

The 2D count-rate map for one of the MDC NIRSpec DEEP Prism simulations is shown in Figure 5.4. The addition of observational noise means only the strongest emission lines can be identified at significant signal to noise (in contrast to the noiseless electron-rate map in the same figure). The three-open-shutter MSA configuration for each target is more prominently seen in the count-rate map than in the electron-rate map, as the sky background illuminates each of the open shutters. A drop in intensity between shutters can be seen due to obscuration by the microshutter pillars (this can be seen more clearly in a cut out of the count-rate map in Figure 5.5). The two outside open shutters, which will have minimal contribution from the source unless significantly extended relative to the shutter size (0.2"×0.46"), will be used for local-background during the extraction process.

From the step 7 input MSA configuration files, nine sets of 2D NIRSpec observations were created, comprising three dithers each with three noddings, for each of the PRISM, and G235M and G395M gratings. A total of 27 count-rate maps are created, and are handed over to step 9 of the Mini Data Challenge for the next stage, which is 2D extraction of the target spectrum.

5.4 Extraction of spectra

Within the MDC, the count-rate maps that are created are handed over to the next step (step 9, see Table 5.1), to exercise extracting the spectra from the mock observations and thereafter to analyse the results. For the purpose of inspecting the S/N of the targets with wavelength, I also independently run the extraction pipeline and analyse the spectra.

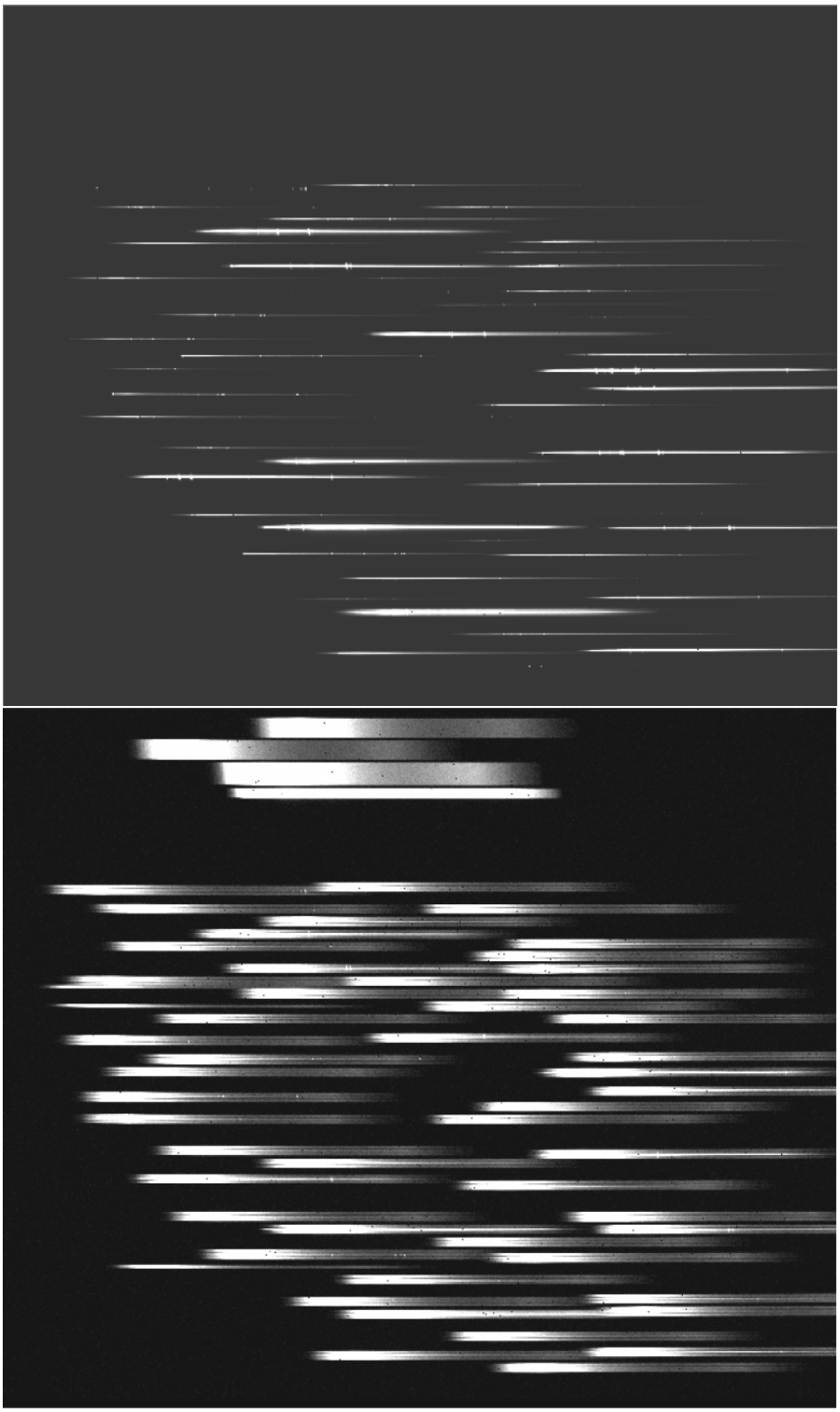

Figure 5.4: TOP: Quadrant 4 of the electron-rate map of the Mini Data Challenge, an effectively noiseless observation. Bottom: The corresponding Count-rate map, set to the NIRSpec DEEP observing strategy with a uniform background. This sky background can be seen clearly in the NIRSpec fixed slits at the top of the image, and in individual cases of "failed-open" shutters.

Two extraction pipelines are currently in development for the tracing and extraction of spectra from NIRSpec MSA observations, the ESA instrument science team's pipeline (NIPS) and the STScI pipeline (which is partly based on NIPS). While neither has finished development, NIPS can provide a rectified 2D and 1D extraction to examine the results of the NIRSpec simulations.

NIPS achieves local sky background subtraction using the three noddings of a given dither. These are flat-fielded and given the input microshutter and chosen GWA mode, the curvature of the spectrum is traced, the spectrum is rectified and extracted as a 2D sub-image (with a 5 pixel spatial aperture, roughly the height of a microshutter on the NIRSpec 0.1" pixel scale) and each pixel assigned a wavelength. The 2D spectrum is re-sampled onto a uniform wavelength grid. Local background subtraction is achieved from the three-shutter configuration by averaging the spectra from the two "background" microshutters (i.e., excluding the object shutter for that particular dither). This is then subtracted from the "source" slit. The background-subtracted 2D spectra (after rectification) from the three nod positions are then averaged to obtain a final 2D spectrum. A 1D extraction of the dispersed light is created by collapsing the 2D rectified spectrum spatially and a flux calibration is then applied to the 2D and 1D spectra using a radiometric model to convert to f_λ flux density units of $ergs^{-1}cm^{-2}$ (see Giardino et al. 2019 and therein, for a more detailed description). I inspected and confirmed the wavelength calibration by checking that the observed wavelength of selected emission lines agreed with the expected wavelength, based on their redshift. An example extracted and rectified 1D spectrum is shown in Figure 5.5 along with the JAGUAR input spectrum, and a cut out of the 2D count-rate map.

5.5 NIRSpec sensitivity from the IPS and the Exposure Time Calculator

The generation of NIRSpec simulations in this work allows the signal to noise of targets to be estimated for this given observation strategy, enabling us to understand whether the extracted spectra would meet the required S/N to achieve the desired science goals. The first check on the achieved S/N is to compare the full IPS simulations to the STScI Exposure Time Calculator (ETC, Pontoppidan et al. 2016). The ETC is a publicly available tool designed to allow astronomers to plan JWST observations, in order to identify what observational strategy would best achieve their

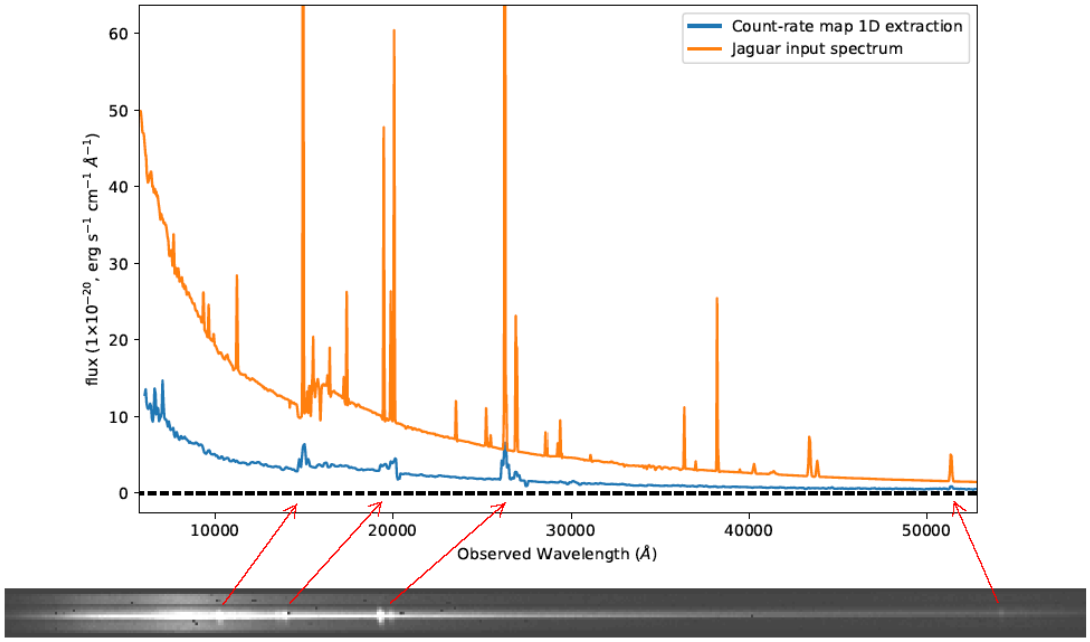

Figure 5.5: Example count-rate map cut-out and the 1D extraction of MDC target against the JAGUAR input spectrum. JAGUAR ID 173079 at $z = 3.0$ is Priority class 7 galaxy and has a half-light radius of 1.1kpc ($\sim 0.24''$). The light profile of this object is larger relative to the 0.2"×0.46" shutter and a median slit-losses across the wavelength range can be seen to account for 69.9% of the flux. To simplify the simulation, only emission lines in Table 5.3 are included and for this galaxies the recovered emission lines are at a sufficiently high S/N to meet class 7 science requirements. In the cut-out of the count-rate map, the obscuration of the microshutter pillars can be seen in the horizontal bands of reduced intensity in the dispersed light. Bad pixel can also be seen and are flagged.

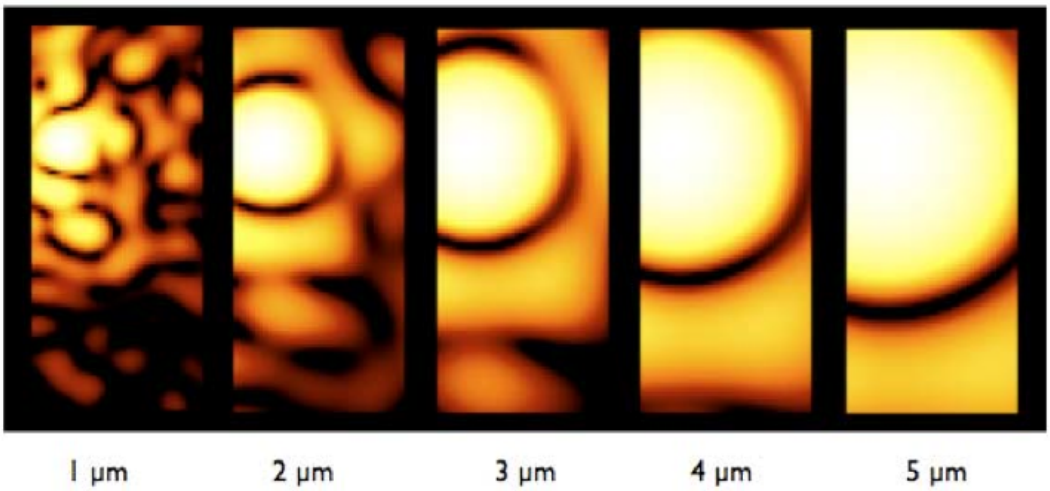

Figure 5.6: The point spread function of NIRSpec relative to the size of a 0.2"×0.46" microshutter. The size of the PSF increases with wavelength, leading to greater slit-losses. The diffraction pattern of the of JWST PSF is relative complex due to the primary mirror being composed of 18 hexagonal segments and effect of the secondary mirror supports, although the secondary maxima (Airy rings) can still be clearly seen in the 2 and 3μm shutters. This figure has been taken from the STScI JWST user documentation[3].

desired science measurement.

The ETC for JWST runs the simulation code "Pandeia" (Pontoppidan et al., 2016), and it allows the signal to noise of observables (e.g., emission lines) for a given observing strategy and input astronomical target spectrum to be determined given a wide variety of telescope and instrument configurations. This includes which of the four science instruments is being used, the number of exposures and individual exposure times, the detector readout-mode, any background subtraction strategy, and the level of the wavelength-dependent background light (which depends on the date of observation and the location of the target on the sky).

Compared to the IPS, Pandeia makes the compromise of improving the usability and dramatically reducing the computational time by simplifying the simulations, with the goal of providing sufficiently accurate S/N estimates to assess the feasibility of JWST proposals. To reduce the computational time calculations are performed

[3]JWST User Documentation, available at https://jwst-docs.stsci.edu/near-infrared-spectrograph/nirspec-apt-templates/nirspec-multi-object-spectroscopy-apt-template/nirspec-mpt-planner

over relatively small (∼few arcseconds) postage-stamp fields of view, unlike the IPS which considers the full field of view of the instrument during simulations. Pandeia also does not consider in detail issues such as the variation of sensitivity across the detector field of view, arising from optical field distortion, PSF variation or the location of bad pixels and failed microshutters. The ETC is deterministic in order to produce the same result for the same input conditions, and so does not consider stochastic effects such as cosmic rays (which the IPS can simulate).

In the 18 months since I ran the IPS simulations, the STScI has updated their ETC, and I now compare the IPS results with those of the latest ETC for a few representative sources from the MDC. I wish to understand what effect the treatment of sources as extended (rather than point sources), or with a spatial offset away from the centre of a microshutter, have on the simulations and the S/N characteristics of the various GWA modes. I will consider each of these in the following sub-sections.

5.5.1 Evaluation of microshutter slit-losses

I use the ETC to test the estimated slit-losses for a set of increasingly realistic treatments. For this test I set the GWA mode to the Prism to inspect the largest range in wavelength, and set the read-out mode to follow the observation strategy of JADES DEEP using NRSIRS2 pattern, with 5 frames per group, 19 groups, 2 integrations per exposure and the respective number of exposures for the Prism to match the total integration time of each dither (33ksec). I use as a test a $z \sim 7$ JAGUAR spectrum and set the size information to be representative of $z \sim 7$ galaxies (half-light radius = 0.1", Sérsic index $n = 1$, Oesch et al. 2010a, see discussion in Chapter 4). I first treat the test galaxy as a well-centred point source where I would expect minimal slit losses, then improve the realism of the estimated slit-losses and S/N by first considering the galaxy as a point source at an off-centre position within the microshutter, then as a well-centred extended source, and finally as an extended off-centred source (shown in Figure 5.7). I test two background subtraction methods. First a local sky subtraction (left panel in Figure 5.7), where the two of the three shutters (not containing the object) are used to measure the background at the location of the object, and then a non-local sky subtraction (right panel in Figure 5.7) which uses an average sky background spectrum for this telescope pointing. Non-local background subtraction would reduce the noise but may leave systematic errors or artefacts

Objects significantly offset from the centre of the shutter will have a greater proportion of their flux fall outside the target microshutter aperture, and I consider a point source in the corner of the shutter, with an offset position (+0.4, +0.4) fractional shutters relative to the centre of the microshutter[4]. This offset reduces the aperture flux to 43% (using local sky subtraction), compared to a point source with the same input spectrum that is well-centred, equivalent to a slit-loss of 57% of the flux (55% slit-loss is reported when using non-local sky subtraction, which avoids self-subtraction). I next consider a well-centred extended source with the same input spectrum, which has a 37% slit-loss relative a well-centred point source (35% for the non-local subtraction). When the target is modelled as both extended and with an offset, the slit-losses are far greater at 69% for local sky subtraction and 65% for non-local, accounting for two-thirds the flux measured for a well-centred point source now falling outside the microshutter. The few percentage difference in the slit-losses between the background subtraction methods comes from self-subtraction of the signal during local sky subtraction, when a portion of a target's flux enters the two outer shutters and is then subtracted from the measured signal.

For an example from the MDC, I inspect JAGUAR ID 173079, a z=3 Prioirty class 7 object which was identified as being extended relative to the shutter size and was treated as extended in the simulation. This galaxy has a JAGUAR half-light radius of 0.14" and a Sérsic index of $n = 2.2$. This galaxy also has fractional shutter offset of (+0.14, +0.38) relative to the centre of the mircoshutter. Comparing the NIPS 1D extraction of the IPS simulation to the JAGUAR input spectrum in Figure 5.5, the effect of slit-losses can be seen. The ratio of the input to the extracted spectrum has a median value of 3.33, equivalent to a slit-loss of 69.9%. In Figure 5.8 for comparison I also plot the ETC estimated spectra for various combinations of point source and extended source, well-centred and offset for the JAGUAR input spectrum in the same manner as the example above, where I use local-sky subtraction (the method used in the NIPS pipeline). When treated as an extended object with an offset, the ETC estimated slit-loss is 66.7% (relative to a well-centred point source). This slit-loss computed from the ETC has good agreement with that derived of the IPS.

[4]where this fraction is in terms of the inter-shutter spacing, so ±0.5 in either direction is in the middle of the bar separating the shutters and ±1 is the centre of the next shutter. The x,y offset is in terms of the dispersion axis (x) and spatial axis (y).

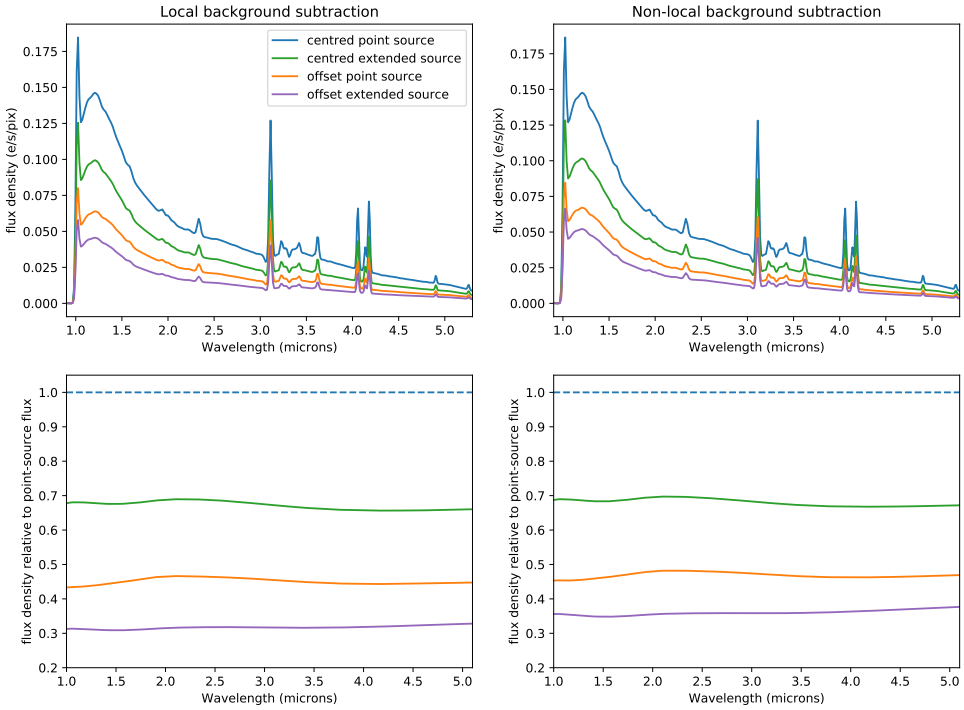

Figure 5.7: Top: ETC-estimated flux density (e/s/pixel) spectra for an example redshift z=7 galaxy with size properties typical for that epoch, half-light radius = 0.1" and Sérsic index $n = 1$ (see Chapter 4). Overlaid are treatments of the same input spectrum as a well-centred point source, an off-centre point source, a well centred extended source, and an off-centre extended source (the colours represent the same treatments in each panel). Offset sources are given a fractional shutter offset of (+0.4, +0.4). Subtraction of the sky background was either done locally (left panels) or non-locally (right panels). Bottom: the ratio of the estimated flux within an aperture to that of a well-centred point source. The difference in estimated slit-losses is dramatic between the different treatments. For a typical $z \sim 7$ galaxy the ETC expects a ∼30-63% slit-loss when treated as extended, depending on the position within the microshutter. Local sky subtraction using the outer shutters of the 1×3 layout leads to greater loss of extracted flux due to self-subtraction, of roughly 4% in this offset-extended scenario.

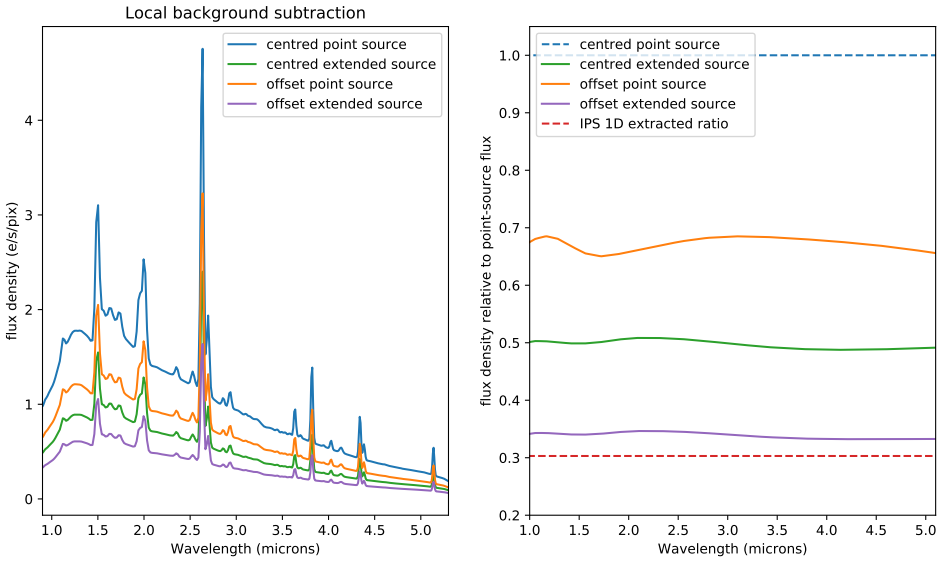

Figure 5.8: Left: ETC estimated flux spectra for JAGUAR ID 173079 redshift z=3 galaxy with size properties, half-light radius = 0.14" and Sérsic index $n = 2.2$. I over-plot the predicted spectrum for a well-centred point source, an off-centre point source, a well centred extended source, and an off-centre extended source. Offset sources are given a fractional shutter offset of (+0.14, +0.38). Right: the ratio of the estimated flux to that of a well-centred point source with the same input spectrum. The estimated slit-loss as an offset extended source from the ETC was $\sim 66.7\%$ while the measure ratio between the input spectrum and the IPS 1D extracted spectrum had a median slit-loss of $\sim 69.9\%$ (shown in red), larger than what the ETC predicted, although not too dissimilar.

5.5.2 Comparison of predicted S/N between ETC and IPS

Ground-based observations in the near-infrared are usually background-limited (i.e. the noise is dominated by the photon-counting statistics of the bright sky background, rather than those of the object counts, and this source of noise dominates over the read-out noise introduced by the detector electronics). However, JWST is in a low-background environment in the near-infrared. Hence the signal-to-noise calculation must take into account all three main sources of stochastic noise (background, object counts and detector noise), along with the additional noise introduced in the background subtraction using the spectra from adjacent microshutters[5]. The background counts also include the contribution from the detector dark current, although this has a negligible impact on the noise (with an average of 0.0092 and 0.0057 e/s/pix for the two detector chips[6]).

The NIRSpec output spectra have units of electrons per second per pixel (the gain correction from detector counts having already been applied, where the gain is close to unity for the two NIRSpec 2K detectors, 0.996 and 1.137 respectively[6]). The detector readout noise for the two NIRSpec detectors is 5.17 and 6.6 electrons for each integration in the NRSIRS2 readout mode, and for each set of observations JADES will do 2 integrations per exposure and either 1 or 4 repeats in the same observation sequence per nod (for the grating and Prism observations in the JADES-DEEP). Hence the noise per pixel for the combined spectrum from an observing sequence should be given by:

$$Noise/pix = \frac{\sqrt{((background + source) \times T_{exp}) + (N_{int} \times readnoise^2)}}{T_{exp}} \quad (5.1)$$

(In units of electrons/s/pix). Where "background" and "source" are in units of e/s/px, and readnoise in e/px. The number of integrations (N_{int}) is 2 or 8 and the exposure time (T_{exp}) is 2.8 or 11ksec for the grating and Prism observations respectively per nod position. The total exposure times will be up to 9 times longer (with three nod positions, and up to three dither positions for some objects).

[5]Systematic noise such as from undetected bad-pixels, cosmic rays or persistence is not considered by the ETC and only in a limited manner by the IPS (some types of bad-pixels).

[6]JWST User Documentation. https://jwst-docs.stsci.edu/near-infrared-spectrograph/nirspec-instrumentation/nirspec-detectors/nirspec-detector-performanceNIRSpecDetectorPerformance-Darkcurrent

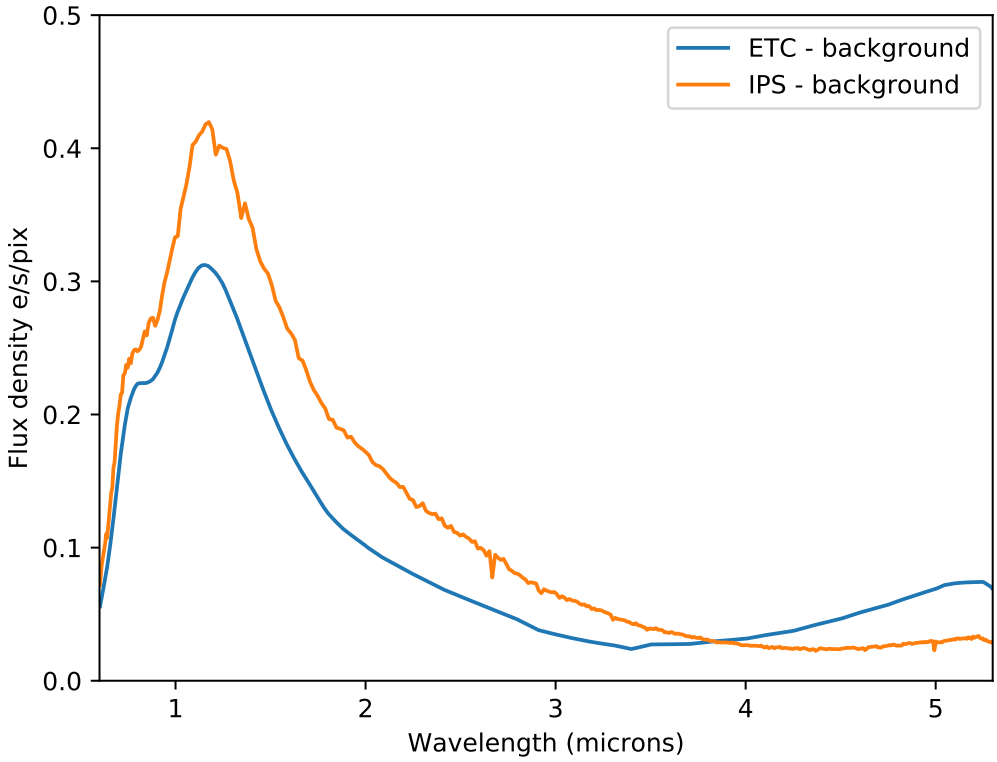

Figure 5.9: The measured background flux density from the IPS and ETC. For the ETC, a "medium" background at the position of the HUDF was chosen. For the IPS, the background model includes contribution from a zodiacal light and a stray light spectrum, following Giardino et al. (2019).

I have verified from the count rate map generated by the IPS that the quoted readnoise is consistent with the standard deviation in the count rate measured in unilluminated portions of the detector ($\sigma \sim 0.0014$ e/s/pix). The sky background, as a function of wavelength, used by the simulations are shown in Figure 5.9 (again in units of e/s/pix). The shot noise from the background flux density is sufficiently large for the background noise to dominate over the read-out noise over the whole wavelength range of the Prism.

I also use the noise from the simulated spectra (from both the ETC and IPS) to determine an estimate of the emission line sensitivity (as I discussed in the previous chapter, see Figure 4.2). To do this, I need to convert from e/s/pix to a flux density - I use the usual CGS units of erg/cm^2/s/Å. I derive this conversion separately for the IPS and the ETC. For the IPS, I have an extracted, wavelength-calibrated and flux-

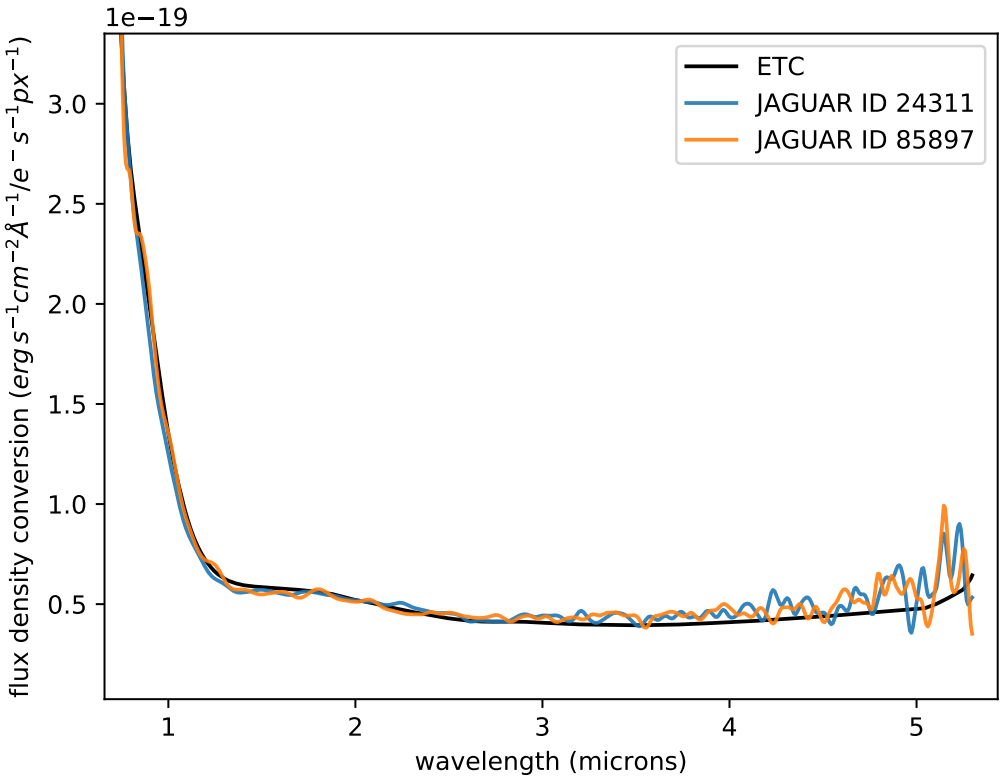

Figure 5.10: flux density calibration derived from a noiseless exposure time calculator (ETC, black) simulated target and two Mini Data Challenge well-centred bright point sources in the Prism IPS simulation (JAGUAR ID 24311 in blue and 85897 in orange). Good agreement between the ETC and IPS flux calibration is found, with the IPS containing noise.

calibrated 1D spectrum output from the NIPS software task (in units of W/m^2/m which I scale by 10^{-7} to obtain erg/cm^2/s/Å). I ratio this spectrum (which was extracted over the full microshutter height of 0.46pixels) to the noiseless electron rate map derived from the source spectrum (summed over 5×0.1arcsec pixels to account for the full microshutter extraction) to recover the calibration curve between e/s/pix and flux density as a function of wavelength (see Figure 5.10), where the pixels in the dispersion (wavelength) direction are the original size (the dispersion varies with wavelength, see Figure 5.2) and are not re-sampled to avoid correlating the noise). For the ETC, no flux-calibrated 1D extraction is generated, but an extracted noiseless count rate map is produced by the software. I use this to ratio to the input spectrum[7] in the case of a well-centred point source (where the slit losses are minimised). I compare these two calibration curves for the IPS and ETC in Figure 5.10, and note they are similar for the majority of the wavelength range, with some deviation at longer wavelengths which I put down to greater noise in the IPS spectra.

I adopt the calibration curve from the ETC (which is based on the noiseless electron rate maps) to flux calibrate the noise spectrum (that is the 1σ uncertainty per pixel in the counts in units of electron/sec as a function of wavelength). Both the ETC and the IPS output a noise (or variance) array for the simulated observations. To derive the sensitivity for background-limited observations, for the ETC I input a faint model continuum (AB = 32 magnitude and flat in f_ν), chosen so the contribution of shot noise to the uncertainty would be minimal. For the IPS, I consider an empty background shutter to get the sensitivity for a background-limited observation. I assume a line of 3px width in the dispersion (wavelength) direction, and I sum over 5 pixels, $\sim$ 1.5*FWHM, to maximise S/N. The 10σ line sensitivity with wavelength is given by:

$$f_{line}(10\sigma) = 10 \times noise \times \sqrt{N_{pix}} \times flux\_calibration \times pixscale \qquad (5.2)$$

Where the "noise" is per spectral pixel in the 1D spectrum, extracted over a full microshutter (i.e., $\sqrt{5}$ times that for an individual pixel for background-limited observations, where 5 pixels is the microshutter height) and f_{line} is in erg/s/cm^2. "Pixscale" is the number of Å/pixel, "flux_calibration" is the conversion of e/s/pix to erg/cm^2/s/Å, and I sum the line flux over N_{pix} pixels in the dispersion direction (I take N_{pix}=5).

[7] I took flat-in-lambda and AB=26mag at 2.19um for prism, AB=22 mag for the grating

I compare the 10σ emission line sensitivities predicted from the IPS and ETC in Figures 5.11 and 5.12, where I have scaled the total integration times to a common value of 10,000sec, by multiplying the sensitivity by sqrt(exposure time in seconds / 10,000s). In these figures I show the line sensitivity for when a fixed 5px aperture is used across the whole wavelength range (top panels) and for when a variable aperture is used (bottom panel). Above 2μm the telescope is diffraction limited and the PSF of the telescope increases linearly with wavelength as the resolution is proportional to $\frac{\lambda}{D_{\text{telescope}}}$ (see Figure 5.6). At shorter wavelengths a narrower aperture could be used to extracted the flux measurement from a compact source and in doing so reduce the noise of the measurement. In the bottom panels I scale the noise to follow an aperture with sensitivity $\propto \frac{\lambda}{5\mu\text{m}}$ down to 2μm and set a fixed minimum aperture of 2pixels below this (where the NIRSpec pixels significantly under sample the PSF).

Both the ETC and the IPS show line sensitivities significantly below the legacy claimed NIRSpec performance when a variable aperture is considered (the simulations are more sensitive). The IPS Prism simulation is on average 1.14 times more sensitive than the NIRSpec claimed line sensitivity when using a variable aperture, the IPS G395M simulation is on average 1.76 times more sensitive while the IPS G235M grating simulation is on average twice (2.00×) as sensitive. However, the latest publically available line sensitivity curves from the JWST user documentation are several years old and were generated before instrument characterisation, which may explain the improvement as the ETC and IPS are based on the latest detector characterised performance. The ETC and IPS show rough consistency, although in the IPS the greater signal (the IPS was based off a 27mag at $\sim 2\mu$m JAGUAR spectrum, whereas the ETC used a faint 32mag flat-in-lambda spectrum) and background (see Figure 5.9) shot noise creates larger sensitivity variability (which I have smoothed at a 10 pixel scale in the figures).

5.5.3 Prism and grating

As detailed in the JADES observing strategy, shown in Table 4.1, the DEEP observations will use the PRISM, all three medium resolution gratings and one high resolution grating. Each mode brings its own advantages: the Prism covers a larger wavelength range, whilst the higher resolution gratings allow more detailed study of emission lines, including deblending nearby lines and measurements of velocity

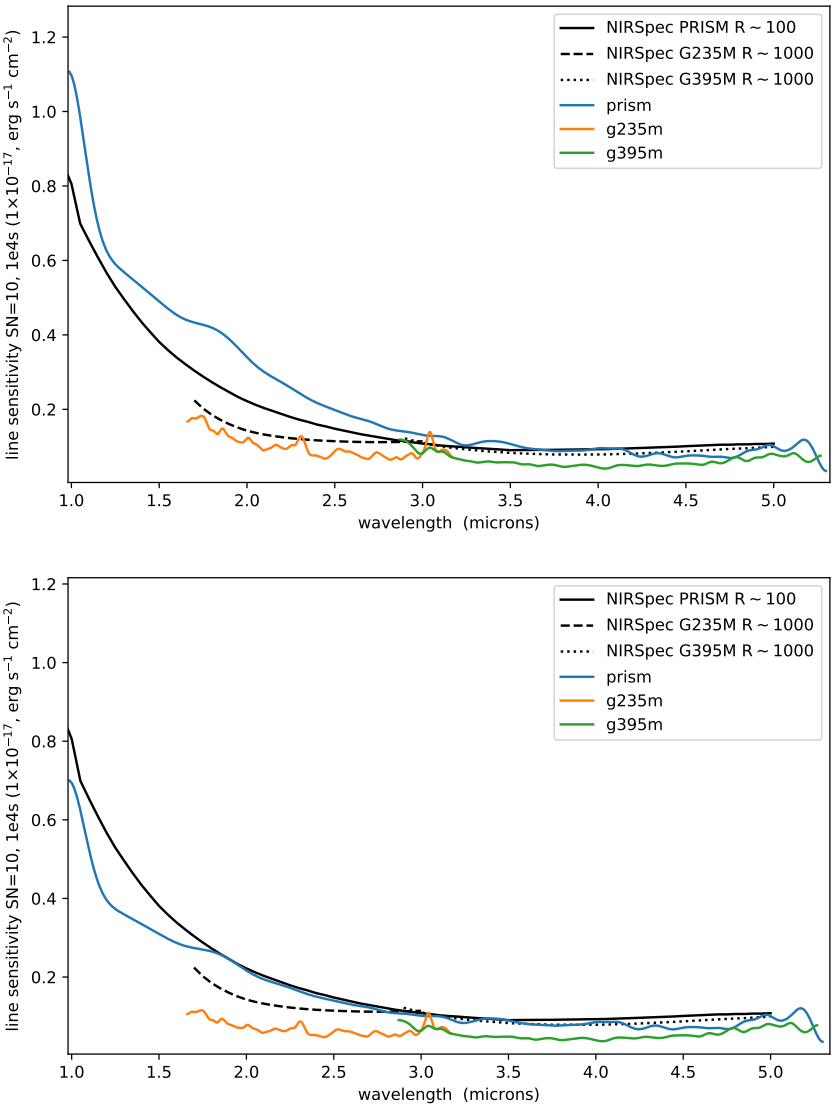

Figure 5.11: IPS derived line sensitivity for a 10ksec exposure. Top: fixed aperture of 5×5 pixels in the dispersion×spatial axis. Bottom: a variable aperture to account for the changing PSF size with wavelength, with the aperture scaled $\propto \frac{\lambda}{5\mu\mathrm{m}}$ above 2μm where the telescope is diffraction limited and fixed to 2pix below this.

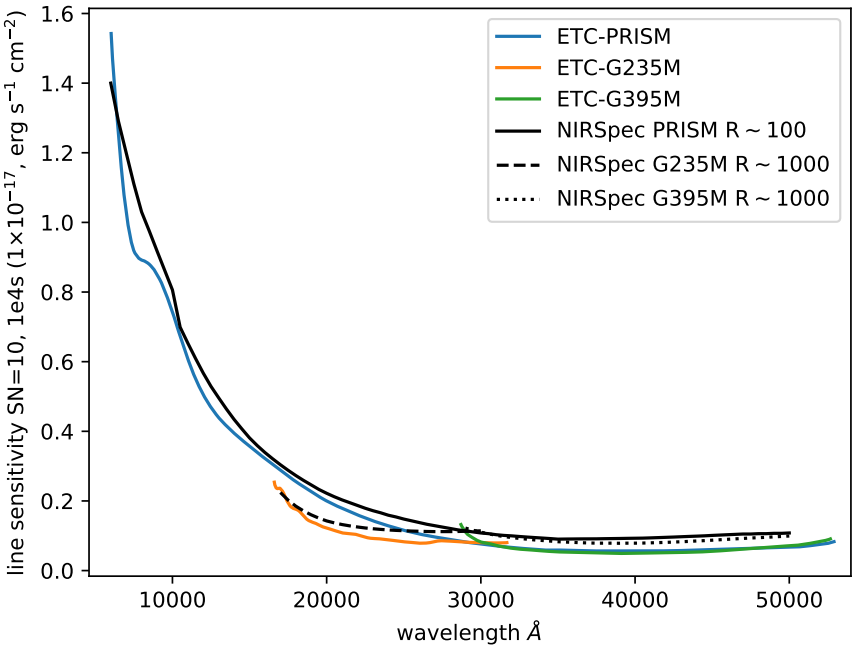

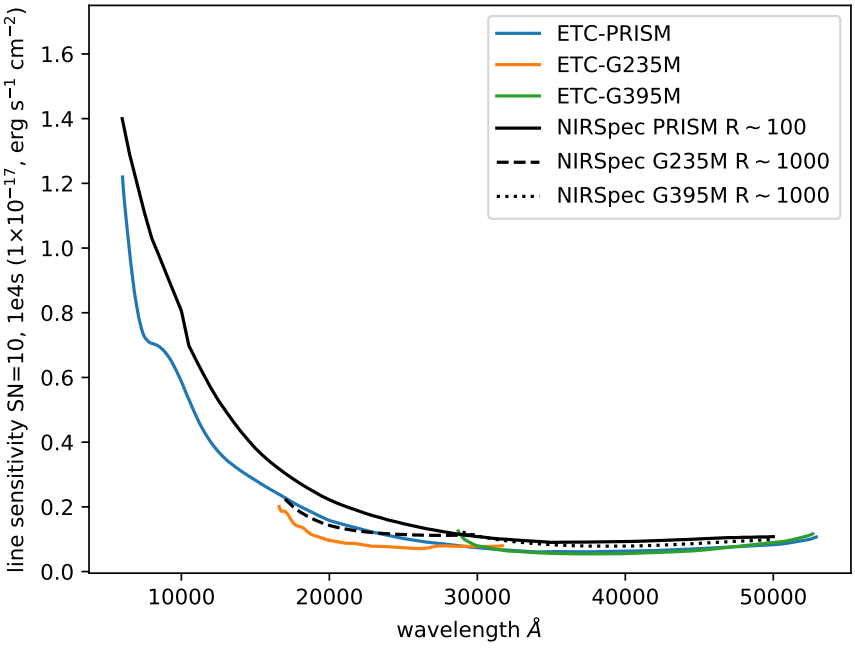

Figure 5.12: As in Figure 5.11, but for a line sensitivity derived from the ETC, for a faint flat-in-lambda AB=32mag source. The background (shown in Figure 5.9) is set to match the HUDF region for a medium sky brightness.

widths. As shown in Figures 5.11 and 5.12, sensitivity to line emission is comparable for the low-dispersion Prism and the medium-dispersion gratings above 3μm for the same exposure time. At shorter wavelengths, the G235M grating shows greater line sensitivity than the PRISM. The shorter wavelength G140M medium resolution grating, which is not simulated in this work but will be used in the real observation, also has greater emission line sensitivity than the Prism. In the real observations the Prism will have a total integration time four times longer than any of the gratings, providing a $\sqrt{4}$ improvement in the relative sensitivity.

Figure 5.13 shows the 1D extracted spectrum from the Prism and two gratings overlaid together for an example galaxy, JAGUAR ID 288701 at z=7.3. For each GWA mode, the 1D extracted spectra from each of the three dithers is averaged to obtained the total exposure time of 100,828s for the Prism and 25,210s for the gratings. The greater continuum sensitivity of the Prism is seen in stark contrast to the two gratings, whilst in the sub-panels which focus on the [OII] and Hβ+[OIII] emission lines show greater spectral resolution in the gratings.

A key feature of the JADES observations with NIRSpec is combining the low-dispersion Prism with higher-dispersion gratings; while the Prism is more sensitive (particularly given the total exposure is four times that of the individual gratings), there is key science enabled by also having the higher spectral resolution - in particular when combined with high S/N measurements of the continuum flux from the prism. For example, the deblending of Hα with the [NII] doublet will enable much better metallicity measurements than was possible in Chapter 2; and the gratings will yield more accurate redshifts and potentially evidence for outflows (different velocities of different ionisation species in spectral lines) as well as more general kinematics (line broadening from motions of gas and stars, and even rotation curves seen across the height of a microshutter which spans $\sim$ 4 resolution elements at short wavelength).

For the JADES observations we will stack up to $\sim$ 4 short spectra in the dispersion direction in the MSA design. The same design is used for the gratings, meaning the spectra overlap - but because the gratings are borderline readnoise-dominated this is not such a problem provided that we can identify which emission line comes from which object - information we get from the Prism exposure.

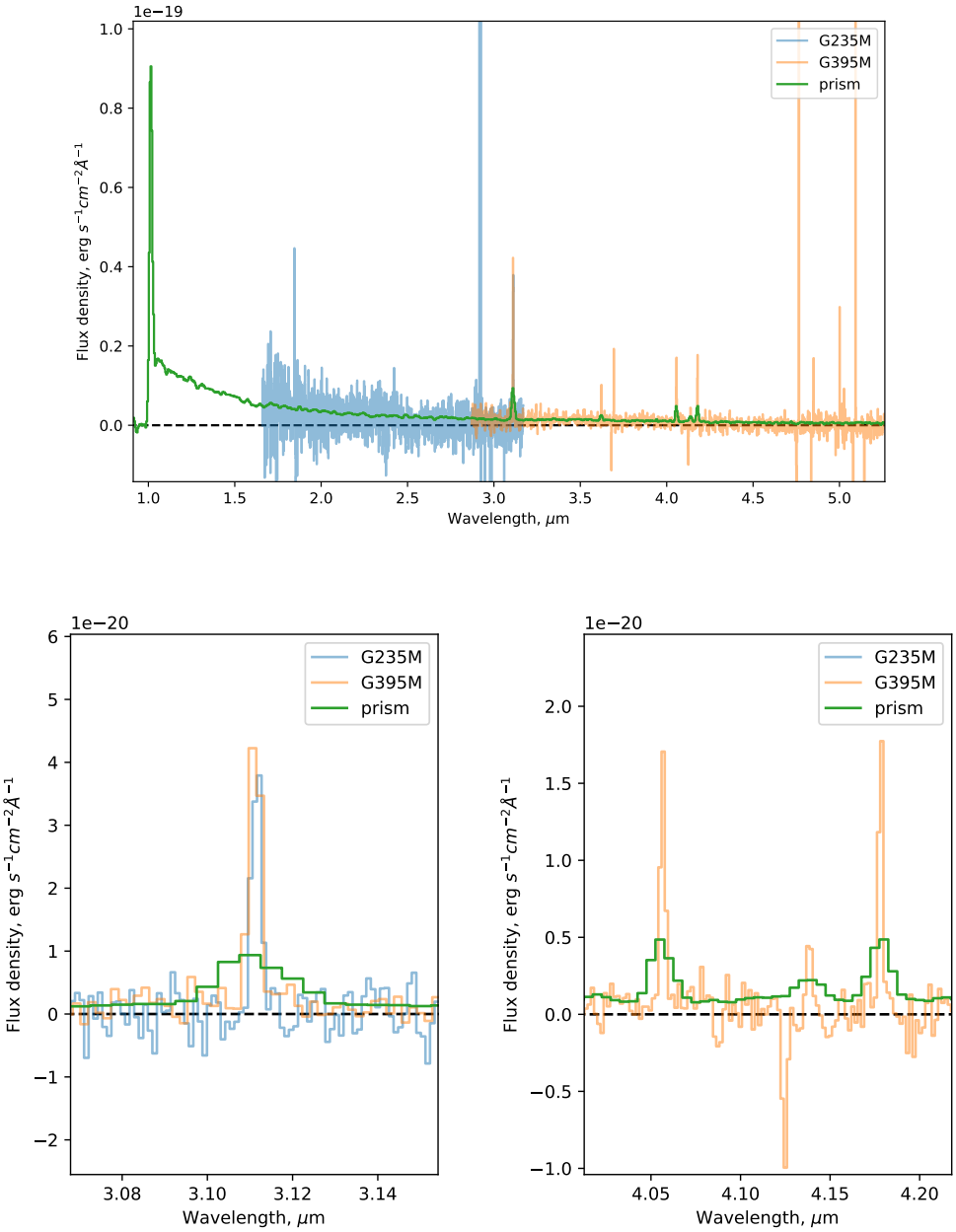

Figure 5.13: Overlaid Prism, G235M and G395M 1D extracted spectra for z=7.3 galaxy JAGUAR ID: 288701. Top: full spectral range, the Prism (green) can be seen to have greater sensitivity in the continuum compared to the G235M (blue) and G395M (orange) gratings. Bottom: Zoom in of the [OII] doublet (left) and the Hβ + [OIII] complex (right), where it can be seen that the gratings have the higher spectral resolution. Examples of bad pixels and cosmic rays can be seen in the top panel. The negative feature at $\sim 4.125\mu$m in the G395M spectrum (lower right panel) is due to an emission line in the dispersed light from another target galaxy overlapping with the sky subtraction aperture and hence causing over-subtraction.

5.6 Signal-to-noise achieved for galaxies in various Priority classes

In the previous Chapter I discussed how targets are allocated into priority classes (see Table 4.2). The top priority classes (1&2) include the highest redshifts candidates ($z \gtrsim 9$) where the main goal of NIRSpec is to spectroscopically confirm the redshift. Other important targets are potential galaxies at $z \sim 6-8$ (within the epoch of reionisation) which are sufficiently bright for JADES to be able to examine their galaxy properties through emission line diagnostics (e.g., SFR, metallicity, ionisation parameter, etc). To achieve these science objectives the recovered galaxy spectrum must have a sufficient signal to noise (particularly in the emission lines). This has led to magnitude requirements being placed on the highest priority classes at rest-UV wavelengths (which is related to the ionising flux powering the line emission) to ensure these signal-to-noise thresholds are likely to be met. Galaxies that are fainter than these thresholds are retained for observation but are set to lower priority classes to be used as filler objects in the MSA configuration.

For the galaxies from the JADES simulations which are allocated to microshutters in the MDC, all of the extracted galaxy spectra are inspected and three representative galaxies from three priority classes are drawn out as examples, to understand whether the priority class requirements achieve the S/N goals. First a priority class 1 object at high redshift, where I wish to determine whether the observing strategy provides sufficient sensitivity to spectrally confirm the redshift. Second, a priority class 4 object where I wish to measure the emission line S/N to determine whether diagnostic analysis could be performed. Finally a priority class 7 objects at lower redshift (z ∼3-4) where I wish to inspect the effect of the slit-losses on the achieved S/N. The galaxy properties of these objects is shown in Table 5.4.

The S/N of the emission lines is measured for the three GWA modes. Tables 5.5, 5.6 and 5.7 present the measured fluxes for three example galaxies for the Prism, G235M and G395M modes. The flux of each line is measured by summing pixels over a wavelength range of $\sim 1.5\times$FWHM, after first subtracting away a model fitted to the continuum level excluding emission lines and spectral breaks (I use `splot` in IRAF, and fit the continuum using a cubic spline function of order 4). The quoted uncertainty in the tables reflects the random noise within the same aperture, but I

Jaguar ID	priority class	z	M_{UV}	M_{F160W}	treatment	HLR[a]	n[b]	offset[c]
298414	1	8.74	-18.7	28.5	Extended	0.03"	0.7	-0.083, -0.037
288701	4	7.35	-20.0	27.0	Point	-	-	-0.048, -0.331
173079	7	3.01	-20.9	23.7	Extended	0.14"	2.2	0.014, 0.377

Table 5.4: Galaxy properties for the three Priority class examples. For 298414 and 288701 (Y-band drop outs), the F160W H-band is the filter above the Lyman break used for the priority class magnitude threshold. For 173079 (a B-band drop-out) the threshold filter is the F775W i-band, which has a AB magnitude of 24.5. 288701 is treated as a point-source and its Half-light radius and Sérsic index are not used in the IPS simulation.
[a] The JAGUAR Half-light radius in arcesconds
[b] The JAGUAR Sérsic index
[c] The fractional inter-microshutter offset from the centre of the shutter for the 1st MSA configuration.

note there may be additional systematic uncertainty introduced by fitting the continuum level.

The first example, Jaguar ID 298414 at z=8.74, is from the highest priority class (comprising candidate high-redshift galaxies where we wish to spectroscopically confirm their redshifts). Figure 5.14 shows the 1D extracted spectrum from one dither position of the Prism observations. The Lyman break is clearly visible in the extracted spectrum and this alone could provide spectroscopic confirmation of the redshift. Additionally, three emission lines ([OII], Hβ and [OIII) are also identifiable in the Prism spectrum which would provide a conclusive redshift. The [OII] and [OIII] doublets are both detected at a S/N$\sim$ 20 in the 33ksec exposure time Prism spectrum (a third of the total exposure time). Due to the shorter exposure time of the gratings (1/4 of the Prism) the S/N of the [OII] doublet is lower at S/N$\sim$ 12 in the G395M grating. In this particular example the G395M spectrum fell across the detector gap, losing coverage of the [OIII]+Hβ complex.

Combining the three dithers of the Prism observations (each of 33ksec) together would result in a higher S/N of $\sim$ 29 for each of the [OIII] and [OII] lines, where I have accounted for the additional noise associated with local sky subtraction (a 25% increase of the background noise). This specific galaxy was treated as an extended source and well centred in the microshutter (Table 5.4). The H-band magnitude of M_{AB}=28.5 mag is 1 magnitude brighter than the threshold of 29.5 mag for inclusion

JAGUAR ID	Emission Line	input	measured	S/N	Slit-loss
298414	[OII]	7.1e-19	5.5±0.3 e-19	16	23±4%
Class 1	Hβ	2.3e-19	2.1±0.4 e-19	6	9±19%
	[OIII]	8.0e-18	*5.0±0.3 e-18	19	*38±4%
288701	[OII]	16.0e-19	15.3±0.4 e-19	38	4±3%
Class 4	Hβ	6.3e-19	5.9±0.3 e-19	23	6±5%
	[OIII]	8.8e-19	8.3±0.3 e-19	30	6±3%
173079	[OII]	6.1e-17	1.09±0.01 e-17	126	82±0.1%
Class 7	Hβ + [OIII]	5.6e-17	1.15±0.01 e-17	113	79±0.2%
	Hα	6.9e-17	1.30±0.01 e-17	213	81±0.1%

Table 5.5: Prism flux measurements taken from one dither (integrated exposure time 33ksec), whilst S/N measurements are representative of the random noise, the uncertainty in fitting and subtracting the background level in the Prism is not accounted for here. For local background subtraction the noise should be 25% higher (S/N should be 20% lower). All flux and uncertainty units are given in erg/s/cm2
* may be underestimated due to coincidence with a bad pixel

JAGUAR ID	Emission Line	input	measured	S/N	Slit-loss
288701	[OII]	16.0e-19	15.5±0.8 e-19	19	3±5%
Class 4	Hβ	6.3e-19	-	-	-
	[OIII]	8.8e-19	-	-	-
173079	[OII]	6.1e-17	-	-	-
Class 7	Hβ	2.1e-17	0.61±0.02 e-17	38	71±1%
	[OIII]	3.5e-17	1.1±0.02 e-17	56	69±1%
	Hα	6.9e-17	2.0±0.02 e-17	131	71±0.2%

Table 5.6: G235M flux measurements. Same as Table 5.5 but for the medium resolution grating. Jaguar ID 298414 did not have emission lines in the wavelength range covered by this grating and hence is not shown here. Units erg/s/cm2

JAGUAR ID	Emission Line	input	measured	S/N	Slit-loss
298414	[OII]	7.1e-19	5.4±0.54 e-19	10	24±8%
Class 1	**Hβ	2.3e-19	-	-	-
	**[OIII]	8.0e-18	-	-	-
288701	[OII]	16.0e-19	15.9±0.5 e-19	31	0±3%
Class 4	Hβ	6.3e-19	5.9±0.5 e-19	12	6±8%
	[OIII]	8.8e-19	8.1±0.5 e-19	17	8±5%

Table 5.7: G395M flux measurements. Same as Table 5.5 but for the medium resolution grating. Jaguar ID 173079 did not have emission lines in the wavelength range covered by this grating and hence is not shown here. Units erg/s/cm2.
** Emission lines were compromised by the chip gap.

in the top priority classes (see Table 4.2). Hence for a fainter object at the magnitude threshold for inclusion in this priority class (and with similar spectral properties to this example) I would expect the S/N to be reduced by a factor of 2.5, which would be S/N$\sim$ 12 for [OIII] and [OII]. This would represent a clear redshift confirmation, and indeed I could tolerate slit losses of up to 60% (due to a source of such brightness being extended and/or lying at the edge of a microshutter) and still achieve a detection at S/N$\sim$ 5 of these lines. I note that an even fainter high-z candidate than the 29.5 magnitude threshold might potentially enter Class 3 (see Table 4.2) as a lower-priority source, and JADES could potentially detect line emission at S/N$\sim$ 4 for targets as faint as 30.5mag.

I also note that the continuum is significantly detected in the Prism spectrum for this example galaxy. The signal-to-noise of the continuum per resolution element ($\sim$ 2 native pixels) for an 11ksec exposure, including the additional 25% noise from local-background subtraction, is shown in Figure 5.14 with wavelength. For the full 100ksec exposure the S/N would be a factor 3 higher. To detect the Lyman break I am interested in a significant detection above the break and no detection below. For a galaxy at $z \sim 9$, the Lyα break is at $\sim$1.2μm where the resolving power of the R100 prism is only R $\sim$ 30, rising to R $\sim$50 at 2μm. Hence there are only about 10 resolution elements in the rest-frame spectral range $1216 < \lambda <$1500Å(from Lyα to CIV and He II), that avoid contamination from emission lines. In this wavelength range above the Lyman break the continuum is detected at a S/N per resolution element of $\sim 6-8$, and is well above the continuum S/N$>$ 3 per spectral element goal for Priority class 1. Summing across this narrow wavelength range gives a continuum S/N$\sim$20 in 11ksec and this would rise to SN=60 in 100Ksec. The faintest galaxy to achieve a S/N=10 break would be at magnitude 30.5 - this includes class 3 objects.

The second example, Jaguar ID 288701 at z=7.35, is from priority class 4 (candidate $z \sim 6-8$ galaxies where we desire sufficient signal to noise in the detected emission lines to perform line ratio diagnostics, achievable with Hα at S/N $>\sim$ 25 where this falls within the NIRSpec coverage). Figure 5.16 shows the 1D extracted Prism spectrum for one 33ksec dither (and is also shown in Figure 5.13 for the 100ksec exposure). This is a bright galaxy with $M_{\rm UV}$=-20.0, and the continuum is detected at a high signal to noise. This galaxy was treated as a point source and the ratio of the extracted continuum to the input JAGUAR continuum is consistent with minimal slit-losses below 3μm with a median ratio of 0.95, measured avoiding emission

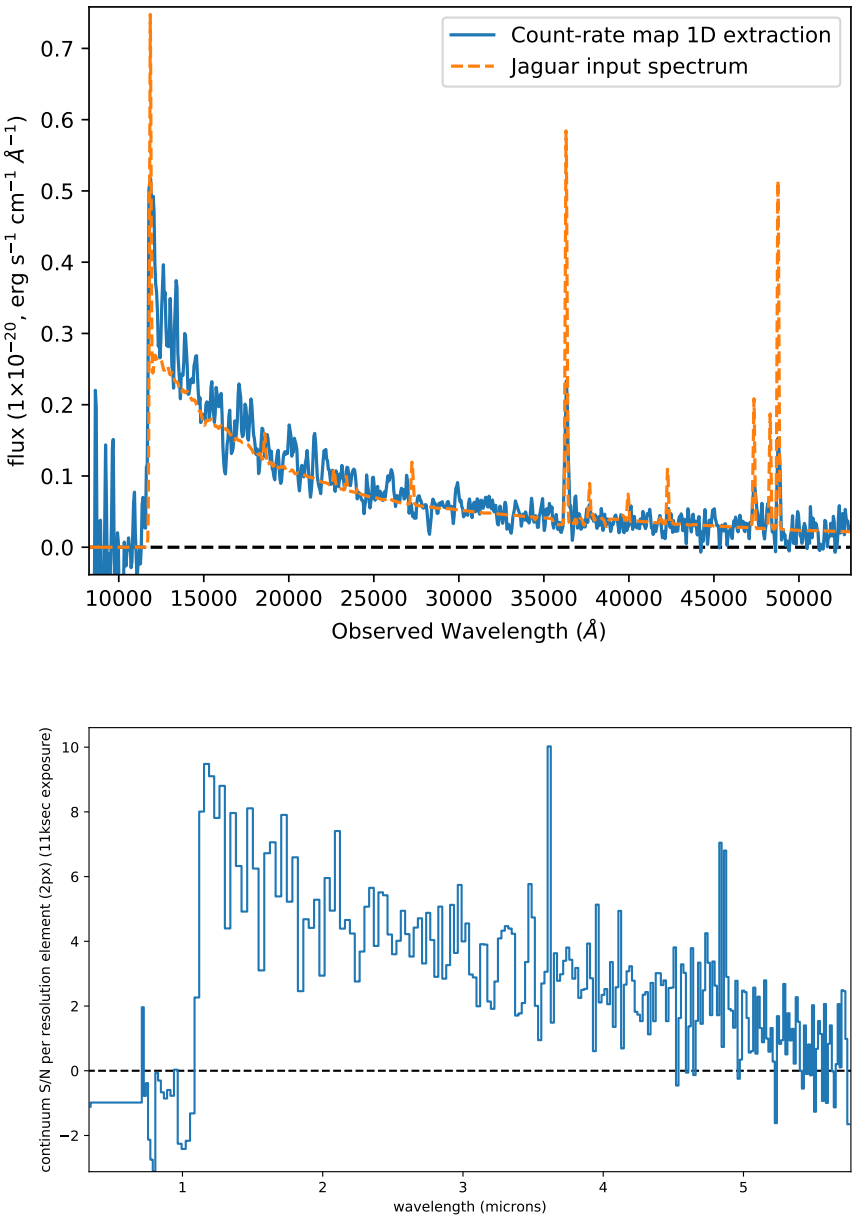

Figure 5.14: Top: 1D extraction of the Prism simulation for one dither (blue), combing the three noddings (exposure time = 33ksec), for JAGUAR ID:298414: Priority class 1, z=8.7. The input JAGUAR spectrum is shown in orange. This particular galaxy was treated as an extended object although was compact (half-light radius = 0.14") and well-centred, and shows minimal slit-losses. The [OII], Hβ and [OIII] emission lines are detected at a sufficient signal to noise to identify the redshift of this galaxy. Bottom: The signal-to-noise of the continuum per resolution element ($\sim$ 2native pixels) for an 11ksec exposure, including the additional 25% noise from local-background subtraction. For the full 100ksec exposure the S/N would be a factor 3 higher. The Lyman break can be clearly identified with the sensitivity of the continuum and is well above the continuum S/N$>$ 3 per spectral element goal for Priority class 1.

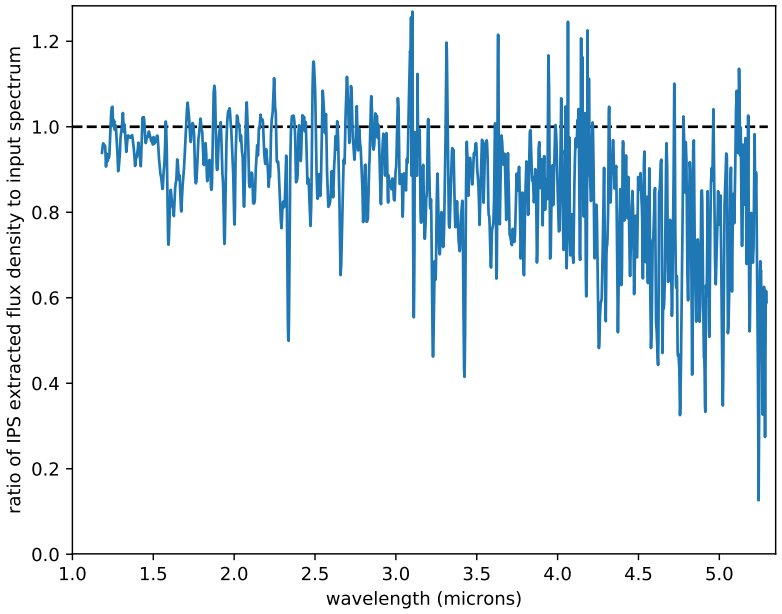

Figure 5.15: The ratio of the NIPS extracted flux density of galaxy 288701 to the JAGUAR input spectrum. The fraction of recovered flux density drops at longer wavelengths due to the larger PSF which is shown in Figure 5.6.

lines (as shown in Figure 5.15). However, at longer wavelengths the spectrum shows increasing slit-losses as the PSF of the telescope increases in angular size (with a median flux ratio of 0.84 above 4μm). The ratio of the measured emission line fluxes to those of the input lines (in both Prism and gratings, see Tables 5.5 and 5.7), is consistent with minimal slit-losses. I note that running the ETC with the same input spectrum and same spatial offsets within the microshutter for this point source returned a slightly higher slit-loss of 18%, rather than than the $\sim$ 6% calculated from the IPS. The origin of this discrepancy is unclear.

For this z=7.3 galaxy, the Lyman break is clearly visible (Figure 5.16), as are multiple emission lines. In the Prism, the [OII] doublet, Hβ and [OIII] doublet can be clearly identified and are detected above a S/N$\sim$ 20 (Table 5.5). These provide a useful measurements for line diagnostics, such as the R23 and O32 diagrams discussed in Chapter 2. I also find broad agreement between the estimated S/N from the IPS and that estimated by the ETC, once the different slit-loss and the slightly higher noise in the ETC model (arising from a higher assumed background flux) are accounted for.

Given that I have good detections at S/N∼20-30 of the key emission lines Hβ, [OII] and [OIII] for this example Lyman break galaxy at z=7.3 in a single 33ksec dither pointing with the R100 prism, I now consider how much fainter I could go in the full 100ksec JADES-Deep Prism spectra and still achieve sufficient S/N for line ratio diagnostic work (the main objective for Priority Class 4 galaxies). In establishing priority class 4, the JADES team took a fiducial limiting S/N∼25 for Hα (if this falls within the NIRSpec spectral coverage at that redshift). The case B flux ratio is f(Hα)/f(Hβ)=2.86 and hence Hβ would have S/N∼ 9 if Hα has S/N∼ 25 assuming no reddening and assuming fairly uniform line sensitivity with wavelength (which is the case for from $\sim$ 2.5μm to $\sim$ 5μm, see Figure 5.11). For z=7.3 (the redshift of the example JAGUAR 288701), Hα falls just beyond the long-wavelength cut-off at 5.3μm, but I am sensitive to Hβ which is detected in the simulated 33ksec spectrum at S/N=18 (assuming local sky subtraction using 2 adjacent microshutters), which would be S/N=31 for the full 100ksec Deep observation. Hence I could observe an Hβ line which is $\sim$ 3.5 times fainter than this example and still meet the S/N requirement for inclusion in Class 4. This particular galaxy has a magnitude of AB(F160W)=27.0 mag, and JADES could potentially include galaxies as faint as AB(F160W)=28.4 mag in Class 4 (assuming the same redshift and spectral properties as this example).

However, I note that the intensity of the emission lines relative to the UV continuum depends in particular on the star formation history. In choosing the magnitude threshold to achieve a Hα S/N, the Kennicutt (1998) relation between L_ν(UV) and Hα was adopted (for a continuous SFR and Salpeter IMF). Variation from this prescription may see a change in the required magnitude threshold, and I find that Jaguar 288701 does have a stronger Hβ line by $\sim$ 50% than would be predicted from the Kennicutt (1998) prescription. This would allow a deeper limiting magnitude cut for inclusion in class 4 (currently set at AB∼27.5, see Table 4.2), potentially by ∼0.5 mag if we are $\sim$ 50% more sensitive to line emission than the historic curves. Alternatively, I can tolerate slit losses of up to 50% for AB=27.5 mag or 28.0 mag (depending on if you're using the conservative Kennicutt (1998) conversion to line flux for a constant SFR)

Figure 5.13 shows the 1D extraction for the Prism and the G235M and G395M gratings. It can be seen how that sensitivity in the continuum is lower in the gratings, with the trade off for enhanced spectral resolution of the emission lines. When

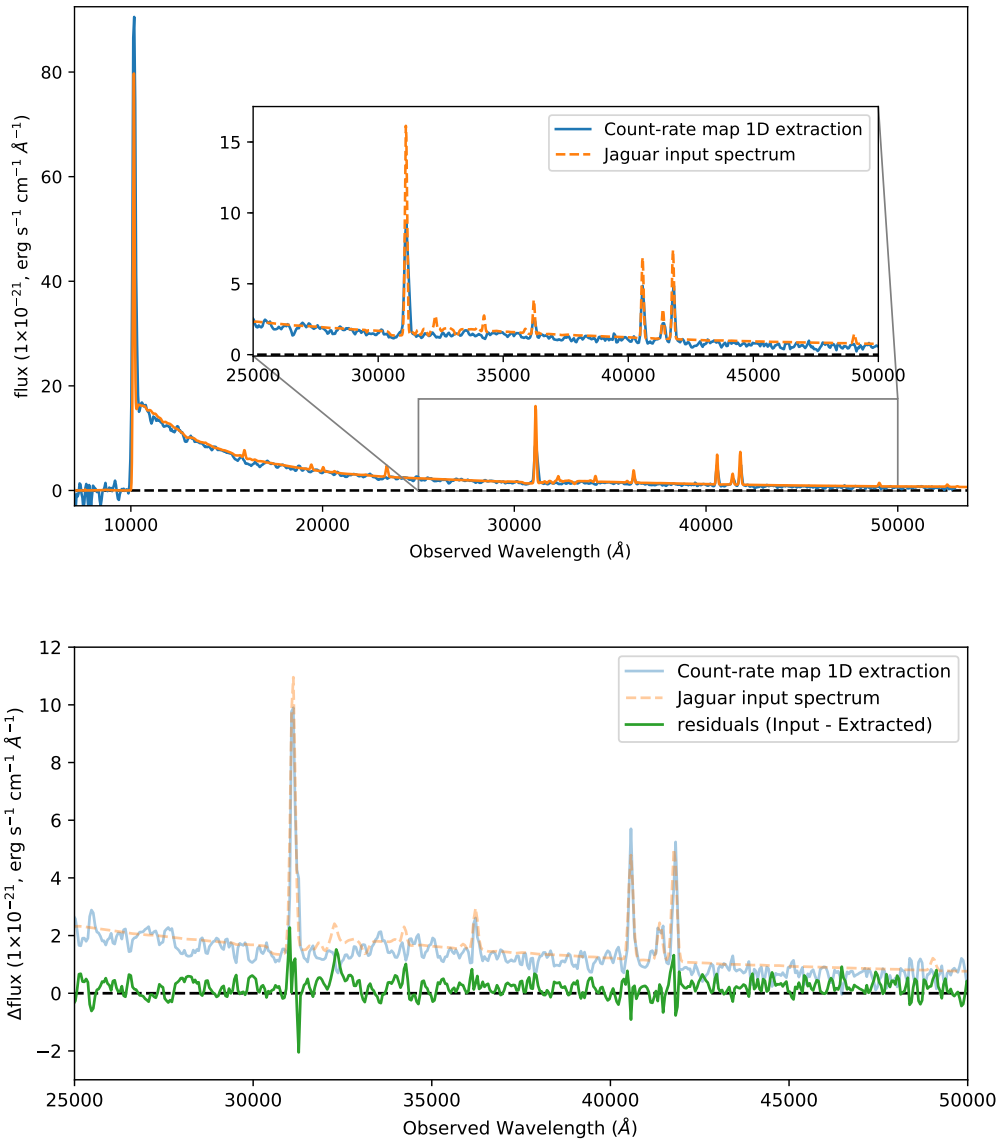

Figure 5.16: Top Panel: 1D extraction of MDC target compared to the JAGUAR input spectrum. JAGUAR ID 288701 at z=7.3 is a Priority class 4 galaxy and is compact relative to the microshutter, so treated as a point-source. To simplify the simulation, only emission lines in Table 5.3 are included and for this galaxies the recovered emission lines are at a sufficiently high S/N to meet the class 4 science requirements. The input JAGUAR spectrum has higher spectral resolution than the R∼100 Prism, hence the peak height of the emission lines is higher, although the integrated flux is almost identical between the input and simulation (subject to the same slit losses as the continuum). Bottom panel: Good agreement is found in the residuals between the input and extracted spectra over the 'zoom-in' range with minimal slit-losses after scaling the input spectrum to the lower resolution of the R∼ 100 Prism.

the emission line fluxes are measured in each of the GWA modes, consistency is found.

A final check on this Class 4 example is to examine the sensitivity on some of the derived properties (using the emission line flux measurements), such as the O32 and R23 line ratio diagnostics discussed in Chapter 2. The O32 and R23 emission line flux ratios for this example galaxy are calculated from the flux measurements (for this 33ksec dither pointing), and both have an achieved S/N of 18 (O32 = 0.407±0.022, R23=4.00±0.22). Following the work in Chapter 2 these measurements can be used to determine the metallicity using the Curti et al. (2017) strong line diagnostics (derived from < 0.25 galaxies), which are $12+\log_{10}(\mathrm{O/H}) = 8.583\pm0.009$ and 8.640 ± 0.017 for the O32 and R23 diagnostic respectively. Despite this galaxy lying at z=7.35 and using only a third of the maximum 100ksec exposure time, this simulated observation provides smaller uncertainties on the strong-line derived metallicity than the typically 0.04 metallicity uncertainty found in the $z \sim 1$ WISPS sample in Chapter 2, which relied on shorter exposure time HST grism slitless and ground-based FORS2 spectroscopy.

The final example, JAGUAR ID 1730079 at z=3.01, is from priority class 7, which comprises lower redshift $z \sim 3-5$ galaxies, where we desire sufficient S/N to use line ratios and spectral continuum shapes to characterise stellar populations at these intermediate redshifts (after the epoch of reionisation). For any individual galaxy in this low priority class, the probability of being allocated to a microshutter on NIRSpec is low, but there are a large number of Lyman break galaxies at these redshifts to draw from (see Chapter 4) and can build up a statistically-significant sample. This Priority class 7 may also contain higher-redshift candidates that were demoted due to being too faint to achieve the anticipated sensitivity. At lower redshifts galaxies tend to be spatially resolved (and physically large), which may lead to greater slit-losses. I wish to inspect a bright galaxy that is extended to understand whether it is still worth allocating to the MSA configuration even with substantial slit-losses. Jaguar ID 173079 is a bright (M_{UV} = -20.9) galaxy with a half-light radius of 0.14" and is offset within the microshutter, with a large spatial-axis offset of (0.014, 0.377) fractional microshutters. This galaxy was treated as extended in the IPS simulation. In Section 5.5 I used the ETC to estimate a slit-loss of 68% which closely matched the that derived from the extracted IPS of 69.9%.

It can be clearly seen in Figure 5.5, that despite the substantial slit-losses (and potentially some self-subtraction from the adjacent background shutters for this extended source), the spectrum is very high S/N in the continuum and in the emission lines (e.g., Hα is detected at a S/N$\sim$ 200 in 33ksec). The slit-losses in the measured emission line flux agree between the Prism and the gratings, which are $\sim$ 80% in the Prism and $\sim$ 70% in the grating. This is an example of a galaxy where I need only hit it in 1 of 3 dithers to achieve the desired continuum and emission line sensitivity (e.g., Hα S/N$>$ 25). Alternatively observing in all three dithers would allow very high S/N, ideal for studies such as the kinematics of emission lines, to look for the presence of AGN components and outflows; for the spatial resolution along the slit for velocity gradients, to measure the evolution of the Tully-Fisher relation (Tully & Fisher, 1977); or to detect weak auroral lines, to provide better metallicity indicators than strong lines.

5.7 Potential further development of the NIRSpec simulations and data reduction pipeline

The Mini Data Challenge took place between December 2019 and February 2020 to emulate the possible 45 day interval between NIRCam and NIRSpec observations within the same visibility window. This first time-limited stage of the MDC culminated in the design of NIRSpec MSA configurations, and then this was used to simulate NIRSpec spectroscopy which has been described in this Chapter. With the first NIRSpec observations after telescope commissioning coming no sooner than mid-2022 (and delays still possible) there will be time available to run another mini data challenge to test the improvements identified in the first challenge, and to further prepare the JADES science team for the real observations. Improvements to step 8 that could be implemented for a second MDC would improve on the previous simplification of treating the targets as circular by using the JAGUAR ellipticity for the input galaxies. For a highly elliptical target the slit losses suffered would be strongly dependent on the orientation of the major axis relative to the rectangular microshutter (See ID 3982 in Figure 5.1 for example of highly elliptical target lying along the open shutters). Further, emission lines could be treated as spectrally resolved to allow outflow and kinematic velocity field physics to be tested during step 11 (which is the derivation of galaxy proprieties from the NIRSpec spectroscopy) - in the current simulations in this Chapter I assumed a narrow intrinsic line width of 100km/s

(spectrally unresolved).

NIPS currently provides a basic 1D extraction, collapsing the 2D spectrum on the detector in the spatial direction over a fixed aperture (the full illuminated extent of a single microshutter). However, the microshutter height of 0.46" (sampled by 5 pixels) is much larger than the size of the PSF, and hence for a compact source an improvement in the S/N could be achieved by using a spatial extraction that is smaller than the full shutter height and better matched to the PSF size (which is wavelength-dependent, see Figure 5.6). A future improvement of the NIPS extraction pipeline could be a variable extract width (depending on the intrinsic size of the target, perhaps inferred from NIRCam imaging, and wavelength) to maximise the S/N of the 1D spectrum. The NIRCam photometry and size/shape measurements will also enable the wavelength-dependent slit loss corrections to total flux to be determined for spectro-photometry.

Several artefacts can be found in the IPS simulations (e.g., the bad pixels visible in the count-rate map in Figure 5.4). As a result of this experiment with the simulations presented in this Chapter, a bad pixel flag has now been added to the count-rate maps and to the NIPS extraction pipeline. This bad pixel mask (made from flat field and dark current exposures) is added as an additional file extension to the 2D count-rate maps. Ultimately, when different nod and dither positions are combined for the same galaxy, the data flagged from the bad pixel can be excluded in the co-addition, so that the 1D extracted spectrum will not suffer from individual bad pixels.

As mentioned in Section 5.5.3, the JADES observations will maximise the number of objects allocated to shutters by stacking up to ~ 4 short spectra in the dispersion direction in the MSA design. However, since the same design is used for the gratings, the dispersed light of multiple targets will overlap as the grating spectrum covers a greater pixel range. The NIPS pipeline therefore must be able to identify which emission lines come from which object using the information from the Prism exposure, but must also be able to avoid subtracting emission lines from overlapping spectra from an individual target's extracted spectrum.

Finally, in the JADES observations careful selection of three MSA configurations for the three dithers will be used to greater effect to create a dither pattern that spans

the detector chip gap. Such that the portion of a spectrum's wavelength coverage lost to the gap in one dither can be recovered in another dither. This is of particular importance for the gratings which span a large pixel range.

5.8 Summary

In this Chapter I have simulated NIRSpec spectra for a realistic set of observations based on the JAGUAR mock catalogue of galaxies. I consider both the low-dispersion Prism (R$\sim$100) and two medium-dispersion gratings (R$\sim$1000) and I replicate the observing strategy that JADES will employ in the Deep tier of the NIRSpec spectroscopy. The simulated spectra include the effects of the galaxies being off-centre in the microshutters, and also model many of the galaxies as being spatially resolved. From this I am able to determine the slit losses (light falling outside the microshutter) as a function of wavelength. I determine the signal-to-noise ratio of the NIRSpec spectra, accounting for the noise from the background light, the photon counting statistics of the source, and the readout noise of the detector. I compare the anticipated emission line flux sensitivity (as a function of wavelength) with older estimates for NIRSpec, and find that the IPS is more sensitive (now that the instrument performance has been better characterised in ground-based testing). The IPS is on average 1.14 times more sensitive in the Prism, 1.76 times more sensitive in the G395M and on average 2.00 times more sensitive in the G235M grating compared to the claimed line sensitivity, when a wavelength dependent variable aperture is used.

I consider whether the mock catalogue galaxies allocated to different priority classes result in spectra of sufficient quality (S/N) to achieve the various science goals (for example: redshift determination of the most distant candidate galaxies from line emission or the Lyα spectral break at $z \gtrsim 9$; line ratio diagnostics for star-forming galaxies at $z \sim$6-8; and characterising stellar populations from the continuum shape and emission lines at $z \sim$2-6). I conclude that the proposed brightness limits from broad-band photometry for the various priority classes in JADES are realistic, and will result in spectra which meet the science requirements even with significant slit losses.

Chapter 6

Conclusion

In this Thesis I have sought to understand the star forming galaxies which are observed to exhibit large nebular emission line equivalent widths. These may be good low-redshift analogues of galaxies beyond $z > 6$ which are believed to drive the ionising radiation field during the Epoch of Reionisation. Through two spectroscopic studies at intermediate redshifts I have utilised HST/WFC3 slitless spectroscopy to select galaxies directly on their emission line strength, and then to create a sample of star-forming galaxies from which the abundance of extreme emission line galaxies (those with high nebular emission line EW) can be determined and their properties studied. I also looked at expanding this work on star-forming galaxies to higher redshifts, which will be made possible through deep extra-galactic surveys using the next generation imaging and multi-object spectroscopy facilities on JWST. NIRSpec spectroscopic follow-up of high redshift galaxies requires a reliable target sample, and I have discussed how a list of potential candidates for NIRSpec spectroscopy has been drawn up from LBGs in the JADES fields and how my uniform re-analysis has allowed these to be compared and prioritised. Finally, I simulated the NIRSpec spectra for high redshift galaxies similar to our potential JADES targets, to determine if our key science goals can be met with the achieved signal-to-noise (in particular redshift confirmation, and metallicity measurements from line ratio diagnostics).

In Chapter 2 I have followed-up galaxies identified through line emission in the near-infrared in the slitless HST/WFC3 WISP survey, using VLT/FORS2 optical spectroscopy to confirm the redshifts and to study the reddening and metallicity of this emission line selected population. Follow-up of these targets is of particular interest, as the typical galaxy in my WISPS sample is fainter than $H_{AB} = 24\,\mathrm{mag}$, and so would not have been included in many well known spectroscopic surveys based on

broad-band magnitude selection. Over 4 WISPS fields, I targeted 85 out of 138 emission line selected objects identified in the WFC3 slitless spectra over a redshift range $0.4 < z < 2$ and I confirm 95% of the initial WFC3 grism redshifts in the 38 cases where lines were detected in the FORS2 spectra, an important result for the WISPS programme, especially because in many cases the WFC3 spectra showed only a single emission line (usually assumed to be Hα). For these single-line WFC3 sources, the FORS2 spectroscopy confirmed the redshifts of 15 out of 17 galaxies (88%).

I measured the Balmer decrement to determine for reddening (after correcting for stellar absorption and blended [NII] emission), and found that the extinction of the WISPS galaxies is consistent with $A(\mathrm{H}\alpha) = 1\,\mathrm{mag}$ with some evidence for an increase in reddening with Hα luminosity, and less reddening than seen in $z \sim 0$ samples. After correction for reddening, good agreement was found between star formation rates derived from the Hα emission line, the rest-frame UV continuum (L_{UV}) and BEAGLE SED fitting (with near-linear slopes of $SFR(L_{UV}) = [SFR(H\alpha)]^{1.15\pm0.10}$ and $SFR(L_{SED}) = [SFR(H\alpha)]^{1.04\pm0.08}$). SED-fitting of the stellar population determined the sample spanned a broad mass range, with a median $\log_{10}(M/M_{\odot}) = 8.94$, and that these emission line selected galaxies have high specific star formation rates and lie above the star-forming main-sequence.

After two likely AGN ($\sim$5% of the sample) were removed, identified using the [SII]-BPT and mass-excitation (MEx) diagnostics, I used the [OII], Hβ and [OIII] line fluxes to derive gas-phase metallicities using the strong-line O32 and R23 diagnostics (using calibrations from Curti et al. 2017). Individual and stacks of galaxies are typically sub-solar metalicity, with a trend of metallicity decreasing with increasing redshift. I also recover the mass–metallicity relation, with the sample lying at lower metallicities than the $z = 0$ relation, consistent with the evolution seen in other high redshift studies, along with evidence for a fundamental relation between SFR, stellar mass and metallicity.

Within this emission line selected sample I find strong dependence of the rest-frame Hα equivalent width of galaxies with redshift, evolving as $EW_0(H\alpha) \propto (1+z)^{1.88\pm0.32}$, consistent with what has been seen in samples at similar redshifts with typically higher masses. Importantly for the study of low-redshift analogues to galaxies during the EOR, when I split the sample by Hα equivalent width at $EW_0(H\alpha) = 100\,\text{Å}$, I found

that higher EW galaxies have a larger [OIII]/Hβ and O32 ratio on average, suggesting a lower metallicity or higher ionisation parameter in these extreme emission line galaxies.

In Chapter 3, I investigated the population of extreme emission line galaxies at $1.700 < z < 2.274$, which are seen as low-redshift analogues of the galaxies during the epoch of reionisation responsible for the strong UV-ionising background. I determine the [OIII]λ5007 equivalent width distribution of rest-frame UV-selected ($M_{UV} < -19$) star forming galaxies in the GOODS North and South fields, making use of deep HDUV broadband photometry catalogues for selection and 3D-HST WFC3/IR grism spectra for measurement of line properties.

The [OIII]λ5007 EW distribution allows the measurement of the abundance of extreme emission line galaxies within this population. I model a log-normal distribution to the [OIII]λ5007 equivalent widths of galaxies in the sample, with a best fit location parameter $\mu = 4.24 \pm 0.07$ and variance parameter $\sigma = 1.33 \pm 0.06$, with a mean [OIII]λ5007 EW of 168$\pm$1Å. The fractions of $z \sim 2$ rest-UV-selected galaxies with [OIII]λ5007 EWs greater than $500, 750$ and 1000Å are measured to be $6.8^{+1.0}_{-0.9}$%, $3.6^{+0.7}_{-0.6}$%, and $2.2^{+0.5}_{-0.4}$% respectively. I determine that the EELG fractions do not vary strongly with UV luminosity in the range $-21.6 < M_{UV} < -19.0$ considered in this work (consistent with findings at higher redshifts).

I compare my $z \sim 2$ results to studies at $z \sim 5$ and $z \sim 7$ where candidate EELGs have been discovered through Spitzer/IRAC colours, and I identify rapid evolution with redshift in the fraction of star forming galaxies observed in an extreme emission line phase (a rise by a factor ~ 10 between $z \sim 2$ and $z \sim 7$). This evolution is consistent with an increased incidence of strong bursts in the galaxy population during the reionisation era. While I determine that this population makes a sub-dominant contribution of the ionising emissivity at $z \simeq 2$, EELGs are likely to dominate the ionising output in the EOR.

Looking towards the future of this field of research, the imminent launch of JWST presents a huge leap forward in the facilities at the community's disposal. I am member of the JADES collaboration, a joint NIRSpec and NIRCam instrument science team GTO programme. The deepest part of the JADES NIRSpec spectroscopy consists of two 100ksec integrated exposures with the goal of observing the most distance

galaxies. One of these exposures will focus on the HUDF in GOODS-South, where existing known targets from deep HST observations will be followed-up, whilst the other will follow up high redshift candidates selected from deep NIRCam imaging, and will include high redshift galaxies that have not been detected in existing HST observations.

In preparation for the follow-up of existing known HST sources, in Chapter 4 I took candidate Lyman break galaxies from the literature, focusing on three large compilations done in the GOODS fields, and I undertook a re-analysis to determine a catalogue of uniform galaxy property measurements to allow comparison for target prioritisation. My re-measurements of the photometry and astrometry for each catalogue used the same well-reduced images (the 3D-HST and the XDF reductions) and was critical to the JADES survey to ensure that we know the correct positions for the galaxies we will target (so that the light will enter the narrow microshutters), and that they are bright enough to achieve the science goals of our survey. As part of the re-analysis I also check if the candidate Lyman break galaxies from the literature hold up as good candidates using our uniformly-measured photometry, and produce photometric redshifts fits from BEAGLE and size information measurements from GALFIT. The result of this work was a target catalogue of 7221 unique galaxies between $3 < z < 10$ that satisfied my re-analysis criteria, including 44 of the highest priority class 1 or 2 galaxies at $z > 8$. Candidate targets that did not make the cut are retained for the target list but are down-weighted to lower priority classes. Within this chapter, systematic offsets were identified in the astrometry of one of the LBG catalogues (Bouwens et al., 2015a), which were significant for the narrow shutter size of the NIRSpec MSA, and would have led targets to have been missed if left uncorrected. A photometric offset was also identified in another input LBG catalogue's reported H-band magnitude, and we bring all the targets onto a uniform photometric and astrometric scheme, and confirm whether or not the Lyman break colours and photometric redshifts are robust, ready for target prioritisation for observation with JWST-NIRSpec in the JADES programme.

The target catalogue of re-analysed galaxies is sorted into the various priority classes based on their redshift and brightness. In Chapter 5, I wished to understand whether these required conditions of our priority classes should achieve the desired signal-to-noise in the NIRSpec observations for our science goals. To this end I cre-

ated a set of mock observation simulations as part of the JADES Mini Data Challenge.

The Mini Data Challenge focused on a simulation of the raw data NIRCam DEEP imaging observations, with the reduction and analysis of these images used to create a source catalogue from which galaxy candidates were selected and allocated to NIRSpec microshutters according to our target priority classes. I led the simulation of the NIRSpec DEEP (100ksec) mock observations using these targets selected by JADES team members from the mock NIRCam observations. In preparation of the Mini Data Challenge, I developed the NIRSpec simulation for the treatment of galaxies as extended objects, to improve the realism of the slit-losses created by the microshutter apertures.

I created 9 NIRSpec simulations (three dithers with three noddings each) for each of the low-resolution Prism, and the G235M and G395M medium resolution gratings (a sub-set of the modes that will be used in the real strategy). I used the in-development ESA science team extraction pipeline to produce 1D rectified wavelength- and flux-calibrated spectra for each target allocated to the simulated MSA configuration. For a representative example target from each priority class, I measured the continuum and emission line slit-losses, which were consistent with the estimates from the JWST STScI Exposure Time Calculator (ETC). For a typical $z \sim 7$ galaxy (Sersic $n = 1$, half-light radius = 0.1") the change in the estimated slit-losses was 33% higher for a well-centred source treated as extended rather than as a point source. This increased up to 69% if the object is also offset 80% of the way to the corner of the illuminated region of the microshutter. I determined that for each of the priority class examples, the NIRSpec sensitivity was sufficient to achieve the desired S/N for the JADES science goals.

This thesis has looked at galaxy evolution, in Chapters 2 & 3 I looked specifically at how the population of actively star forming galaxies (selected through rest-optical emission lines with high equivalent width) changes with redshift. My observations have explored this at z 0.5-2 using existing HST data (coupled with ground-based follow-up to determine metallicities), and JWST-NIRSpec will continue these studies to higher redshifts, potentially $z \sim 7$ using Hα, and $z \sim 9$ using [OIII]. Key goals of the JADES GTO programme are to characterise the star formation rates, the assembly of stellar mass, and the chemical enrichment of galaxies over cosmic time, and

to assess the contribution of star forming galaxies to the ultraviolet ionising background (particularly in the epoch of reionisation) using similar analysis techniques to my work at lower redshifts. The impact of the work I have done in this thesis is in the measurement that the fraction of extreme equivalent width emission line galaxies increases with increasing redshift, meaning that JWST-NIRSpec spectroscopy will likely be very successful at identifying these objects at high redshifts (being highly sensitive to emission lines). In Chapter 4 I have identified good candidate Lyman break galaxies in the JADES fields (including young star-forming galaxies within the EOR which may well be EELGs) and in Chapter 5 I have checked that the proposed selection criteria for NIRSpec spectroscopic targets at high-redshift will deliver sufficient S/N of key spectral features to confirm (or disprove) the photometric redshift estimates, enabling real science to be done without the inherent uncertainties of using estimated redshifts. For the brighter galaxies targeted for specific sub-programmes (which form some high priority selection in the JADES project), I show that NIRSpec has sufficient sensitivity to go beyond simple redshift confirmation, and to determine metallicity, dust attenuation and other physical conditions in these distant galaxies.

All the work in this thesis will allow me, as a JADES science team member, to leverage the optimum target selection and strategy design to study galaxy evolution. As part of my upcoming post-doctoral research fellowship at the University of Melbourne, I will improve the constraints I made on the EW distribution redshift evolution using higher redshift galaxy samples and will push my study of Hα-derived SFRs beyond the redshift range probed by WISPS out to $z \sim 7$. I will also be involved in the early release science (ERS) programme GLASS (the successor to the HST Grism Lens-Amplified Survey from Space "GLASS" programme) and the General Observer (GO) programme PASSAGE (A pure-parallel slitless spectroscopy programme).

Appendix A

Appendix to JADES - Target selection

A.1 Additional colour-colour diagrams

In addition to the colour-colour diagrams for the i-, z- and Y-band drop-outs presented in Figures 4.12 and 4.13, I now present the B- and V-band drop-out colour-colour diagrams for the Bouwens et al. (2015a) catalogue galaxies. I also present the respective B-, V-, i-, z- and Y-band drop-out colour-colour diagrams for the Harikane et al. (2016) and Finkelstein et al. (2015) catalogue galaxies. These are shown in Figures A.1 to A.6. The colour-colour space criteria for each drop-out filter is identified by the purple shaded region, and is adopted from Bouwens et al. (2015a) (see Table 4.9).

A.2 Target selection priority Class 4 & 6 catalogues and catalogue column description

In Table 4.16 I presented the re-measured 0.36" diameter aperture photometry (corrected for aperture losses appropriate for a point-source) for the priority class 1 & 2 Y- and J-band drop-out galaxies from Bouwens et al. (2015a) and Finkelstein et al. (2015) that met the re-analysis criteria set out in Chapter 4 (the Harikane et al. 2016 catalogue did not include any Y- or J-band drop-outs). The criteria imposed to clean the catalogue included: detection of the target at $> 4\sigma$ in the H-band; not to be flagged for an astrometric offset[1], to ensure I have the same object; agreement with the colour criteria to be classed as "good", "possible high-z" or "unlikely"(those lying within 1σ of the colour criteria); the BEAGLE photometric redshift to agree

[1]After correcting for the measured Bouwens et al. (2015a) systematic offset.

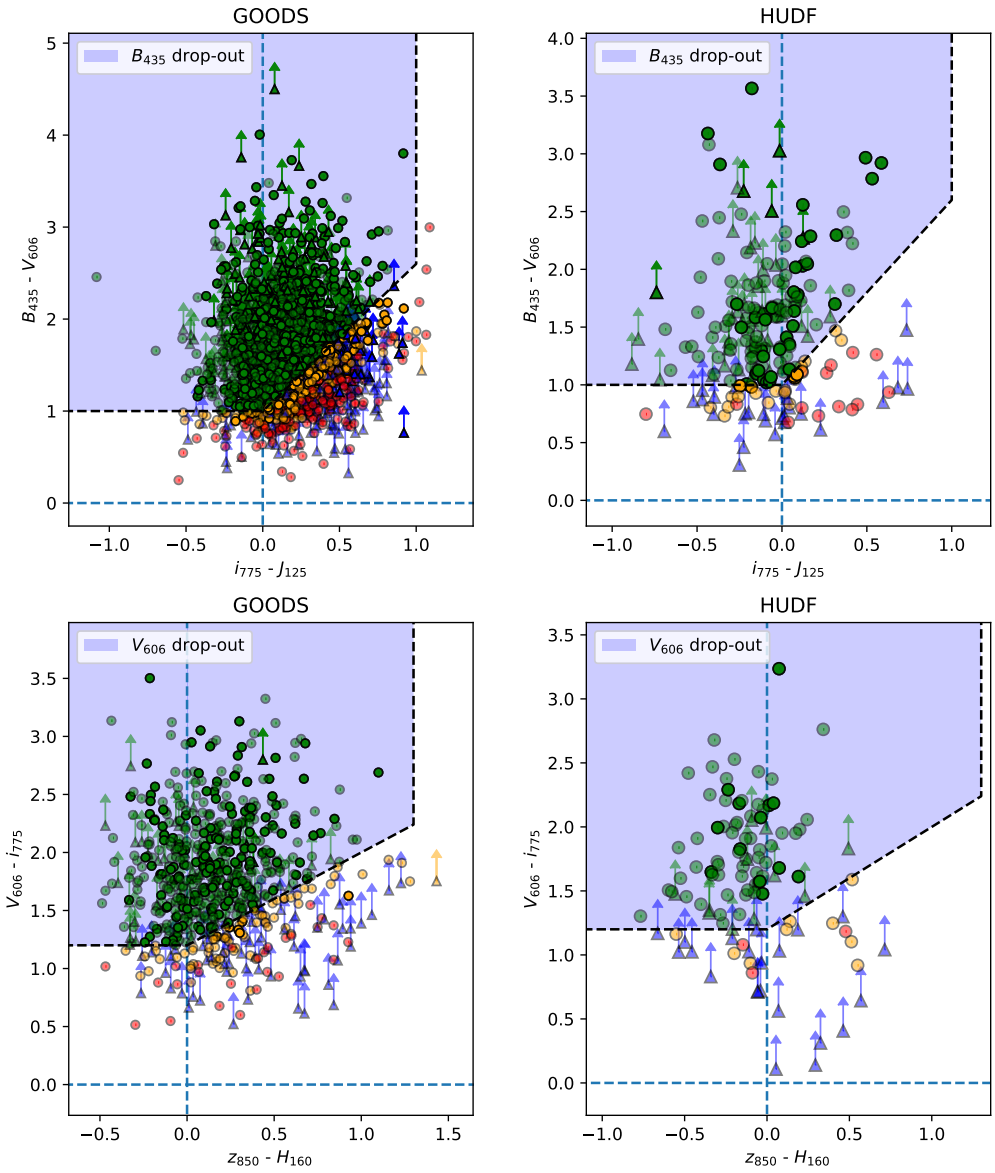

Figure A.1: As for Figure 4.12, but the B- and V-band drop-outs in Bouwens et al. (2015a) at z$\sim$ 4 & 5 are shown. For clarity a S/N cut in the i- and z-band has been set at 10 (in both the GOODS and HUDF fields) and at 5 (in the GOODS fields) respectively for B- and V-band drop-outs in this plot (so that the figure is not swamped by low-significance points with large error bars), but all galaxies are retained as part of the analysis. Some B- and V-band galaxies would be candidates for Priority class 7 in the JADES NIRSpec target selection, where we will give priority to galaxies with high enough star formation rates for emission lines to be detectable at high significance with NIRSpec — this translates to a magnitude limit on a rest-UV waveband above the Lyα break (in the case of the B-drops this would be the F775W i-band, and for V-drops this would be F850LP z-band). Those objects meeting this requirement of $AB = 26.5$ mag for the Medium pointings within GOODS, and 27.5 mag in the Deep NIRSpec pointing on the HUDF, are shown as bold symbols.

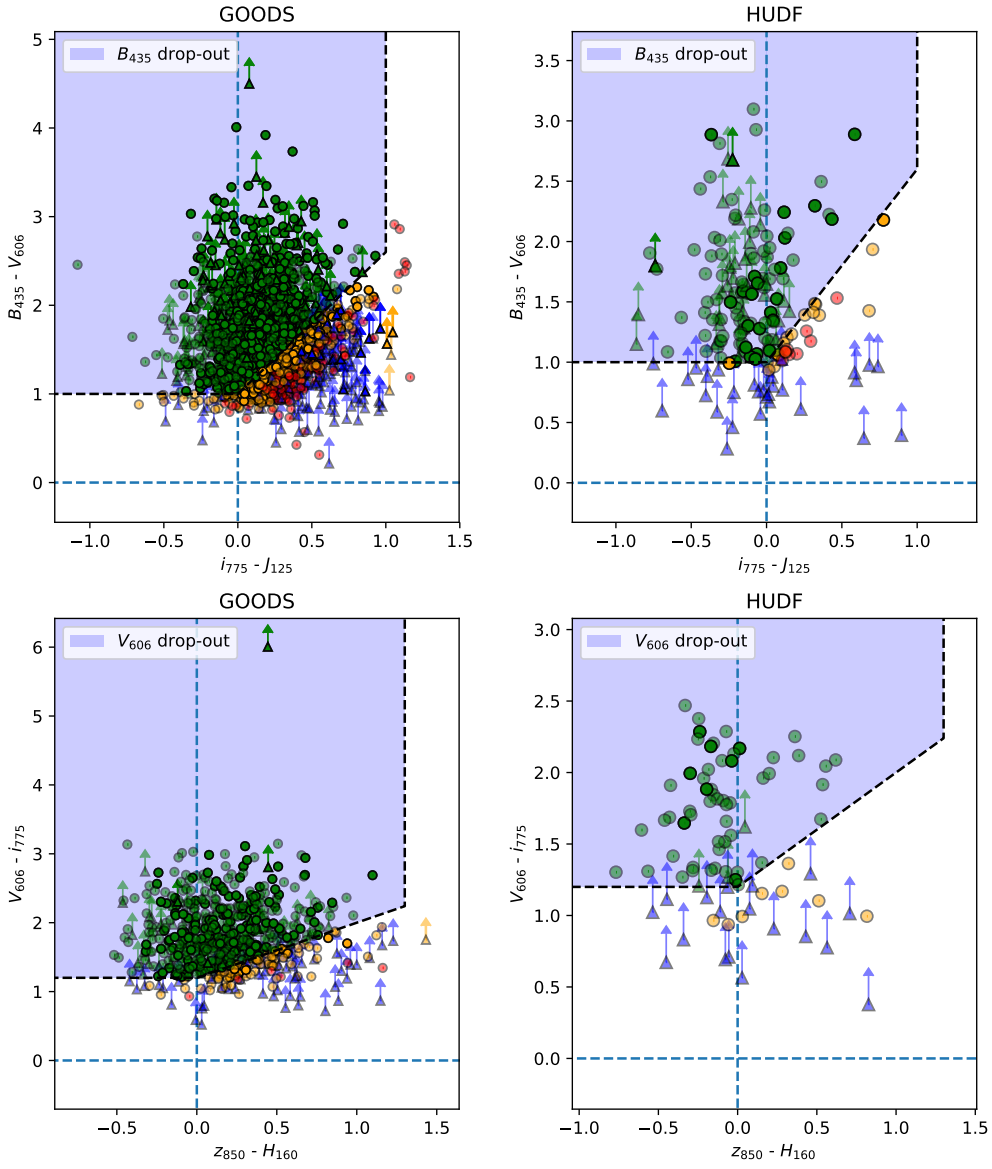

Figure A.2: As for Figure 4.12, but the B- and V-band drop-outs in Harikane et al. (2016) at z$\sim$ 4 & 5 are shown. For clarity a S/N cut in the i- and z-band has been set at 10 (in both the GOODS and HUDF fields) and at 5 (in the GOODS fields) respectively for B- and V-band drop-outs in this plot (so that the figure is not swamped by low-significance points with large error bars), but all galaxies are retained as part of the analysis. Some B- and V-band galaxies would be candidates for Priority class 7 in the JADES NIRSpec target selection, where we will give priority to galaxies with high enough star formation rates for emission lines to be detectable at high significance with NIRSpec and this translates to a magnitude limit on a rest-UV waveband above the Lyα break (in the case of the B-drops this would be the F775W i-band, and for V-drops this would be F850LP z-band). Those objects meeting this requirement of $AB = 26.5$ mag for the Medium pointings within GOODS, and 27.5 mag in the Deep NIRSpec pointing on the HUDF, are shown as bold symbols.

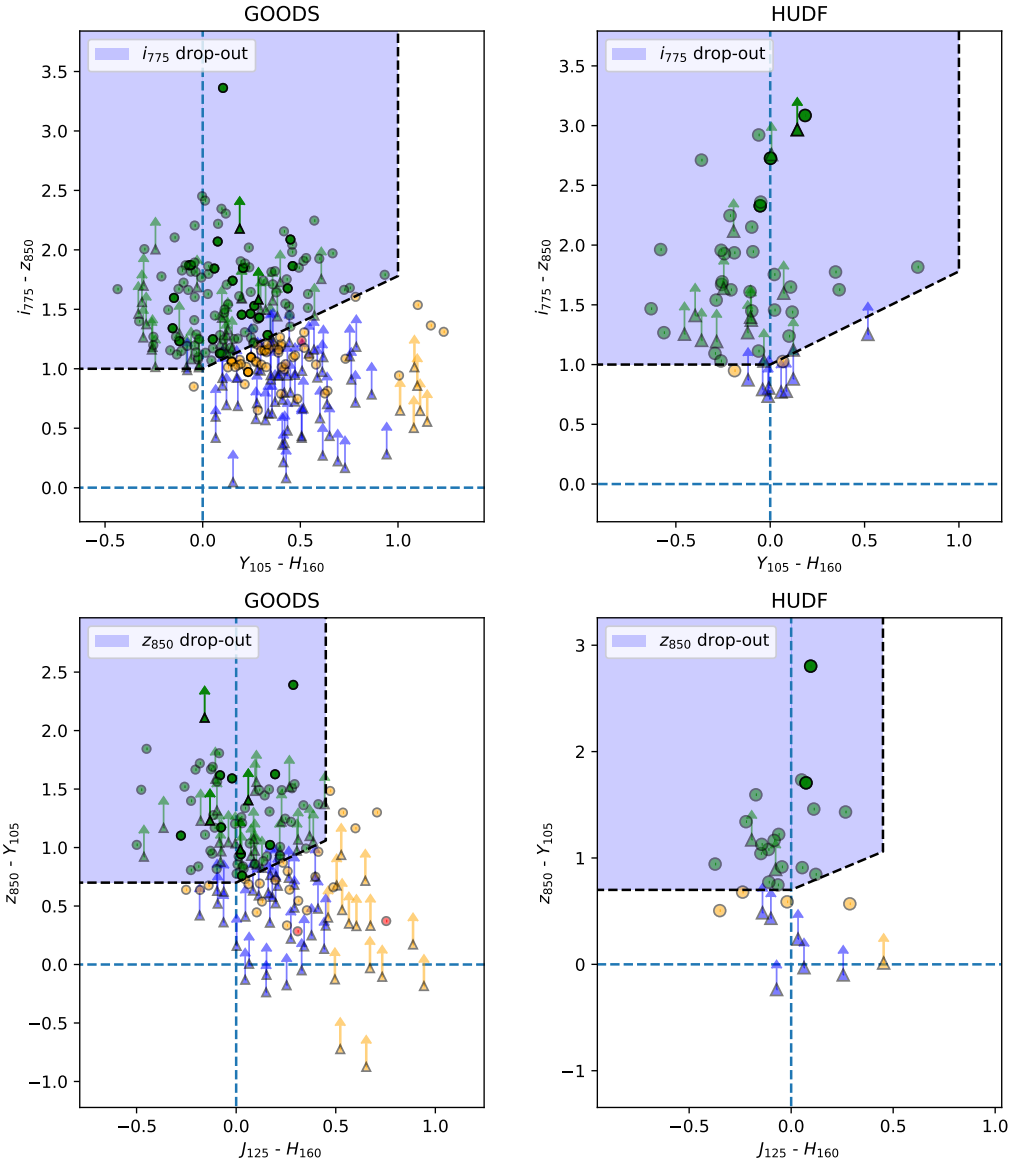

Figure A.3: As for Figure 4.12, but the i- and z-band drop-outs in Harikane et al. (2016) at z$\sim$ 6 & 7 are shown. For clarity a Y-band S/N cut has been set at 5 for the i and z-band drop-out GOODS plots, but all galaxies are retained as part of the analysis. Some i- and z-drops would be candidates for Priority class 4 in the JADES NIRSpec target selection, where we will give priority to galaxies with high enough star formation rates for emission lines to be detectable at high significance with NIRSpec and this translates to a magnitude limit on a rest-UV waveband above the Lyα break (in the case of the z-drops this would be the J-band). Those objects meeting this requirement of $AB = 26.5$ mag for the Medium pointings within GOODS, and 27.5 mag in the Deep pointing on the HUDF, are shown as bold symbols.

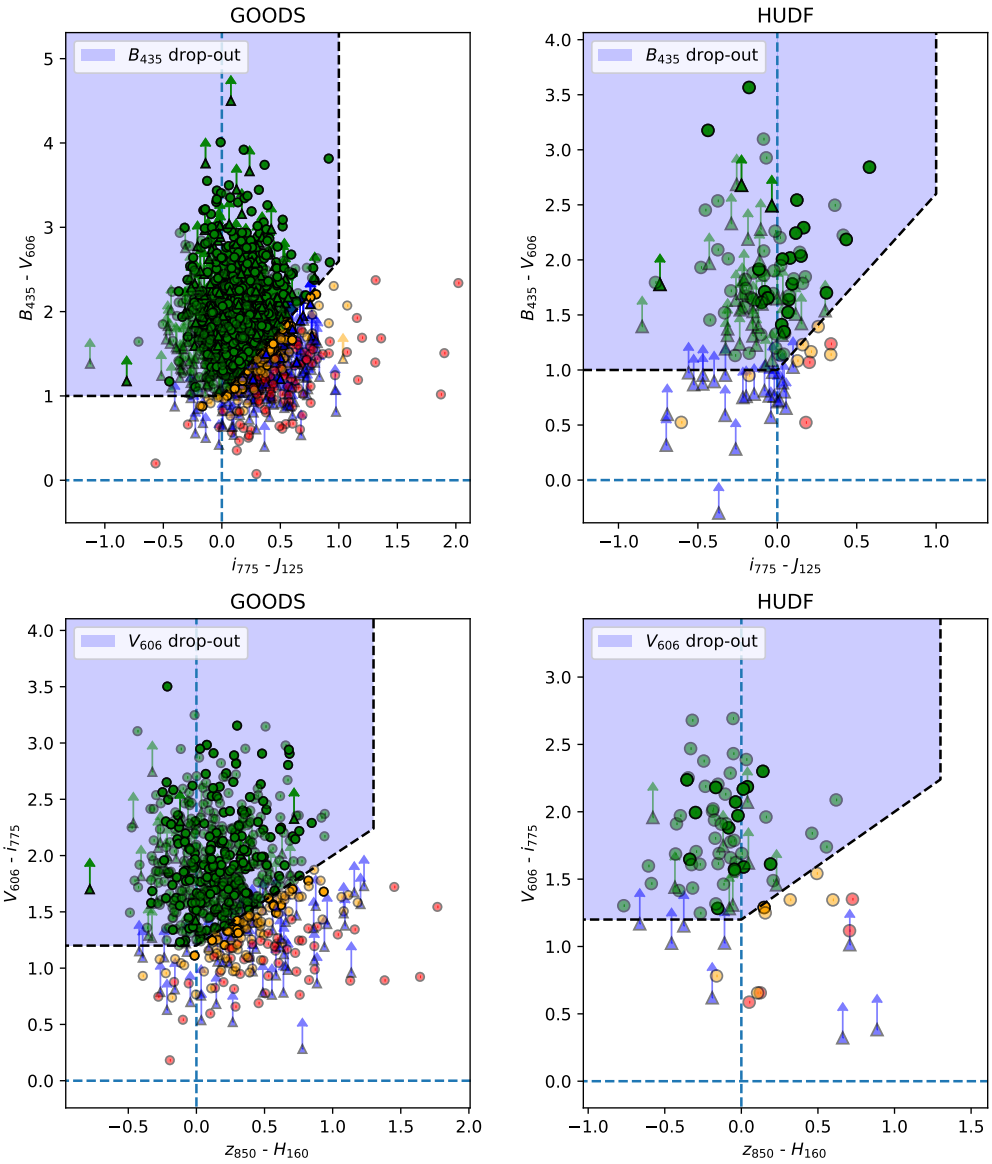

Figure A.4: As for Figure 4.12, but the z$\sim$ 4 & 5 Finkelstein et al. (2015) galaxies that correspond to B- and V-band drop-outs are shown. For clarity a S/N cut in the i- and z-band has been set at 10 (in both the GOODS and HUDF fields) and at 5 (in the GOODS fields) respectively for B- and V-band drop-outs in this plot, but all galaxies are retained as part of the analysis. Some B- and V-band galaxies would be candidates for Priority class 7 in the JADES NIRSpec target selection, where we will give priority to galaxies with high enough star formation rates for emission lines to be detectable at high significance with NIRSpec and this translates to a magnitude limit on a rest-UV waveband above the Lyα break (in the case of the B-drops this would be the F775W i-band, and for V-drops this would be F850LP z-band). Those objects meeting this requirement of $AB = 26.5$ mag for the Medium pointings within GOODS, and 27.5 mag in the Deep NIRSpec pointing on the HUDF, are shown as bold symbols. Finkelstein et al. (2015) selected high-z candidates through photometric redshifts and did not enforce colour criteria, hence allowing galaxies with redder spectral slopes and weaker breaks to enter the sample compared to Bouwens et al. (2015a) and Harikane et al. (2016) who enforce the colour cuts and this can be seen in the broader distribution of points in this sample.

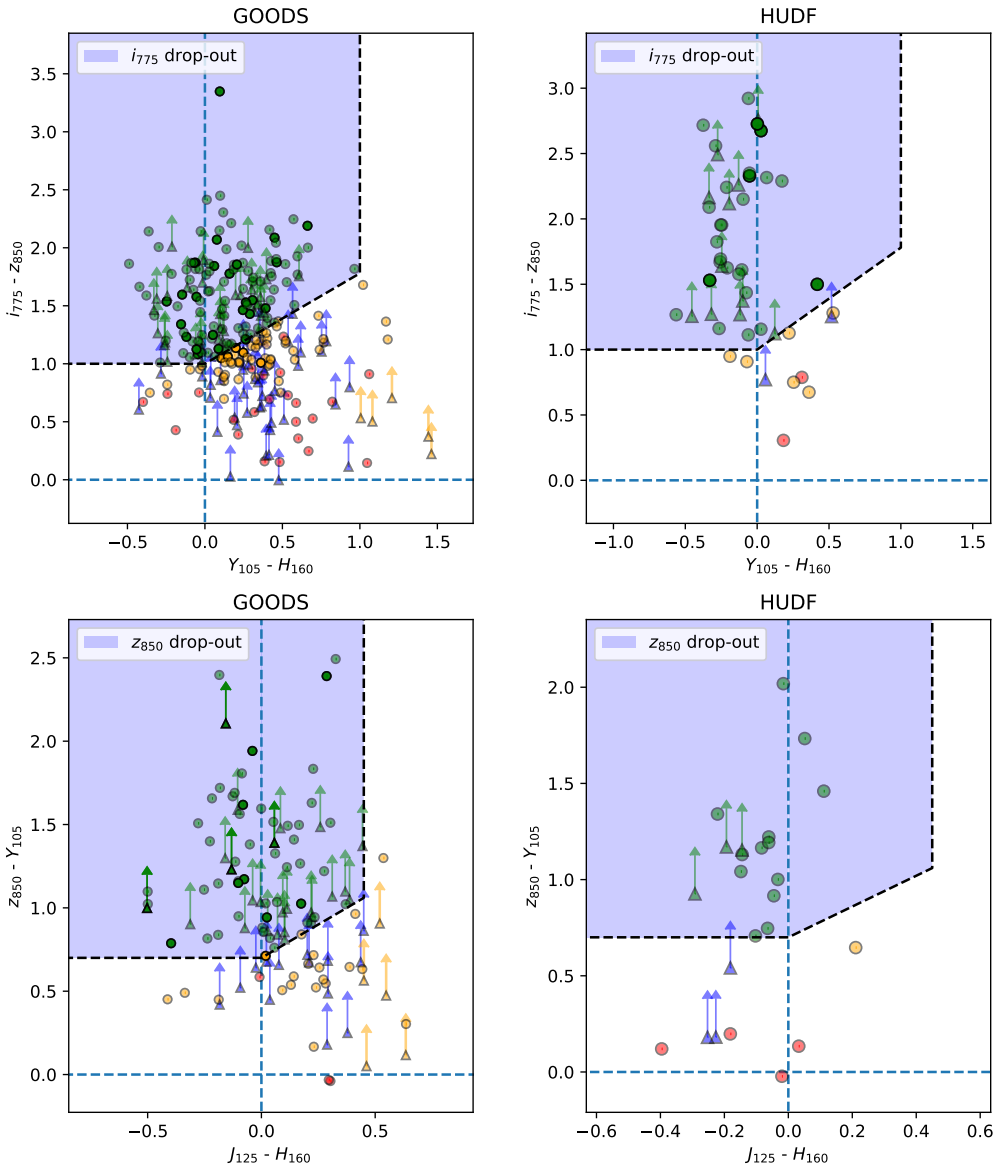

Figure A.5: As for Figure 4.12, but the z$\sim$ 6 & 7 Finkelstein et al. (2015) galaxies that correspond to i- and z-band drop-outs are shown. For clarity a Y-band S/N cut has been set at 5 for the i and z-band drop-out GOODS plots, but all galaxies are retained as part of the analysis. Some i- and z-drops would be candidates for Priority class 4 in the JADES NIRSpec target selection, where we will give priority to galaxies with high enough star formation rates for emission lines to be detectable at high significance with NIRSpec and this translates to a magnitude limit on a rest-UV waveband above the Lyα break (in the case of the z-drops this would be the J-band). Those objects meeting this requirement of $AB = 26.5$ mag for the Medium pointings within GOODS, and 27.5 mag in the Deep pointing on the HUDF, are shown as bold symbols.

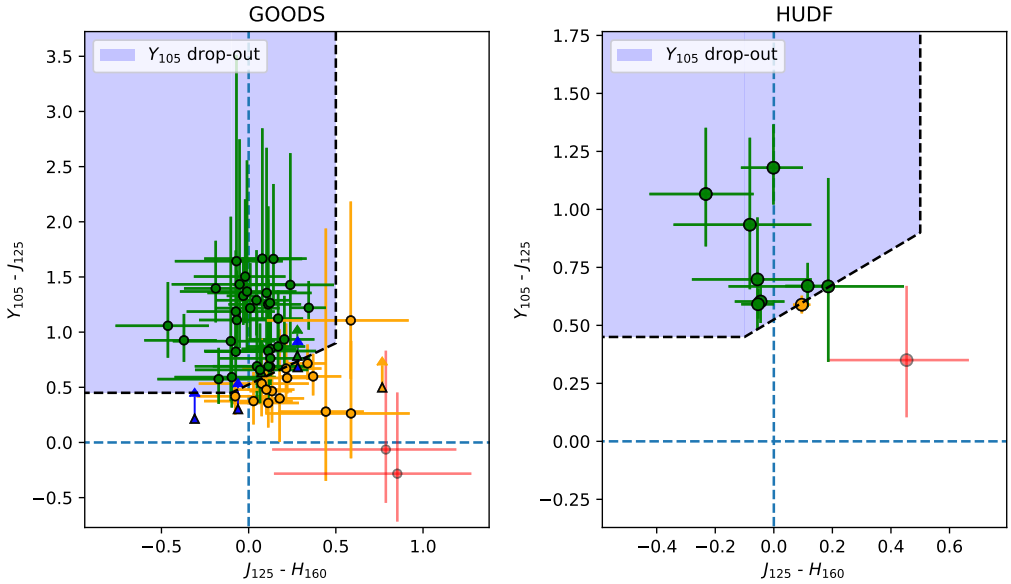

Figure A.6: As for Figure 4.12, but the z$\sim$ 8 Finkelstein et al. (2015) galaxies that correspond to Y-band drop-outs are shown. Some Y-band galaxies would be candidates for Priority classes 1 & 2, where we will give priority to the high-z galaxies that are sufficiently bright to confirm the redshift with NIRSpec and this translates to a magnitude limit for the Y-drops in the H-band. Those objects meeting this requirement of $AB = 28.5$ mag for the Medium pointings within GOODS, and 29.5 mag in the Deep pointing on the HUDF, are also in bold. Errorbars are presented for the Y-band drop-out panels as the numbers are sufficiently low to avoid over-crowding.

with the catalogue reported drop-out filter redshift range (for Finkelstein et al. 2015 I require the catalogue photometric redshift and the BEAGLE redshift to lie in the same drop-out filter redshift range) to remove galaxies with lower redshift solutions (interlopers). I also matched galaxies that appeared in multiple catalogues, so only one entry per unique galaxy was presented.

The priority class 4 and 6 galaxies taken from the i- and z-band drop-outs that meet the re-analysis criteria are presented in Tables A.2 and A.7. The magnitude limits imposed for the Class 4 objects are 27.5 mag in the DEEP and 26.5 mag in the MEDIUM, in the a band longer than the drop-out filter. This is the Y-band for i-band drop-outs and the J-band for the z-band drop-outs. Galaxies fainter than this are down weighted to Class 6, where objects have a 28 and 29 magnitude requirement in the MEDIUM and DEEP fields respectively (in the previously mentioned bands above the drop-out filter). Galaxies fainter still or those that didn't met the criteria are retained in the catalogues for lower priority follow-up.

I also provide three machine-readable tables[2] for the complete galaxy sample, including the galaxies that did not meet the re-analysis criteria. These tables are split by the three input catalogues and are provided for 0.36" and 0.6" diameter aperture photometry (corrected for aperture losses). These tables contain the flux density and uncertainty in each of the 8 filters (B-, V-, i-, z-, Y-, J-, JH- and H-band) as well as additional flags, galaxy properties (as measured through GALFIT surface brightness profile analysis, see Section 4.3.6) and redshift information (from the input catalogue and the BEAGLE photometric redshift analysis, see Section 4.3.5). The complete list of columns presented is given in Table A.1. Which I will now go through in further detail.

From the astrometric analysis, the astrometric_flag identifies galaxies that are greater than 3σ from the average positional offset, as defined by fitting a Gaussian to the distribution of position changes (input to re-centred coordinates). During photometry re-measurement using `IRAF.phot`, I set warning flags (mag_flag) for the when the H-band photometry is at a low significance ($< 2\sigma$) or off image (returning INDEF), and for when there was a reasonably large change in the magnitude between the input catalogue photometry and the re-measured value. During the Lyman break colour-colour analysis, the Colour_Flag is set to between 1 and 7 depending on how

[2]https://github.com/Kitboyett/Supplementary-Thesis-material

well a galaxy met the colour criteria. If a galaxy's photometry met the colour criteria this was set to 1. When a galaxy was non-detected in the drop-out band and is consistent with being a high redshift object, this was set to 2. When a galaxy was within 1σ of the criteria, this was set to 3. The remaining targets are given codes 4-7 if they are considered to not meet the criteria, present detections below the drop-out filter, present non-detections above the drop-out filter, or lack coverage in any of the criteria filters respectively. Finally, during GALFIT analysis, quality flags are added to the GALFIT output parameters to highlight poor convergence. If Galfit cannot converge it does not provide an output and a Galfit Error code of 1 is given. Galfit results are then also flagged as follows; (+2) if the Galfit magnitude, used as a parameter in the model light profile, varies by $\Delta\text{mag} \geq 2.5$ from the `phot` value; (+4) if the Galfit centred coordinate, which is free to vary up to a max of $2px$, is more than $\Delta\text{Position} = 1.9px$ in either RA or Dec from the input position, highlighting targets where Galfit has mistakenly converge on a nearby bright object; (+8) if Galfit returns a double star warning '**' where the measured axis ratio is < 0.1 or the Galfit characteristic radius is $< 0.5px$ and Galfit is known to no longer effectively converge as it cannot achieve a required pixel gradient. These errors are additive so an error of '6' would pick out a galaxy which converged but has poor agreement with the input magnitude and coordinates.

Column	Units	Column	Description
X_Deg, Y_Deg	Degrees	0, 1	H-band centred position in Degrees, using *IRAF.center*
X_pix, Y_Pix	–	2, 3	H-band centred position in Pixels, for the appropriate image given in column 'Image_used'
X-band_Flux	erg/s/cm^2/Hz	4 - 19	Phot 0.36" or 0.6" diameter aperture flux density in band 'X', with applied aperture and zeropoint correction. -99 if off-image.
X-band_error	erg/s/cm^2/Hz	–	Phot 0.36" or 0.6" diameter aperture flux density error in band 'X', with applied aperture and zeropoint correction. -99 if off-image
Image_used	–	20	North, South or XDF - which set of images the analysis was carried out on
R_s	Pixels	21	Galfit's Characteristic radius parameter using an Exponential light profile model. Where effective radii is given by $R_e = 1.678R_s$
Axis_Ratio	–	22	Galfit's Axis ratio parameter given as the ratio of the semi-minor axis to the semi-major axis.
Position_Angle_Degrees	Degrees	23	Galfit's Position Angle Parameter, given in Degrees. Increasing as the Semi-major axis moves away - anti-clockwise - from the Y axis.
Galfit_Error_Code	–	24	Galfit Error Warning 0: No Galfit error warning 1: Galfit could not converge +2: Δ H-Mag ≥ 2.5 between Galfit Magnitude parameter and H-band Phot Magnitude +4: $\Delta RA \vert \Delta Dec \geq 1.9px$ between the H-band *center* position and the Galfit Centred position +8: Double starred warning, Axis_Ratio <0.1 and/or $R_s < 0.5px$
Astrometric_Flag	–	25	0: within 3σ of Gaussian offset 99: H-band Centered position is greater than 3σ from the fitted Gaussian distribution offset
A_CIER	–	26	IRAF.center output error code: 0: No *center* error warning 107: Big Shift: greater than 1px 103: Low S/N 101: Off image (If 101: All Galfit and Astrometric_Flag values are set to 101)
Mag_Flag	–	27	Warning flag comparing Catalogued and Phot Magnitude 0: No warning : Δ H-mag < 0.2 or 5σ 99: INDEF in H-band 98: 2σ flux limited in H-band 97: Δ H-mag ≥ 0.2 and 5σ
Colour_Flag	–	28	Warning flag based on Colour criteria for each drop-out filter 1: meets the appropriate colour criteria 2: non-detection ($< 2\sigma$) in drop-out filter and consistent with remaining colour criteria 3: Within 1σ of colour criteria 4: detected ($> 2\sigma$) in waveband shorter than the drop-out filter 5: Any criteria filter or H-band had no coverage (off-image) 6: non-detection ($< 2\sigma$) in a band above the drop-out filter 7: Does not match the colour criteria within 1σ
input_z	–	29	Input catalogue redshift (photometric redshift for Bouwens et al. 2015a; Finkelstein et al. 2015 and drop-out redshift for Harikane et al. 2016)
redshift_beagle_1	–	30	BEAGLE primary redshift solution
Outlier_value	–	31	Normalised offset between BEAGLE primary redshift solution and input catalogue redshift $\vert \Delta z \vert$ / $(1 + z_{input}) < 0.15$ are considered good candidates
P1/P2	–	32	BEAGLE ratio of primary and secondary redshift solution probabilities. Redshift solutions with P1/P2 < 2 are ambiguous.
drop_out_agree	–	33	1: agreement between beagle redshift solution and input catalogue (-99 if disagreement)

Table A.1: The column descriptions for the full sample re-analysed catalogues. Note 1: In addition to these columns the original catalogues take up columns $34 - 44$ for (Bouwens et al., 2015a) and (Finkelstein et al., 2015) and $34 - 56$ for (Harikane et al., 2016)
Note 2: X-band is in order B, V, i, z, Y, J, JH, H
Note 3: The Finkelstein et al. (2015) catalogue does not contain H-band magnitudes for their galaxies and therefore no comparison can be made, this limits the use of the Mag_Flag. For those targets the flags are 0, 98 and 99 with no 97 warnings.
Note 4: Not all bands have complete coverage of the fields, JH and Y particularly have 'holes' within the image. A target detected in the H-band that is off-image in another band will have '-101' recorded in the photometry.

ID(B15)	ID(F15)	ID(H16)	RA [Deg]	Dec [Deg]	Z-Flux/Err	Y-Flux/Err	J-Flux/Err	H-Flux/Err
GNWZ-7256517434	z7_GNW_24443	z7_gdnw_30223	189.3568689	62.2953259	0.731±0.068	2.151±0.089	3.391±0.12	3.162±0.119
GSDZ-2372848546	-	-	53.1553227	-27.8151656	0.296±0.016	1.417±0.035	1.861±0.044	1.796±0.064
-	z7_GNW_17001	z7_gdnw_14856	189.0324964	62.2164158	0.25±0.052	1.108±0.087	1.759±0.103	1.633±0.097
GNDZ-6446716154	-	-	189.1862198	62.2708562	0.098±0.06	0.854±0.103	1.194±0.067	1.55±0.085
-	-	z7_gdnd_31258	189.1792828	62.2759112	0.06±0.072	0.739±0.129	1.068±0.064	1.13±0.08
GNDZ-6549212147	z7_GND_34860	z7_gdnd_14328	189.2288579	62.2040107	0.32±0.061	0.815±0.045	0.971±0.055	1.13±0.077
GNDZ-6542012155	z7_GND_34730	z7_gdnd_14372	189.2258317	62.2042171	0.243±0.058	0.579±0.049	1.054±0.065	1.076±0.086
-	z7_GND_29556	-	189.0958769	62.2200729	0.171±0.061	0.316±0.135	0.878±0.08	1.062±0.094
GNWZ-7222118310	z7_GNW_22375	z7_gdnw_32319	189.3426050	62.3085239	0.152±0.066	0.583±0.093	0.798±0.117	0.93±0.119
-	-	z7_gdsd_19890	53.0485690	-27.8317842	0.235±0.07	0.524±0.061	0.737±0.058	0.915±0.077
GSDZ-2360044417	z7_GSD_1273	-	53.1500218	-27.7449241	0.122±0.069	0.731±0.037	0.938±0.061	0.904±0.075
GNWZ-6086408599	z7_GNW_7284	z7_gdnw_3383	189.0360597	62.1499146	0.028±0.077	0.473±0.088	0.619±0.106	0.875±0.16
-	-	z7_gdsd_23882	53.1549364	-27.8157355	0.042±0.058	0.483±0.029	0.705±0.046	0.87±0.067
-	z6_GND_20074	z7_gdnd_24397	189.2810199	62.2473157	0.244±0.063	0.564±0.055	0.708±0.054	0.865±0.074
GNDZ-6335818304	-	-	189.1399412	62.3083616	0.331±0.064	0.555±0.158	0.768±0.059	0.848±0.075
GNWZ-7455218088	z7_GNW_23317	-	189.4396825	62.3023866	0.031±0.062	0.375±0.104	0.671±0.123	0.78±0.118
-	z7_GSW_9685	z7_gdsw_3370	53.1032452	-27.9057219	0.051±0.078	0.557±0.094	0.584±0.127	0.778±0.149
GNDZ-7209312060	-	z7_gdnd_13809	189.3372244	62.2015848	0.263±0.063	0.587±0.043	0.755±0.055	0.771±0.071
GSDZ-2406944167	z7_GSD_568	z7_gdsd_43756	53.1695564	-27.7379767	0.044±0.07	0.441±0.04	0.69±0.05	0.758±0.071
-	z6_GND_10245	z7_gdnd_31396	189.2774138	62.2764052	0.237±0.061	0.767±0.069	0.843±0.053	0.758±0.067
GSDZ-2371848566	-	-	53.1549340	-27.8157260	0.072±0.015	0.535±0.034	0.627±0.04	0.73±0.057
-	z7_GNW_32653	z7_gdnw_36750	189.2787589	62.3574797	0.014±0.065	0.561±0.084	0.57±0.132	0.723±0.118
GNDZ-7130712063	z7_GND_35507	z7_gdnd_13828	189.3044627	62.2016864	0.107±0.067	0.413±0.045	0.551±0.054	0.719±0.072
GNWZ-7103021596	z6_GNW_18532	-	189.2929458	62.3664899	0.403±0.065	0.724±0.104	0.985±0.153	0.713±0.159
-	z7_GNW_20329	-	189.2549467	62.3218796	0.064±0.06	0.638±0.1	0.523±0.086	0.707±0.104

Table A.2: Photometric 0.36" diameter aperture flux densities with a correction for aperture losses for the priority class 4 samples, constructed form Bouwens et al. (2015a); Finkelstein et al. (2015); Harikane et al. (2016) (B15, F15, H16) z-band drop-outs that meet the re-analysis criteria. Fluxes and errors are given in [1xe-30 erg/s/cm2/Hz]. All objects are undetected in the B-, V-, i-band ACS filters. Since JH is not used in the colour-colour work in Section 4.3.4 it is not reported here but is part of the online material made available, as are the ACS filter fluxes and the 0.6" diameter aperture photometry catalogues for all the galaxies in each catalogue. Galaxies that appear in multiple catalogues have only been entered once. The horizontal line represents H-band 26.5 magnitude limit for MEDIUM surveys in the GOODS field.

ID(B15)	ID(F15)	ID(H16)	RA [Deg]	Dec [Deg]	Z-Flux/Err	Y-Flux/Err	J-Flux/Err	H-Flux/Err
GNDZ-7214611055	z7_GND_40057	z7_gdnd_9868	189.3394498	62.1847623	0.047±0.07	0.442±0.043	0.431±0.057	0.701±0.072
GSWZ-2367154420	z6_GSW_10661	z7_gdsw_2681	53.1529756	-27.9116683	0.243±0.064	0.64±0.091	0.561±0.081	0.698±0.109
-	z6_GSW_3993	z7_gdsw_7906	53.2400867	-27.8770439	0.301±0.076	0.719±0.099	0.556±0.108	0.69±0.159
-	z7_GNW_10658	z7_gdnw_6137	189.0246764	62.1706622	0.128±0.07	0.504±0.081	0.615±0.101	0.685±0.124
-	z6_GNW_7317	z7_gdnw_3409	189.0692389	62.1501849	0.253±0.066	0.537±0.096	0.661±0.093	0.684±0.115
GNDZ-6420316564	-	-	189.1751210	62.2822645	0.32±0.066	0.497±0.097	0.719±0.065	0.683±0.069
GNDZ-6474113374	z6_GND_27273	-	189.1975761	62.2270237	0.189±0.066	0.593±0.069	0.601±0.057	0.666±0.072
GNDZ-7035815571	z7_GND_13456	z7_gdnd_28891	189.2649738	62.2657991	0.112±0.054	0.513±0.061	0.802±0.059	0.657±0.076
-	-	z7_gdnw_3281	189.1831517	62.1493132	0.094±0.067	0.285±0.117	0.637±0.081	0.655±0.103
-	z6_GND_18696	-	189.3029036	62.2512120	0.186±0.066	0.338±0.066	0.454±0.063	0.649±0.087
GNWZ-7179419175	z6_GNW_20456	z7_gdnw_34026	189.3247647	62.3214461	0.192±0.052	0.501±0.099	0.706±0.118	0.647±0.13
-	z7_GSD_4968	z7_gdsd_37892	53.0833581	-27.7643876	0.152±0.071	0.469±0.056	0.502±0.069	0.647±0.08
-	z6_GSW_6395	z7_gdsw_5634	53.2391054	-27.8894013	0.271±0.07	0.779±0.094	0.763±0.107	0.641±0.145
XDFZ-2425646566	-	z7_xdf_3886	53.1773175	-27.7823931	0.108±0.016	0.519±0.009	0.589±0.011	0.634±0.011
-	z7_GND_8389	z7_gdnd_33554	189.2251431	62.2862878	0.032±0.062	0.245±0.045	0.479±0.06	0.628±0.075
GNWZ-7268117400	-	z7_gdnw_30099	189.3617127	62.2943897	0.061±0.063	0.551±0.087	0.868±0.118	0.621±0.12
GNDZ-6452018113	z7_GND_42808	-	189.1883950	62.3030374	0.085±0.053	0.799±0.222	0.728±0.045	0.612±0.058
GNDZ-6372717115	z7_GND_8358	z7_gdnd_33589	189.1553027	62.2864620	0.12±0.065	0.551±0.043	0.672±0.054	0.601±0.066
GSDZ-2288549126	z7_GSD_22760	z7_gdsd_22813	53.1202559	-27.8201986	0.158±0.071	0.286±0.038	0.478±0.061	0.597±0.075
-	-	z7_gdnd_24006	189.3606326	62.2455704	0.005±0.064	0.262±0.047	0.467±0.056	0.596±0.073
-	z7_GSD_1559	-	53.1997936	-27.7473300	0.118±0.092	0.195±0.041	0.456±0.055	0.592±0.076
GNDZ-6364715350	z7_GND_15642	z7_gdnd_27388	189.1519933	62.2596307	0.212±0.064	0.415±0.093	0.555±0.052	0.585±0.07
GSDZ-2199347106	z7_GSD_11730	z7_gdsd_31744	53.0830651	-27.7862669	0.011±0.072	0.43±0.047	0.413±0.051	0.579±0.069
GNDZ-7078316214	z6_GND_11304	z7_gdnd_30559	189.2826612	62.2724986	0.14±0.063	0.352±0.065	0.525±0.055	0.569±0.069
GSDZ-2307950272	z7_GSD_29430	-	53.1283046	-27.8408878	0.038±0.072	0.259±0.042	0.429±0.055	0.557±0.069
GNWZ-7259418092	z7_GNW_23360	z7_gdnw_31410	189.3580584	62.3024807	0.14±0.061	0.502±0.1	0.679±0.121	0.556±0.114
GNWZ-8024316291	z7_GNW_28182	-	189.5101231	62.2746425	0.1±0.061	0.48±0.096	0.491±0.105	0.55±0.131
-	-	z7_gdsd_21666	53.1486036	-27.8249695	0.065±0.053	0.257±0.042	0.354±0.053	0.546±0.069
-	z7_GSW_12155	-	53.1402249	-27.9230775	0.015±0.071	0.349±0.102	0.361±0.102	0.546±0.135
GNDZ-6492614442	-	-	189.2052392	62.2455381	-0.014±0.064	0.353±0.07	0.491±0.054	0.545±0.075
GNWZ-5516510357	z7_GNW_11595	-	188.9652801	62.1764944	0.074±0.067	0.323±0.099	0.542±0.119	0.541±0.115
GNWZ-7152917458	-	-	189.3137285	62.2959706	0.333±0.067	0.604±0.094	0.5±0.107	0.541±0.118
GNDZ-7062215374	-	-	189.2759294	62.2603214	0.096±0.067	0.25±0.063	0.461±0.057	0.537±0.075
-	z6_GSD_18942	z7_gdsd_25697	53.1985028	-27.8081145	0.101±0.066	0.333±0.039	0.319±0.055	0.523±0.07
GSDI-2373552229	-	z7_gdsw_8783	53.1556268	-27.8730617	0.286±0.07	0.516±0.105	0.633±0.071	0.502±0.088

Table A.3: Continuation of Appendix Table A.2

ID(B15)	ID(F15)	ID(H16)	RA [Deg]	Dec [Deg]	Z-Flux/Err	Y-Flux/Err	J-Flux/Err	H-Flux/Err
-	-	z7_gdsw_6262	53.1526117	-27.8858036	-0.02±0.073	0.21±0.091	0.325±0.073	0.497±0.102
-	z7_GNW_24671	-	189.3617528	62.2943615	0.175±0.064	0.481±0.087	0.786±0.114	0.496±0.118
GNDZ-7081016204	-	-	189.2837109	62.2722452	0.053±0.065	0.221±0.062	0.405±0.057	0.495±0.075
-	-	z7_gdsd_28937	53.1392668	-27.7957999	0.297±0.071	0.553±0.039	0.553±0.056	0.487±0.067
GNDZ-6439012555	-	-	189.1829440	62.2153371	0.017±0.078	0.39±0.105	0.33±0.065	0.487±0.101
-	z6_GNW_15435	-	188.9796070	62.2013952	0.172±0.071	0.312±0.105	0.384±0.096	0.485±0.12
GNDZ-6371117347	z7_GND_43951	z7_gdnd_34930	189.1546092	62.2929153	0.053±0.065	0.41±0.046	0.52±0.048	0.484±0.063
GNDZ-6332416324	-	z7_gdnd_31243	189.1385289	62.2756064	0.005±0.065	0.352±0.046	0.517±0.053	0.482±0.074
GNDZ-6486116321	z7_GND_10527	z7_gdnd_31229	189.2025801	62.2755124	0.108±0.063	0.571±0.097	0.518±0.059	0.478±0.075
GSDZ-2313750347	-	z7_gdsd_16897	53.1307212	-27.8429794	0.005±0.071	0.257±0.038	0.411±0.054	0.477±0.069
GNWZ-7216017387	-	-	189.3400030	62.2940196	0.057±0.061	0.224±0.099	0.436±0.107	0.477±0.104
GSDZ-2160647576	z7_GSD_16137	z7_gdsd_27952	53.0669357	-27.7993607	0.119±0.071	0.383±0.05	0.402±0.051	0.47±0.071
-	z6_GND_39946	-	189.3195548	62.1852490	0.106±0.071	0.274±0.053	0.459±0.06	0.467±0.081
GSDZ-2355051091	z7_GSD_32342	z7_gdsd_14110	53.1479344	-27.8525247	0.094±0.063	0.327±0.038	0.503±0.051	0.464±0.065
-	z7_GND_34204	z7_gdnd_14822	189.3596729	62.2059801	0.044±0.061	0.252±0.054	0.447±0.058	0.462±0.073
-	z7_GSD_22842	z7_gdsd_22756	53.0990519	-27.8204541	-0.074±0.063	0.414±0.05	0.534±0.049	0.461±0.058
-	-	z7_gdsw_6839	53.1472278	-27.8825685	0.077±0.06	0.256±0.1	0.239±0.078	0.459±0.104
GNDZ-6379317005	-	z7_gdnd_32962	189.1580573	62.2834010	-0.002±0.063	0.308±0.047	0.406±0.056	0.458±0.065
GNDZ-6526614180	z7_GND_23288	-	189.2193872	62.2382389	0.187±0.06	0.283±0.075	0.537±0.058	0.452±0.075
-	z7_GND_39528	z7_gdnd_10485	189.3065658	62.1874526	0.203±0.067	0.393±0.05	0.357±0.056	0.441±0.069
-	z7_GND_37645	z7_gdnd_12002	189.1895383	62.1939009	0.075±0.068	0.182±0.044	0.302±0.053	0.441±0.075
GNDZ-6427518385	z7_GND_41647	-	189.1781230	62.3106363	0.071±0.068	0.432±0.188	0.408±0.05	0.44±0.068
GNDZ-6288817417	z7_GND_43797	z7_gdnd_35407	189.1203236	62.2948736	-0.023±0.067	0.329±0.047	0.356±0.063	0.436±0.082
GNDZ-6355614173	-	-	189.1481886	62.2380637	0.039±0.048	0.194±0.088	0.382±0.058	0.426±0.073
GNDZ-6331416282	-	-	189.1381148	62.2744266	-0.007±0.064	0.248±0.045	0.332±0.053	0.424±0.069
GNDZ-7070810474	-	z7_gdnd_8821	189.2795328	62.1797649	0.082±0.068	0.28±0.045	0.395±0.057	0.406±0.072
-	-	z7_gdsd_31674	53.1271409	-27.7865734	0.086±0.072	0.271±0.038	0.318±0.05	0.399±0.07
GSDZ-2180650493	-	-	53.0752650	-27.8470140	0.148±0.078	0.271±0.056	0.42±0.048	0.395±0.07
GNDZ-7294714256	z7_GND_22525	z7_gdnd_22778	189.3728184	62.2403705	0.05±0.064	0.322±0.051	0.368±0.059	0.394±0.088
GNDZ-6489016066	z7_GND_12621	z7_gdnd_29560	189.2037174	62.2684216	0.059±0.062	0.394±0.097	0.385±0.054	0.391±0.07
GNDZ-7019109476	-	-	189.2578663	62.1631332	0.018±0.062	0.145±0.042	0.252±0.052	0.384±0.071
GNDZ-6333916313	z7_GND_10568	z7_gdnd_31184	189.1391595	62.2753090	0.047±0.068	0.227±0.057	0.265±0.065	0.381±0.078
-	-	z7_gdsd_23287	53.1086279	-27.8182312	0.059±0.072	0.276±0.054	0.247±0.048	0.373±0.067
GNDZ-7027917001	z7_GND_8888	z7_gdnd_32937	189.2616598	62.2832659	0.006±0.066	0.3±0.045	0.342±0.052	0.371±0.074
-	z7_GSD_14558	-	53.0469184	-27.7946214	-0.004±0.067	0.141±0.048	0.242±0.052	0.37±0.072

Table A.4: Continuation of Appendix Table A.2

ID(B15)	ID(F15)	ID(H16)	RA [Deg]	Dec [Deg]	Z-Flux/Err	Y-Flux/Err	J-Flux/Err	H-Flux/Err
-	z7_GSD_6239	-	53.0623600	-27.7694880	-0.04±0.078	0.281±0.063	0.376±0.064	0.367±0.083
-	z7_GND_41319	-	189.2297251	62.3027110	0.004±0.063	0.146±0.046	0.204±0.051	0.367±0.07
GSDZ-2455950175	z6_GSD_28705	z7_gdsd_18219	53.1899848	-27.8382061	0.15±0.078	0.364±0.042	0.556±0.068	0.367±0.074
-	z7_GND_8450	-	189.1277459	62.2889272	0.095±0.07	0.17±0.047	0.243±0.051	0.366±0.069
GSDZ-2372245383	-	-	53.1551245	-27.7606545	0.204±0.016	0.504±0.04	0.443±0.029	0.365±0.044
-	z7_GND_2173	z7_gdnd_6627	189.2727385	62.1674279	0.046±0.053	0.247±0.042	0.39±0.053	0.358±0.07
-	-	z7_gdsd_21523	53.2145272	-27.8255632	0.074±0.073	0.158±0.048	0.389±0.051	0.355±0.071
-	-	z7_gdsd_16791	53.0792247	-27.8433187	0.081±0.064	0.183±0.056	0.313±0.044	0.355±0.061
GSDZ-2067447158	-	z7_gdsd_31277	53.0281180	-27.7877063	-0.061±0.092	0.197±0.05	0.347±0.062	0.354±0.083
GNDZ-6391816550	z7_GND_44859	-	189.1632679	62.2818686	-0.015±0.066	0.233±0.046	0.259±0.059	0.351±0.075
-	z6_GND_17020	-	189.3626597	62.2558185	0.159±0.064	0.443±0.05	0.442±0.06	0.35±0.079
-	z7_GND_30554	-	189.3940113	62.2170445	0.028±0.063	0.24±0.056	0.21±0.056	0.348±0.073
-	-	z7_gdnd_33308	189.2431424	62.2850384	0.086±0.059	0.468±0.044	0.525±0.053	0.347±0.072
-	-	z7_gdsd_32646	53.0427522	-27.7836037	0.005±0.074	0.145±0.046	0.256±0.053	0.347±0.069
-	-	z7_gdsd_26058	53.1001922	-27.8065299	0.243±0.07	0.437±0.05	0.407±0.051	0.344±0.069
GNDZ-6187914126	z6_GND_23763	z7_gdnd_21965	189.0783093	62.2367649	0.092±0.062	0.375±0.091	0.436±0.059	0.343±0.079
-	-	z7_gdsd_35268	53.0700157	-27.7747638	0.022±0.071	0.304±0.049	0.215±0.054	0.343±0.074
GSDZ-2125047568	z7_GSD_16078	z7_gdsd_28035	53.0521239	-27.7991242	0.134±0.06	0.295±0.049	0.406±0.05	0.341±0.065
GNDZ-7270315213	-	-	189.3626440	62.2558654	-0.054±0.061	0.305±0.051	0.237±0.061	0.339±0.08
GNDZ-6431516569	-	-	189.1798243	62.2823945	0.01±0.062	0.317±0.088	0.346±0.06	0.336±0.07
-	-	z7_gdsd_36177	53.1257957	-27.7712833	0.026±0.072	0.238±0.037	0.353±0.055	0.333±0.067
-	-	z7_gdnd_28593	189.1768422	62.2645387	0.067±0.056	0.279±0.09	0.248±0.054	0.325±0.081
GNDZ-7088616402	z7_GND_9908	-	189.2870022	62.2777759	-0.083±0.061	0.228±0.062	0.212±0.059	0.317±0.069
GNDZ-6577914338	-	-	189.2408500	62.2426237	0.197±0.071	0.468±0.073	0.45±0.055	0.311±0.076
GSDI-2364745240	-	z7_gdsd_39598	53.1519605	-27.7566923	0.15±0.063	0.247±0.039	0.23±0.054	0.307±0.068
GNDZ-7291612311	-	z7_gdnd_15502	189.3715258	62.2085812	0.118±0.053	0.358±0.058	0.302±0.054	0.301±0.069
GNDZ-7239112259	-	-	189.3496125	62.2071378	-0.033±0.065	0.213±0.043	0.188±0.053	0.298±0.074
-	-	z7_gdnd_32452	189.1487312	62.2809466	-0.025±0.061	0.218±0.048	0.313±0.058	0.295±0.073
-	-	z7_gdsd_30003	53.1245612	-27.7922274	0.035±0.069	0.088±0.038	0.18±0.053	0.292±0.068
-	-	z7_gdsd_21124	53.1034711	-27.8271995	0.052±0.057	0.134±0.05	0.251±0.044	0.288±0.059
GSDZ-2406745116	z6_GSD_2545	z7_gdsd_40414	53.1694789	-27.7532143	0.008±0.086	0.266±0.046	0.34±0.054	0.287±0.07
GSDZ-2361451030	z7_GSD_32054	z7_gdsd_14715	53.1505850	-27.8508592	0.012±0.064	0.282±0.044	0.241±0.052	0.274±0.067
-	-	z7_gdsd_37730	53.1373850	-27.7651123	0.075±0.071	0.298±0.038	0.422±0.049	0.272±0.067
XDFZ-2421846277	-	-	53.1757967	-27.7743994	0.104±0.015	0.263±0.009	0.26±0.012	0.245±0.012
XDFZ-2367747536	z6_MAIN_5507	z7_xdf_1550	53.1532185	-27.7982201	0.127±0.016	0.252±0.007	0.235±0.011	0.221±0.01

Table A.5: Continuation of Appendix Table A.2. Line represents H-band 27.5 magnitude limit for MEDIUM surveys in the XDF field. Double horizontal lines represent H-band 28 magnitude priority class 6 limit for MEDIUM surveys.

ID(B15)	ID(F15)	ID(H16)	RA [Deg]	Dec [Deg]	Z-Flux/Err	Y-Flux/Err	J-Flux/Err	H-Flux/Err
-	z6_MAIN_2568	z7_xdf_4135	53.1560115	-27.7809044	0.085±0.014	0.222±0.008	0.211±0.012	0.184±0.01
XDFZ-2363747162	-	z7_xdf_3021	53.1515766	-27.7878376	0.042±0.013	0.183±0.008	0.185±0.01	0.158±0.011
XDFZ-2383546118	z7_MAIN_938	z7_xdf_5435	53.1598311	-27.7699697	0.046±0.017	0.129±0.009	0.179±0.012	0.156±0.014
XDFZ-2405646435	z7_MAIN_2184	z7_xdf_4451	53.1690259	-27.7787655	0.077±0.014	0.18±0.008	0.159±0.011	0.152±0.01
XDFZ-2415947044	z6_MAIN_3338	z7_xdf_3588	53.1733155	-27.7845776	0.051±0.014	0.15±0.007	0.141±0.011	0.13±0.011
XDFZ-2443046452	-	z7_xdf_4391	53.1846129	-27.7792074	0.086±0.014	0.161±0.008	0.154±0.011	0.124±0.01

Table A.6: Continuation of Appendix Table A.2. The horizontal line represents H-band 29 magnitude priority class 6 limit for DEEP surveys.

ID(B15)	ID(F15)	ID(H16)	RA [Deg]	Dec [Deg]	Z-Flux/Err	Y-Flux/Err	J-Flux/Err	H-Flux/Err
-	z6_GNW_15549	-	188.9276021	62.2024193	0.324±0.054	1.349±0.067	2.055±0.126	2.726±0.181
GSWI-2390352230	-	-	53.1626083	-27.8730773	0.312±0.059	1.68±0.078	1.912±0.11	2.616±0.13
GNDI-7171617247	z6_GNW_25620	-	189.3214684	62.2900993	0.125±0.047	0.94±0.065	1.181±0.081	2.173±0.104
-	z6_GSD_21666	z6_gdsd_23550	53.0544608	-27.8168732	0.241±0.056	1.621±0.075	1.993±0.066	2.139±0.09
GNWI-7124218284	z6_GNW_22555	z6_gdnw_32168	189.3017488	62.3078101	0.055±0.044	1.119±0.057	1.661±0.107	1.826±0.143
GNWI-5590112456	z6_GNW_16618	z6_gdnw_14073	188.9958760	62.2125748	0.333±0.047	1.242±0.062	1.356±0.095	1.772±0.136
GSDI-2182948556	-	z6_gdsd_23990	53.0762420	-27.8154472	0.002±0.055	0.837±0.072	1.433±0.058	1.707±0.071
GNDI-7326614165	z6_GND_23382	z6_gdnd_22136	189.3861256	62.2378499	0.14±0.05	0.962±0.066	1.115±0.104	1.689±0.076
-	-	z6_gdsd_22476	53.2253897	-27.8210904	0.05±0.074	0.85±0.107	1.294±0.065	1.684±0.092
GSDI-2540949159	-	-	53.2254094	-27.8210847	0.074±0.075	0.991±0.109	1.271±0.066	1.652±0.093
GSDI-2433449203	-	z6_gdsd_22250	53.1806085	-27.8223198	0.285±0.054	0.822±0.072	1.143±0.027	1.531±0.064
GNDI-6496110393	z6_GND_3649	z6_gdnd_8336	189.2067311	62.1775073	0.148±0.053	0.823±0.062	1.0±0.046	1.529±0.076
-	z6_GSW_9970	z6_gdsw_3161	53.2163583	-27.9073225	0.392±0.053	1.508±0.071	1.208±0.103	1.514±0.157
GNDI-6596914547	-	-	189.2487422	62.2484538	0.271±0.054	0.832±0.066	1.142±0.072	1.434±0.075
GSDI-2175546251	z6_GSD_7500	z6_gdsd_35522	53.0731227	-27.7736365	0.271±0.059	0.944±0.083	0.9±0.057	1.361±0.075
-	z6_GNW_32731	-	189.2553891	62.3577507	0.236±0.051	0.921±0.065	0.927±0.131	1.33±0.21
-	z6_GNW_21773	z6_gdnw_32897	189.3549929	62.3126159	0.445±0.046	1.258±0.069	1.216±0.1	1.319±0.127
GSDI-2281848186	z6_GSD_17985	z6_gdsd_26357	53.1174582	-27.8051836	0.142±0.054	0.8±0.073	1.073±0.036	1.293±0.072
GSWI-2519154263	-	-	53.2162987	-27.9073120	0.226±0.053	0.838±0.071	0.735±0.104	1.287±0.156
GNWI-5489612251	z6_GNW_16070	z6_gdnw_12952	188.9540099	62.2068924	0.203±0.051	0.838±0.063	1.003±0.1	1.285±0.13
-	-	z6_gdsd_38352	53.1707660	-27.7622162	0.235±0.044	0.767±0.057	0.946±0.045	1.284±0.072
GNWI-6241411435	z6_GNW_14511	z6_gdnw_10568	189.1005436	62.1953545	0.157±0.055	0.706±0.068	0.771±0.098	1.266±0.22
-	-	z6_gdnw_6788	189.0684234	62.1749300	0.367±0.052	0.9±0.069	1.018±0.108	1.261±0.218
GNWI-5508811587	z6_GNW_15180	z6_gdnw_11492	188.9620358	62.1995827	0.208±0.054	1.108±0.071	1.189±0.104	1.217±0.146
GNDI-6377810356	z6_GNW_11543	z6_gdnw_7029	189.1574564	62.1764944	0.338±0.047	1.137±0.061	1.392±0.097	1.21±0.109

Table A.7: Photometric 0.36" diameter aperture flux densities with a correction for aperture losses for the priority class 4 samples, constructed form Bouwens et al. (2015a); Finkelstein et al. (2015); Harikane et al. (2016) (B15, F15, H16) *i*-band drop-outs that meet the re-analysis criteria. Fluxes and errors are given in [1xe-30 erg/s/cm2/Hz]. All objects are undetected in the B-, V-band ACS filters. Since JH is not used in the colour-colour work in Section 4.3.4 it is not reported here but is part of the online material made available, as are the ACS filter fluxes and the 0.6" diameter aperture photometry catalogues for all the galaxies in each catalogue. Galaxies that appear in multiple catalogues have only been entered once.

ID(B15)	ID(F15)	ID(H16)	RA [Deg]	Dec [Deg]	Z-Flux/Err	Y-Flux/Err	J-Flux/Err	H-Flux/Err
-	z5_GND_33500	-	189.2613280	62.2080153	0.311±0.051	0.948±0.067	0.948±0.046	1.209±0.075
GNWI-6164110300	z5_GNW_11324	-	189.0683877	62.1749312	0.376±0.052	0.988±0.07	1.093±0.106	1.204±0.219
GNDI-6166715343	-	-	189.0694907	62.2594252	0.303±0.05	0.868±0.062	0.845±0.066	1.174±0.083
-	-	z6_gdnw_3388	189.1756982	62.1504814	0.104±0.046	0.615±0.058	0.72±0.146	1.173±0.134
-	z6_GSD_29074	-	53.1567864	-27.8395521	0.305±0.055	0.867±0.07	0.967±0.043	1.162±0.067
GSWI-2368352010	z6_GSW_2202	z6_gdsw_10297	53.1534611	-27.8669560	0.151±0.055	0.732±0.073	0.816±0.11	1.135±0.09
GSDI-2376250224	-	-	53.1567641	-27.8395393	0.296±0.056	0.857±0.069	0.885±0.043	1.121±0.067
GSDI-2452349098	-	-	53.1884653	-27.8194037	0.376±0.053	0.926±0.071	0.992±0.029	1.107±0.062
GSDI-2460349297	z6_GSD_24282	z6_gdsd_21644	53.1918171	-27.8249178	0.219±0.053	1.089±0.072	0.961±0.033	1.107±0.071
GSWI-2364153267	z6_GSW_6659	z6_gdsw_5379	53.1517288	-27.8907404	0.132±0.053	0.872±0.074	0.89±0.093	1.098±0.12
GNWI-5487812257	z6_GNW_16088	z6_gdnw_13023	188.9532501	62.2070795	0.34±0.054	0.902±0.064	0.958±0.108	1.098±0.122
-	z6_MAIN_1864	z6_xdf_4424	53.1519328	-27.7781815	0.061±0.008	0.748±0.015	1.08±0.01	1.081±0.013
GNDI-6138614216	z6_GND_22789	z6_gdnd_22515	189.0577650	62.2392640	0.242±0.052	0.752±0.065	1.016±0.064	1.067±0.073
GSWI-2223355438	z6_GSW_12728	z6_gdsw_1248	53.0930400	-27.9288366	0.176±0.057	0.594±0.079	0.692±0.108	1.061±0.143
-	z5_GND_14430	-	189.3423039	62.2628308	0.374±0.044	0.994±0.056	0.936±0.047	1.058±0.088
GNWI-7331118044	z6_GNW_23437	z6_gdnw_31181	189.3879948	62.3011781	0.121±0.052	0.685±0.067	1.118±0.092	1.04±0.127
-	z6_GSD_17530	z6_gdsd_26645	53.0741213	-27.8037761	0.246±0.046	0.713±0.067	0.79±0.055	1.04±0.076
GNWI-6282309537	z6_GNW_9770	z6_gdnw_5310	189.1176560	62.1648287	0.065±0.058	0.518±0.071	0.611±0.104	1.034±0.127
-	-	z6_gdnw_23605	189.4551342	62.2606200	0.168±0.048	0.736±0.062	0.491±0.09	1.01±0.166
GNDI-6212614224	-	-	189.0886554	62.2394856	0.245±0.049	0.682±0.064	0.605±0.092	0.984±0.077
-	-	z6_gdsw_1758	53.1261474	-27.9219918	0.11±0.056	0.635±0.075	0.813±0.112	0.972±0.148
GSDI-2260346450	z6_GSD_9255	z6_gdsd_33920	53.1084692	-27.7791700	0.044±0.045	0.365±0.067	0.548±0.038	0.969±0.074
GNWI-5588610175	z6_GNW_10822	z6_gdnw_6275	188.9952721	62.1714805	0.211±0.052	0.618±0.061	0.671±0.088	0.968±0.126
-	z6_GNW_10897	-	188.9760804	62.1719007	0.333±0.051	0.904±0.064	0.999±0.107	0.959±0.149
GNWI-7398919596	z6_GNW_22717	z6_gdnw_35230	189.4161676	62.3331466	0.243±0.052	0.668±0.069	0.821±0.113	0.955±0.117
-	-	z6_gdsd_39475	53.1303743	-27.7569949	0.131±0.056	0.604±0.075	0.486±0.036	0.946±0.068
GNWI-7165421239	z6_GNW_32543	z6_gdnw_36710	189.3189240	62.3565504	0.133±0.055	0.744±0.066	0.999±0.1	0.945±0.116
GSDI-2522348046	z6_GSD_16763	z6_gdsd_27376	53.2175802	-27.8013171	0.084±0.054	0.705±0.07	0.848±0.049	0.945±0.081
GSDI-2263348266	z6_GSD_18691	z6_gdsd_25816	53.1097319	-27.8074074	0.044±0.052	0.572±0.072	0.55±0.039	0.917±0.076
GSDI-2484848588	z6_GSD_21576	z6_gdsd_23753	53.2020328	-27.8163616	0.12±0.054	0.576±0.074	0.817±0.04	0.915±0.07
GNDI-6458911585	z6_GND_36100	z6_gdnd_13219	189.1912655	62.1995089	0.235±0.058	0.752±0.068	0.727±0.108	0.912±0.083
GSDI-2312945251	-	-	53.1303731	-27.7569638	0.206±0.056	0.605±0.074	0.533±0.036	0.899±0.067
XDFI-2340946472	z6_MAIN_2345	z6_xdf_4290	53.1420537	-27.7797804	0.086±0.008	0.735±0.015	0.942±0.007	0.897±0.009
GNDI-7310813124	z6_GND_29564	z6_gdnd_18089	189.3795600	62.2200322	0.103±0.053	0.658±0.068	0.584±0.06	0.891±0.076
GSWI-2296455045	-	-	53.1235410	-27.9179075	0.124±0.052	0.477±0.074	0.696±0.104	0.887±0.144

Table A.8: Continuation of Appendix Table A.7. The Horizontal line represents H-band 26.5 magnitude limit for the priority class 4 MEDIUM surveys in the GOODS field.

ID(B15)	ID(F15)	ID(H16)	RA [Deg]	Dec [Deg]	Z-Flux/Err	Y-Flux/Err	J-Flux/Err	H-Flux/Err
GSWI-2263556267	z6_GSW_13472	z6_gdsw_504	53.1098057	-27.9407727	0.004±0.054	0.438±0.07	0.62±0.106	0.882±0.153
GSDI-2499846561	z6_GSD_10367	-	53.2082534	-27.7822697	0.285±0.059	1.218±0.076	0.927±0.037	0.881±0.069
GSDI-2273847282	z6_GSD_13403	-	53.1141087	-27.7911836	0.14±0.053	0.743±0.071	0.732±0.04	0.867±0.069
-	z6_GSD_35016	z6_gdsd_10189	53.0599636	-27.8674026	0.181±0.057	0.453±0.077	0.586±0.06	0.862±0.08
GNWI-7538116328	z6_GNW_27915	-	189.4741905	62.2756810	0.281±0.063	0.797±0.076	0.742±0.094	0.86±0.124
GSWI-2538151496	z6_GSW_1698	z6_gdsw_11178	53.2241905	-27.8637769	-0.052±0.057	0.453±0.068	0.638±0.105	0.859±0.147
GSWI-2063146344	z6_GSD_8350	-	53.0262718	-27.7762290	0.194±0.052	0.7±0.072	0.586±0.061	0.85±0.124
-	z6_GNW_13256	z6_gdnw_9054	188.9455766	62.1874863	0.082±0.053	0.594±0.066	0.579±0.106	0.85±0.174
-	z6_GNW_30051	-	189.4551934	62.2606376	0.249±0.049	0.808±0.063	0.603±0.094	0.85±0.164
GNWI-6376006558	z6_GNW_2045	z6_gdnw_678	189.1566816	62.1154261	0.044±0.051	0.405±0.064	0.476±0.094	0.849±0.133
GSDI-2134146463	z6_GSD_9400	-	53.0558931	-27.7795574	-0.021±0.055	0.684±0.07	0.658±0.052	0.846±0.074
-	z6_GNW_21404	z6_gdnw_33315	189.4036217	62.3155301	0.25±0.055	0.777±0.066	0.933±0.098	0.836±0.126
GNDI-7092816189	z6_GND_11494	z6_gdnd_30392	189.2886651	62.2718108	0.077±0.048	0.671±0.062	0.763±0.065	0.834±0.078
-	z6_GSD_1852	-	53.1473327	-27.7492005	0.203±0.054	0.748±0.069	0.741±0.04	0.831±0.069
-	z6_GND_9813	-	189.1115389	62.2779373	0.043±0.048	0.512±0.069	0.591±0.074	0.824±0.078
GSWI-2225156275	z6_GSW_13480	z6_gdsw_497	53.0938279	-27.9409738	0.069±0.052	0.639±0.067	0.807±0.113	0.816±0.132
-	z5_GND_13996	z6_gdnd_28377	189.1621431	62.2638152	-0.019±0.043	0.364±0.059	0.572±0.095	0.795±0.074
GSDI-2143952025	-	-	53.0599459	-27.8674085	0.132±0.056	0.388±0.077	0.586±0.06	0.794±0.08
GSDI-2150249506	z6_GSD_26186	-	53.0626029	-27.8307345	0.106±0.068	0.512±0.085	0.592±0.075	0.786±0.081
GNDI-7286314415	z6_GND_20879	z6_gdnd_23786	189.3693106	62.2448012	-0.01±0.048	0.47±0.065	0.54±0.051	0.781±0.066
GNDI-6453818026	z6_GND_43125	-	189.1891376	62.3006619	0.169±0.043	0.733±0.057	0.975±0.229	0.781±0.061
-	z6_GNW_14534	-	188.9859823	62.1953344	0.361±0.054	0.867±0.065	0.851±0.101	0.779±0.126
-	z6_GSW_8203	z6_gdsw_4268	53.0816262	-27.8985794	0.137±0.055	0.415±0.077	0.57±0.1	0.772±0.133
-	z6_GSW_13289	z6_gdsw_715	53.1040327	-27.9371471	0.014±0.057	0.638±0.082	0.437±0.122	0.765±0.175
GNDI-6267812556	-	-	189.1116263	62.2153980	0.057±0.046	0.432±0.058	0.634±0.097	0.762±0.089
GSWI-2243104798	z6_GSD_30912	z6_gdsd_15876	53.1014112	-27.8466708	0.118±0.055	0.62±0.07	0.74±0.051	0.761±0.069
GSDI-2186047590	z6_GSD_16277	z6_gdsd_27761	53.0775200	-27.7997346	0.106±0.052	0.541±0.074	0.505±0.046	0.756±0.072
GNWI-6175209083	-	z6_gdnw_3666	189.0729897	62.1522413	-0.054±0.053	0.328±0.065	0.507±0.104	0.754±0.134
GSWI-2086346349	z6_GSD_8391	z6_gdsd_34794	53.0359645	-27.7763822	0.144±0.054	0.414±0.075	0.552±0.051	0.752±0.077
-	z5_GSD_11278	-	53.0710548	-27.7849996	0.196±0.052	0.43±0.073	0.662±0.055	0.742±0.071
GNWI-6046112281	z6_GNW_16141	z6_gdnw_13116	189.0192575	62.2077235	0.117±0.052	0.486±0.064	0.656±0.091	0.74±0.119
GSDI-2060447055	z6_GSD_11224	-	53.0251815	-27.7848700	-0.004±0.068	0.601±0.097	0.552±0.047	0.74±0.109
-	z6_GSW_8683	z6_gdsw_3973	53.0887495	-27.9009227	0.27±0.047	0.686±0.064	0.63±0.087	0.734±0.15
-	z6_GNW_3671	-	189.2035033	62.1279730	-0.007±0.048	0.2±0.064	0.31±0.141	0.732±0.133
-	z6_GSD_14480	z6_gdsd_29225	53.0694025	-27.7944156	0.078±0.043	0.568±0.06	0.661±0.052	0.72±0.07

Table A.9: Continuation of Appendix Table A.7.

ID(B15)	ID(F15)	ID(H16)	RA [Deg]	Dec [Deg]	Z-Flux/Err	Y-Flux/Err	J-Flux/Err	H-Flux/Err
-	-	z6_gdnd_4965	189.2446040	62.1572437	0.109±0.041	0.363±0.05	0.444±0.044	0.716±0.073
GNWZ-7103021596	z6_GNW_18532	-	189.2929588	62.3664862	0.035±0.05	0.411±0.065	0.733±0.104	0.713±0.159
-	z6_GNW_25652	z6_gdnw_29056	189.4892249	62.2880788	0.051±0.051	0.322±0.067	0.383±0.097	0.706±0.137
-	-	z6_gdnw_4678	189.1678404	62.1602060	0.197±0.051	0.597±0.063	0.542±0.098	0.703±0.122
GNDI-7082817153	z6_GND_8220	z6_gdnd_33793	189.2845610	62.2875081	0.079±0.05	0.439±0.065	0.433±0.065	0.699±0.066
GSDI-2340645185	z6_GSD_2947	z6_gdsd_39949	53.1419330	-27.7551543	0.125±0.053	0.621±0.074	0.52±0.036	0.692±0.064
-	z5_GSW_13489	-	53.1270638	-27.9411276	0.201±0.053	0.527±0.074	0.479±0.114	0.685±0.156
-	z5_GNW_6364	-	189.2119884	62.1454575	0.186±0.05	0.42±0.061	0.506±0.133	0.683±0.112
-	-	z6_gdsd_28798	53.1993567	-27.7962097	-0.034±0.061	0.382±0.074	0.49±0.045	0.681±0.073
-	z6_GNW_8973	-	189.1678008	62.1602051	0.179±0.051	0.604±0.063	0.64±0.098	0.674±0.122
GSDI-2157047074	-	z6_gdsd_31970	53.0654020	-27.7853990	0.081±0.055	0.594±0.073	0.626±0.053	0.671±0.074
GSDI-2149449365	z6_GSD_24869	z6_gdsd_21190	53.0622636	-27.8268241	0.16±0.056	0.621±0.073	0.605±0.068	0.67±0.071
-	z6_GSW_13664	-	53.0999559	-27.9494121	0.255±0.053	0.575±0.072	0.598±0.111	0.669±0.152
GSDI-2215049287	-	z6_gdsd_21646	53.0896030	-27.8246892	0.111±0.054	0.455±0.074	0.579±0.054	0.668±0.059
-	z5_GND_7766	-	189.1399809	62.2918129	0.085±0.058	0.437±0.079	0.449±0.065	0.663±0.087
GNDI-7161310114	z6_GND_2469	z6_gdnd_6999	189.3172126	62.1697770	0.035±0.05	0.489±0.06	0.597±0.049	0.653±0.093
-	z5_GSW_7405	z6_gdsw_4854	53.2528499	-27.8944162	0.037±0.075	0.331±0.094	0.47±0.096	0.652±0.139
GNWI-6325106317	-	-	189.1354387	62.1087306	0.13±0.043	0.464±0.057	0.643±0.106	0.643±0.144
GNDI-6335917308	-	-	189.1399826	62.2918351	0.012±0.058	0.383±0.077	0.434±0.067	0.637±0.09
GNDI-7010016590	z6_GND_8934	z6_gdnd_32855	189.2541993	62.2829733	0.01±0.051	0.443±0.064	0.484±0.06	0.636±0.069
GSDI-2279049420	-	-	53.1162912	-27.8283355	0.148±0.054	0.716±0.07	0.628±0.043	0.634±0.068
GNDI-6378010341	z6_GNW_11480	z6_gdnw_6980	189.1574804	62.1760831	0.153±0.045	0.404±0.06	0.493±0.1	0.633±0.111
-	z6_GSW_9110	z6_gdsw_3714	53.2213140	-27.9028511	0.048±0.055	0.524±0.073	0.577±0.098	0.632±0.151
-	z6_GSD_1388	-	53.1557595	-27.7460458	-0.033±0.054	0.624±0.072	0.637±0.04	0.632±0.075
GSWI-2148550338	z6_GSD_30000	z6_gdsd_16919	53.0619128	-27.8427361	0.089±0.053	0.523±0.073	0.608±0.062	0.63±0.077
-	-	z6_gdnw_2811	189.1628815	62.1458519	0.142±0.051	0.311±0.064	0.656±0.13	0.629±0.12
-	z6_GSW_4329	z6_gdsw_7490	53.1387823	-27.8790402	0.192±0.053	0.616±0.068	0.432±0.093	0.622±0.084
GNDI-7220413557	z6_GND_25400	-	189.3419535	62.2320601	0.158±0.044	0.488±0.055	0.596±0.055	0.621±0.079
-	-	z6_gdnd_27417	189.3139104	62.2598590	0.08±0.05	0.426±0.063	0.447±0.063	0.618±0.084
-	z6_GND_36554	-	189.1563938	62.1976460	0.157±0.045	0.437±0.061	0.552±0.1	0.609±0.087
-	-	z6_gdnd_16081	189.1392924	62.2113228	0.141±0.047	0.512±0.061	0.819±0.094	0.607±0.1
GSWI-2539351007	z6_GSW_501	-	53.2247084	-27.8502062	0.087±0.055	0.351±0.075	0.499±0.108	0.605±0.096
GNDI-6288218160	-	z6_gdnd_37355	189.1200906	62.3043843	0.105±0.062	0.584±0.08	0.48±0.043	0.602±0.107
GSDI-2294145378	z6_GSD_4098	z6_gdsd_38779	53.1225479	-27.7604963	-0.002±0.056	0.532±0.071	0.609±0.036	0.601±0.07
-	z6_GSD_8999	z6_gdsd_34174	53.1300123	-27.7783063	0.231±0.057	0.513±0.076	0.49±0.037	0.598±0.069

Table A.10: Continuation of Appendix Table A.7.

ID(B15)	ID(F15)	ID(H16)	RA [Deg]	Dec [Deg]	Z-Flux/Err	Y-Flux/Err	J-Flux/Err	H-Flux/Err
GNWI-7138219247	z6_GNW_20152	z6_gdnw_34253	189.3076220	62.3234574	0.099±0.05	0.451±0.063	0.423±0.095	0.598±0.127
GSDI-2489446514	-	z6_gdsd_33371	53.2039276	-27.7809503	0.179±0.058	0.76±0.074	0.62±0.04	0.596±0.068
GNWI-6191208310	z6_GNW_5756	z6_gdnw_2414	189.0797187	62.1418774	0.092±0.052	0.583±0.066	0.783±0.1	0.595±0.119
GSDI-2345447559	z6_GSD_15972	-	53.1439441	-27.7988885	0.128±0.008	0.53±0.016	0.613±0.051	0.592±0.06
GSDI-2478547463	-	-	53.1993571	-27.7962257	0.022±0.009	0.305±0.02	0.548±0.051	0.592±0.065
-	z6_GNW_25971	-	189.3347262	62.2861340	-0.009±0.053	0.462±0.067	0.478±0.092	0.591±0.116
GSDI-2247947588	z6_GSD_16267	z6_gdsd_27868	53.1033102	-27.7996685	0.192±0.052	0.888±0.074	0.631±0.048	0.589±0.071
GSDI-2449546076	z6_GSD_6105	-	53.1873020	-27.7687842	0.019±0.056	0.398±0.073	0.424±0.041	0.585±0.072
GNDI-6554515087	z6_GND_18287	z6_gdnd_25665	189.2310286	62.2523362	-0.008±0.048	0.602±0.058	0.73±0.074	0.584±0.072
GNWI-7253518456	z6_GNW_21823	z6_gdnw_32933	189.3555634	62.3125865	0.232±0.05	0.7±0.07	0.736±0.106	0.583±0.139
-	z6_GND_36553	-	189.1563618	62.1977867	0.18±0.045	0.594±0.06	0.52±0.087	0.577±0.081
GSDI-2112346564	z6_GSD_10379	z6_gdsd_32963	53.0467948	-27.7823479	0.186±0.053	0.592±0.073	0.581±0.051	0.577±0.071
GSDI-2276848529	z6_GSD_21046	z6_gdsd_24201	53.1153366	-27.8146920	0.063±0.055	0.37±0.072	0.33±0.039	0.572±0.073
GSDI-2415747442	z6_MAIN_5160	-	53.1732060	-27.7956102	0.033±0.009	0.392±0.017	0.556±0.013	0.571±0.015
GSDI-2470349499	z6_GSD_26147	z6_gdsd_20219	53.1959760	-27.8305374	0.204±0.055	0.584±0.071	0.54±0.038	0.569±0.066
GNWI-6390708452	-	-	189.1627947	62.1458169	0.098±0.05	0.39±0.066	0.548±0.126	0.566±0.123
GNWI-6220315137	-	z6_gdnd_25990	189.0918243	62.2537344	0.219±0.046	0.707±0.062	0.577±0.058	0.561±0.074
GSDI-2465349583	z6_GSD_26917	z6_gdsd_19651	53.1938940	-27.8329018	0.103±0.052	0.455±0.075	0.47±0.04	0.558±0.069
GNDI-7200314537	z6_GND_19744	-	189.3334162	62.2481528	0.051±0.039	0.178±0.053	0.355±0.044	0.548±0.074
-	z6_GSW_964	-	53.1990093	-27.8562185	0.005±0.048	0.199±0.061	0.432±0.101	0.544±0.113
GNDI-7062411451	z6_GND_37114	z6_gdnd_12397	189.2760009	62.1958073	-0.004±0.053	0.25±0.065	0.376±0.048	0.541±0.075
GSDI-2373552229	-	z7_gdsw_8783	53.1556276	-27.8730499	0.048±0.054	0.307±0.07	0.524±0.103	0.54±0.087
-	-	z6_gdsd_28194	53.1358507	-27.7983189	0.136±0.056	0.732±0.07	0.594±0.039	0.539±0.072
-	z6_GNW_4155	-	189.1303234	62.1313737	0.195±0.05	0.458±0.066	0.496±0.104	0.537±0.127
GSDI-2140952189	-	-	53.0587466	-27.8719285	0.119±0.051	0.36±0.074	0.473±0.054	0.535±0.084
-	-	z6_gdsw_5411	53.1500283	-27.8910146	-0.001±0.052	0.249±0.071	0.385±0.091	0.53±0.117
-	z6_GNW_23409	-	189.4708128	62.3016200	0.04±0.054	0.282±0.066	0.512±0.108	0.529±0.121
GNDI-7087412256	-	-	189.2864058	62.2070423	0.121±0.05	0.523±0.066	0.445±0.044	0.526±0.072
GSDI-2323746214	z6_GSD_7215	-	53.1348898	-27.7726294	0.006±0.047	0.459±0.059	0.581±0.037	0.523±0.067
GNWI-5503611497	-	-	188.9598904	62.1970590	0.036±0.052	0.349±0.064	0.383±0.095	0.518±0.115
GNDI-7278411465	-	z6_gdnd_12512	189.3660038	62.1961787	0.161±0.046	0.551±0.064	0.465±0.045	0.516±0.083
GNWI-6000113261	z5_GNW_17522	-	189.0000812	62.2238407	0.243±0.052	0.697±0.064	0.741±0.082	0.516±0.111
GSWI-2549003286	-	-	53.2287174	-27.8424242	0.095±0.058	0.181±0.072	0.389±0.099	0.511±0.122
-	z5_GSD_15249	z6_gdsd_28676	53.0622819	-27.7967716	0.14±0.045	0.415±0.062	0.313±0.042	0.505±0.068
GNDI-6507911018	z6_GND_40316	z6_gdnd_9639	189.2116002	62.1837540	0.03±0.063	0.294±0.083	0.428±0.048	0.505±0.077

Table A.11: Continuation of Appendix Table A.7.

ID(B15)	ID(F15)	ID(H16)	RA [Deg]	Dec [Deg]	Z-Flux/Err	Y-Flux/Err	J-Flux/Err	H-Flux/Err
-	-	z6_gdsd_43833	53.1718007	-27.7376268	0.221±0.053	0.697±0.072	0.456±0.04	0.503±0.073
GNWI-7144820170	-	-	189.3103041	62.3379722	0.115±0.05	0.413±0.064	0.359±0.092	0.5±0.119
-	z6_GSD_25386	-	53.1066162	-27.8282701	0.194±0.054	0.532±0.069	0.567±0.049	0.498±0.068
GNDI-7019412263	z5_GND_33776	z6_gdnd_15133	189.2580789	62.2072511	0.032±0.056	0.228±0.07	0.184±0.057	0.497±0.088
-	z6_GSD_15617	-	53.1428743	-27.7980134	0.033±0.009	0.254±0.017	0.423±0.053	0.495±0.066
-	z6_GSW_4428	z6_gdsw_7398	53.1450223	-27.8795891	0.163±0.056	0.424±0.075	0.335±0.093	0.495±0.112
GNDI-6499613560	z6_GND_25488	z6_gdnd_20794	189.2081924	62.2321319	0.137±0.051	0.631±0.06	0.72±0.071	0.492±0.073
-	z6_GSD_15795	-	53.1358598	-27.7983210	0.136±0.008	0.587±0.015	0.69±0.048	0.487±0.06
GNDI-7014917288	z6_GND_44138	z6_gdnd_34567	189.2562123	62.2912526	-0.013±0.047	0.232±0.058	0.274±0.048	0.477±0.073
-	-	z6_gdsd_28368	53.1428400	-27.7978775	-0.004±0.053	0.18±0.076	0.273±0.044	0.474±0.076
GNWI-7428619417	-	z6_gdnw_34769	189.4285617	62.3281917	0.045±0.052	0.531±0.068	0.618±0.099	0.474±0.117
GNDI-7145309590	z6_GND_2041	-	189.3105810	62.1663172	0.183±0.05	0.463±0.065	0.481±0.045	0.472±0.1
GSDI-2359645099	z6_GSD_2446	-	53.1498346	-27.7527512	0.008±0.051	0.234±0.069	0.455±0.036	0.471±0.066
GSDI-2431745175	-	-	53.1798901	-27.7548759	0.133±0.055	0.582±0.07	0.462±0.045	0.47±0.071
GNDI-6570914030	z6_GND_24765	z6_gdnd_21249	189.2378636	62.2341118	0.094±0.055	0.455±0.067	0.508±0.075	0.469±0.083
GSDI-2523847534	z6_GSD_15744	z6_gdsd_28276	53.2182684	-27.7981677	0.071±0.059	0.433±0.075	0.377±0.044	0.467±0.084
GSDI-2218250289	z6_GSD_29590	z6_gdsd_17339	53.0909508	-27.8413600	0.041±0.053	0.369±0.076	0.356±0.049	0.461±0.057
-	-	z6_xdf_4725	53.1561006	-27.7757835	-0.004±0.008	0.244±0.014	0.403±0.008	0.46±0.012
GNDI-6496713551	-	z6_gdnd_20749	189.2070247	62.2319170	0.05±0.053	0.383±0.068	0.495±0.075	0.459±0.082
GSDI-2063447220	-	-	53.0264757	-27.7894476	0.057±0.07	0.199±0.092	0.261±0.052	0.452±0.078
GSDI-2258246513	-	z6_gdsd_33406	53.1075728	-27.7809258	0.121±0.045	0.393±0.058	0.43±0.04	0.452±0.071
XDFI-2350547402	-	-	53.1460698	-27.7944931	0.013±0.008	0.234±0.015	0.379±0.007	0.45±0.012
GNDI-6326418256	z6_GND_42241	z6_gdnd_37954	189.1360139	62.3070537	0.149±0.048	0.447±0.064	0.32±0.053	0.45±0.081
GNDI-6297212561	-	-	189.1238627	62.2155010	0.08±0.051	0.383±0.062	0.246±0.094	0.447±0.093
GNDI-6255417241	z6_GND_44248	z6_gdnd_34343	189.1064715	62.2899713	0.031±0.05	0.302±0.065	0.323±0.045	0.445±0.082
GSDI-2147447587	-	z6_gdsd_27882	53.0614022	-27.7996447	0.312±0.051	0.921±0.067	0.523±0.05	0.441±0.073
-	-	z6_gdsd_34867	53.2029696	-27.7760586	0.052±0.061	0.181±0.071	0.381±0.042	0.439±0.072
GSDI-2299747027	z6_GSD_10956	-	53.1248944	-27.7841346	0.241±0.055	0.482±0.071	0.603±0.033	0.434±0.071
GSDI-2485646173	z6_GSD_6874	z6_gdsd_36115	53.2023335	-27.7714912	0.078±0.06	0.325±0.076	0.292±0.047	0.432±0.084
GNDI-6582114532	z6_GND_19841	-	189.2425660	62.2480060	0.05±0.051	0.363±0.066	0.343±0.076	0.43±0.075
GSDI-2337848076	z6_GSD_17018	-	53.1407446	-27.8021082	0.072±0.008	0.449±0.015	0.376±0.05	0.427±0.06
-	-	z6_gdsd_26116	53.1547396	-27.8064544	0.077±0.055	0.316±0.069	0.153±0.039	0.423±0.072
GSDI-2284847073	-	-	53.1186846	-27.7853853	-0.048±0.056	0.279±0.072	0.364±0.042	0.421±0.074
GSDI-2229748055	-	z6_gdsd_27378	53.0957310	-27.8015533	0.029±0.043	0.24±0.058	0.278±0.05	0.421±0.073
-	z6_GND_3337	z6_gdnd_8056	189.2447477	62.1756139	0.016±0.051	0.142±0.063	0.29±0.048	0.417±0.077

Table A.12: Continuation of Appendix Table A.7.

ID(B15)	ID(F15)	ID(H16)	RA [Deg]	Dec [Deg]	Z-Flux/Err	Y-Flux/Err	J-Flux/Err	H-Flux/Err
GSDI-2342847522	z6_GSD_15616	-	53.1428494	-27.7978739	0.059±0.008	0.236±0.016	0.247±0.052	0.416±0.066
GNDI-6369212204	z6_GND_34344	z6_gdnd_14703	189.1538213	62.2055907	0.003±0.048	0.426±0.056	0.343±0.096	0.412±0.085
-	z6_GND_31073	z6_gdnd_17108	189.1239104	62.2154809	0.037±0.053	0.289±0.063	0.272±0.096	0.411±0.092
-	-	z6_gdsd_31583	53.1255102	-27.7866787	0.06±0.056	0.19±0.074	0.352±0.04	0.408±0.071
-	z6_GND_29625	z6_gdnd_18071	189.4036221	62.2198724	-0.012±0.048	0.21±0.062	0.297±0.071	0.407±0.075
GSDI-2334247448	z6_GSD_14965	-	53.1392717	-27.7958027	0.054±0.008	0.391±0.015	0.567±0.045	0.406±0.056
GSDI-2348045458	-	-	53.1450187	-27.7627106	0.07±0.055	0.307±0.071	0.382±0.042	0.405±0.074
-	z6_GSD_4137	z6_gdsd_38714	53.1190779	-27.7607392	-0.088±0.051	0.432±0.063	0.539±0.044	0.405±0.073
GNDI-6362112180	z6_GND_34565	z6_gdnd_14567	189.1508447	62.2049389	0.081±0.052	0.443±0.063	0.331±0.096	0.404±0.089
-	-	z6_gdsd_7021	53.0665531	-27.8816349	-0.02±0.056	0.201±0.079	0.144±0.061	0.402±0.089
-	z6_GND_15034	z6_gdnd_27803	189.1220452	62.2613200	0.119±0.051	0.413±0.06	0.275±0.034	0.397±0.067
GSDI-2178548171	-	-	53.0743795	-27.8047699	0.118±0.047	0.241±0.067	0.417±0.064	0.397±0.083
GNDI-7103811556	z6_GND_36192	-	189.2932370	62.1986945	0.04±0.053	0.238±0.067	0.155±0.053	0.393±0.083
GSDI-2150046238	z6_GSD_7400	z6_gdsd_35641	53.0624899	-27.7732848	0.013±0.054	0.34±0.07	0.395±0.051	0.386±0.069
-	-	z6_gdsd_29287	53.1226760	-27.7946114	-0.045±0.062	0.362±0.081	0.224±0.045	0.379±0.078
-	-	z6_gdnd_29859	189.1010049	62.2695570	0.035±0.049	0.2±0.064	0.209±0.053	0.379±0.071
GNDI-7152015370	z5_GND_15432	z6_gdnd_27561	189.3133030	62.2602208	0.08±0.048	0.314±0.065	0.267±0.064	0.377±0.084
GSDI-2109048094	-	-	53.0454533	-27.8026162	0.074±0.043	0.181±0.057	0.344±0.054	0.376±0.072
GNWI-6474712002	-	-	189.1978091	62.1999822	0.094±0.054	0.498±0.07	21.63±9.735	0.374±0.07
GSDI-2174547388	z6_GSD_14417	z6_gdsd_29448	53.0727249	-27.7941286	0.039±0.044	0.408±0.062	0.493±0.049	0.373±0.067
GNDI-7010312280	-	-	189.2543040	62.2077102	0.25±0.053	0.545±0.062	0.531±0.046	0.37±0.067
GSDI-2487648069	z6_GSD_16979	z6_gdsd_27272	53.2032001	-27.8019272	0.052±0.059	0.433±0.075	0.377±0.044	0.37±0.064
-	z6_GSD_4551	-	53.1449931	-27.7627479	0.05±0.054	0.243±0.068	0.302±0.041	0.365±0.072
GSDI-2281451341	z6_GSD_33775	z6_gdsd_12265	53.1172805	-27.8594736	0.057±0.042	0.303±0.057	0.375±0.05	0.363±0.071
GNDI-7244411342	z6_GND_38003	z6_gdnd_11724	189.3517709	62.1927464	0.066±0.05	0.439±0.065	0.365±0.041	0.358±0.077
GSDI-2301245179	z6_GSD_2913	z6_gdsd_40021	53.1255332	-27.7549643	0.048±0.055	0.192±0.072	0.24±0.033	0.351±0.067
-	-	z6_gdsd_31903	53.0792335	-27.7857714	0.047±0.06	0.245±0.078	0.33±0.065	0.351±0.082
-	-	z6_gdnd_35068	189.1495061	62.2935047	-0.007±0.049	0.228±0.063	0.318±0.049	0.349±0.067
GNDI-6598214577	z6_GND_19428	-	189.2492423	62.2492631	0.115±0.052	0.26±0.068	0.424±0.075	0.349±0.081
-	-	z6_gdsd_7766	53.0808323	-27.8776657	0.051±0.054	0.276±0.074	0.328±0.052	0.349±0.073
-	z6_GND_32873	-	189.1898303	62.2101584	0.079±0.044	0.194±0.057	0.24±0.109	0.348±0.067
GNDI-6440313146	-	-	189.1835086	62.2206305	0.197±0.046	0.491±0.056	0.58±0.09	0.347±0.072
-	-	z6_gdsd_24701	53.1704894	-27.8124294	0.014±0.055	0.305±0.072	0.263±0.028	0.346±0.063
-	-	z6_gdsd_28235	53.1359812	-27.7983940	0.004±0.056	0.333±0.075	0.309±0.04	0.345±0.075
GNDI-7356113437	-	-	189.3984168	62.2287167	0.088±0.051	0.207±0.067	0.261±0.082	0.344±0.079

Table A.13: Continuation of Appendix Table A.7. The horizontal line represents H-band 27.5 magnitude limit for priority class 4 DEEP surveys in the XDF field.

ID(B15)	ID(F15)	ID(H16)	RA [Deg]	Dec [Deg]	Z-Flux/Err	Y-Flux/Err	J-Flux/Err	H-Flux/Err
-	z5_GND_16761	z6_gdnd_26645	189.1330967	62.2565291	0.147±0.049	0.409±0.064	0.203±0.05	0.344±0.076
GNDI-6434014203	z6_GND_23050	z6_gdnd_22446	189.1808841	62.2388666	0.106±0.05	0.261±0.062	0.309±0.059	0.341±0.065
GSDI-2345950117	z6_GSD_28183	z6_gdsd_18683	53.1441533	-27.8365998	0.116±0.048	0.373±0.063	0.39±0.045	0.338±0.081
GNDI-6412516086	z6_GND_12436	z6_gdnd_29671	189.1719457	62.2689856	0.048±0.049	0.205±0.064	0.229±0.108	0.337±0.079
-	z5_GSD_12992	-	53.0842308	-27.7898860	0.18±0.048	0.457±0.065	0.438±0.051	0.336±0.065
GSDI-2252850209	z6_GSD_28975	z6_gdsd_17958	53.1053263	-27.8391375	0.071±0.044	0.375±0.06	0.36±0.046	0.335±0.056
-	z6_GND_31645	-	189.3171994	62.2136640	0.078±0.051	0.197±0.063	0.269±0.051	0.33±0.075
GSDI-2168151080	z6_GSD_32291	z6_gdsd_14279	53.0700587	-27.8522134	0.11±0.041	0.299±0.058	0.323±0.055	0.33±0.068
GSDI-2122848213	z6_GSD_18240	-	53.0512104	-27.8059058	0.098±0.056	0.326±0.072	0.238±0.051	0.326±0.072
GSDI-2355350055	z6_GSD_27580	z6_gdsd_19126	53.1480272	-27.8348742	-0.001±0.062	0.273±0.078	0.301±0.042	0.326±0.074
GSDI-2390645387	z6_MAIN_101	-	53.1627722	-27.7607680	0.133±0.008	0.544±0.016	0.44±0.013	0.325±0.016
-	-	z6_gdsd_32409	53.1005915	-27.7843226	0.07±0.045	0.191±0.059	0.165±0.035	0.325±0.068
XDFI-2369745576	z6_MAIN_452	z6_xdf_5653	53.1540559	-27.7659983	0.031±0.008	0.271±0.016	0.336±0.008	0.32±0.01
-	-	z6_gdsd_17911	53.0977368	-27.8392749	0.05±0.049	0.348±0.072	0.362±0.045	0.317±0.059
-	z5_GND_21520	z6_gdnd_23443	189.0919439	62.2431427	0.104±0.05	0.313±0.063	0.341±0.08	0.316±0.076
GSDI-2264948318	-	z6_gdsd_25570	53.1103921	-27.8088717	-0.088±0.061	0.218±0.077	0.247±0.036	0.309±0.073
-	-	z6_gdsd_15198	53.1383432	-27.8492443	0.036±0.046	0.165±0.062	0.175±0.041	0.309±0.075
GNDI-7163514576	z6_GND_19416	z6_gdnd_24856	189.3181997	62.2492642	-0.021±0.05	0.27±0.067	0.379±0.047	0.308±0.07
GSDI-2372045292	-	z6_gdsd_39284	53.1550450	-27.7581268	0.028±0.046	0.202±0.062	0.227±0.04	0.306±0.074
-	z6_GND_38075	z6_gdnd_11673	189.2603521	62.1925561	0.1±0.05	0.266±0.069	0.288±0.051	0.305±0.073
GNDI-7161212494	-	z6_gdnd_16685	189.3171961	62.2136415	0.08±0.05	0.215±0.062	0.362±0.052	0.303±0.075
GSDI-2364745240	-	z7_gdsd_39598	53.1519664	-27.7566770	-0.075±0.047	0.15±0.063	0.265±0.039	0.299±0.068
GSDI-2531949442	z6_GSD_25631	z6_gdsd_20623	53.2216332	-27.8289528	0.05±0.054	0.459±0.074	0.377±0.045	0.297±0.074
-	z6_GSD_22818	z6_gdsd_22827	53.1041155	-27.8203495	0.046±0.054	0.417±0.072	0.31±0.052	0.294±0.057
GSDI-2383251063	z6_GSD_32191	z6_gdsd_14407	53.1596921	-27.8517644	-0.04±0.054	0.228±0.073	0.205±0.041	0.289±0.067
GSDI-2350848068	-	-	53.1461677	-27.8018835	0.013±0.008	0.182±0.016	0.175±0.054	0.285±0.06
-	z6_GND_19366	-	189.3681865	62.2493607	-0.027±0.054	0.413±0.07	0.211±0.047	0.284±0.069
-	-	z6_gdsd_14118	53.1511904	-27.8527420	0.081±0.047	0.166±0.063	0.196±0.039	0.283±0.066
GSDI-2409148447	-	-	53.1704775	-27.8124252	0.061±0.008	0.269±0.015	0.312±0.034	0.283±0.049
-	-	z6_gdsd_40943	53.1469987	-27.7510393	0.029±0.053	0.255±0.069	0.245±0.041	0.274±0.068
GSDI-2364348341	-	-	53.1518585	-27.8095261	0.071±0.008	0.265±0.015	0.334±0.047	0.266±0.058
XDFI-2382747512	z6_MAIN_5458	z6_xdf_1626	53.1595046	-27.7975835	0.072±0.008	0.319±0.015	0.298±0.007	0.247±0.011
GSDI-2427948032	-	-	53.1783315	-27.8009027	0.011±0.008	0.254±0.015	0.238±0.045	0.223±0.055
XDFI-2430246236	z6_MAIN_1225	-	53.1792773	-27.7732390	0.006±0.008	0.223±0.015	0.285±0.009	0.221±0.012
XDFI-2447046454	z6_MAIN_2277	-	53.1862596	-27.7792911	0.046±0.008	0.194±0.016	0.236±0.01	0.21±0.011

Table A.14: Continuation of Appendix Table A.7. The horizontal line represents H-band 28.0 magnitude limit for priority class 6 MEDIUM surveys in the GOODS field.

ID(B15)	ID(F15)	ID(H16)	RA [Deg]	Dec [Deg]	Z-Flux/Err	Y-Flux/Err	J-Flux/Err	H-Flux/Err
GSDI-2425948088	-	-	53.1774900	-27.8024535	0.05±0.008	0.281±0.016	0.379±0.046	0.205±0.047
-	z6_MAIN_976	z6_xdf_5266	53.1660952	-27.7719665	0.004±0.008	0.248±0.015	0.2±0.008	0.201±0.011
XDFI-2387847107	-	z6_xdf_3245	53.1616030	-27.7863476	0.034±0.008	0.151±0.014	0.179±0.008	0.197±0.011
XDFI-2423646157	-	-	53.1765136	-27.7710335	0.102±0.008	0.322±0.015	0.224±0.009	0.188±0.012
GSDI-2313048082	z6_GSD_17921	-	53.1304195	-27.8022841	0.04±0.005	0.226±0.008	0.273±0.024	0.174±0.033
XDFI-2394545434	z6_MAIN_158	-	53.1643972	-27.7620653	0.02±0.008	0.214±0.015	0.223±0.012	0.171±0.015
XDFI-2385446175	z6_MAIN_929	z6_xdf_5310	53.1606032	-27.7715355	0.032±0.009	0.254±0.016	0.201±0.009	0.165±0.013
-	z6_MAIN_2957	-	53.1440667	-27.7827799	0.016±0.008	0.139±0.016	0.148±0.01	0.158±0.015
XDFI-2397748121	-	-	53.1657450	-27.8033809	0.052±0.009	0.219±0.017	0.168±0.01	0.147±0.013
XDFI-2397946337	z6_MAIN_1609	z6_xdf_4817	53.1657878	-27.7760440	0.01±0.008	0.122±0.015	0.151±0.008	0.143±0.012
-	z5_MAIN_4394	-	53.1389911	-27.7903110	0.052±0.008	0.151±0.015	0.139±0.009	0.143±0.011
XDFI-2391248184	-	z6_xdf_828	53.1630346	-27.8051314	0.023±0.008	0.116±0.014	0.138±0.007	0.141±0.01
-	z6_MAIN_3201	-	53.1348212	-27.7841195	0.029±0.009	0.198±0.018	0.186±0.017	0.137±0.021
XDFI-2405548026	z6_MAIN_5666	-	53.1689794	-27.8007161	-0.001±0.008	0.13±0.015	0.154±0.01	0.137±0.013
XDFI-2401047389	z6_MAIN_4980	z6_xdf_2103	53.1670984	-27.7941667	0.057±0.009	0.159±0.017	0.132±0.008	0.124±0.01
-	z6_MAIN_303	-	53.1527189	-27.7641973	0.029±0.008	0.083±0.015	0.099±0.016	0.121±0.021
XDFI-2368147582	-	z6_xdf_1434	53.1534045	-27.7995033	0.057±0.009	0.158±0.016	0.147±0.009	0.112±0.012
-	z6_MAIN_1575	-	53.1808891	-27.7766875	0.015±0.009	0.048±0.017	0.065±0.011	0.106±0.021
XDFI-2426947749	z6_MAIN_3487	z6_xdf_3413	53.1778354	-27.7853587	0.023±0.008	0.1±0.015	0.116±0.008	0.105±0.01
XDFI-2381547333	-	z6_xdf_2329	53.1589817	-27.7926021	0.021±0.008	0.117±0.016	0.108±0.008	0.101±0.011
XDFI-2340346372	-	-	53.1417882	-27.7770135	0.016±0.008	0.052±0.016	0.069±0.011	0.1±0.016
-	z6_MAIN_847	-	53.1515012	-27.7731604	0.019±0.009	0.036±0.016	0.071±0.01	0.099±0.011
XDFI-2376846215	z6_MAIN_1117	z6_xdf_5201	53.1570362	-27.7726394	0.007±0.008	0.105±0.015	0.12±0.008	0.096±0.012

Table A.15: Continuation of Appendix Table A.7. The horizontal line represents H-band 29.0 magnitude limit for priority class 6 DEEP surveys in the XDF field.

Bibliography

Abel T., Bryan G. L., Norman M. L., 2002, Science, 295, 93

Abraham R. G., van den Bergh S., Glazebrook K., Ellis R. S., Santiago B. X., Surma P., Griffiths R. E., 1996, The Astrophysical Journal Supplement Series, 107, 1

Alexander D. M., et al., 2003, The Astronomical Journal, 126, 539

Alloin D., Collin-Souffrin S., Joly M., Vigroux L., 1979, Astronomy and Astrophysics, 78, 200

Amorín R. O., Pérez-Montero E., Vílchez J. M., 2010, The Astrophysical Journal Letters, 715, L128

Amorín R., et al., 2015, Astronomy and Astrophysics, 578, A105

Appenzeller I., et al., 1998, The Messenger, 94, 1

Atek H., et al., 2010, The Astrophysical Journal, 723, 104

Atek H., et al., 2011, The Astrophysical Journal, 743, 121

Bacon R., et al., 2010, in McLean I. S., Ramsay S. K., Takami H., eds, Society of Photo-Optical Instrumentation Engineers (SPIE) Conference Series Vol. 7735, Ground-based and Airborne Instrumentation for Astronomy III. p. 773508, doi:10.1117/12.856027

Baldwin J. A., Phillips M. M., Terlevich R., 1981, Publications of the Astronomical Society of the Pacific, 93, 5

Balestra I., et al., 2010, Astronomy and Astrophysics, 512, A12

Bassett R., Ryan-Weber E. V., Cooke J., Meštrić U., Kakiichi K., Prichard L., Rafelski M., 2021, Monthly Notices of the Royal Astronomical Society,

Becker G. D., Bolton J. S., 2013, Monthly Notices of the Royal Astronomical Society, 436, 1023

Becker R. H., et al., 2001, The Astronomical Journal, 122, 2850

Becker G. D., Bolton J. S., Lidz A., 2015, Publications of the Astronomical Society of Australia, 32, e045

Beckwith S. V. W., et al., 2006, The Astronomical Journal, 132, 1729

Bertin E., Arnouts S., 1996, Astronomy and Astrophysicss, 117, 393

Bouwens R. J., et al., 2010, The Astrophysical Journal Letters, 709, L133

Bouwens R. J., Illingworth G. D., Oesch P. A., 2015a, The Astrophysical Journal, 803, 34

Bouwens R. J., Illingworth G. D., Oesch P. A., Caruana J., Holwerda B., Smit R., Wilkins S., 2015b, The Astrophysical Journal, 811, 140

Bouwens R. J., et al., 2021, The Astrophysical Journal, 162, 47

Boylan-Kolchin M., 2018, Monthly Notices of the Royal Astronomical Society, 479, 332

Brammer G. B., van Dokkum P. G., Coppi P., 2008, The Astrophysical Journal, 686, 1503

Brammer G. B., et al., 2012, The Astrophysical Journal Supplement Series, 200, 13

Bromm V., Larson R. B., 2004, Annual Review of Astronomy and Astrophysics, 42, 79

Brunker S. W., Salzer J. J., Janowiecki S., Finn R. A., Helou G., 2020, The Astrophysical Journal, 898, 68

Bruzual G., Charlot S., 2003, Monthly Notices of the Royal Astronomical Society, 344, 1000

Bunker A. J., Stanway E. R., Ellis R. S., McMahon R. G., 2004, Monthly Notices of the Royal Astronomical Society, 355, 374

Bunker A., Stanway E., Ellis R., Lacy M., McMahon R., Eyles L., Stark D., Chiu K., 2008, in Bridle A. H., Condon J. J., Hunt G. C., eds, Astronomical Society of the Pacific Conference Series Vol. 395, Frontiers of Astrophysics: A Celebration of NRAO's 50th Anniversary. p. 73 (arXiv:0909.1565)

Bunker A. J., et al., 2010, Monthly Notices of the Royal Astronomical Society, 409, 855

Bunker A. J., NIRSPEC Instrument Science Team JAESs Collaboration 2020, in da Cunha E., Hodge J., Afonso J., Pentericci L., Sobral D., eds, Proceedings of the International Astronomical Union Vol. 352, Uncovering Early Galaxy Evolution in the ALMA and JWST Era. pp 342–346, doi:10.1017/S1743921319009463

Caldwell R. R., Dave R., Steinhardt P. J., 1998, Physical Review Letters, 80, 1582

Calzetti D., 2001, Publications of the Astronomical Society of the Pacific, 113, 1449

Calzetti D., Armus L., Bohlin R. C., Kinney A. L., Koornneef J., Storchi-Bergmann T., 2000, The Astrophysical Journal, 533, 682

Cappellari M., 2017, Monthly Notices of the Royal Astronomical Society, 466, 798

Cardamone C., et al., 2009, Monthly Notices of the Royal Astronomical Society, 399, 1191

Cardelli J. A., Clayton G. C., Mathis J. S., 1989, The Astrophysical Journal, 345, 245

Castellano M., et al., 2017, The Astrophysical Journal, 839, 73

Chabrier G., 2003, Publications of the Astronomical Society of the Pacific, 115, 763

Charlot S., Fall S. M., 2000, The Astrophysical Journal, 539, 718

Chevallard J., Charlot S., 2016, Monthly Notices of the Royal Astronomical Society, 462, 1415

Chevallard J., et al., 2018, Monthly Notices of the Royal Astronomical Society, 479, 3264

Cochrane R. K., Best P. N., Sobral D., Smail I., Geach J. E., Stott J. P., Wake D. A., 2018, Monthly Notices of the Royal Astronomical Society, 475, 3730

Coe D., et al., 2013, The Astrophysical Journal, 762, 32

Coil A. L., et al., 2015, The Astrophysical Journal, 801, 35

Colbert J. W., et al., 2013, The Astrophysical Journal, 779, 34

Coleman G. D., Wu C. C., Weedman D. W., 1980, The Astrophysical Journal Supplement Series, 43, 393

Colless M., 1999, Philosophical Transactions of the Royal Society of London Series A, 357, 105

Conselice C. J., 2014, Annual Review of Astronomy and Astrophysics, 52, 291

Cullen F., Cirasuolo M., McLure R. J., Dunlop J. S., Bowler R. A. A., 2014, Monthly Notices of the Royal Astronomical Society, 440, 2300

Cullen F., et al., 2019, Monthly Notices of the Royal Astronomical Society, 487, 2038

Curti M., Cresci G., Mannucci F., Marconi A., Maiolino R., Esposito S., 2017, Monthly Notices of the Royal Astronomical Society, 465, 1384

Curti M., Mannucci F., Cresci G., Maiolino R., 2020, Monthly Notices of the Royal Astronomical Society, 491, 944

Davis M., et al., 2003, in Guhathakurta P., ed., Society of Photo-Optical Instrumentation Engineers (SPIE) Conference Series Vol. 4834, Discoveries and Research Prospects from 6- to 10-Meter-Class Telescopes II. pp 161–172 (arXiv:astro-ph/0209419), doi:10.1117/12.457897

De Barros S., Oesch P. A., Labbé I., Stefanon M., González V., Smit R., Bouwens R. J., Illingworth G. D., 2019, Monthly Notices of the Royal Astronomical Society, 489, 2355

Dijkstra M., Haiman Z., Loeb A., 2004, The Astrophysical Journal, 613, 646

Doherty M., Bunker A. J., Ellis R. S., McCarthy P. J., 2005, Monthly Notices of the Royal Astronomical Society, 361, 525

Domínguez A., et al., 2013, The Astrophysical Journal, 763, 145

Domínguez A., Siana B., Brooks A. M., Christensen C. R., Bruzual G., Stark D. P., Alavi A., 2015, Monthly Notices of the Royal Astronomical Society, 451, 839

Dressel L., 2021, Wide Field Camera 3 Instrument Handbook, Version 13.0. STScI, Baltimore, USA

Duncan K., et al., 2019, The Astrophysical Journal, 876, 110

Ellis R. S., et al., 2013, The Astrophysical Journal Letters, 763, L7

Elmegreen D. M., Elmegreen B. G., Ravindranath S., Coe D. A., 2007, The Astrophysical Journal, 658, 763

Emami N., Siana B., Alavi A., Gburek T., Freeman W. R., Richard J., Weisz D. R., Stark D. P., 2020, The Astrophysical Journal, 895, 116

Endsley R., Stark D. P., Chevallard J., Charlot S., 2021, Monthly Notices of the Royal Astronomical Society, 500, 5229

Erb D. K., Steidel C. C., Shapley A. E., Pettini M., Reddy N. A., Adelberger K. L., 2006, The Astrophysical Journal, 647, 128

Eyles L. P., Bunker A. J., Stanway E. R., Lacy M., Ellis R. S., Doherty M., 2005, Monthly Notices of the Royal Astronomical Society, 364, 443

Eyles L. P., Bunker A. J., Ellis R. S., Lacy M., Stanway E. R., Stark D. P., Chiu K., 2007, Monthly Notices of the Royal Astronomical Society, 374, 910

Faisst A. L., Masters D., Wang Y., Merson A., Capak P., Malhotra S., Rhoads J. E., 2018, The Astrophysical Journal, 855, 132

Fan X., et al., 2001, The Astronomical Journal, 122, 2833

Faucher-Giguère C.-A., Lidz A., Hernquist L., Zaldarriaga M., 2008, The Astrophysical Journal Letters, 682, L9

Fazio G. G., et al., 2004, The Astrophysical Journal Supplement Series, 154, 10

Finkelstein S. L., Ryan Jr. R. E., Papovich C., 2015, The Astrophysical Journal, 810, 71

Finkelstein S. L., et al., 2019, The Astrophysical Journal, 879, 36

Fletcher T. J., Tang M., Robertson B. E., Nakajima K., Ellis R. S., Stark D. P., Inoue A., 2019, The Astrophysical Journal, 878, 87

Foreman-Mackey D., Hogg D. W., Lang D., Goodman J., 2013, Publications of the Astronomical Society of the Pacific, 125, 306

Franx M., et al., 2003, The Astrophysical Journal Letters, 587, L79

Freeman K. C., 1970, The Astrophysical Journal, 160, 811

Freudling W., Romaniello M., Bramich D. M., Ballester P., Forchi V., García-Dabló C. E., Moehler S., Neeser M. J., 2013, Astronomy and Astrophysics, 559, A96

Fruchter A. S., Hook R. N., 2002, Publications of the Astronomical Society of the Pacific, 114, 144

Fukugita M., Ichikawa T., Gunn J. E., Doi M., Shimasaku K., Schneider D. P., 1996, The Astronomical Journal, 111, 1748

Fumagalli M., et al., 2012, The Astrophysical Journal Letters, 757, L22

Gardner J. P., et al., 2006, Space Science Reviews, 123, 485

Garilli B., et al., 2008, Astronomy and Astrophysics, 486, 683

Giallongo E., Menci N., Fiore F., Castellano M., Fontana A., Grazian A., Pentericci L., 2012, The Astrophysical Journal, 755, 124

Giallongo E., et al., 2015, Astronomy and Astrophysics, 578, A83

Giardino G., et al., 2019, in Teuben P. J., Pound M. W., Thomas B. A., Warner E. M., eds, Astronomical Society of the Pacific Conference Series Vol. 523, Astronomical Data Analysis Software and Systems XXVII. p. 645

Giavalisco M., et al., 2004, The Astrophysical Journal Letters, 600, L93

Gordon K. D., Clayton G. C., Misselt K. A., Landolt A. U., Wolff M. J., 2003, The Astrophysical Journal, 594, 279

Graham A. W., Driver S. P., 2005, Publications of the Astronomical Society of Australia, 22, 118

Grazian A., et al., 2018, Astronomy and Astrophysics, 613, A44

Grogin N. A., et al., 2011, The Astrophysical Journal Supplement Series, 197, 35

Groves B., Brinchmann J., Walcher C. J., 2012, Monthly Notices of the Royal Astronomical Society, 419, 1402

Gunn J. E., Peterson B. A., 1965, The Astrophysical Journal, 142, 1633

Guo Y., et al., 2013, The Astrophysical Journal Supplement Series, 207, 24

Gutkin J., Charlot S., Bruzual G., 2016, Monthly Notices of the Royal Astronomical Society, 462, 1757

Haardt F., Madau P., 2012, The Astrophysical Journal, 746, 125

Hainline K. N., Shapley A. E., Kornei K. A., Pettini M., Buckley-Geer E., Allam S. S., Tucker D. L., 2009, The Astrophysical Journal, 701, 52

Hainline K. N., et al., 2020, The Astrophysical Journal, 892, 125

Hamuy M., Walker A. R., Suntzeff N. B., Gigoux P., Heathcote S. R., Phillips M. M., 1992, Publications of the Astronomical Society of the Pacific, 104, 533

Hamuy M., Suntzeff N. B., Heathcote S. R., Walker A. R., Gigoux P., Phillips M. M., 1994, Publications of the Astronomical Society of the Pacific, 106, 566

Harikane Y., Ouchi M., Ono Y., More S., 2016, The Astrophysical Journal, 821, 123

Henry A., et al., 2013, The Astrophysical Journal Letters, 776, L27

Henry A., et al., 2021, The Astrophysical Journal, 919, 143

Hinshaw G., et al., 2013, The Astrophysical Journal Supplement Series, 208, 19

Hirano S., Hosokawa T., Yoshida N., Umeda H., Omukai K., Chiaki G., Yorke H. W., 2014, The Astrophysical Journal, 781, 60

Hogg D. W., 1999, arXiv e-prints, pp astro–ph/9905116

Hopkins A. M., Connolly A. J., Haarsma D. B., Cram L. E., 2001, The Astronomical Journal, 122, 288

Hopkins A. M., et al., 2003, The Astrophysical Journal, 599, 971

Hubble E. P., 1926, The Astrophysical Journal, 64, 321

Hubble E., 1929, Proceedings of the National Academy of Science, 15, 168

Hubble E. P., 1936, Realm of the Nebulae

Hunt L., et al., 2012, Monthly Notices of the Royal Astronomical Society, 427, 906

Hutchison T. A., et al., 2019, The Astrophysical Journal, 879, 70

Illingworth G. D., et al., 2013, The Astrophysical Journal Supplement Series, 209, 6

Izotov Y. I., Guseva N. G., Thuan T. X., 2011, The Astrophysical Journal, 728, 161

Izotov Y. I., Schaerer D., Thuan T. X., Worseck G., Guseva N. G., Orlitová I., Verhamme A., 2016, Monthly Notices of the Royal Astronomical Society, 461, 3683

Izotov Y. I., Worseck G., Schaerer D., Guseva N. G., Thuan T. X., Fricke Verhamme A., Orlitová I., 2018, Monthly Notices of the Royal Astronomical Society, 478, 4851

Jaskot A. E., Dowd T., Oey M. S., Scarlata C., McKinney J., 2019, The Astrophysical Journal, 885, 96

Jiang L., et al., 2021, Nature Astronomy, 5, 256

Juneau S., Dickinson M., Alexander D. M., Salim S., 2011, The Astrophysical Journal, 736, 104

Kaasinen M., Kewley L., Bian F., Groves B., Kashino D., Silverman J., Kartaltepe J., 2018, Monthly Notices of the Royal Astronomical Society, 477, 5568

Kennicutt Robert C. J., 1998, Annual Review of Astronomy and Astrophysics, 36, 189

Kewley L. J., Dopita M. A., 2002, The Astrophysical Journal Supplement Series, 142, 35

Kewley L. J., Dopita M. A., Sutherland R. S., Heisler C. A., Trevena J., 2001, The Astrophysical Journal, 556, 121

Kewley L. J., Groves B., Kauffmann G., Heckman T., 2006, Monthly Notices of the Royal Astronomical Society, 372, 961

Kewley L. J., Maier C., Yabe K., Ohta K., Akiyama M., Dopita M. A., Yuan T., 2013a, The Astrophysical Journal Letters, 774, L10

Kewley L. J., Dopita M. A., Leitherer C., Davé R., Yuan T., Allen M., Groves B., Sutherland R., 2013b, The Astrophysical Journal, 774, 100

Kewley L. J., Zahid H. J., Geller M. J., Dopita M. A., Hwang H. S., Fabricant D., 2015, The Astrophysical Journal Letters, 812, L20

Koekemoer A. M., Fruchter A. S., Hook R. N., Hack W., 2003, in HST Calibration Workshop : Hubble after the Installation of the ACS and the NICMOS Cooling System. p. 337

Koekemoer A. M., et al., 2011, The Astrophysical Journal Supplement Series, 197, 36

Kurk J., et al., 2013, Astronomy and Astrophysics, 549, A63

Labbé I., et al., 2013, The Astrophysical Journal Letters, 777, L19

Lanzetta K. M., Yahil A., Fernández-Soto A., 1996, Nature, 381, 759

Laporte N., Nakajima K., Ellis R. S., Zitrin A., Stark D. P., Mainali R., Roberts-Borsani G. W., 2017, The Astrophysical Journal, 851, 40

Lara-López M. A., et al., 2010, Astronomy and Astrophysics, 521, L53

Le Fèvre O., et al., 2005, Astronomy and Astrophysics, 439, 845

Le Fèvre O., et al., 2015, Astronomy and Astrophysics, 576, A79

Lee J. C., Kennicutt R. C., Funes S. J. J. G., Sakai S., Akiyama S., 2007, The Astrophysical Journal Letters, 671, L113

Lee J. C., et al., 2012, Publications of the Astronomical Society of the Pacific, 124, 782

Lilly S. J., Le Fevre O., Hammer F., Crampton D., 1996, The Astrophysical Journal Letters, 460, L1

Lilly S. J., Carollo C. M., Stockton A. N., 2003, The Astrophysical Journal, 597, 730

Lilly S. J., et al., 2007, The Astrophysical Journal Supplement Series, 172, 70

Lilly S. J., Carollo C. M., Pipino A., Renzini A., Peng Y., 2013, The Astrophysical Journal, 772, 119

Lorenzoni S., Bunker A. J., Wilkins S. M., Stanway E. R., Jarvis M. J., Caruana J., 2011, Monthly Notices of the Royal Astronomical Society, 414, 1455

Ly C., Lee J. C., Dale D. A., Momcheva I., Salim S., Staudaher S., Moore C. A., Finn R., 2011, The Astrophysical Journal, 726, 109

Ly C., Malkan M. A., Rigby J. R., Nagao T., 2016, The Astrophysical Journal, 828, 67

Madau P., 1995, The Astrophysical Journal, 441, 18

Madau P., Dickinson M., 2014, Annual Review of Astronomy and Astrophysics, 52, 415

Madau P., Haardt F., 2015, The Astrophysical Journal Letters, 813, L8

Madau P., Ferguson H. C., Dickinson M. E., Giavalisco M., Steidel C. C., Fruchter A., 1996, Monthly Notices of the Royal Astronomical Society, 283, 1388

Mainali R., Kollmeier J. A., Stark D. P., Simcoe R. A., Walth G., Newman A. B., Miller D. R., 2017, The Astrophysical Journal Letters, 836, L14

Mainali R., et al., 2018, Monthly Notices of the Royal Astronomical Society, 479, 1180

Maiolino R., Mannucci F., 2019, Astronomy and Astrophysicsr, 27, 3

Maiolino R., et al., 2008, Astronomy and Astrophysics, 488, 463

Mannucci F., Cresci G., Maiolino R., Marconi A., Gnerucci A., 2010, Monthly Notices of the Royal Astronomical Society, 408, 2115

Mannucci F., et al., 2021, Monthly Notices of the Royal Astronomical Society, 508, 1582

Mármol-Queraltó E., McLure R. J., Cullen F., Dunlop J. S., Fontana A., McLeod D. J., 2016, Monthly Notices of the Royal Astronomical Society, 460, 3587

Maseda M. V., et al., 2018, The Astrophysical Journal, 854, 29

Masters D., et al., 2014, The Astrophysical Journal, 785, 153

McGreer I. D., Mesinger A., D'Odorico V., 2015, Monthly Notices of the Royal Astronomical Society, 447, 499

McLure R. J., et al., 2011, Monthly Notices of the Royal Astronomical Society, 418, 2074

Merlin E., et al., 2021, Astronomy and Astrophysics, 649, A22

Mingozzi M., et al., 2020, Astronomy and Astrophysics, 636, A42

Mobasher B., et al., 2004, The Astrophysical Journal Letters, 600, L167

Momcheva I. G., et al., 2016, The Astrophysical Journal Supplement Series, 225, 27

Mouhcine M., Lewis I., Jones B., Lamareille F., Maddox S. J., Contini T., 2005, Monthly Notices of the Royal Astronomical Society, 362, 1143

Naidu R. P., Tacchella S., Mason C. A., Bose S., Oesch P. A., Conroy C., 2020, The Astrophysical Journal, 892, 109

Nakajima K., Ouchi M., Shimasaku K., Hashimoto T., Ono Y., Lee J. C., 2013, The Astrophysical Journal, 769, 3

Nakajima K., Ellis R. S., Robertson B. E., Tang M., Stark D. P., 2020, The Astrophysical Journal, 889, 161

Netzer H., 2015, Annual Review of Astronomy and Astrophysics, 53, 365

Neufeld D. A., 1991, The Astrophysical Journal Letters, 370, L85

Newman J. A., et al., 2013, The Astrophysical Journal Supplement Series, 208, 5

Newman S. F., et al., 2014, The Astrophysical Journal, 781, 21

Oesch P. A., et al., 2010a, The Astrophysical Journal Letters, 709, L21

Oesch P. A., et al., 2010b, The Astrophysical Journal Letters, 725, L150

Oesch P. A., et al., 2014, The Astrophysical Journal, 786, 108

Oesch P. A., et al., 2018, The Astrophysical Journal Supplement Series, 237, 12

Oke J. B., Gunn J. E., 1983, The Astrophysical Journal, 266, 713

Ono Y., et al., 2013, The Astrophysical Journal, 777, 155

Osterbrock D. E., 1989, Astrophysics of gaseous nebulae and active galactic nuclei

Osterbrock D. E., Ferland G. J., 2006, Astrophysics of gaseous nebulae and active galactic nuclei

Pagel B. E. J., Edmunds M. G., Blackwell D. E., Chun M. S., Smith G., 1979, Monthly Notices of the Royal Astronomical Society, 189, 95

Pahl A. J., Shapley A., Steidel C. C., Chen Y., Reddy N. A., 2021, Monthly Notices of the Royal Astronomical Society, 505, 2447

Partridge R. B., Peebles P. J. E., 1967, The Astrophysical Journal, 147, 868

Peebles P. J. E., 1968, The Astrophysical Journal, 153, 1

Peng C. Y., Ho L. C., Impey C. D., Rix H.-W., 2002, The Astronomical Journal, 124, 266

Perlmutter S., et al., 1999, The Astrophysical Journal, 517, 565

Planck Collaboration et al., 2020, Astronomy and Astrophysics, 641, A6

Pontoppidan K. M., et al., 2016, in Peck A. B., Seaman R. L., Benn C. R., eds, Society of Photo-Optical Instrumentation Engineers (SPIE) Conference Series Vol. 9910, Observatory Operations: Strategies, Processes, and Systems VI. p. 991016 (arXiv:1707.02202), doi:10.1117/12.2231768

Rasappu N., Smit R., Labbé I., Bouwens R. J., Stark D. P., Ellis R. S., Oesch P. A., 2016, Monthly Notices of the Royal Astronomical Society, 461, 3886

Ravindranath S., et al., 2006, The Astrophysical Journal, 652, 963

Reddy N. A., Steidel C. C., 2009, The Astronomical Journal, 692, 778

Reddy N. A., et al., 2015, The Astrophysical Journal, 806, 259

Reddy N. A., et al., 2018, The Astrophysical Journal, 869, 92

Renzini A., Peng Y.-j., 2015, The Astrophysical Journal Letters, 801, L29

Richards G. T., et al., 2006, The Astronomical Journal, 131, 2766

Rieke M., 2020, in da Cunha E., Hodge J., Afonso J., Pentericci L., Sobral D., eds, Proceedings of the International Astronomical Union Vol. 352, Uncovering Early Galaxy Evolution in the ALMA and JWST Era. pp 337–341, doi:10.1017/S1743921319008950

Rieke G. H., et al., 2004, The Astrophysical Journal Supplement Series, 154, 25

Rieke M. J., Kelly D., Horner S., 2005, in Heaney J. B., Burriesci L. G., eds, Society of Photo-Optical Instrumentation Engineers (SPIE) Conference Series Vol. 5904, Cryogenic Optical Systems and Instruments XI. pp 1–8, doi:10.1117/12.615554

Riess A. G., et al., 1998, The Astronomical Journal, 116, 1009

Rivera-Thorsen T. E., et al., 2017, Astronomy and Astrophysics, 608, L4

Roberts-Borsani G. W., et al., 2016, The Astrophysical Journal, 823, 143

Roberts-Borsani G. W., Ellis R. S., Laporte N., 2020, Monthly Notices of the Royal Astronomical Society, 497, 3440

Robertson B. E., Ellis R. S., Furlanetto S. R., Dunlop J. S., 2015, The Astrophysical Journal Letters, 802, L19

Rodighiero G., et al., 2011, The Astrophysical Journal Letters, 739, L40

Rodighiero G., et al., 2014, Monthly Notices of the Royal Astronomical Society, 443, 19

Rubin V. C., Ford W. K. J., Thonnard N., 1978, The Astrophysical Journal Letters, 225, L107

Salmon B., et al., 2015, The Astrophysical Journal, 799, 183

Salpeter E. E., 1955, The Astrophysical Journal, 121, 161

Sanders R. L., et al., 2016, The Astrophysical Journal, 816, 23

Sanders R. L., Shapley A. E., Zhang K., Yan R., 2017, The Astrophysical Journal, 850, 136

Sanders R. L., et al., 2018, The Astrophysical Journal, 858, 99

Sanders R. L., et al., 2021, The Astrophysical Journal, 914, 19

Santini P., et al., 2009, Astronomy and Astrophysics, 504, 751

Schenker M. A., Ellis R. S., Konidaris N. P., Stark D. P., 2014, The Astrophysical Journal, 795, 20

Schmidt K. B., et al., 2017, The Astrophysical Journal, 839, 17

Schreiber C., et al., 2015, Astronomy and Astrophysics, 575, A74

Seager S., Sasselov D. D., Scott D., 2000, The Astrophysical Journal Supplement Series, 128, 407

Sérsic J. L., 1963, Boletin de la Asociacion Argentina de Astronomia La Plata Argentina, 6, 41

Sérsic J. L., 1968, Atlas de Galaxias Australes

Shanks T., et al., 2015, Monthly Notices of the Royal Astronomical Society, 451, 4238

Shapley A. E., et al., 2019, The Astrophysical Journal Letters, 881, L35

Shivaei I., et al., 2018, The Astrophysical Journal, 855, 42

Skelton R. E., et al., 2014, The Astrophysical Journal Supplement Series, 214, 24

Smit R., et al., 2014, The Astrophysical Journal, 784, 58

Smit R., et al., 2015, The Astrophysical Journal, 801, 122

Smoot G. F., et al., 1992, The Astrophysical Journal Letters, 396, L1

Sobral D., et al., 2009, Monthly Notices of the Royal Astronomical Society, 398, 75

Speagle J. S., Steinhardt C. L., Capak P. L., Silverman J. D., 2014, The Astrophysical Journal Supplement Series, 214, 15

Stanway E. R., Bunker A. J., McMahon R. G., 2003, Monthly Notices of the Royal Astronomical Society, 342, 439

Stanway E. R., Eldridge J. J., Becker G. D., 2016, Monthly Notices of the Royal Astronomical Society, 456, 485

Stark D. P., 2016, Annual Review of Astronomy and Astrophysics, 54, 761

Stark D. P., Schenker M. A., Ellis R., Robertson B., McLure R., Dunlop J., 2013, The Astrophysical Journal, 763, 129

Stark D. P., et al., 2015a, Monthly Notices of the Royal Astronomical Society, 450, 1846

Stark D. P., et al., 2015b, Monthly Notices of the Royal Astronomical Society, 454, 1393

Stark D. P., et al., 2017, Monthly Notices of the Royal Astronomical Society, 464, 469

Steidel C. C., Giavalisco M., Dickinson M., Adelberger K. L., 1996a, The Astronomical Journal, 112, 352

Steidel C. C., Giavalisco M., Pettini M., Dickinson M., Adelberger K. L., 1996b, The Astrophysical Journal Letters, 462, L17

Steidel C. C., Bogosavljević M., Shapley A. E., Reddy N. A., Rudie G. C., Pettini M., Trainor R. F., Strom A. L., 2018, The Astrophysical Journal, 869, 123

Storey P. J., Zeippen C. J., 2000, Monthly Notices of the Royal Astronomical Society, 312, 813

Strom A. L., Steidel C. C., Rudie G. C., Trainor R. F., Pettini M., Reddy N. A., 2017, The Astrophysical Journal, 836, 164

Sulentic J. W., Marziani P., del Olmo A., Dultzin D., Perea J., Negrete C. A., 2014, Astronomy and Astrophysics, 570, A96

Sullivan M., Mobasher B., Chan B., Cram L., Ellis R., Treyer M., Hopkins A., 2001, The Astrophysical Journal, 558, 72

Tang M., Stark D. P., Chevallard J., Charlot S., 2019, Monthly Notices of the Royal Astronomical Society, 489, 2572

Tang M., Stark D. P., Chevallard J., Charlot S., Endsley R., Congiu E., 2021a, Monthly Notices of the Royal Astronomical Society, 501, 3238

Tang M., Stark D. P., Chevallard J., Charlot S., Endsley R., Congiu E., 2021b, Monthly Notices of the Royal Astronomical Society, 503, 4105

Thompson D., Djorgovski S. G., 1995, The Astronomical Journal, 110, 982

Thompson D., Djorgovski S., Trauger J., 1995, The Astronomical Journal, 110, 963

Topping M. W., Shapley A. E., Stark D. P., Endsley R., Robertson B., Greene J. E., Furlanetto S. R., Tang M., 2021, The Astrophysical Journal Letters, 917, L36

Trebitsch M., Blaizot J., Rosdahl J., Devriendt J., Slyz A., 2017, Monthly Notices of the Royal Astronomical Society, 470, 224

Tremonti C. A., et al., 2004, The Astrophysical Journal, 613, 898

Tully R. B., Fisher J. R., 1977, Astronomy and Astrophysics, 500, 105

Vale Asari N., Couto G. S., Cid Fernandes R., Stasińska G., de Amorim A. L., Ruschel-Dutra D., Werle A., Florido T. Z., 2019, Monthly Notices of the Royal Astronomical Society, 489, 4721

Vanzella E., et al., 2008, Astronomy and Astrophysics, 478, 83

Vanzella E., et al., 2016, The Astrophysical Journal, 825, 41

Vanzella E., et al., 2020, Monthly Notices of the Royal Astronomical Society, 491, 1093

Veilleux S., Osterbrock D. E., 1987, The Astrophysical Journal Supplement Series, 63, 295

Werner M. W., et al., 2004, The Astrophysical Journal Supplement Series, 154, 1

Wilkins S. M., Bunker A. J., Stanway E., Lorenzoni S., Caruana J., 2011, Monthly Notices of the Royal Astronomical Society, 417, 717

Wilkins S. M., Stanway E. R., Bremer M. N., 2014, Monthly Notices of the Royal Astronomical Society, 439, 1038

Williams R. E., et al., 1996, The Astronomical Journal, 112, 1335

Williams C. C., et al., 2018, The Astrophysical Journal Supplement Series, 236, 33

Wolf C., Meisenheimer K., Röser H. J., 2001, Astronomy and Astrophysics, 365, 660

Worthey G., 1994, The Astrophysical Journal Supplement Series, 95, 107

Wuyts S., et al., 2013, The Astrophysical Journal, 779, 135

Xue Y. Q., et al., 2011, The Astrophysical Journal Supplement Series, 195, 10

Xue Y. Q., Luo B., Brandt W. N., Alexander D. M., Bauer F. E., Lehmer B. D., Yang G., 2016, The Astrophysical Journal Supplement Series, 224, 15

Yabe K., et al., 2014, Monthly Notices of the Royal Astronomical Society, 437, 3647

York D. G., et al., 2000, The Astronomical Journal, 120, 1579

Zel'dovich Y. B., Kurt V. G., Syunyaev R. A., 1969, Soviet Journal of Experimental and Theoretical Physics, 28, 146

Zheng W., et al., 2012, Nature, 489, 406

Zurita A., Rozas M., Beckman J. E., 2000, Astronomy and Astrophysics, 363, 9

Zwicky F., 1933, Helvetica Physica Acta, 6, 110

da Cunha E., Charlot S., Elbaz D., 2008, Monthly Notices of the Royal Astronomical Society, 388, 1595

de Vaucouleurs G., 1948, Annales d'Astrophysique, 11, 247

van Dokkum P. G., 2001, Publications of the Astronomical Society of the Pacific, 113, 1420

van der Wel A., et al., 2011, The Astrophysical Journal, 742, 111

van der Wel A., et al., 2012, The Astrophysical Journal Supplement Series, 203, 24

A long time ago in a galaxy far, far away....